

**THE INTERACTION BETWEEN A BEAM
AND A LAYER OF MICROWAVE-ABSORBING
MATERIAL**

A Dissertation

Presented to the Faculty of the Graduate School
of Cornell University

in Partial Fulfillment of the Requirements for the Degree of
Doctor of Philosophy

by

Walter H. Hartung

May 1996

© 1996 Walter H. Hartung

ALL RIGHTS RESERVED

THE INTERACTION BETWEEN A BEAM AND A LAYER OF MICROWAVE-ABSORBING MATERIAL

Walter H. Hartung, Ph.D.

Cornell University 1996

A phased luminosity upgrade of the CESR electron-positron storage ring is in progress. The upgrade program calls for the installation of superconducting radio-frequency (RF) cavities with strongly damped higher-order modes (HOMs). The cavity is designed to allow all HOMs to propagate into the beam pipe, where they are damped by a layer of microwave-absorbing ferrite. RF measurements with a copper cavity and loads made of a nickel-zinc ferrite indicate that the design gives adequate HOM damping. Because the absorbing layer is on the beam pipe, there is a direct parasitic interaction with the beam. To quantify this parasitic interaction, the complex permeability and complex permittivity of the ferrite were measured as a function of frequency. These results were used to predict the beam coupling impedance of the ferrite loads via numerical and analytic techniques. The predictive methods were checked using the pulse-on-a-wire method for measuring the coupling impedance. Beam stability predictions based on the calculated impedance indicate that there should be no beam instabilities due to the direct interaction between the beam and the ferrite layer for a 183-bunch beam with a total current of 2 A per beam. The average power dissipation in the ferrite, including both direct and indirect power transfer from the beam, is predicted to be 82 W/cm^2 with 2 A per beam. To test the predictions, beam measurements were done in CESR on a ferrite load of magnified coupling impedance. The beam-induced power dissipation in the ferrite layer was within a factor of 2 of the predicted value. It was difficult to see an effect on the beam due to the presence of the ferrite, a result that is consistent with our present understanding.

Biographical Sketch

by T. Hays & J. Knobloch

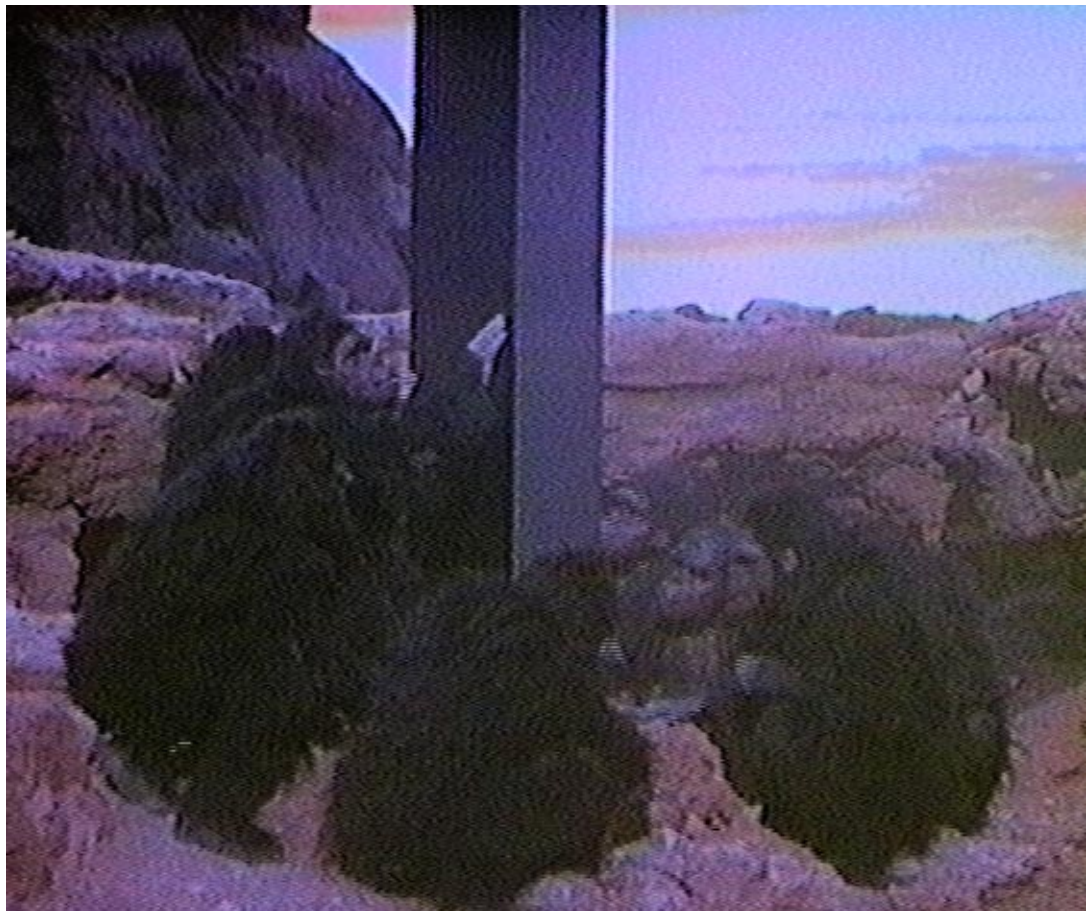
Walter H. Hartung was born June 27, 1965 in Madison, Wisconsin to Richard and Mary Hartung. He attended East Lansing High School and graduated in 1983 upon which he entered Cornell University as an undergraduate. He obtained two Bachelors degrees in 1987 from Cornell; a B.S. in Mechanical and Aerospace Engineering and a B.A. in Physics.

As a graduate student he continued his studies at Cornell and completed a Master of Engineering in Mechanical Engineering in 1988. At that time he entered the Applied Physics Ph.D. program leading to this thesis.

In 1985, while still an undergraduate, he joined the Cornell SRF group as part of a college work/study program. He continued working with the group part time during the semesters and full time during the summers. The only significant time he spent away from the group was a period of 6 months in 1991 working on superconducting RF at CERN as a *attaché non rémunéré*.

Some of his diverse activities as an SRF researcher include designing the “tongue” coupler used in the BB1 Cornell superconducting cavity, coining the name “TeSLA” for the TeV Superconducting Linear Accelerator, and founding the Cornell SRF Software Library.

For his future plans, Walter is not ruling out playing piano on the Paris Metro.



2001: A Space Odyssey © 1968 Turner Entertainment Co. All rights reserved.

Microwave-absorbing ferrite tile is revealed to early accelerator scientists.

Acknowledgements

I thank my chief thesis advisors, H. S. Padamsee and D. L. Rubin, and my other committee members, R. A. Buhrman and P. C. T. de Boer, for their guidance and support. I thank D. L. Moffat for guiding me through much of the experimental work described herein and P. E. Barnes for making the ferrite beam test possible. I thank the members of the SRF group at Cornell for their support and friendship, especially K. Akai, S. A. Belomestnykh, R. C. Chiang, E. P. Chojnacki, A. C. Crawford, J. H. Graber, T. R. Hays, J. L. Kirchgessner, J. Knobloch, D. Metzger, H. J. Muller, M. J. Pekeler, J. O. Sears, A. G. Tribendis, and V. Veshcherevich. I thank the staff of the Laboratory of Nuclear Studies for the many ways in which they made my thesis work easier and more enjoyable (and just plain possible), especially C. A. Ball, S. E. Ball, T. Banta, M. G. Billing, S. S. Chapman, J. A. Dobbins, C. R. Dunnam, W. J. Edwards, D. M. Eklund, R. M. Eshelman, C. W. Firenze, M. Giannella, S. Greenwald, Z. Greenwald, T. M. Gruber, H. H. Hansteen, D. L. Hartill, G. P. Hellmann, P. L. Hutchings, J. T. Hylas, J. P. Kaminski, R. P. Kaplan, D. J. Kematick, D. L. Kubik, R. H. Lobdell, W. R. Lou, S. H. Marks, D. W. Miller, E. A. Miller, R. L. Miller, N. B. Mistry, R. D. Mitstifer, P. Morehouse, D. L. Morse, R. W. Patten, S. B. Peck, T. A. Pelaia, M. Pisharody, R. E. Prouty, P. V. H. Prymmer, V. P. Rao, M. E. Ray, J. J. Reilly, T. F. Reitz, D. H. Rice, R. L. Rice, J. T. Rogers, R. E. Seely, N. A. Sherwood, J. P. Sikora, J. Swale, R. M. Talman, C. Y. Tan, A. B. Temnykh, M. Tigner, D. C. Sagan, R. Sproul, J. W. Swat, C. A. Valentino, J. J. Welch, and E. M. Young. I thank our collaborators for their many contributions to this work, especially N. Akasaka, I. E. Campisi, F. Caspers, Y. H. Chin, J. F. DeFord, M. S. de Jong, T. G. Flynn, K. W. Smolenski, T. Tajima, and L. S. Walling. I thank my family and friends for their encouragement, support, and patience. This work was supported by the National Science Foundation, with supplementary support from U. S.-Japan collaboration.

Contents

Biographical Sketch	iii
Acknowledgements	v
Table of Contents	vi
List of Tables	viii
List of Figures	ix
List of Symbols	xii
1 Introduction	1
1.1 The Subject	1
1.2 High-Current Accelerators	3
1.3 The CESR Upgrade Program	4
1.4 A Superconducting RF System for CESR	4
1.5 The Higher-Order Mode Loads for the Superconducting RF System	6
1.6 The Beam-Ferrite Interaction: Overview	8
2 Measurements of Microwave Properties	12
2.1 Theory	13
2.2 Experimental Techniques	16
2.3 Results	17
2.4 Interpretations	23
2.5 Summary	26
3 Coupling Impedance Predictions	28
3.1 The Beam Coupling Impedance and Its Importance	28
3.2 Methods for Predicting the Coupling Impedance	31
3.3 Coupling Impedance Predictions	34
3.4 A Highly Simplified Impedance Model	49
3.5 Predicted Dependence on Material Properties	54
3.6 Predicted Dependence on Load Geometry	56
3.7 Summary	57
4 Power Transfer and Beam Instability Predictions	60
4.1 Machine Parameters	61
4.2 The Effective Elastance	63
4.3 Beam-Induced Power Dissipation	69
4.4 Static Effects	73
4.5 Modes of Oscillation to Linear Order	78
4.6 Mode Coupling	84
4.7 Microwave Instability	89
4.8 Multi-Bunch Effects	91
4.9 Summary	98

5	A Beam Test of a Ferrite-Lined Chamber	99
5.1	Load Fabrication	99
5.2	Overview of the Beam Test	100
5.3	Calorimetric Measurements	106
5.4	RF Power Measurements	110
5.5	Frequency Shift and Damping Rate Measurements	110
5.6	Refinements to the Loss Factor Predictions	115
5.7	Load Performance	118
5.8	Other Related Beam Tests	119
5.9	Summary	121
6	Conclusion	122
6.1	The Beam-Ferrite Interaction: Review	122
6.2	Discussion	124
6.3	Possibilities for Future Work	125
A	Permittivity and Permeability Models for AMOS	128
B	The Effective Porcupine Elastance: AMOS vs. Analytic	132
C	Model for the CESR Loss Factor	135
	Bibliography	137

List of Tables

Table of Contents	vi
2.1 Characteristics of four absorbing materials.	12
3.1 Assumed load dimensions.	35
3.2 Parameters determining the validity of the simplified impedance model for four different ferrites.	50
3.3 Monopole resonator parameters for Porcupine loads made of different materials.	54
4.1 Selected CESR-III.5 and CESR-V machine parameters.	62
4.2 Some derived parameters for CESR-III.5 and CESR-V.	63
4.3 Predictions for direct power transfer from the beam to the loads for CESR-III.5 and CESR-V.	70
4.4 Predictions for indirect power transfer from the beam to the loads for CESR-III.5 and CESR-V.	72
4.5 Predictions for the total power transfer from the beam to the loads for CESR-III.5 and CESR-V.	72
4.6 Predictions for the wake-induced transverse orbit shift and transverse beam size for Porcupine loads in CESR-V.	78
4.7 Predicted microwave instability threshold currents due to Porcupine loads in CESR-V.	93
4.8 Predicted multi-bunch longitudinal growth rates per unit current per bunch for Porcupine loads in CESR-V.	97
4.9 Predicted multi-bunch transverse $l = 0$ frequency shifts and growth rates per unit current per bunch for Porcupine loads in CESR-V.	97
4.10 Predicted values of the current per bunch at the threshold for various instabilities produced by Porcupine loads in CESR-V.	98
5.1 Selected CESR machine parameters.	103
5.2 Comparison of measured and predicted single-bunch transverse frequency shift and damping rate slopes.	115
A.1 Relaxation model parameters used in AMOS.	131
C.1 Scaling laws for CESR elements.	136

List of Figures

1.1	A numerical simulation of the wake fields produced as a bunch passes through a cavity.	2
1.2	A schematic representation of CESR and its injector.	5
1.3	A schematic representation of the new CESR RF system.	7
1.4	Drawing of the Porcupine HOM load.	9
1.5	Photograph of a Porcupine HOM load.	10
1.6	The procedure through which power transfer and beam stability predictions for the Porcupine load were obtained.	11
2.1	A transmission line filled with a length d of material.	15
2.2	Measured values of μ for Ferrite-50.	19
2.3	Measured values of ϵ for Ferrite-50.	20
2.4	Measured values of μ for TT2-111V, CMD10, and IB-004 ferrites. . .	21
2.5	Measured values of ϵ for TT2-111V, CMD10, and IB-004 ferrites. . .	22
2.6	Measured values of the real part of μ for samples of different lengths.	25
2.7	Comparison of measured values of $\text{Re } \mu$ and $\text{Re } \epsilon$ to values predicted from the imaginary parts for TT2-111V.	27
3.1	Assumed load geometry.	34
3.2	Measured and fitted values of μ for TT2-111V used in the coupling impedance predictions.	36
3.3	Measured and fitted values of ϵ for TT2-111V used in the coupling impedance predictions.	37
3.4	Predicted monopole coupling impedance for the Porcupine load. . . .	38
3.5	Predicted dipole coupling impedance for the Porcupine load.	39
3.6	Predicted loss factors for the Porcupine load.	41
3.7	Predicted monopole coupling impedance for the L3 load.	42
3.8	Predicted dipole coupling impedance for the L3 load.	43
3.9	Predicted loss factors for the L3 load.	44
3.10	Predicted monopole coupling impedance for the small Ferrite-50 model.	46
3.11	Predicted dipole coupling impedance for the small Ferrite-50 model. .	47
3.12	Predicted monopole loss factor for a full-size TT2-111-series load mock-up.	48
3.13	An HOM load with the ferrite layer protruding inward.	49
3.14	Measured values of $1/\mu$ for four different ferrites.	51
3.15	Comparison of the real part of the monopole coupling impedance predicted by the analytic formula and by the resonator model for the case of the Porcupine load.	53
3.16	Real part of the predicted monopole coupling impedance for Porcupine loads made of various materials.	55
3.17	Comparison of predicted monopole loss factors as a function of the length of a TT2-111V Porcupine load.	57

3.18	Comparison of predicted monopole loss factors as a function of the inner radius of a TT2-111V Porcupine load.	58
3.19	Comparison of predicted monopole loss factors as a function of the ferrite layer thickness of a TT2-111V Porcupine load.	59
4.1	Comparison of summed and integrated values of the effective monopole elastance for one Porcupine load, based on the coupling impedance from AMOS.	67
4.2	Comparison of summed and integrated values of the effective dipole elastance for one Porcupine load, based on the coupling impedance from AMOS.	68
4.3	Comparison of X_s values and σ_z/σ_{z0} values based on the Taylor method and the differentiation method.	75
4.4	Predicted longitudinal mode frequencies for CESR-V with Porcupine loads.	80
4.5	Predicted transverse mode frequencies for CESR-V with Porcupine loads.	82
4.6	Predicted transverse mode growth rates for CESR-V with Porcupine loads.	83
4.7	Predicted frequencies and growth rates for the longitudinal $l = \pm 1$ modes, with coupling, for CESR-V with Porcupine loads.	86
4.8	Detail of the predicted growth rates for the longitudinal $l = \pm 1$ modes, with coupling.	87
4.9	Predicted frequencies and growth rates for the transverse $l = 0$ and $l = -1$ modes, with coupling, for CESR-V with Porcupine loads.	88
4.10	Detail of the predicted growth rates for the transverse $l = 0$ and $l = -1$ modes, with coupling.	89
4.11	Frequency spectrum for a bunch with $\sigma_z = 10$ mm; dependence of $ Z_0^{\parallel}(\omega)/\omega $ and $ Z_1^{\parallel}(\omega)/\omega $ on frequency for the analytic Porcupine impedance.	92
4.12	Detail of the dependence of $ Z_0^{\parallel}(\omega)/\omega $ and $ Z_1^{\parallel}(\omega)/\omega $ on frequency.	93
4.13	Dependence of the effective monopole microwave impedance of the Porcupine load on the frequency shift.	94
4.14	The imaginary part of the effective multi-bunch monopole elastance as a function of the multi-bunch mode index s for a few even values of j	96
5.1	One unit of the ferrite structure.	101
5.2	One completed unit of the ferrite structure.	102
5.3	Tiles being soldered to one unit of the ferrite structure.	104
5.4	Drawing of the assembled ferrite structure; installation of the assembly in CESR.	105
5.5	Calorimetrically measured single-bunch loss factor of the ferrite section as a function of beam current, and bunch length (with predictions).	107
5.6	Calorimetrically measured 9-bunch loss factor of the ferrite section as a function of beam current, and bunch length (with predictions).	108

5.7	Calorimetrically measured and predicted 2-bunch power loss factor of the ferrite as a function of spacing.	109
5.8	Calorimetrically measured and predicted loss factor of the ferrite section as a function of the vertical displacement of the beam.	111
5.9	Measured and predicted loss factor of CESR, with and without ferrite present.	112
5.10	Comparison of synchrotron frequency measurements with and without ferrite.	114
5.11	Comparison of single-bunch measurements of the vertical betatron frequency and the corresponding damping rate, with and without ferrite.	116
5.12	Comparison of analytically-predicted and measured loss factors for three different bunch lengths.	118
5.13	Comparison of the measured power dissipation during the cavity and L3 beam tests.	120
A.1	Measured and fitted values of μ for Ferrite-50 used in the coupling impedance predictions.	129
A.2	Measured and fitted values of ϵ for Ferrite-50 used in the coupling impedance predictions.	130
B.1	Comparison of AMOS and analytic values for the effective monopole elastance for one Porcupine load, based on the integral formulation.	133
B.2	Comparison of AMOS and analytic values for the effective dipole elastance for one Porcupine load, based on the integral formulation.	134

List of Symbols

a	Inner conductor radius for measurements of μ and ϵ
b	Outer conductor radius for measurements of μ and ϵ
$b_m(y, x)$	Parameter in analytic impedance formulae (complex)
$b'_m(y, x)$	Parameter in analytic impedance formulae (complex)
b_+, b_-	Parameters in the simplified impedance model
c	Speed of light
C	Accelerator circumference
C'	Capacitance per unit length in a transmission line
d	Sample length for measurements of μ and ϵ
E_0	Energy per particle divided by the charge of the particle
$\operatorname{erfc}(y)$	Complementary error function (complex)
f	Frequency
f_0	Revolution frequency
f_s	Synchrotron frequency
f_v	Vertical betatron frequency
f_Δ	Frequency shift in the analysis of the microwave instability
G_0^{\parallel}	Monopole loss factor in Gaussian units
$h(t)$	A time-domain function
$H(\omega)$	The Fourier transform of $h(t)$
i	An imaginary number of unit magnitude
I	Current per beam
I_b	Current per bunch
I_{th}	Threshold current for the microwave instability
\mathbf{I}	Identity matrix
j	Integer
$J_m(x)$	Bessel function of the first kind of order m (complex)
$J'_m(x)$	First derivative of $J_m(x)$ (complex)
k	Wave-number for propagation in vacuum ($\equiv \omega/c$)
k_z	Propagation wave-number of a transmission line (complex)
\bar{k}_r	Radial wave-number for material (complex)
k^{\parallel}	Total loss factor
k_m^{\parallel}	Loss factor associated with the m th multipole moment
$K_{l,l'}$	Mode coupling matrix element
\mathbf{K}	Mode coupling matrix
l	Azimuthal mode index
L	Length of the ferrite layer
L'	Inductance per unit length in a transmission line

$\text{Ln}(y)$	“Principal” natural logarithm
m	Multipole moment index for the bunch’s charge distribution
M	Number of bunches per beam
n	Radial mode index
N	Number of whole wavelengths in the length of the sample
N_0	Value of N at the starting frequency
$N_m(x)$	Bessel function of the second kind of order m (complex)
$N'_m(x)$	First derivative of $N_m(x)$ (complex)
p	Summation index
$\langle p_0 \rangle$	average power density induced by a beam with a purely monopole charge distribution
$\langle p_1 \rangle$	average power density induced by a beam with a purely dipole charge distribution
p_{max}	maximum power density in the material layer
\vec{p}	Momentum (vector)
P_d	Power lost by the beam due to a coupling impedance
P_0^{\parallel}	Power loss factor for 2-bunch measurements
$\mathbf{P}_m(t)$	Normalised multipole moment of the bunch’s charge distribution (matrix)
q_b	Charge per bunch
q_e	Electron charge (magnitude)
q_w	Charge of witness particle
Q	“Quality factor” of a resonator
r	Radial coordinate (in cylindrical coordinate system)
\hat{r}	Radial unit vector
r_o	Outer radius of the ferrite layer
r_x	Inner radius of the ferrite layer
R_s	Shunt impedance (non-linac definition) of a resonator
s	Multi-bunch mode index
S_{11}	Forward reflection coefficient in the μ and ϵ measurements (complex)
S_{12}	Reverse transmission coefficient in the μ and ϵ measurements (complex)
S_{21}	Forward transmission coefficient in the μ and ϵ measurements (complex)
S_{22}	Reverse reflection coefficient in the μ and ϵ measurements (complex)
t	Time
T	Transmission coefficient for propagation through a length d of a longitudinally homogeneous transmission line (complex)
U	Energy lost by a bunch via wake fields as it travels through a structure
U_0	Energy lost by a particle in one turn via synchrotron radiation
v	Speed of particles in the beam
V_f	Amplitude of the incident wave in the μ and ϵ measurements (complex)

$w(y)$	Function associated with $\operatorname{erfc}(y)$ (complex)
$w_m^{\parallel}(t)$	Single-particle longitudinal wake function
$w_m^{\perp}(t)$	Single-particle transverse wake function
$\mathbf{W}_m^{\parallel}(t)$	Bunch longitudinal wake function (matrix)
$\mathbf{W}_m^{\perp}(t)$	Bunch transverse wake function (matrix)
x	Parameter in the simplified impedance model
x_{\perp}	Transverse displacement of the beam
$x_{\perp 0}$	Unperturbed transverse displacement of the beam
X_s	Effective reactance
Y_0, Y_1	Parameters in the analysis of the bananer effect
z	Longitudinal coordinate (in cylindrical coordinate system)
\hat{z}	Longitudinal unit vector
\bar{z}	Displacement of the mean position of the bunch relative to the zero crossing of the RF voltage
Z	Characteristic impedance of a transmission line (complex)
Z_0	Characteristic impedance of vacuum
$Z_m^{\parallel}(\omega)$	Longitudinal coupling impedance (complex)
$Z_m^{\perp}(\omega)$	Transverse coupling impedance (complex)
α	Damping rate
α_j	Relaxation model parameter
α_v	Damping rate for betatron oscillation in the vertical plane
β_j	Relaxation model parameter
β_Z	Transverse betatron function at the location of the impedance
γ_j	Relaxation model parameter
Γ	Reflection coefficient for a transmission line with a vacuum-material interface (complex)
δ	Relative energy difference
$\Delta f'$	Frequency shift per unit current (per bunch)
Δz	Spacing between bunches in the 2-bunch measurements
$\Delta \alpha'$	Damping rate shift per unit current (per bunch)
$\Delta \omega$	Angular frequency shift
$\epsilon(\omega)$	Complex permittivity
ϵ_0	Permittivity of free space
ζ	Parameter in the analysis of μ and ϵ measurements (complex)
η	Slippage factor
Θ_j	Dipole effective elastance (complex)
κ	Material parameter in the simplified impedance model
λ_z	Wavelength of TEM propagation inside a material
Λ_0	Effective monopole microwave impedance

Λ_1	Effective dipole microwave impedance
$\mu(\omega)$	Complex permeability
μ_0	Permeability of free space
ξ	Chromaticity
$\Xi_{0,j}$	Monopole effective elastance (complex)
$\Xi_{1,j}$	Achromatic dipole effective elastance (complex)
ρ	bunch charge density
σ_e	Electrical conductivity
σ_x	Standard deviation in the transverse charge distribution for a Gaussian bunch
σ_z	Standard deviation in the longitudinal charge distribution for a Gaussian bunch (bunch “length”)
σ_{z0}	Undistorted σ_z
σ_δ	Relative momentum spread of the beam
ϕ	Azimuthal coordinate (in cylindrical coordinate system)
$\hat{\phi}$	Azimuthal unit vector
Φ	Trigonometric matrix ($\Phi^t =$ transpose of Φ)
χ	Head-tail phase
ψ	Material parameter in the simplified impedance model
Ψ	Trigonometric matrix ($\Psi^t =$ transpose of Ψ)
ω	Angular frequency
ω_0	Revolution angular frequency
ω_p	Angular frequency of the side-band of the p th revolution harmonic
ω_R	Resonant angular frequency
ω_s	Synchrotron angular frequency
ω_{s0}	Undistorted synchrotron angular frequency
ω_β	Betatron angular frequency
ω_Δ	Angular frequency shift in the analysis of the microwave instability
ω_ξ	Chromatic angular frequency
Ω	Complex angular frequency of a mode of oscillation of the beam
$\Omega_{n,l}$	Complex angular frequency of the single-bunch mode of oscillation of the beam with radial index n and azimuthal index l
$\Omega_{n,l,s}$	Complex angular frequency of the multi-bunch mode with radial index n , azimuthal index l , and multi-bunch mode index s
	Dangerous bend

Chapter 1

Introduction

1.1 The Subject

Consider a collection of charged particles travelling at a speed v slightly smaller than the speed of light c . The particles carry an electric field (being charged) and a magnetic field (being in motion) with them; as $v \rightarrow c$, both fields become purely transverse. If they are in free space, the particles will continue to travel at the same speed indefinitely. The same can be said if the particles are travelling through a tube of uniform cross-section with perfectly conducting walls (see Figure 1.1a); a surface charge and surface current are induced on the walls of the tube, but there is no energy dissipation. On the other hand, if the tube’s cross-section varies or if its walls are not perfectly conducting, the beam of particles will lose energy to its surroundings, and its momentum will decrease.

A classic example is the case of a beam travelling through a cavity discontinuity in a tube. A time-domain simulation of the interaction between a bunched beam and a cavity is shown in Figure 1.1. The calculation was done using the program ABCI [1], which solves the Maxwell Equations in the time domain, given the passing beam’s charge distribution as a source term. As can be seen, the passing bunch leaves behind electromagnetic energy in the cavity. Another well-known example, which can be worked out analytically, is the case of a metallic tube with a good but imperfect conductivity, the “resistive wall” problem. Our interest will focus on a generalisation of the latter, the case of a conducting tube with a layer (of finite length) of material inside it. Being a discontinuity, the layer can store electromagnetic energy like a cavity; moreover, the material can be an absorber of electromagnetic energy, converting the beam’s electromagnetic field into heat, like the resistive wall.

If we bend our conducting beam tube into a hollow ring and apply a static magnetic field to make our beam follow a circular path, we obtain a storage ring. With each revolution of the beam, energy will be stored or dissipated whenever the tube departs from an ideal conductor of uniform cross-section. Electromagnetic energy left behind by a bunch—the bunch’s wake field—will act back on the charged particles in the bunch. The wake field can produce a significant force on individual particles in the bunch; generally speaking, the force will depend on the particle’s position relative to the centroid of the bunch. This effect produces a current-dependent distortion of the bunch’s charge distribution. If the wake fields left behind by the bunch are stored in a cavity with sufficiently low dissipation, there will be a force left to act on the

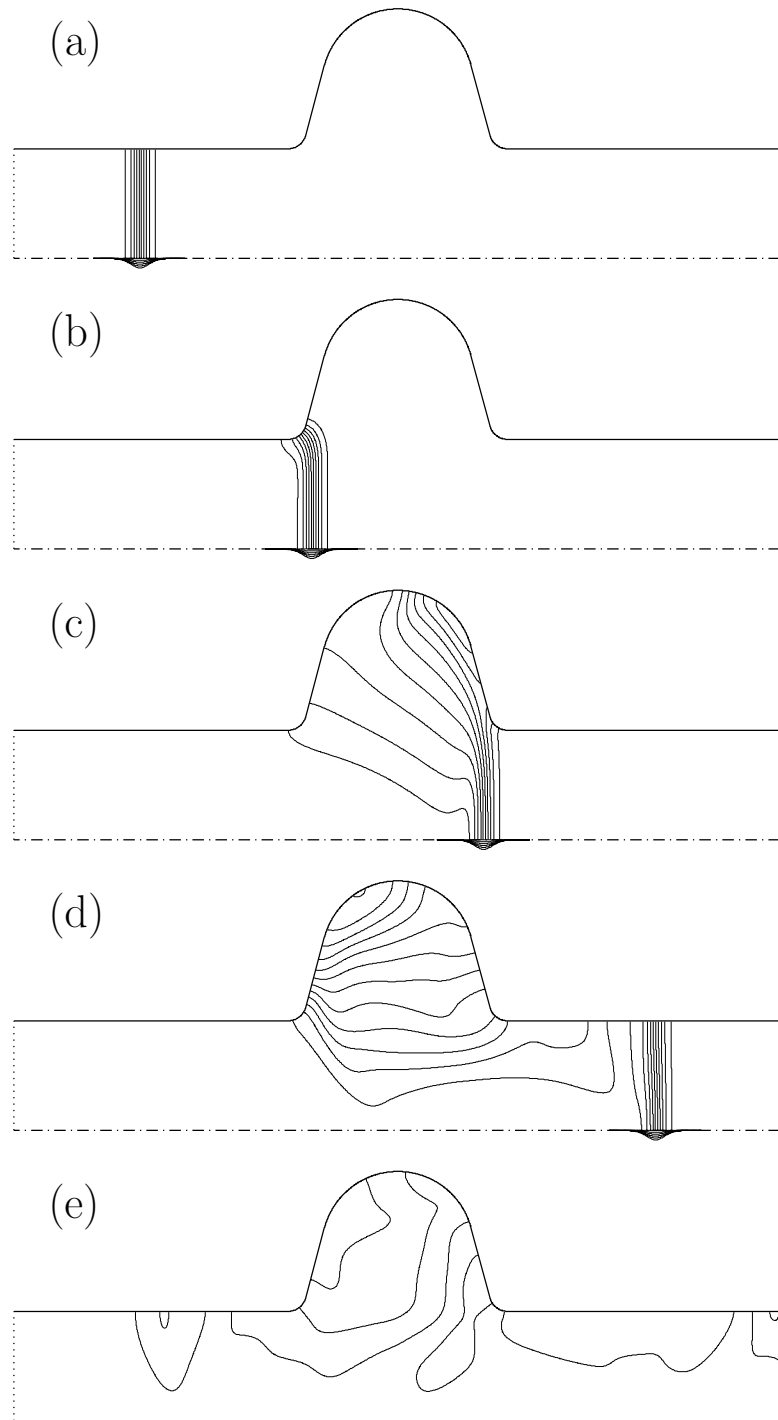


Figure 1.1. A numerical simulation of the wake fields produced as a bunch passes through a cavity. The beam passes along the dashed line, about which the cavity is axisymmetric. Electric field lines are shown above the dashed line; the longitudinal charge distribution of the bunch is indicated below the line. The walls of the beam tube and cavity are assumed to be perfectly conducting.

bunch upon its next passage. Similarly, if more than one bunch is circulating, the wake left behind from one bunch can produce a force on the next bunch. The force on an individual particle is proportional to the charge per bunch, so, given enough charge per bunch, multi-turn and multi-bunch forces can produce instabilities in the beam's motion. The wake fields produced by a layer of material on the inside of a beam tube; the resulting power dissipation, static distortion, and instabilities of a bunched beam in a storage ring bearing a section of material-lined tube: these are the topics that will be covered in this thesis. Before going into more detail, we will first discuss the motivation for studying this subject.

1.2 High-Current Accelerators

In elementary particle physics, the demand has been mostly for increasing beam energy, in the effort to discover particles of increasingly higher mass. In recent years, however, there has been growing interest in higher luminosity machines, with which rare processes can be studied. The luminosity of a colliding-beam machine is a measure of the number of collisions per unit time. A high luminosity is crucial in the study of particles which are produced infrequently. The primary aim of the CESR upgrade program [2], as well as the PEP-II [3] and KEK-B [4] projects, is to study CP violation in the decay of the B meson (a B meson, according to theory, is composed of a b quark and either a u or a d quark). The hope is that a better understanding of CP violation will yield new insight into fundamental questions (for example, it might help explain the observed disparity between matter and anti-matter in our universe). Since B mesons are produced infrequently to begin with (in typical CESR operation, about 10^7 bunch collisions are required to produce a single B meson), a high luminosity is crucial to a study of rare B decays. It is estimated that a meaningful measurement could be made with a luminosity of about $3(10^{37}) \text{ m}^{-2}\text{s}^{-1}$, which is about a factor of 10 higher than the CESR luminosity in 1995. There is also interest in building high-luminosity machines at other energies for the study of particles such as the ϕ meson and the τ lepton.

For all of the aforementioned projects, it is envisaged that the higher luminosity will be obtained mostly by an increase in the beam current. Higher currents are also being sought in accelerators for use as x-ray sources, such as SOLEIL [5]. The higher beam current can be obtained by increasing the current per bunch or the number of bunches; the latter scheme is favoured over the former, mostly because the beam-beam interaction is expected to be too disruptive in collisions between bunches of higher charge. With more bunches, however, the spacing between successive bunches must decrease; hence there is less time available for the wake fields produced by one bunch's passage through the cavities and other elements to dissipate before the arrival of the next bunch: the problem of multi-bunch beam instabilities becomes more severe.

There are several cures for these multi-bunch instabilities. One cure is to find a combination of conditions such that the net wake force is stabilising, rather than destabilising. Typically, this is done by adjusting the frequencies of the parasitic cavity resonances relative to the revolution frequency. Another cure is a feedback

system, which must basically provide an external electromagnetic force on the beam that cancels out the net destabilising force of the wake field. A third cure is to hasten the decay of the wake fields and thereby lessen the wake force experienced by a bunch due to the previous bunch's passage. The latter approach has been adopted for the CESR upgrade, although some feedback is also required due to the resistive wall wake fields of the aluminum beam tube.

1.3 The CESR Upgrade Program

The Cornell Electron Storage Ring (CESR), depicted schematically in Figure 1.2, is an electron-positron collider. The bunched electron and positron beams share the same vacuum chamber, and collide at a single interaction point. Parasitic collisions are avoided via a “pretzel” scheme—the beams are deflected into transversely oscillatory orbits in such a way as to produce horizontal separation between the beams at all of the parasitic bunch crossings.

In the upgrade program alluded to in the previous section, the CESR luminosity is being increased via higher beam current, which, in turn, is being obtained with more bunches. There will also be some increase in the transverse focussing at the interaction point, which, supplemented by a decrease in the bunch length, will further increase the luminosity. The spacing between bunches is being made non-uniform, because parasitic collisions cannot be avoided with more than 9 uniformly spaced bunches using the pretzel scheme (to get beyond 9 bunches would require the wavelength of the transverse oscillation of the beam to be unrealistically short); instead, the bunches are being grouped into trains. In the early 1990's, CESR operated with head-on collisions of 7 bunches of electrons with 7 bunches of positrons. In 1994, a modified pretzel scheme was introduced in which the bunches collide with a slight crossing angle, thereby allowing trains of closely spaced bunches to be stored without parasitic collisions; in 1995, CESR operated with 9 trains and 2 bunches per train. The short-term goal (“CESR-III”) is to increase the number of bunches per train to 5. In the longer term, separate vacuum chambers for the two beams might be built, so that a larger number of uniformly-spaced bunches can be stored. More exotic possibilities are being considered as well.

An increase in the number of bunches requires more power transfer to the beam (since more particles are losing energy in the form of x-rays as they travel around the ring). A decrease in the bunch length requires more cavity voltage (to provide more longitudinal focussing). Because of the decrease in the bunch-to-bunch spacing, fast dissipation of the wake fields is also necessary. It is planned to meet these requirements by installing a new Radio Frequency (RF) system in CESR.

1.4 A Superconducting RF System for CESR

The RF cavities provide a standing-wave time-varying electromagnetic field. Particles which pass through the cavities at the right time are accelerated by the longitudi-

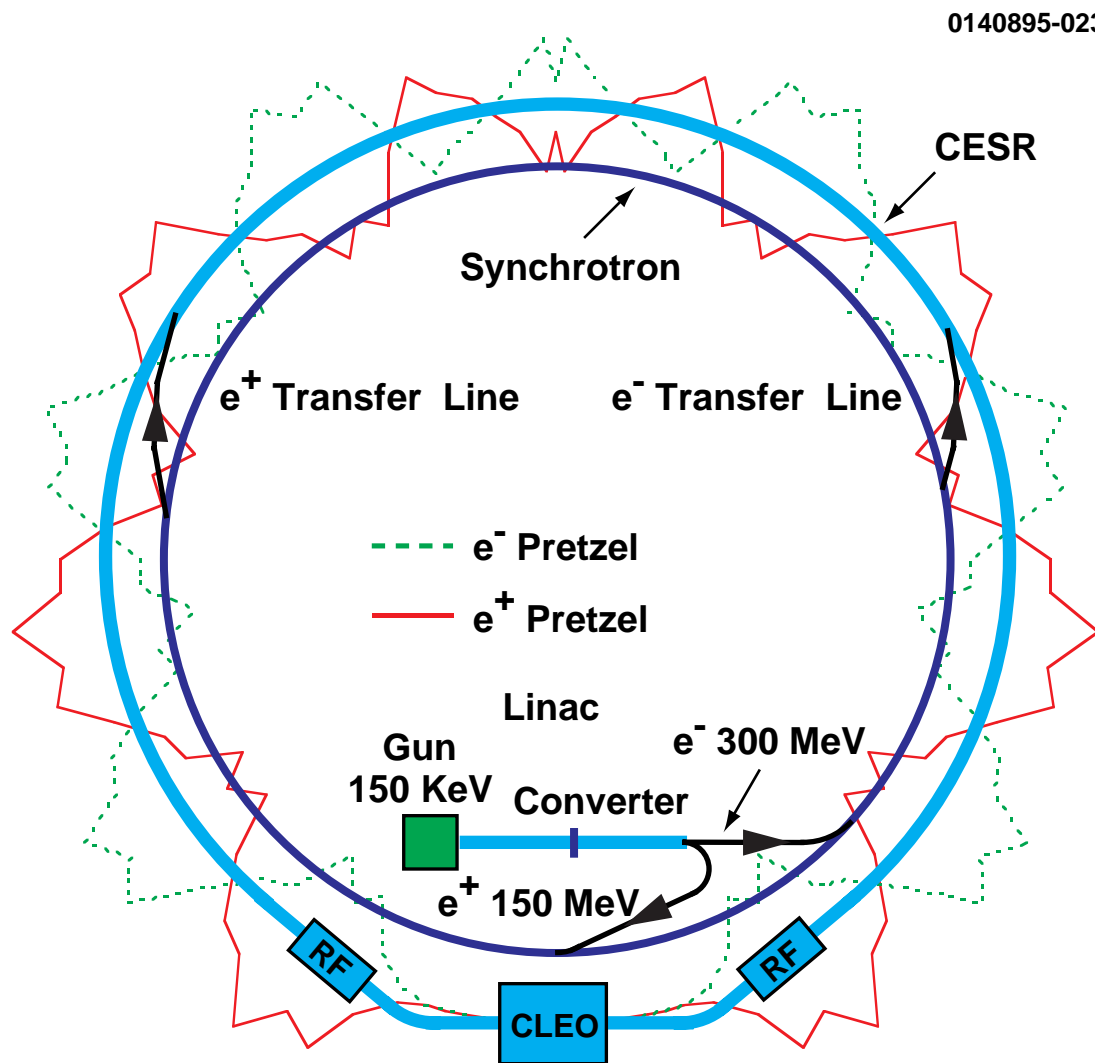


Figure 1.2. A schematic representation of CESR and its injector. The storage ring's diameter is about 245 m. The pretzel orbits for 7-bunch operation with head-on collisions in the CLEO detector are also shown. When they follow these orbits, the bunches are separated horizontally at each of the 13 parasitic crossing points, and collide only in CLEO. The transverse displacement due to the pretzels is exaggerated—the actual displacements are a few cm.

nal electric field of the cavity's fundamental mode. The cavities replace the energy radiated by the beam as it travels through the bending magnets. Because the energy received depends on the time at which a particle travels through the cavity, the cavities also provide a longitudinal restoring force; the net cavity voltage determines the equilibrium bunch length. As was seen in Figure 1.1, the cavities represent a significant disruption in the vacuum chamber, and are a major source of unwanted wake fields.

The present RF system in CESR consists of four penta-cell normal conducting RF cavities [6]. A new RF system, shown in Figure 1.3, has been designed for operation at higher current [7]. The new cavities are superconducting, thereby allowing operation at a higher voltage per cell (due to the reduced power dissipation in the walls of the cavity). With a higher voltage per cell, fewer cells are required, which reduces the wake force per turn. Because of the higher power transferred from the cavities to the beam, single-cell cavities, each with a dedicated RF power input, are used (in the present system, the power from one input line is shared by all 5 cells). Prototypes for the new cavity [8], cryostat [9], tuner [10], input coupler [11], RF window [12, 13], and loads have been tested. A fully-equipped single-cavity RF system was tested in CESR in August 1994 [14].

In designing the new RF system, the goal was to avoid long-lived wake fields, *i.e.* to have no dangerous parasitic resonances in the structure. To ensure a low Q for all of the dangerous higher-order modes (HOMs) of the cavity, a large beam tube diameter was chosen. With the addition of “flutes” to one of the tubes (see Figure 1.3), all of the monopole and dipole HOMs were found to be above the cutoff frequencies for propagation into the beam tube via waveguide modes. Even with all the HOM frequencies above cutoff, there is the possibility of “trapped” HOMs that couple poorly to the beam pipe [15, 16]; however, a search for trapped even monopole modes found no modes with excessively low coupling into the beam tube for our choice of cavity shape [17]. To produce a low Q in the propagating modes, a section of beam tube with a layer of microwave-absorbing material is placed nearby. Because of the large amount of power transferred from the beam to the cavity HOMs, the absorbing material must be placed outside the cryostat. Our interest will focus on the HOM loads, the sections of beam tube that bear the layer of lossy material. We will see that, in addition to providing the desired damping of cavity HOMs, the lossy layer will interact directly with the electromagnetic field of the beam, as described in Section 1.1.

1.5 The Higher-Order Mode Loads for the Superconducting RF System

A nickel-zinc ferrite was tentatively chosen as the absorbing material for the loads. RF measurements by V. Veshcherevich on a full-size copper model of the superconducting

3180196-002

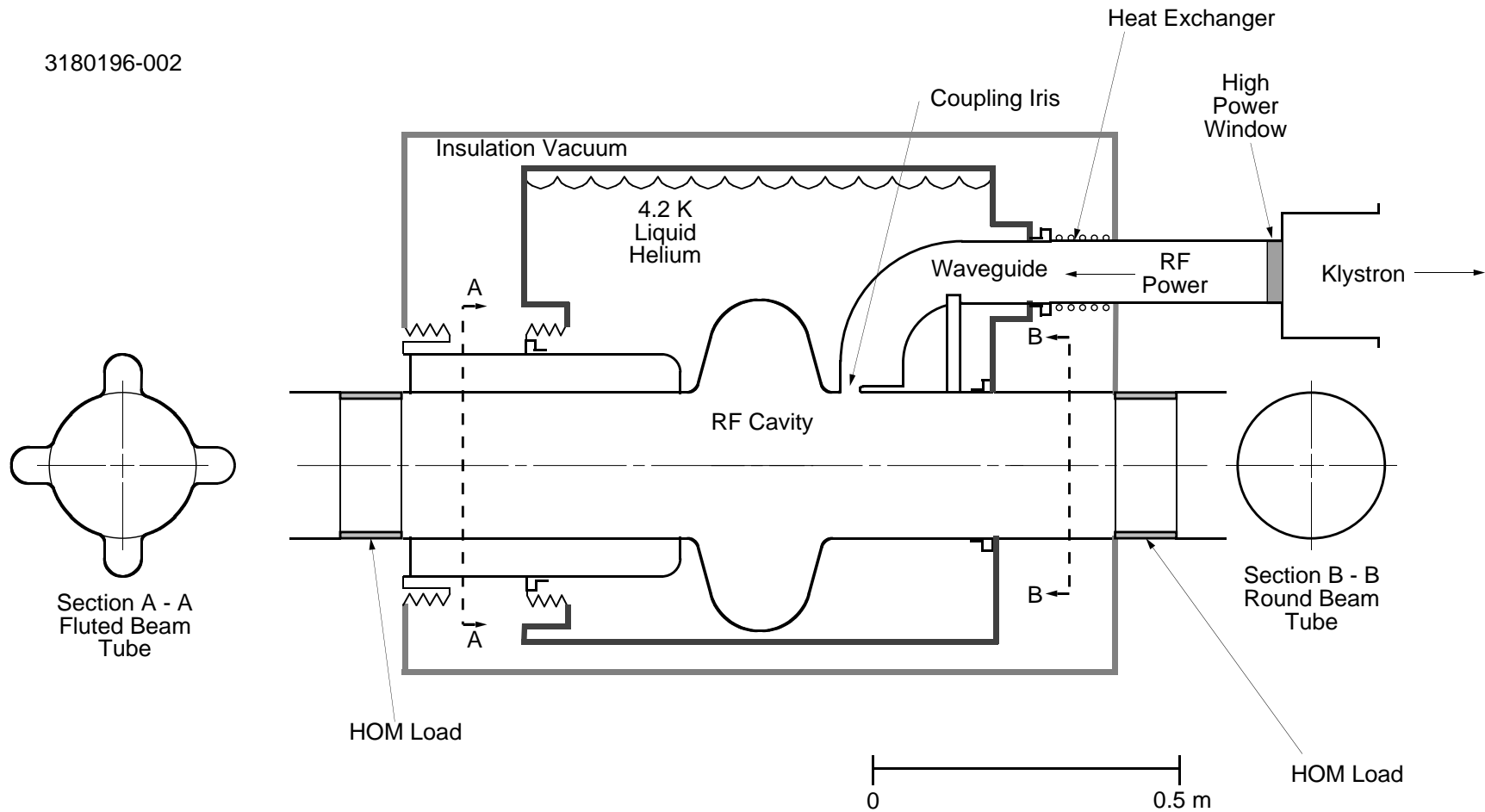


Figure 1.3. A schematic representation of the new CESR RF system. The beam travels through the structure on or near the axis. The HOM loads and high-power window are not drawn to scale. The tapered transitions to the smaller CESR beam tube cross-section are not shown.

cavity with loads made of a particular variety of Ni-Zn ferrite, TT2-111R¹, indicated that reasonably strong damping of dangerous HOMs could be obtained [18]. Damping predictions were also made [19, 20], based on the measured microwave properties of TT2-111R, using two computer programs, SEAFISH [21] and CLANS [22].

In addition to providing adequately low Q 's for cavity HOMs, the loads must satisfy several other requirements, including (i) ability to dissipate high power (tens of kW per load) in continuous operation, (ii) compatibility with an ultra-high vacuum environment, (iii) compatibility with a dust-free environment, and (iv) compatibility with stray radiation from the beam. A development effort was necessary in order to fabricate a device that satisfies all of these requirements simultaneously. The prototype ‘‘Porcupine’’ load (so named because of the many small cooling tubes that protrude from the load shell) is shown in Figures 1.4 and 1.5.

The Porcupine damping scheme is a departure from the better-established method of damping HOMs by placing a coupling hole near the cavity to allow the HOMs to propagate away via a waveguide or coaxial line, sending the HOM power through an RF window, and dissipating it in a high-power termination. The Porcupine load has the advantage of providing more damping over a larger band-width. The disadvantages of the Porcupine scheme include the more stringent fabrication requirements mentioned above. As indicated above, there is another disadvantage: because the microwave absorbing material is on the surface of the beam tube, it has the opportunity to interact directly with the electromagnetic fields carried by the beam, in addition to the indirect interaction via the cavity HOMs. This direct parasitic interaction will be the subject of this thesis.

1.6 The Beam-Ferrite Interaction: Overview

The parasitic interaction between the HOM loads and the beam will produce additional power dissipation in the loads and, at sufficiently high beam currents, distortion in the bunches and beam instabilities. The purpose of this thesis was to make predictions about the beam-induced power dissipation in the HOM loads and about the influence of the HOM loads’ wake on the behaviour of the beam, and test these predictions via a dedicated beam test in CESR. The predictive portion is outlined in Figure 1.6. The motivation was to find out whether the HOM load as designed could be expected to function satisfactorily in future incarnations of CESR and find out what improvements could be made in a redesign.

The first step was to measure the electromagnetic properties of the microwave-absorbing material, to wit the complex permittivity ϵ and complex permeability μ as a function of frequency. Measurements were done on several different materials; a nickel-zinc ferrite was chosen for the fabrication of the first few load prototypes. The measurements are discussed in Chapter 2.

The next step was to use the measured μ and ϵ of the material to make predictions about the wake field produced by the passage of a bunch through an HOM

¹A product of Trans-Tech, Inc.

3180196-003

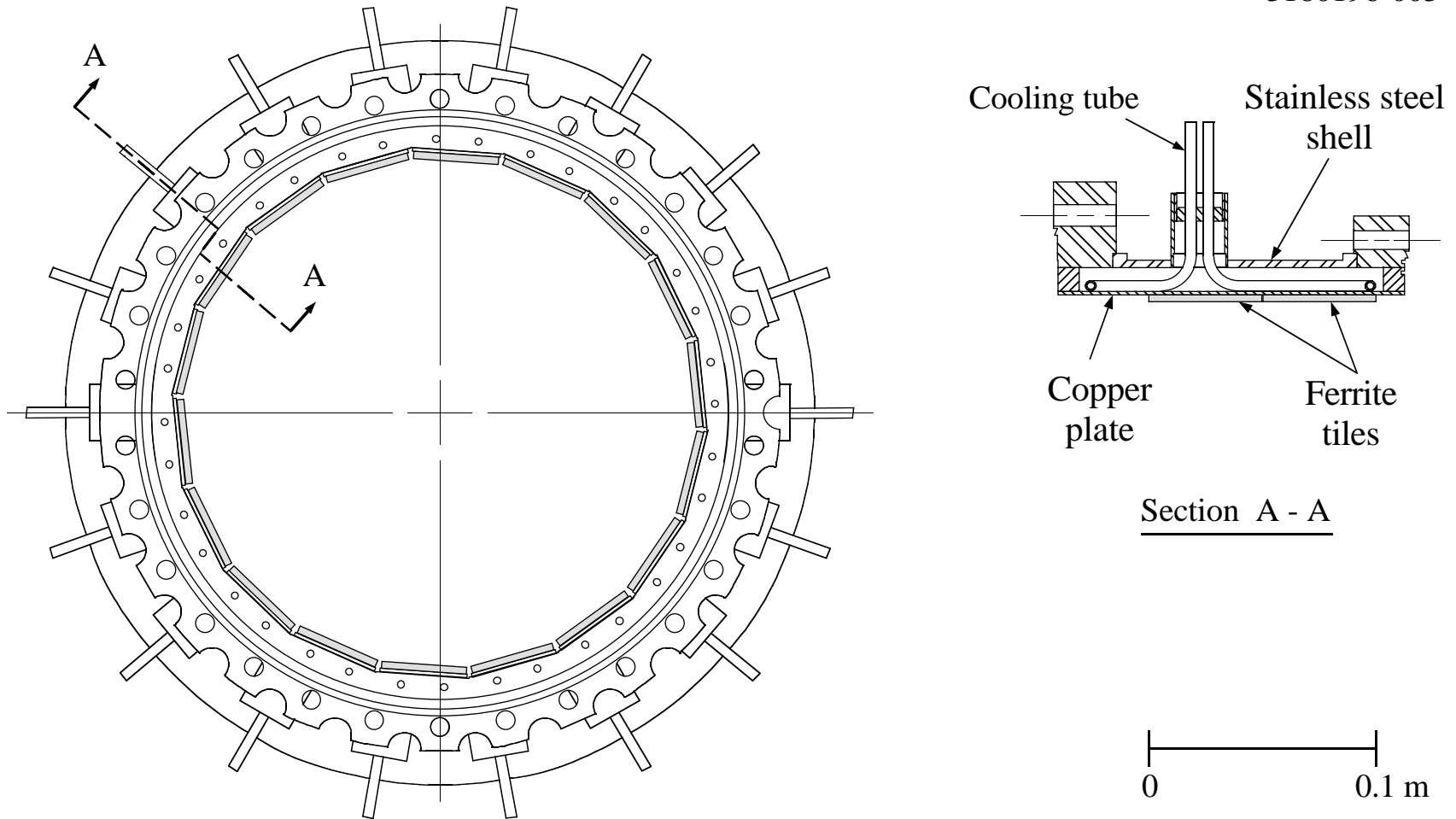


Figure 1.4. Drawing of the Porcupine HOM load. The tiles of microwave-absorbing ferrite are soldered to copper plates with water cooling on the other side and assembled into a vacuum-tight shell.

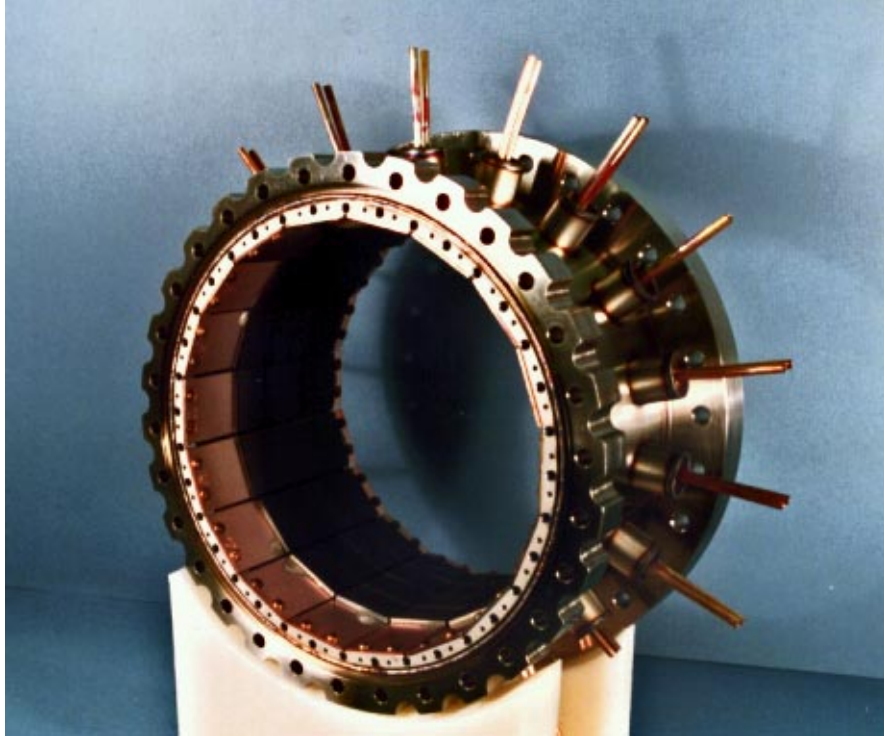


Figure 1.5. Photograph of a Porcupine HOM load.

load. The effect of the wake field on particles in the passing bunch and in subsequent bunches can be expressed in terms of a frequency-dependent beam coupling impedance. The coupling impedance predictions were made via both numerical simulation and an analytic approximation. To supplement these predictions, some measurements were made on load mock-ups using a “wire method” to simulate the beam. These predictions and measurements are the subject of Chapter 3.

The last predictive step was to use the calculated coupling impedance of a Porcupine load to make predictions about the direct power transfer to the HOM loads and about the response of the beam to the HOM loads’ wake fields in an upgraded CESR. These predictions are discussed in Chapter 4. Although predictions will be given only for nickel-zinc ferrite, the models presented in Chapters 3 and 4 will be applicable to any microwave-absorbing materials that can be characterised by a complex ϵ and μ .

A last experimental step was to install a ferrite load of magnified coupling impedance in CESR and measure its effect on the beam, as a test of the predictive ability of the coupling impedance and beam stability models. The measurements made in and predictions done for this beam test are the subject of Chapter 5.

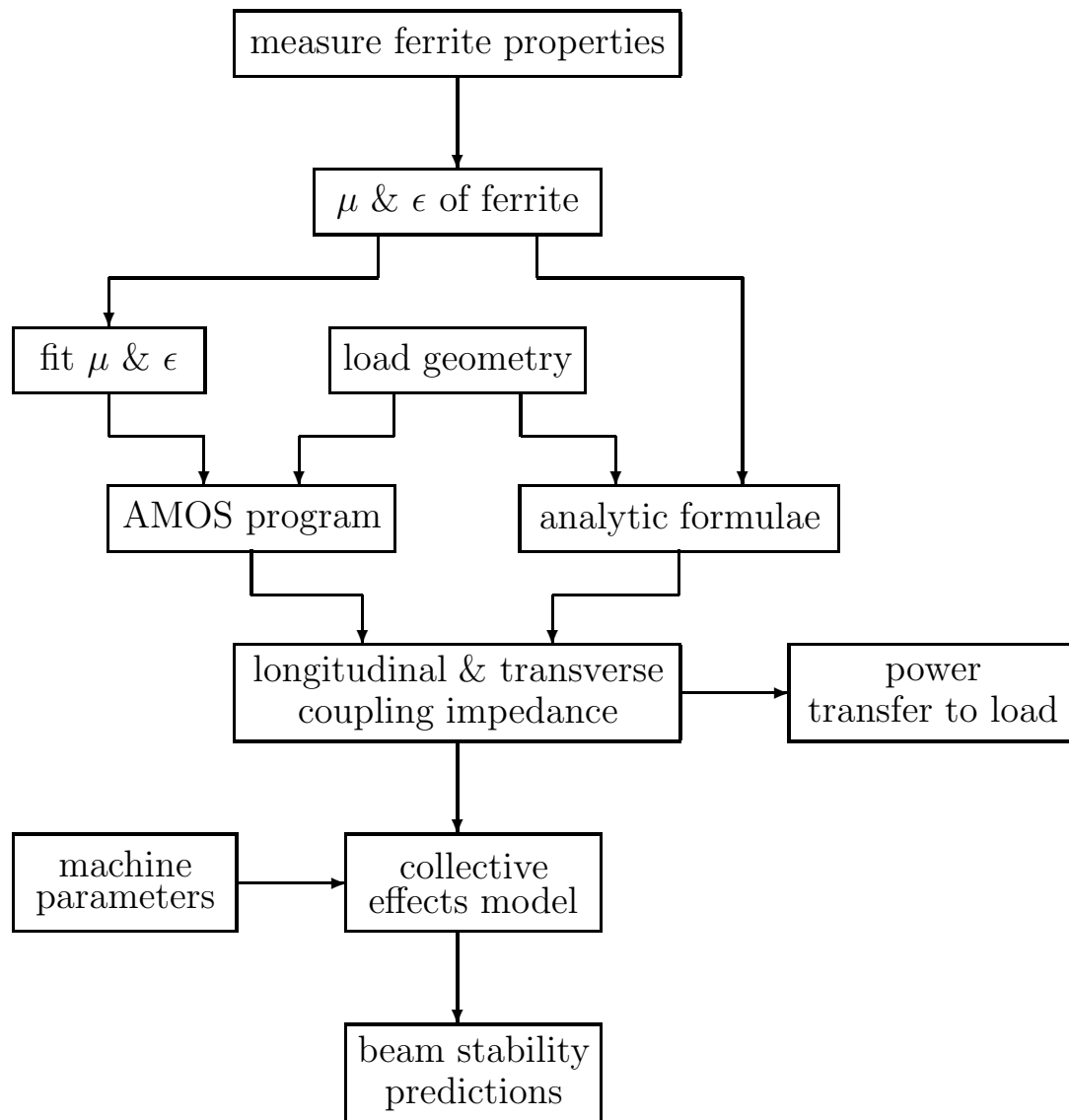


Figure 1.6. The procedure through which power transfer and beam stability predictions for the Porcupine load were obtained.

Chapter 2

Measurements of Microwave Properties

Several commercially-available materials were considered in the search for a microwave-absorbing layer for the HOM loads. We measured the properties of some of the more promising materials. A total of ten materials were measured [23, 24, 25]; the results for four of these, listed in Table 2.1, will be discussed in this chapter. All four materials are ceramic ferrites. As mentioned in the previous chapter, RF measurements showed that reasonably strong damping of cavity higher-order modes could be obtained with TT2-111-series ferrite; measured HOM Q 's with Ferrite-50 were of the same order [18]. As we will see, the properties of CMD10 and IB-004 are quite similar to TT2-111-series ferrite, so they can be expected to provide reasonable HOM damping as well. In the absence of any large differences in HOM damping ability between these four materials, TT2-111-series ferrite was chosen for fabrication of the first few prototypes, primarily on the basis of more favourable mechanical properties [26]. The positive experience with TT2-111-series ferrite in an ultra-high vacuum environment [27] was also a factor.

Mechanisms which produce microwave absorption in ferrites include domain wall motion, domain rotation, and electrical resistivity. In the absence of an applied magnetic field, the magnetic domains (regions in which the magnetic dipole moments are all aligned in a particular direction) in the ferrite are randomly oriented. When a magnetic field is applied, the domains whose magnetisation is aligned with the field

Table 2.1. Characteristics of four absorbing materials. The DC resistivity values were supplied by the manufacturers.

Material	Manufacturer	Type	DC Resistivity [Ωm]
Ferrite-50	Trans-Tech	Nickel-zinc	$0.25^{+0.75}_{-0.15}$
TT2-111-series	Trans-Tech	Nickel-zinc	8 to 10^5
CMD10	Ceramic Magnetics	Nickel-zinc	10^5
IB-004	TDK	Manganese-zinc	

grow in size, while other domains shrink; in the case of a time-varying magnetic field, the motion of the domain walls produces dissipation at low frequencies. At higher frequencies, the domain walls are no longer able to respond to the field, but the direction of the dipole moment inside individual domains rotates under the influence of the applied field, also producing dissipation. Moreover, the electrical resistivity of the ferrite produces Ohmic dissipation in the presence of a time-varying (or static) electric field.

Because our purpose is to analyse the direct interaction between the bunched beam and a layer of material, the relevant frequency range for microwave properties measurements is determined by the frequency spectrum of the beam. The lowest frequency present in the beam spectrum is the synchrotron frequency, (a few tens of kHz for CESR). At high frequencies, the spectrum of a beam consisting of Gaussian bunches in the time domain falls off as a Gaussian in the frequency domain; for the present case ($\sigma_z \geq 10$ mm), the standard deviation in the frequency domain is ≤ 4.8 GHz, so we would like to know the microwave properties up to frequencies well beyond 5 GHz. The largest practical frequency range, as set by our network analysers, was from 300 kHz to 20 GHz, so this is the range that we used in our measurements. Although the microwave properties of some of the materials of interest have been measured by other researchers (as will be discussed further in Section 2.3), none of the measurements on commercially-available ferrites have covered such an unusually large frequency range (although measurements have been done over a suitably large frequency range for nickel-zinc ferrites of various stoichiometries [28]).

The materials were assumed to be linear in their response to electric and magnetic fields, homogeneous, and isotropic. Strictly speaking, none of these assumptions are valid for ferrite materials, but they can be expected to give a reasonable description of the materials' behaviour on a macroscopic scale in the presence of electromagnetic fields of moderate intensity. With these assumptions, the microwave properties may be described by a complex magnetic permeability μ and a complex electric permittivity ϵ . Since the materials are assumed isotropic, μ and ϵ are scalars, rather than tensors. The permeability and permittivity were measured using the coaxial transmission line technique. In this chapter, we will cover the main points of the theory of the measurement (including an alternate approach to resolving some of the ambiguities in the data reduction), experimental methods (including some techniques that we found to be helpful for avoiding systematic errors), results, and a few interpretations. Details on the theory and techniques and a discussion of an improved analysis procedure for materials with known μ or known ϵ may be found elsewhere [24].

2.1 Theory

Descriptions of the transmission line technique for measuring microwave properties may be found in the literature [29, 30, 31]. As we will see, the basic strategy is to fill part of a transmission line with the material, measure the complex reflection and transmission coefficients at the frequencies of interest with a network analyser, and calculate μ and ϵ from these coefficients.

Consider a travelling wave propagating through a coaxial transmission line. Suppose the voltage and current vary sinusoidally in time at angular frequency ω . We assume that the actual voltage and current are the real parts of complex quantities. When introducing complex quantities, we must choose a sign convention, so we will suppose that the time dependence in the complex voltage and current is given by $e^{i\omega t}$ (the convention used by our network analysers). Equivalently, we can consider the Fourier transform in time of the voltage and current, with the Fourier transform $H(\omega)$ of a time domain function $h(t)$ given by

$$H(\omega) = \int_{-\infty}^{\infty} h(t)e^{-i\omega t} dt . \quad (2.1)$$

With this sign convention, we expect the imaginary parts of μ and ϵ to be negative in a microwave-absorbing material.

The permeability $\mu(\omega)$ and the permittivity $\epsilon(\omega)$ can be deduced from the complex characteristic impedance Z of the line and the complex propagation wave-number k_z :

$$\mu = \frac{k_z Z}{\omega} \quad (2.2)$$

$$\epsilon = \frac{k_z}{Z\omega} . \quad (2.3)$$

The impedance and wave-number, in turn, can be deduced from “reduced” transmission and reflection coefficients T and Γ :

$$k_z = \frac{i}{d} \ln(T) \quad (2.4)$$

$$Z = Z_0 \frac{1 + \Gamma}{1 - \Gamma} . \quad (2.5)$$

In Equations (2.4) and (2.5), T is the complex ratio of the voltages (in a forward-travelling wave propagating through an infinitely long line that is completely filled with material) at two planes a distance d apart; Γ is the reflection coefficient at the interface between a semi-infinite vacuum-filled line and a semi-infinite material-filled line; Z_0 is the characteristic impedance of the vacuum-filled line (vacuum and air are indistinguishable at the level of precision of our measurements). T and Γ cannot be measured directly, but they can be calculated from the transmission and reflection coefficients S_{21} and S_{11} corresponding to the situation depicted in Figure 2.1. One can show that

$$\Gamma = \zeta \pm \sqrt{\zeta^2 - 1} \quad (2.6)$$

$$T = \frac{S_{11} + S_{21} - \Gamma}{1 - (S_{11} + S_{21})\Gamma} , \quad (2.7)$$

where

$$\zeta = \frac{S_{11}^2 - S_{21}^2 + 1}{2S_{11}} . \quad (2.8)$$

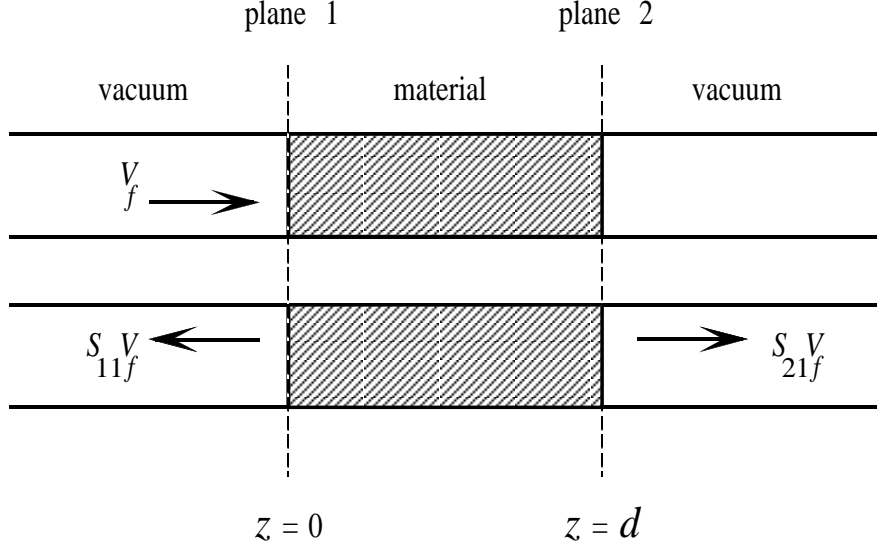


Figure 2.1. A transmission line filled with a length d of material with vacuum on both sides. A TEM wave with complex amplitude V_f is incident from the left; the phases are measured relative to the reference planes (dashed lines).

Equations (2.2) through (2.8) allow us to deduce μ and ϵ from measured values of S_{11} and S_{21} for a sample of length d inserted into a coaxial air line.

A sign choice must be made in Equation (2.6). This choice determines the signs of k_z and Z (corresponding to two different directions of propagation). However, because μ and ϵ depend only on $k_z Z$ and k_z/Z , the final result is independent of which sign we choose in Equation (2.6). We chose the sign to make $|\Gamma| < 1$, which should give $\text{Re } k_z > 0$.

A phase ambiguity also arises from the complex logarithm in Equation (2.4): the imaginary part of $\ln(T)$ is ambiguous by an integer multiple of 2π . This ambiguity reflects the fact that $\text{Re } k_z d$ is the phase change for a wave travelling from $z = 0$ to $z = d$; knowing only T , we cannot deduce the total phase change without knowing the number of whole wavelengths that exist in the length d . We can write

$$k_z d = 2\pi N + i \text{Ln}(T) , \quad (2.9)$$

where $\text{Ln}(T)$ is the “principal value” of $\ln(T)$, whose imaginary part is between 0 and -2π (so that $\text{Re } i \text{Ln}(T)$ is between 0 and 2π), and N is an integer (equal to the number of whole wavelengths that fit in the length d). We can calculate $\text{Ln}(T)$ directly from T , but we need to know N in order to get $k_z d$. Two methods have been used to resolve this dilemma. The first, introduced by W. Weir [29], is, in effect, to determine N by comparing the phase velocity to the group velocity. Since this approach only works for materials in which $\mu\epsilon$ is constant, it is not so useful for our materials, whose properties depend strongly on frequency. The other method, used by W. Barry [31], is to make sure that the sample length is less than the wavelength

in the material

$$\lambda_z = \frac{2\pi}{\text{Re } k_z} \quad (2.10)$$

over the entire frequency spectrum, in which case $N = 0$. In practice, this is a reasonable solution because there are usually maxima in the measurement error near frequencies at which d is an integer multiple of $\lambda_z/2$, so samples shorter than λ_z yield better results. Nevertheless, because we were concerned about reproducibility and needed to look at different sample lengths, we wanted to analyse data with $d \geq \lambda_z$, so we sought another method of determining N .

It is convenient to divide the problem into two parts: (i) What is the correct value of N at the starting frequency in the spectrum? (ii) At what frequencies must we change N as we sweep through the frequency spectrum? Question (ii) is the more straightforward one. We can expect $k_z d$ to be a continuous function of frequency. However, $\text{Re } i\text{Ln}(T)$ will jump from about 2π to about 0 at frequencies where N increases by 1. We found that the variation in $i\text{Ln}(T)$ with frequency allowed us to easily identify the frequencies at which we needed to change N under most circumstances.

Question (i) is more complicated. We cannot deduce the starting value N_0 of N from measurements on a single sample, since we do not know *a priori* how many whole wavelengths fit in a length d at the starting frequency. The only way to find N_0 in general is through repeated measurements with different sample lengths: if we choose the N_0 's correctly, we expect that $k_z d$ will depend on d but k_z will not. We made guesses for the N_0 's and compared the resulting $\text{Re } k_z$ values for different samples. The choice of $N_0 = 0$ (at 300 kHz) gave consistent results in all cases. It is difficult to rule out all the other possible values of N_0 with this method. However, in the case of Ferrite-50, whose microwave properties were measured at 2.4 GHz using the resonator technique (which does not suffer from phase ambiguities) by our colleagues at Chalk River [32], we have an independently determined value for $\text{Re } k_z$ which agrees with our choice of $N_0 = 0$.

2.2 Experimental Techniques

Samples of the material to be measured were machined into cylindrical ‘‘beads’’ using diamond-coated tools (all the materials were ceramics). The samples were measured in custom-made 7 mm coaxial air lines. Precision 7 mm connectors were used, as they were found to give less systematic error than type N connectors. The S-parameters of the air line with its material insert were measured from 300 kHz to 20 GHz using two Hewlett-Packard network analysers, an 8753C and an 8720A. All four S-parameters were measured. The analysers were interfaced to an HP 9816 computer; BASIC programs were written to control the S-parameter measurements and analyse the data [33, 34].

The network analysers were calibrated using the standard ‘‘full 2-port’’ procedure. The reference planes were extended to the faces of the sample using the analysers’ port extension feature and the known lengths of the air line and sample. The sample

location inside the air line could not be controlled very well because of the spring-loaded centre conductor; to ensure that the reference planes coincided with the faces of the sample, the phases of S_{11} and S_{22} were compared after extending the ports and the port extensions were adjusted to eliminate any systematic phase differences. A particular recipe for averaging during the calibration was found to give less noise in subsequent measurements [24, 25].

In order to get reproducible results, we found it necessary to machine the samples to relatively close tolerances and further improve the contact between the sample and air line with a layer of liquid metal. We used a eutectic alloy of gallium and indium with a melting point of 16°C. Filling the gaps between the sample and the air line without coating the faces of the sample with metal or leaving drops of liquid metal in the air line proved to be a difficult technique to master, so we would not call this an ideal solution.

To check the validity of our techniques, some dielectric materials were measured. These measurements were done in commercially-made air lines without liquid metal. The results suggest that our measurement techniques are valid, but sensitive to the fit between the sample and air line, and susceptible to large errors for some combinations of sample length and wavelength. Further measurements done by R. Chiang indicate that our custom-made air lines give about the same accuracy for teflon as the commercial air lines [25].

2.3 Results

Selected information on the four materials is given in Table 2.1 above. There is significant variation in the DC resistivity of the TT2-111-series material, possibly related to the interest in higher conductivity that we expressed to the manufacturer. The TT2-111-series measurements presented herein were done on a batch with a stated DC resistivity of 435 Ωm , which we designate “TT2-111V” (the manufacturer’s designation for all varieties is TT2-111R). The variation in properties of Ferrite-50 batches we received was less extreme (stated DC resistivities ranged from 0.14 to 0.50 Ωm).

The μ and ϵ values were measured for two or more samples of different length (ranging from 0.8 to 10.9 mm) for each material, with liquid metal filling the gaps. In almost all cases, different samples of the same material were machined from the same piece. We tried to choose the sample length d to minimise the error in our μ and ϵ values. We followed the usual strategy for choosing d , a rationalisation for which can be found elsewhere [30]. Briefly stated, the strategy is to (i) avoid having d close to an integer multiple of $\lambda_z/2$ (which produces a minimum in S_{11} and a maximum in S_{21}) and (ii) avoid having $\lambda_z \gg d$. Constraint (i) is not as important in absorbing materials as it is in low-loss materials. As a rule of thumb, we tried to satisfy the following condition:

$$\frac{\lambda_z}{8} \leq d \leq \frac{3\lambda_z}{8} . \quad (2.11)$$

The choice of $\lambda_z/8$ was rather arbitrary (and difficult to adhere to). We used (2.11)

to choose the “best” sample length for each frequency in the spectrum, dividing the spectrum into several ranges. Forward (from S_{11} and S_{21}) and reverse (from S_{22} and S_{12}) values were treated as independent in order to get some indication of the accuracy.

Our results for Ferrite-50 are shown in Figures 2.2 and 2.3. Values measured at 2.4 GHz using the resonator method [32] are also shown. The resonator results agree relatively well with ours. The measured values of $\text{Im } \epsilon$ are close to what one would expect from the DC resistivity for purely Ohmic losses.

Results for TT2-111V, CMD10, and IB-004 are shown in Figures 2.4 and 2.5. Both the real and imaginary parts of ϵ are quite a bit smaller than in Ferrite-50. In TT2-111V, $\text{Im } \epsilon$ appears to be Ohmic at low frequencies. In CMD10 and IB-004, $\text{Im } \epsilon$ is small enough to make it difficult to measure with this technique. For the ferrites shown in Figures 2.4 and 2.5, we approach full transmission ($S_{11} = 0$ and $S_{21} = 1$) at low frequencies, which amplifies the error in the results. The rapid increase in μ and ϵ with decreasing frequency actually helps: λ_z varies more slowly with frequency, so that we can get the same accuracy with a smaller set of sample lengths (relative to materials with constant or slowly-varying μ and ϵ).

W. Barry [31] has measured the properties of NZ-51 material from Emerson & Cuming (from 500 MHz to 5.5 GHz), which is said to be similar to the TT2-111-series material. He used the transmission line technique with a strip-line arrangement. Our results for TT2-111V are quite close to his. T. Tajima [35] has measured the properties of IB-004 (from 30 MHz to 3 GHz) using the coaxial transmission line method; our results agree well with his. R. Boni *et al.* [36] have measured the properties of TT2-111-series ferrite (from 500 MHz to 2.5 GHz) using a shorted transmission line with two different sample lengths. Their results are significantly different from ours. We do not yet understand the reason for this discrepancy; their measured values for $\text{Im } \mu$ and $\text{Im } \epsilon$ have opposite signs, which, when taken at face value, would seem to be unphysical.

Our results for two other nickel-zinc-like ferrites, three other manganese-zinc ferrites, and an “artificial dielectric” material may be found elsewhere [23, 24, 25]. Further measurements on different batches of TT2-111-series ferrite were also done, along with an examination the effect of various thermal cycles (required for the fabrication of the HOM loads) on the properties of TT2-111-series and IB-004 ferrite (the latter in collaboration with our colleagues at KEK). The results of these studies are given in a separate report by R. Chiang [25]. The batch-to-batch variation in $\text{Im } \epsilon$ was as much as a factor of 20 for TT2-111-series ferrite; the corresponding variation in $\text{Re } \epsilon$ was about a factor of 2 above 10 MHz, and larger at low frequencies. The batch-to-batch variation in μ was small in comparison to the batch-to-batch variation in ϵ . The significant variation in the ϵ values of the TT2-111-series ferrite actually does not have a very large influence on the interaction with the beam, as will be discussed in Section 5.6.

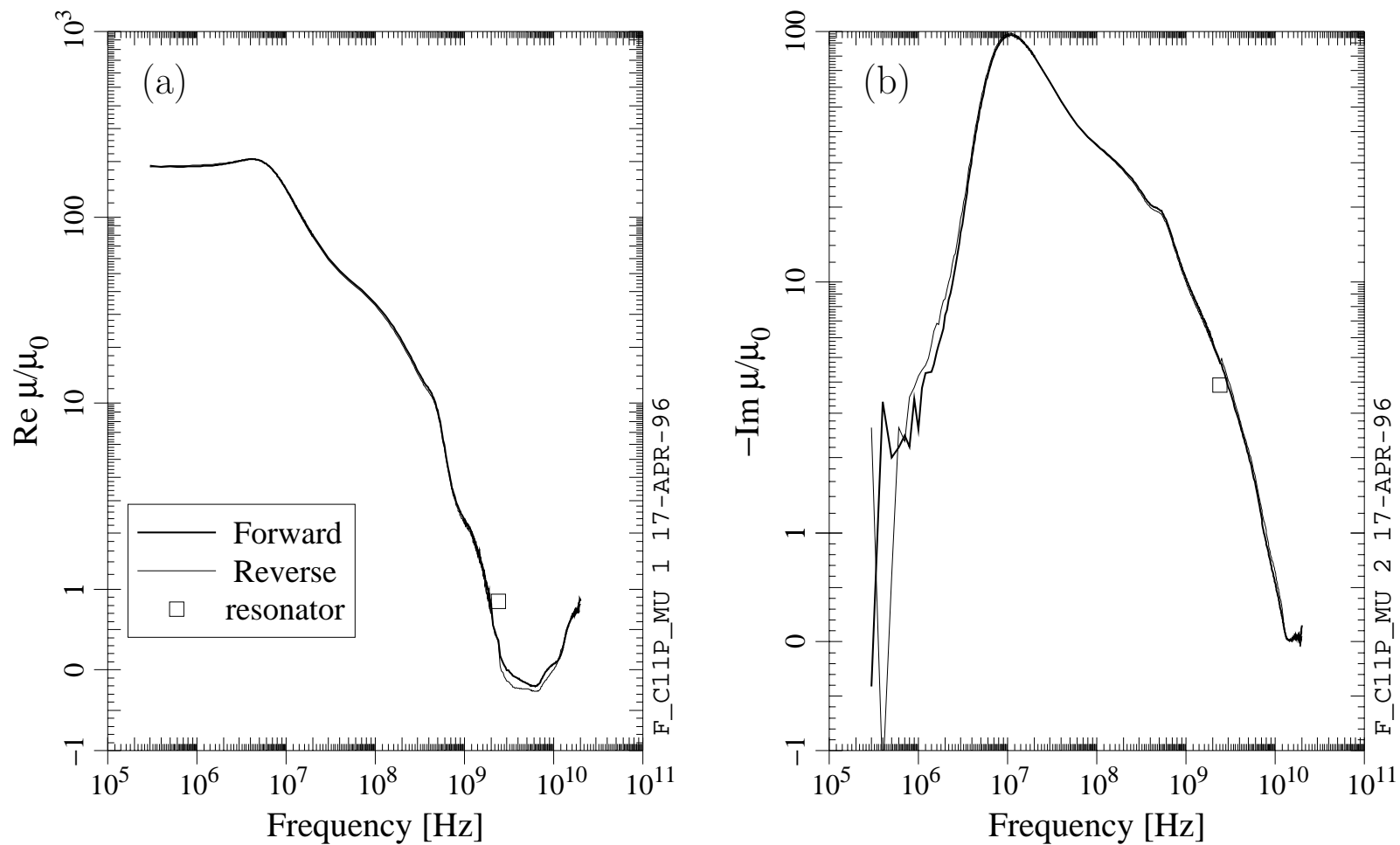


Figure 2.2. Measured values of (a) the real part and (b) the imaginary part (times -1) of μ for Ferrite-50. Values measured using the resonator method [32] are also shown.

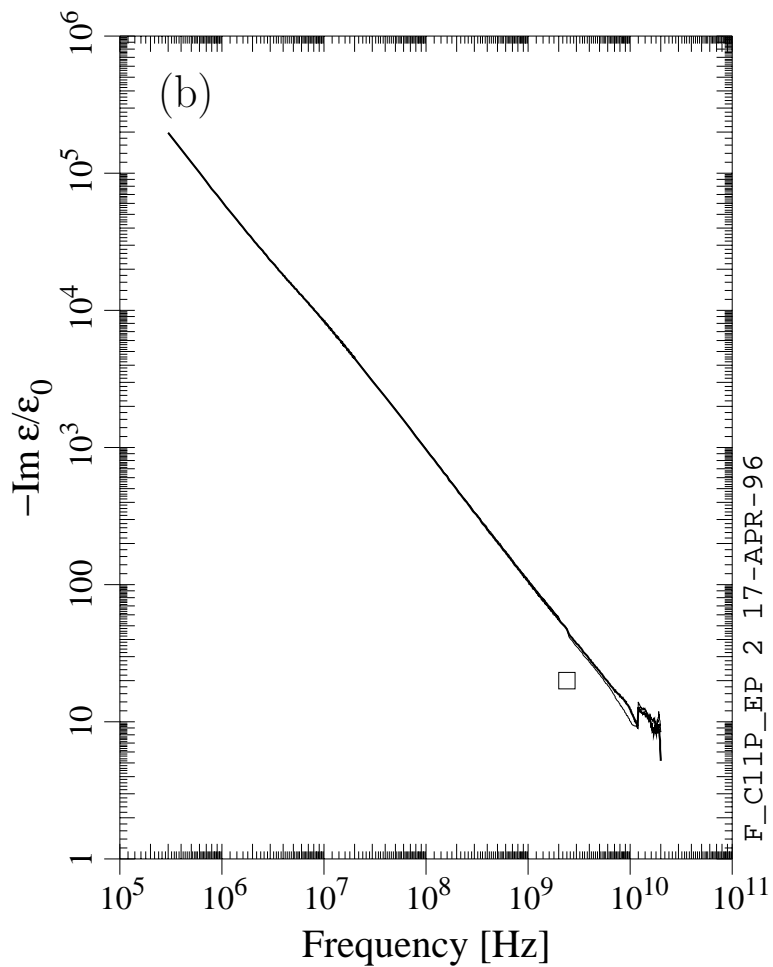
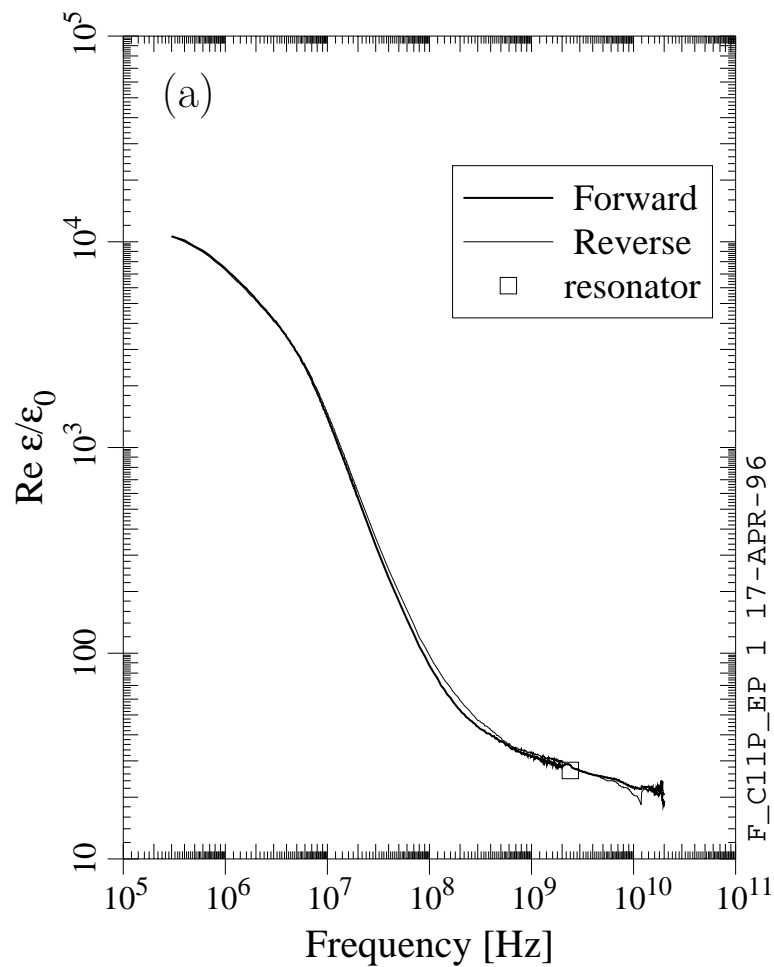


Figure 2.3. Measured values of (a) the real part and (b) the imaginary part (times -1) of ϵ for Ferrite-50. Values measured using the resonator method [32] are also shown.

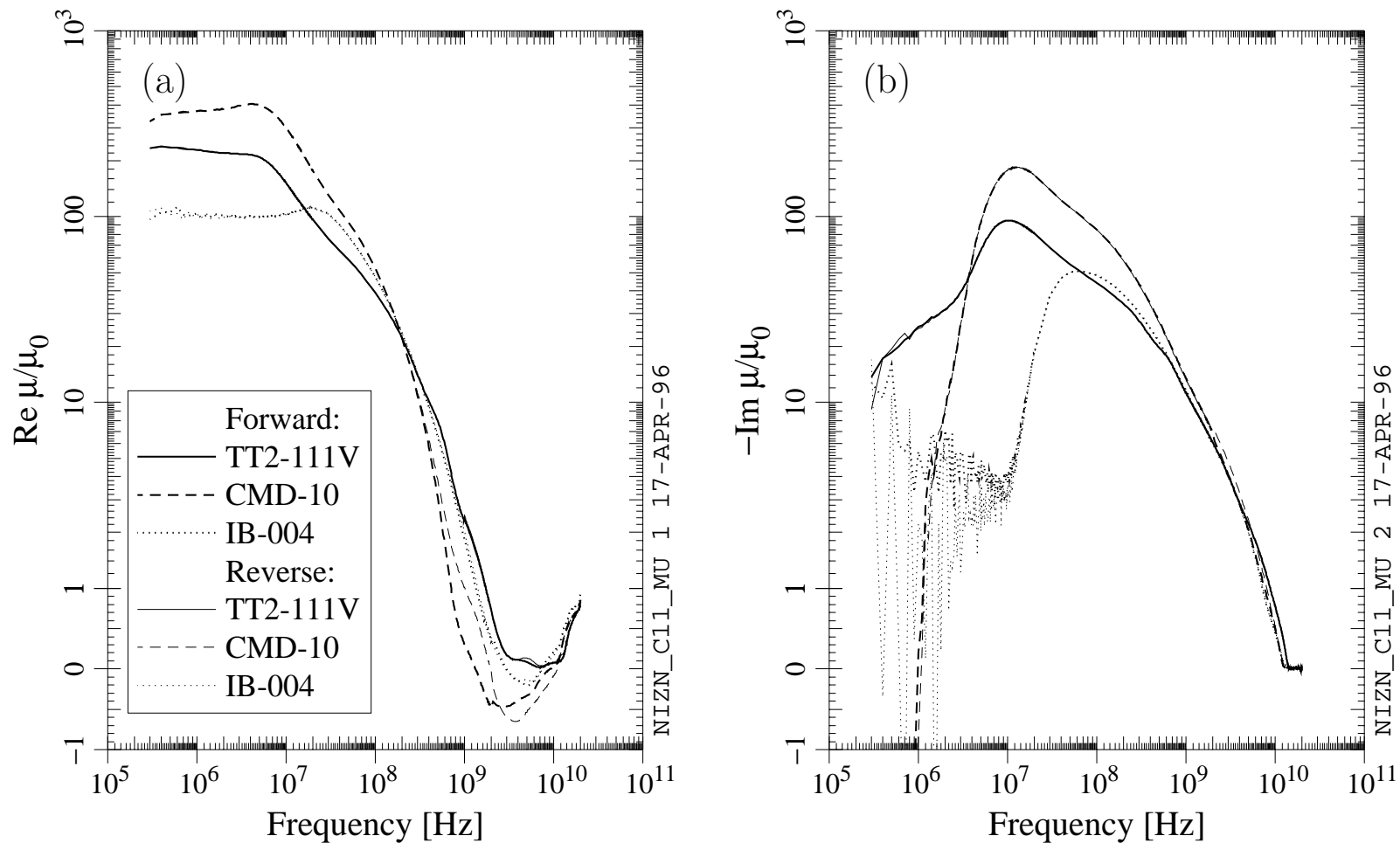


Figure 2.4. Measured values of (a) the real part and (b) the imaginary part (times -1) of μ for TT2-111V, CMD10, and IB-004 ferrites.

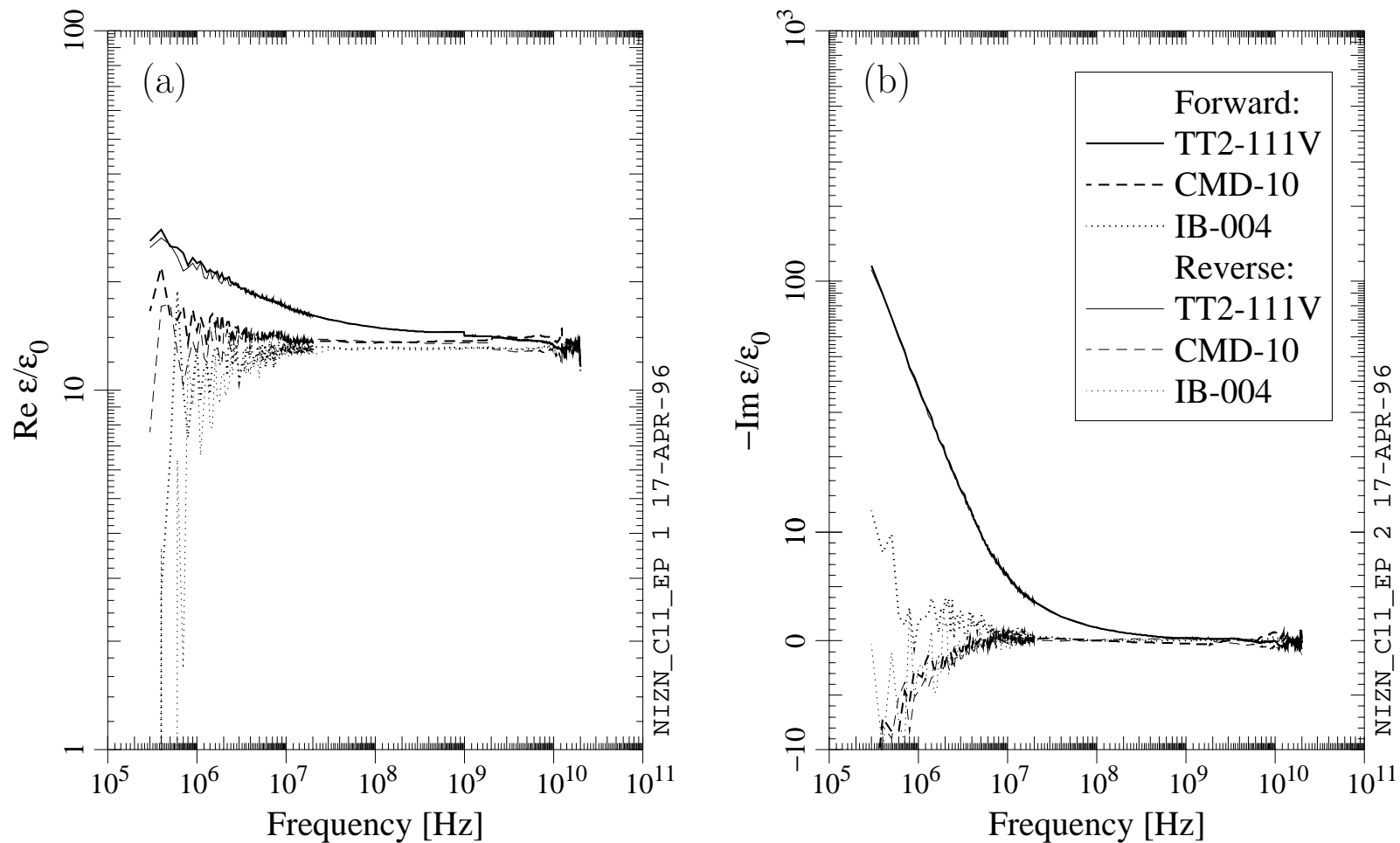


Figure 2.5. Measured values of (a) the real part and (b) the imaginary part (times -1) of ϵ for TT2-111V, CMD10, and IB-004 ferrites.

2.4 Interpretations

The measured values of μ and ϵ show features that might be considered extreme: significant variation with frequency, large values at low frequencies (μ/μ_0 and ϵ/ϵ_0 exceeding 100 and 10^4 , respectively), and very small values at high frequencies in some cases, with $\text{Re } \mu/\mu_0$ sometimes less than 1. Nevertheless, all of these features have been seen in previous measurements of nickel-zinc ferrites [28]. In all four ferrites, there is a maximum in $-\text{Im } \mu$ between 10^6 and 10^8 Hz, accompanied by a rapid decrease in $\text{Re } \mu$ as a function of frequency. This behaviour is characteristic of the domain wall motion resonance [37].

The Influence of Air Gaps

Measurements were done on Ferrite-50 and TT2-111-series ferrite to evaluate the effect of air gaps. Three cases were examined: (i) samples machined without tight tolerances, which fit loosely inside the air line, (ii) samples with tighter tolerances, which fit snugly inside the line, and (iii) samples with slightly relaxed tolerances, but with the liquid metal present in the gap between the sample and air line. The ϵ values changed dramatically between different cases in Ferrite-50 and less dramatically in the TT2-111-series ferrite; the effect was most pronounced for the largest ϵ values. The reproducibility of the ϵ results was found to improve in going from method (i) to method (iii). Very little change in μ values was seen.

A simple DC analysis can provide a qualitative explanation for these observations. In the static limit, k_z and Z are determined by the inductance per unit length L' and the capacitance per unit length C' . In the case of a coaxial line that is completely filled with material, as assumed in the standard analysis, L' and C' are proportional to μ and ϵ , respectively. If there are air gaps between the material and the air line, however, the proportionality is no longer exact: extra terms appear which depend on the gap size. The correction term for μ is always small as long as the gaps are small compared to the inner and outer conductor radii a and b and as long as μ is not small compared to μ_0 . Thus we can expect that air gaps will not have a strong influence on measured μ values under most circumstances. The correction term for ϵ , on the other hand, is small if the gaps are small compared to a and b and ϵ is not *large* compared to ϵ_0 . If ϵ/ϵ_0 is an appreciable fraction of a (or b) divided by the gap length, we can expect a significant correction due to the air gaps. These conclusions are qualitatively consistent with our observations.

Reproducibility

There are small steps in the measured μ and ϵ values which occur when we switch from one sample length to another. Differences between the results for different samples can give us some clues about the reproducibility of the measurements. Of the materials covered herein, the worst reproducibility in measured μ values was seen in CMD10 and IB-004. To illustrate, measured values of $\text{Re } \mu$ for two CMD10 samples are shown in Figure 2.6a. Poor agreement can be seen near 1 GHz and at low frequencies. In

the case of the longer sample, a spike can also be seen when d is equal to $\lambda_z/2$. Even greater variation was seen in measurements on other manganese-zinc ferrites [23, 24]. Measured μ values for Ferrite-50 and TT2-111V were somewhat more reproducible, as illustrated in Figure 2.6b. On the other hand, there was quite a bit of variation in the measured $\text{Im } \epsilon$ values for TT2-111V.

To identify the source of this irreproducibility, three measurements on TT2-111V were compared: (i) a first measurement on a short sample, (ii) a second measurement on the same sample, done after removing and re-applying the liquid metal, and (iii) a measurement on a second sample of about the same length. The μ results for the three cases do not show much difference, but the two measurements of ϵ on the first sample agreed significantly better with each other than they did with the measurement on the second sample. Similar agreement between repeated measurements on a longer sample was also seen. This suggests that the reproducibility problems stem mostly from variation in the properties or the machining from one sample to another.

Kramers-Kronig Relations

The electric field and the electric polarisation must both be real-valued functions in the time domain. With the additional requirement that the relationship between these two quantities be causal, one can obtain constraints on the complex permittivity, the so-called Kramers-Kronig relations (see [38], for example). In our notation, the constraints require that

$$\text{Re } \epsilon(\omega) = 1 - \frac{1}{\pi} \text{PV} \int_{-\infty}^{\infty} \frac{\text{Im } \epsilon(\omega')}{\omega' - \omega} d\omega', \quad (2.12)$$

where PV denotes the principal value. A similar expression for $\text{Im } \epsilon$ in terms of an integral involving $\text{Re } \epsilon$ can also be derived.

Equation (2.12) implies that we can deduce $\text{Re } \epsilon(\omega)$ for any ω from a measurement of $\text{Im } \epsilon(\omega)$ for all ω . We have measured ϵ only over a finite frequency range, but if $\text{Im } \epsilon$ is small outside of this range, we can expect to obtain a reasonable prediction for $\text{Re } \epsilon$ from $\text{Im } \epsilon$ and Equation (2.12). The Kramers-Kronig relations hence allow us to check our measured values of ϵ for consistency.

The magnetic field and the magnetisation must also be real-valued and causal; consequently, the real and imaginary parts of μ must satisfy an equation of the same form as (2.12). Thus, the above arguments apply to μ as well.

The measured values of $\text{Re } \mu$ for TT2-111V are compared to predicted values obtained from $\text{Im } \mu$ via Equation (2.12) in Figure 2.7a. The agreement is quite good, which suggests that our measured μ values are self-consistent. The analogous comparison for ϵ is made in Figure 2.7b. In the case of ϵ , there is the complication that $\text{Im } \epsilon$, unlike $\text{Im } \mu$, is not small at low frequencies (see Figures 2.4 and 2.5). In obtaining the prediction shown in Figure 2.7b, we assumed $\text{Im } \epsilon(\omega)$ to have resistive behaviour for frequencies below the measured range. We chose the DC resistivity based on the lowest measured values of $\text{Im } \epsilon$. With this assumption for the low-frequency behaviour of $\text{Im } \epsilon$, we see that the predicted $\text{Re } \epsilon$ has approximately the right frequency

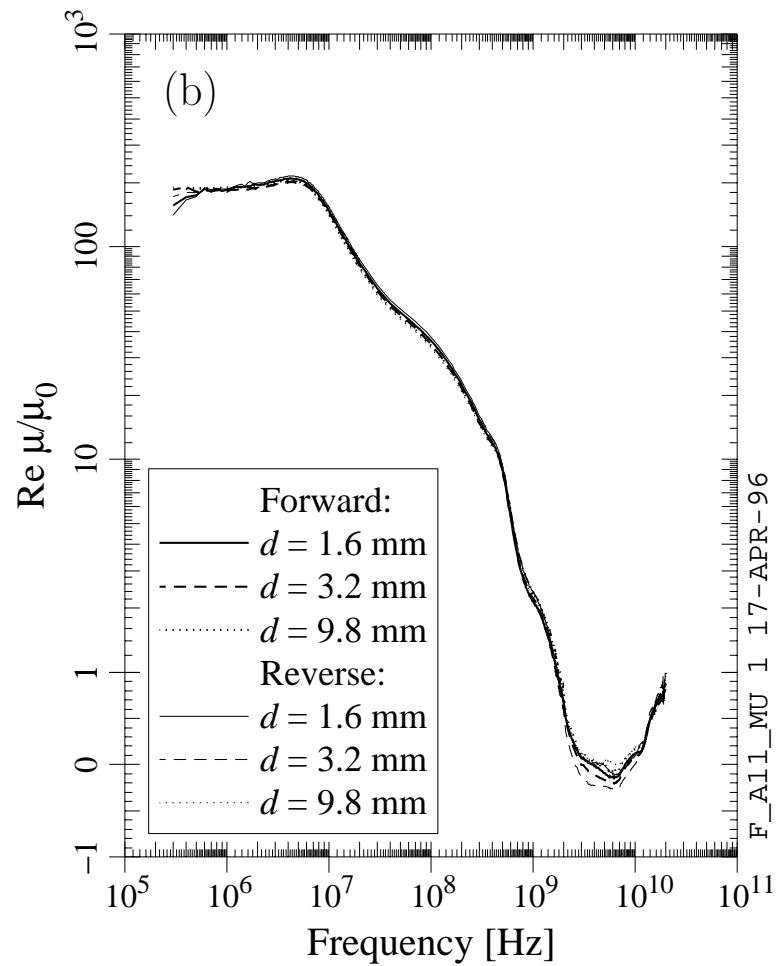
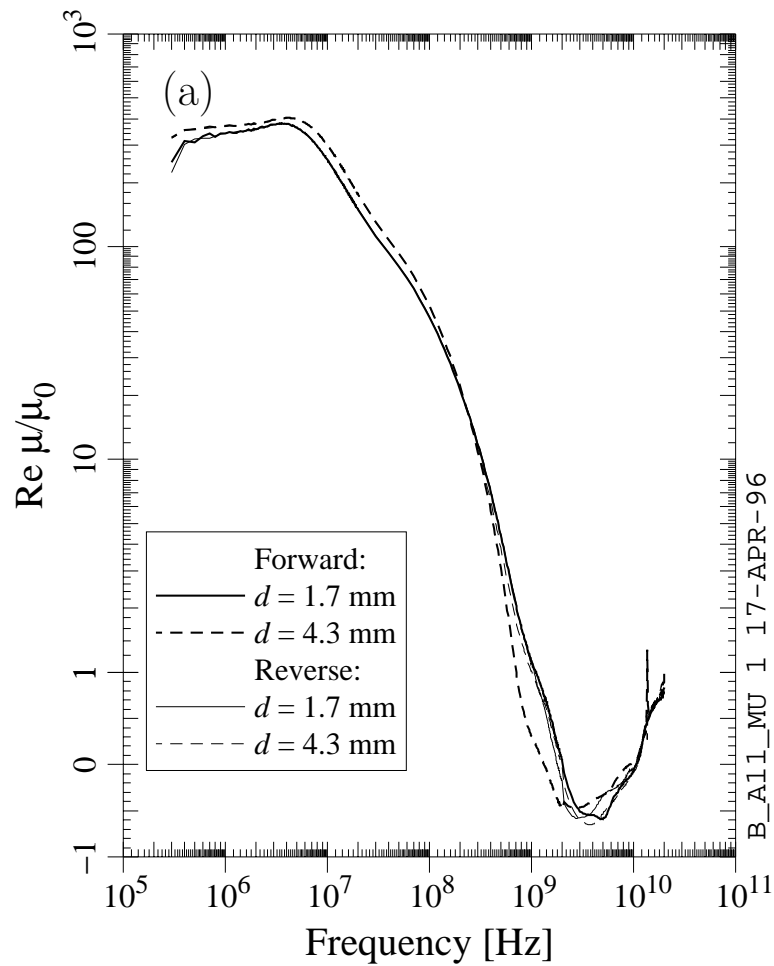


Figure 2.6. Measured values of the real part of μ , for (a) two CMD10 samples and (b) for three Ferrite-50 samples of different length.

dependence, but that there is a significant offset between the prediction and the measurement. Such an offset would be expected if $\text{Im } \epsilon$ becomes large again above the maximum frequency in our measurement (a high-frequency increase in $\text{Im } \epsilon$ cannot be expected to have much impact on the problem at hand, because the beam power spectrum is typically quite small above 20 GHz). Hence, our measured ϵ values are not necessarily inconsistent.

2.5 Summary

We used the coaxial transmission line technique to measure the microwave properties of absorbing materials between 300 kHz and 20 GHz. The method seems to be adequate for the materials we have examined, if precautions are taken to eliminate air gaps and no assumptions are made about dependence of the phase and group velocities on frequency. We cannot accurately measure real or imaginary parts of μ or ϵ that are close to zero with this method, however. The biggest problem with the measurements has been the lack of reproducibility between different samples. Our results are in reasonable agreement with the majority of the measurements we have seen in the literature, for the frequency range of overlap.

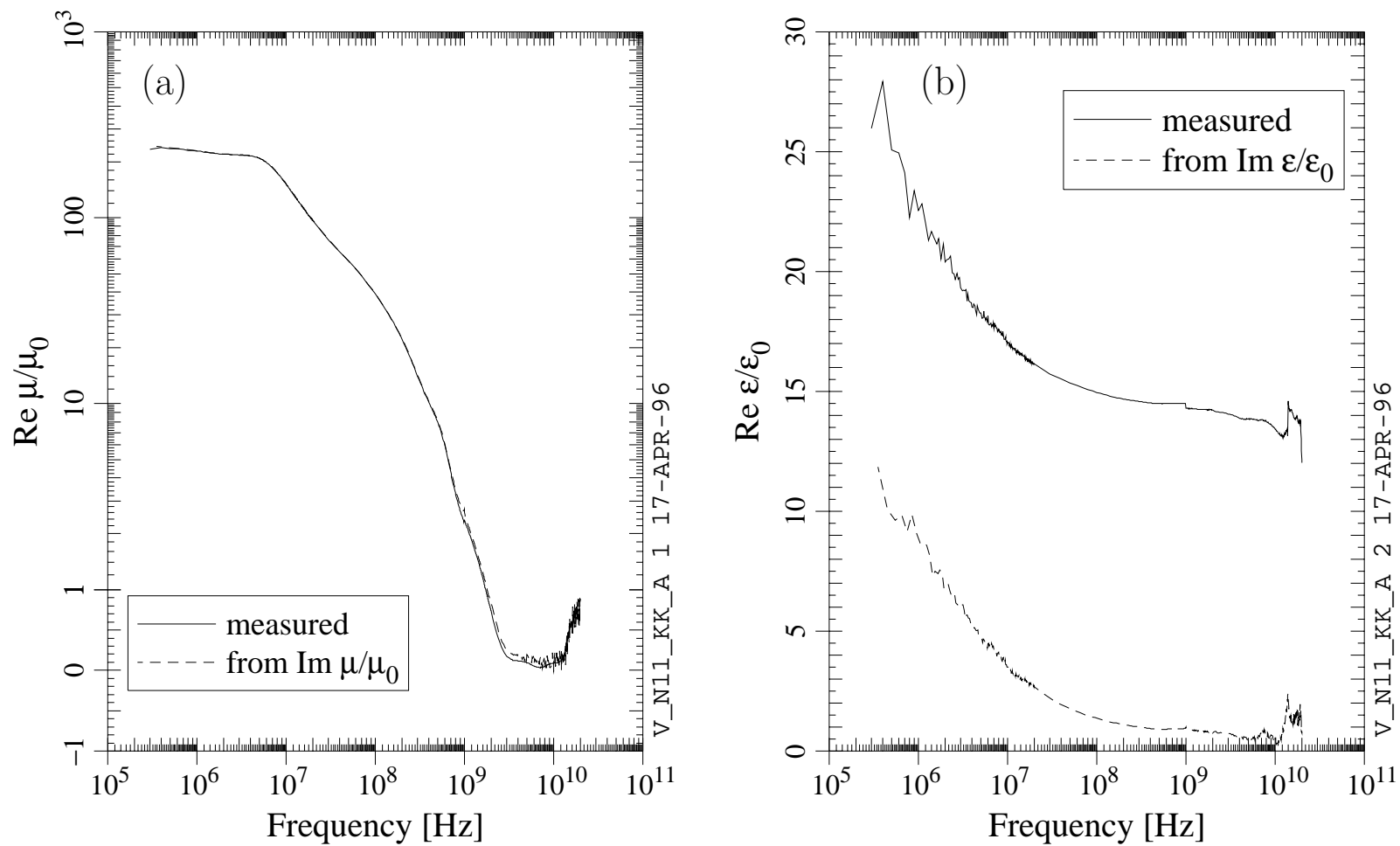


Figure 2.7. Comparison of (a) measured values of $\text{Re } \mu$ to values predicted from $\text{Im } \mu$ and (b) measured values of $\text{Re } \epsilon$ to values predicted from $\text{Im } \epsilon$ for TT2-111V.

Chapter 3

Coupling Impedance Predictions

Predictions for the coupling impedance of the Porcupine load via numerical, semi-numerical, and analytic techniques will be presented in this chapter. Predictions for a load of magnified impedance, the “L3 load” (which was used for measurements with the CESR beam, as will be discussed in Chapter 5), will also be given. Predictions and wire measurements for two other cases will be discussed as well. We will conclude with a simplified model for the Porcupine impedance and some discussion of the impedance’s dependence on the microwave properties of the material and the geometry of the load. To begin with, though, we will review some fundamentals about the interaction of beam line devices with high-energy beams and introduce the basic tools of the trade, namely the wake function and the coupling impedance.

3.1 The Beam Coupling Impedance and Its Importance

There is an extensive literature on the general subject of wake fields, wake functions, and coupling impedances; we mention a few of the many accelerator school and review articles in the bibliography [39, 40, 41, 42]. The subject is also treated in a recent book by A. Chao [43].

A Beam’s Interaction with its Surroundings in a Storage Ring

In Section 1.1, we argued that a bunched beam travelling through a storage ring will exchange energy with its surroundings due to the imperfect conductivity of the walls of the beam tube and because of variation in the beam tube’s cross-section. We asserted that the wake fields produced as a bunch interacts with its surroundings could act back on the particles in the bunch and produce a distortion in the bunch shape or unstable motion of the bunch as a whole. We need to quantify the effect of the wake fields produced by the passage of a bunch on the particles in the beam. In the general case, the beam will consist of multiple bunches, so the wake force from one bunch can act on particles in the same bunch or in other bunches.

In Section 1.1, we considered a beam travelling at a speed approaching the speed of light c . This may seem unrealistic, but it is in fact a good approximation for our purposes: an electron or positron beam with an energy of 5.3 GeV per particle (which

is typical of CESR) travels at a speed which differs from c by less than one part in 10^8 . As a consequence, in order to determine the force acting on the particles in a bunch as they travel through a structure, we do not need to take into account the effect of the wake force on the motion of the particles: the approximation that their velocity remains unaffected is an excellent one. This will simplify the problem considerably, because we will be able to treat the bunch's trajectory as a known quantity, instead of having to find a self-consistent solution to the Maxwell Equations with both the electromagnetic field and the bunch's trajectory as unknown quantities.

The Wake Function

The most intuitive picture for the beam-environment interaction can be found in the time domain. Suppose we wish to characterise a beam's interaction with some beam line device (a cavity, a section of beam pipe with a material layer, or some other disruptive element). Let us assume that the beam pipe and device are both axisymmetric, and use cylindrical coordinates (r, z, ϕ) . Let us send a bunch with a given charge distribution through this device at velocity $c\hat{z}$. After a time t , let us send a small witness charge q_w through, also at velocity $c\hat{z}$. The witness particle experiences no change in its velocity, but it does experience a change $\Delta\vec{p}(t)$ in its momentum. $\Delta\vec{p}(t)$ depends on q_w , the transverse position (r, ϕ) of the witness charge, and the bunch's charge distribution. Thus, $\Delta\vec{p}(t)$ is difficult to calculate in general. If most of the bunch's charge distribution is close to the z axis, however, it is useful to do a multipole expansion of the bunch's transverse charge distribution. The result is

$$\Delta\vec{p}(t) = -\frac{q_w}{c} \sum_{m=0}^{\infty} \left[r^m \hat{z} \Phi^t \mathbf{W}_m^{\parallel}(t) + m r^{m-1} (\hat{r} \Phi^t + \hat{\phi} \Psi^t) \mathbf{W}_m^{\perp}(t) \right]. \quad (3.1)$$

In Equation (3.1), $\mathbf{W}_m^{\parallel}(t)$ and $\mathbf{W}_m^{\perp}(t)$ are the longitudinal and transverse wake functions (also known as wake potentials), respectively. $\mathbf{W}_m^{\parallel}(t)$, $\mathbf{W}_m^{\perp}(t)$, Φ , and Ψ are 2 by 1 matrices, with

$$\Phi \equiv \begin{bmatrix} \cos(m\phi) \\ \sin(m\phi) \end{bmatrix} \quad (3.2)$$

$$\Psi \equiv \begin{bmatrix} -\sin(m\phi) \\ \cos(m\phi) \end{bmatrix}. \quad (3.3)$$

Φ^t denotes the transpose of Φ . $\mathbf{W}_m^{\parallel}(t)$ and $\mathbf{W}_m^{\perp}(t)$ depend on the characteristics of the beam line device and on the bunch's charge distribution. The first two terms in the sum are usually the most important, in which case

$$\Delta\vec{p}(t) \approx -\frac{q_w}{c} \left[\hat{z} \Phi^t \mathbf{W}_0^{\parallel}(t) + (\hat{r} \Phi^t + \hat{\phi} \Psi^t) \mathbf{W}_1^{\perp}(t) \right]. \quad (3.4)$$

$\mathbf{W}_m^{\parallel}(t)$ and $\mathbf{W}_m^{\perp}(t)$ are related to the wake functions $w_m^{\parallel}(t)$ and $w_m^{\perp}(t)$ engendered by a single particle with a pure multipole moment oriented so that the charge

distribution goes as $\cos(m\phi)$:

$$\mathbf{W}_m^{\parallel,\perp}(t) = \int_{-\infty}^{\infty} \mathbf{P}_m(t') w_m^{\parallel,\perp}(t-t') dt' , \quad (3.5)$$

where $\mathbf{P}_m(t)$ is obtained through a multipole expansion of the bunch's transverse charge distribution:

$$\mathbf{P}_m(t) \equiv c \int_{-\infty}^{\infty} \int_0^{2\pi} \Phi r^m \rho(r, z, \phi, t + z/c) r d\phi dr , \quad (3.6)$$

where $\rho(r, z, \phi, t)$ is the bunch's charge density (since ρ depends only on $ct - z$, the above integral is independent of z). $\mathbf{P}_m(t)$ gives the longitudinal distribution of the m th multipole moment of the bunch. The single-particle wake functions $w_m^{\parallel}(t)$ and $w_m^{\perp}(t)$ depend only on the characteristics of the device. Mathematically, $w_m^{\parallel}(t)$ and $w_m^{\perp}(t)$ are Green functions.

The Beam Coupling Impedance

A less intuitive but equally valid description of the beam-environment interaction can be found in the frequency domain. The time and frequency domain descriptions are two sides of the same coin, each with its virtues. The frequency domain quantity analogous to the wake function is the beam coupling impedance, which is a measure of the strength of the interaction of the device with a sinusoidal beam. The wake function and the coupling impedance form a Fourier transform pair. We follow the sign convention for Fourier transforms given in Equation (2.1) in Section 2.1. Several authors use the opposite sign convention, in which case their impedance is the complex conjugates of ours. A. Chao [43] uses the same Fourier transform convention, but he defines the wake function with the opposite sign in its argument, so his impedance is the complex conjugate of ours as well.

The Fourier transforms of $w_m^{\parallel}(t)$ and $\frac{1}{i}w_m^{\perp}(t)$ are the longitudinal and transverse coupling impedances, $Z_m^{\parallel}(\omega)$ and $Z_m^{\perp}(\omega)$, respectively (the factor of i is used by convention). It can be shown that $Z_m^{\parallel}(\omega) = \frac{\omega}{c}Z_m^{\perp}(\omega)$. $Z_0^{\parallel}(\omega)$ and $Z_1^{\perp}(\omega)$ are sometimes simply called the longitudinal and transverse impedances (note that, according to Equation (3.1), $\mathbf{W}_0^{\perp}(t)$ does not produce any momentum change, so $Z_0^{\perp}(\omega)$ can be ignored). The Fourier transforms of $W_m^{\parallel}(t)$ and $\frac{1}{i}W_m^{\perp}(t)$ are equal to the product of the Fourier transform of $\mathbf{P}_m(t)$ with $Z_m^{\parallel}(\omega)$ and $Z_m^{\perp}(\omega)$, respectively.

Knowledge of either the wake function or the coupling impedance gives us complete information about the interaction of the device with a beam; all of the information we need to predict instabilities can be obtained from either of these quantities. Furthermore, the integral of $\mathbf{W}_0^{\parallel}(t)$ or $Z_0^{\parallel}(\omega)$ with the appropriate bunch charge distribution gives the total energy U lost by the bunch, and hence the power transferred to the device. The energy loss is usually computed in terms of the loss factor

$$k^{\parallel} \equiv \frac{1}{q_b^2} U, \quad (3.7)$$

where q_b is the total charge of the bunch. The loss factor depends on the device and the bunch's charge distribution. The dominant terms are the monopole and dipole loss factors, k_0^{\parallel} and k_1^{\parallel} . In the single-pass case, k_0^{\parallel} and k_1^{\parallel} can be obtained from Z_0^{\parallel} and Z_1^{\parallel} via

$$k_m^{\parallel}(\sigma_z) = \frac{1}{2\pi} \int_{-\infty}^{\infty} d\omega Z_m^{\parallel}(\omega) \exp\left(-\frac{\omega^2 \sigma_z^2}{c^2}\right) \quad (3.8)$$

in the case of a Gaussian bunch with standard deviation σ_z . For the problem at hand, the single-pass loss factor is adequate to determine the power dissipation in the multi-turn case, a point which we will return to in Section 4.2.

3.2 Methods for Predicting the Coupling Impedance

We will now discuss five methods for predicting the coupling impedance or, equivalently, the wake function. The first two rely on a bench RF measurement of the device, while the last three involve modelling the device.

Wire Method—Time Domain

The fields engendered by a bunch travelling through a device at speed c are approximately the same as those of a pulse travelling down a small-diameter wire, provided the longitudinal distribution of surface charges on the wire is approximately the same as the longitudinal distribution of charge in the bunch. By comparing the pulse transmitted through a beam line device to a reference pulse transmitted through the same length of “ideal” beam pipe, one can estimate the wake function. A single pulse travelling down a single wire gives $\mathbf{W}_0^{\parallel}(t)$; pulses of opposite voltage travelling down a pair of wires give $\mathbf{W}_1^{\perp}(t)$. The appropriate integral of $\mathbf{W}_0^{\parallel}(t)$ gives the loss factor. The apparatus and methods we used for this measurement are described elsewhere [44].

Wire Method—Frequency Domain

By using a sinusoidal wave with angular frequency ω instead of a pulse, one can measure the coupling impedance approximately. By comparing the amplitude and phase of a wave transmitted through the beam line device to those of a reference wave, one can estimate $Z_0^{\parallel}(\omega)$ (with one wire) or $Z_1^{\perp}(\omega)$ (with two wires carrying waves that are 180° out of phase). The techniques are discussed in a separate paper [45].

Numerical Simulation

Programs such as TBCI [46] and ABCI [1] have been used extensively to model wake effects for geometrical devices (cavities, cross-sectional changes, *etc*). AMOS

[47] is a program similar in spirit to TBCI and ABCI, but able to model devices containing dispersive materials. AMOS solves the Maxwell equations in the time domain on a finite-difference rectangular mesh. The device must be axisymmetric, but the beam need not be, so that both the longitudinal and transverse impedances can be calculated. Materials with complex frequency-dependent permeability μ and permittivity ϵ are fitted to simplified models. For the calculations discussed herein, we used a “relaxation” model for μ with up to 3 terms:

$$\frac{\mu(\omega)}{\mu_0} = 1 + \sum_j \frac{\alpha_j}{2} \left(\frac{1}{\beta_j - \gamma_j - i\omega} - \frac{1}{\beta_j + \gamma_j - i\omega} \right), \quad (3.9)$$

where α_j , β_j , and γ_j are real. For ϵ , we used the relaxation model or the “constant/conductivity” model in which $\text{Re } \epsilon$ is assumed to be constant and $\text{Im } \epsilon$ is assumed equal to $-\sigma_e/\omega$, where σ_e is the (frequency-independent) electrical conductivity. As we will see, the relaxation model does not fit our measured μ and ϵ values very well over the entire frequency range, but it approximates μ quite well over several decades; the main advantage of the model is that the numerical solution of the Maxwell Equations in the time domain is particularly simple.

Analytic Calculation

In simple situations, the coupling impedance can be calculated analytically. The best-known analytic calculation is probably the resistive wall impedance, a thorough overview of which has been presented recently [39]. The longitudinal impedance of some more complicated cases involving multiple layers of various materials have also been derived [48, 49]. We used the same general approach to derive formulae for the longitudinal and transverse impedance per unit length of an infinitely long, perfectly conducting beam pipe with a layer of material with complex permeability μ and complex permittivity ϵ . The coupling impedance of a beam pipe section of finite length is obtained by multiplying by its length. The result is only approximate, since the effects associated with the finite length of the material lining are not taken into account.

The approach is to solve the Maxwell equations twice, first in the vacuum region and then in the material region. One assumes a known charge density and current density distribution in the vacuum region, which yields a solution for the electromagnetic field containing terms with various powers of r . In the material region, the general solution involves linear combinations of Bessel functions. The appropriate boundary conditions at $r = r_o$ and the appropriate continuity conditions at $r = r_x$ (see Figure 3.1 below) must be satisfied. This yields formulae for the electromagnetic field as a function of the assumed charge and current density, from which the coupling impedance can be derived. The longitudinal impedance for $m = 0$ is

$$Z_0^{\parallel}(\omega) = \frac{-i}{2\pi} \sqrt{\frac{\mu_0}{\epsilon_0}} \frac{L}{r_x} \left[\frac{kr_x}{2} + \frac{k}{k_r} \frac{\epsilon}{\epsilon_0} b_0(\bar{k}_r r_o, \bar{k}_r r_x) \right]^{-1} \quad (3.10)$$

and the transverse impedance for $m > 0$ is

$$Z_m^\perp(\omega) = \frac{-i}{\pi} \sqrt{\frac{\mu_0}{\epsilon_0}} \frac{L}{kr_x^{2m+1}} \left\{ \frac{kr_x}{m+1} - \frac{m}{kr_x} + \frac{k}{\bar{k}_r} \left[\frac{\epsilon}{\epsilon_0} b_m(\bar{k}_r r_o, \bar{k}_r r_x) + \frac{\mu}{\mu_0} b'_m(\bar{k}_r r_o, \bar{k}_r r_x) - \frac{2m}{\bar{k}_r r_x} \right] \right\}^{-1}. \quad (3.11)$$

L is the length of the material-lined section, $k \equiv \omega/c$, $\bar{k}_r \equiv \omega\sqrt{\mu\epsilon - \mu_0\epsilon_0}$, and

$$b_m(y, x) \equiv \frac{N_m(y)J'_m(x) - J_m(y)N'_m(x)}{N_m(y)J_m(x) - J_m(y)N_m(x)} \quad (3.12)$$

$$b'_m(y, x) \equiv \frac{N'_m(y)J'_m(x) - J'_m(y)N'_m(x)}{N'_m(y)J_m(x) - J'_m(y)N_m(x)}. \quad (3.13)$$

$J_m(x)$ and $N_m(x)$ are the Bessel functions of the first and second kind of order m , respectively, while $J'_m(x)$ and $N'_m(x)$ are their first derivatives. It is worth noting that for $|x| \gg 1$ and $|y| \gg 1$,

$$b_m(y, x) \approx -\cot(y-x) \quad (3.14)$$

$$b'_m(y, x) \approx \tan(y-x). \quad (3.15)$$

The above approximations were used in circumstances in which the imaginary parts of $\bar{k}_r r_x$ and $\bar{k}_r r_o$ were large enough in magnitude to make it impractical to calculate b_m and b'_m via the exact formulae.

Equations (3.10) and (3.11) reduce to the familiar resistive wall formulae in the appropriate limit. Equation (3.10) also agrees with the formula for a resistive wall with a dielectric layer [45]. It can also be shown that the coupling impedance goes to infinity when the phase velocity for a waveguide mode of propagation (with the same azimuthal dependence in the fields) is equal to c .

It is possible to obtain (3.10) by solving for the modes of propagation in a pipe with a material layer and an inner conductor, using the wire method to predict Z_0^\parallel , and taking the limit in which the radius of the inner conductor goes to zero.

The Akasaka Field Matching Method

Consider the case of a layer of material of finite length imbedded in a perfecting conducting pipe (see Figure 3.1 below). One can write down the general monopole solution to the Maxwell Equations in the vacuum region ($r < r_x$); the same can be done in the material region ($r_x < r < r_o$ and $0 < z < L$). The constraint that the appropriate fields be continuous at the interface ($r = r_x$) yields a matrix equation. After solving this matrix equation for a particular ω , one can deduce $Z_0^\parallel(\omega)$. Strictly speaking, the dimensions of the matrices are infinite; however, an approximate numerical solution can be obtained by including only a finite number of terms. The field matching approach was first applied to the special case of $\mu = \mu_0$ and $\epsilon = \epsilon_0$ (*i.e.* a pillbox cavity with beam tubes, but without a material layer)—the

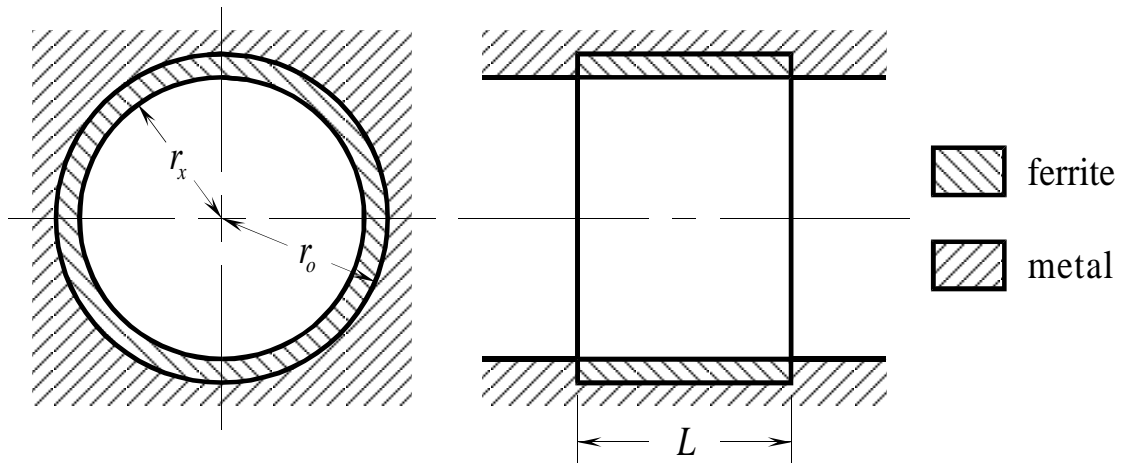


Figure 3.1. Assumed load geometry.

technique is described in a recent review article [42]. The approach was generalised to the case of arbitrary but real μ and ϵ by K. Yokoya, and to the case of complex μ and ϵ by N. Akasaka [50].

As we will see, the Akasaka method complements the purely analytic approximation and the purely numerical approach taken by AMOS. The Akasaka method has the advantage of accounting for the finite length of the material layer, while still providing a more direct solution than the time domain simulation done by AMOS (in particular, it does not require an approximate fit to the frequency dependence of μ and ϵ , and it generally can be expected to give better accuracy with much less computation time). On the other hand, the purely numerical approach used by AMOS can be used to solve more complicated geometries, while the analytic approach offers a simpler (*i.e.* closed-form) solution. Only the monopole field matching solution has been worked out for complex μ and ϵ , although the dipole solution for the case of $\mu = \mu_0$ and $\epsilon = \epsilon_0$ is known [51].

3.3 Coupling Impedance Predictions

The methods described above were used to predict the coupling impedance for the full-size Porcupine load (see Figures 1.4 and 1.5) and the L3 load (see Figures 5.1 and 5.2). Additional predictions and wire measurements were done on a small Ferrite-50 model and a large TT2-111V load mock-up to check the predictive methods. A generic load geometry is depicted in Figure 3.1; the dimensions used in the calculations are given in Table 3.1. In reality, only the small Ferrite-50 model is actually axisymmetric; the rest of the loads were made by attaching ferrite tiles to the inside of a shell.

We will predict the coupling impedance of the Porcupine load alone, although, strictly speaking, it would be preferable to predict the coupling impedance of the entire RF system assembly, including the cavity cell, tapers, and flutes, along with the

Table 3.1. Assumed load dimensions.

Type	L [mm]	r_x [mm]	r_o [mm]
Porcupine	101.6	114.1	117.3
L3	600.0	42.9	46.0
Small model	31.0	22.8	25.9
Full-size mock-up	152.4	119.3	122.6

two Porcupine loads (see Figure 1.3). However, calculating the impedance of such a complicated structure would be rather difficult. Instead, we will invoke the “composition rule” [52], which states that the total impedance of a structure is approximately equal to the sum of the impedances of each of its elements. We will return to this point in Section 5.8.

TT2-111-Series Porcupine Load

We predicted the coupling impedance of a Porcupine load made of TT2-111V material using AMOS, the analytic formulae, and (in the monopole case) the Akasaka field matching method. A three-term relaxation model and a constant/conductivity model were used to input the μ and ϵ , respectively, of TT2-111V into AMOS. The measured values are compared to the fits in Figures 3.2 and 3.3. The fitted parameters are given in Appendix A.

The monopole and dipole impedance predicted for one Porcupine load are compared in Figures 3.4 and 3.5. All three calculated Z_0^{\parallel} values agree reasonably well for frequencies below about 1 GHz; the AMOS and Akasaka predictions agree quite well up to about 12 GHz. The large dip in the AMOS and Akasaka predictions at 1 GHz occurs at the cutoff frequency for the first monopole waveguide mode in the metal beam pipe. Above 1 GHz, the finite length of the ferrite lining has the effect of significantly increasing the impedance. A likely explanation for this difference is that the localised fields produce about the same amount of coupling in both cases, but that the net effect ends up being close to zero at most frequencies in the infinitely long structure because of cancellation. It can be shown that $Z_0^{\parallel} \rightarrow \infty$ according to the analytic formula if the phase velocity for propagation of a monopole waveguide mode in the ferrite-lined pipe is equal to c . This presumably accounts for the spike in the analytically-predicted impedance at 17.4 GHz¹. In contrast, when the finite length is accounted for, the impedance is nearly constant over a large frequency range.

The behaviour predicted above 12 GHz is probably not accurate in any of the three

¹The result that $Z_0^{\parallel} \rightarrow \infty$ might seem unphysical, but it is no more unphysical than the claim that $Q \rightarrow \infty$ for a cavity with perfectly conducting walls; both can occur only at discrete set of frequencies, and neither limit is ever reached if losses are present.

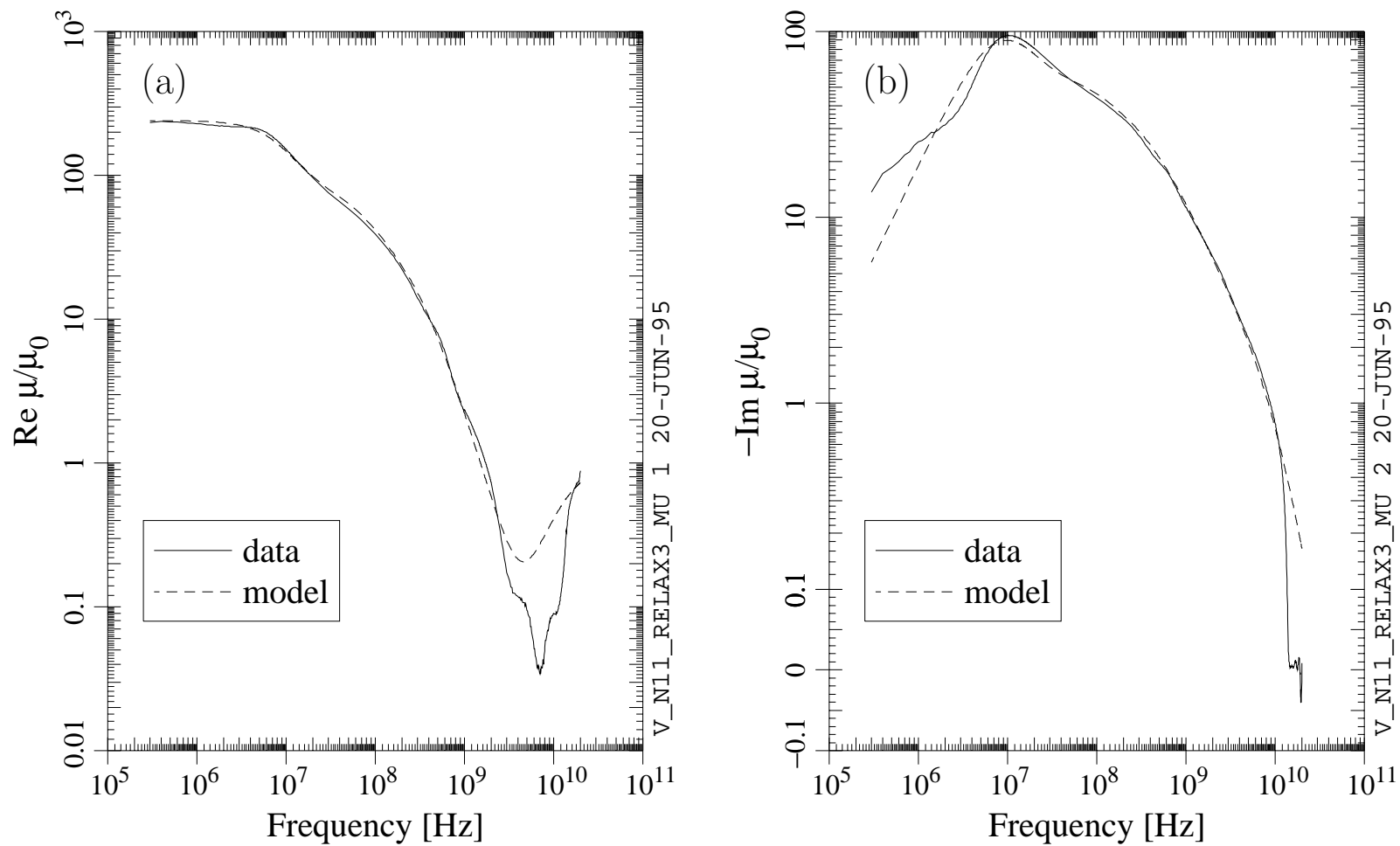


Figure 3.2. Measured and fitted values of (a) the real part and (b) the imaginary part (times -1) of μ for TT2-111V used in the coupling impedance predictions.

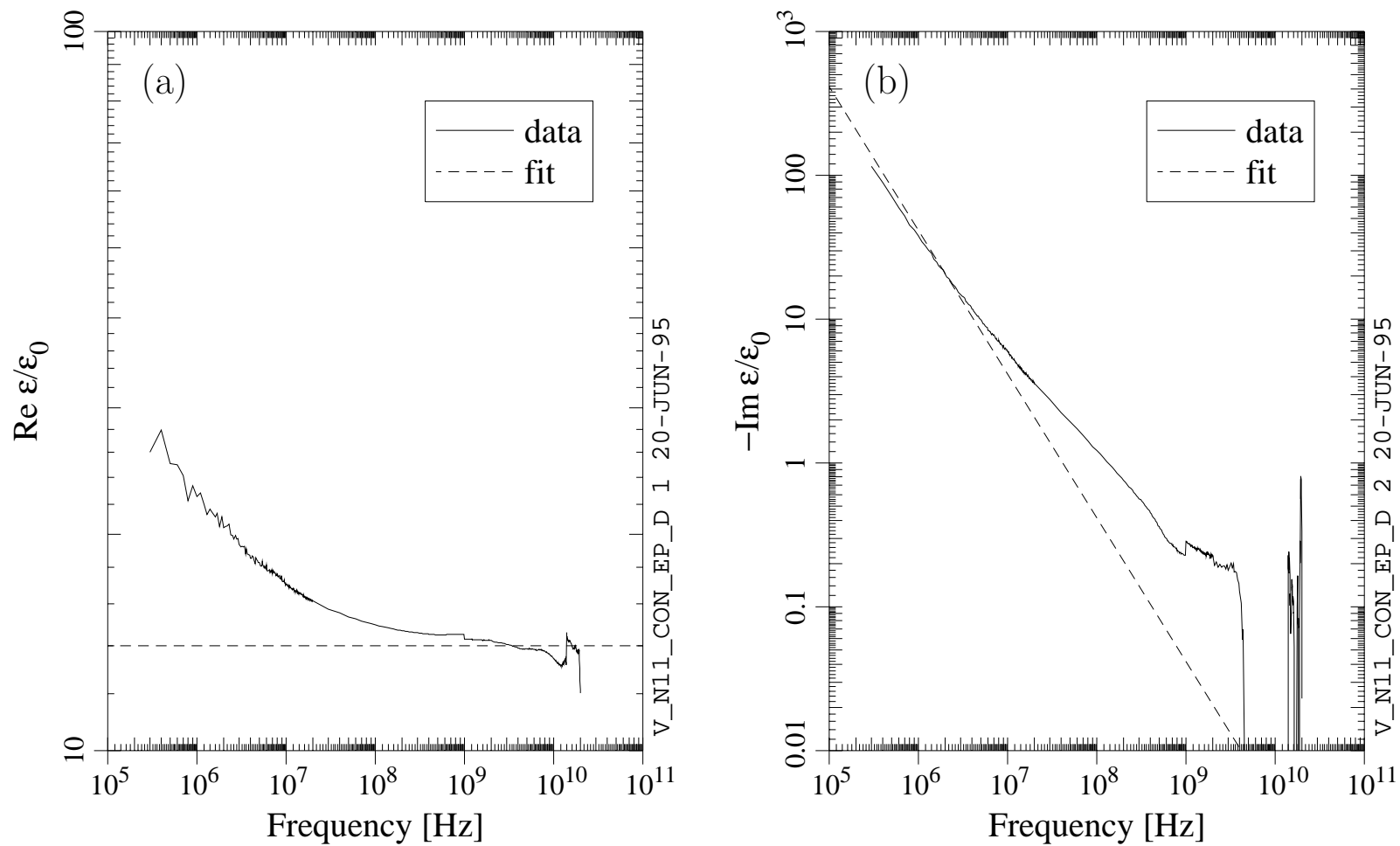


Figure 3.3. Measured and fitted values of (a) the real part and (b) the imaginary part (times -1) of ϵ for TT2-111V used in the coupling impedance predictions.

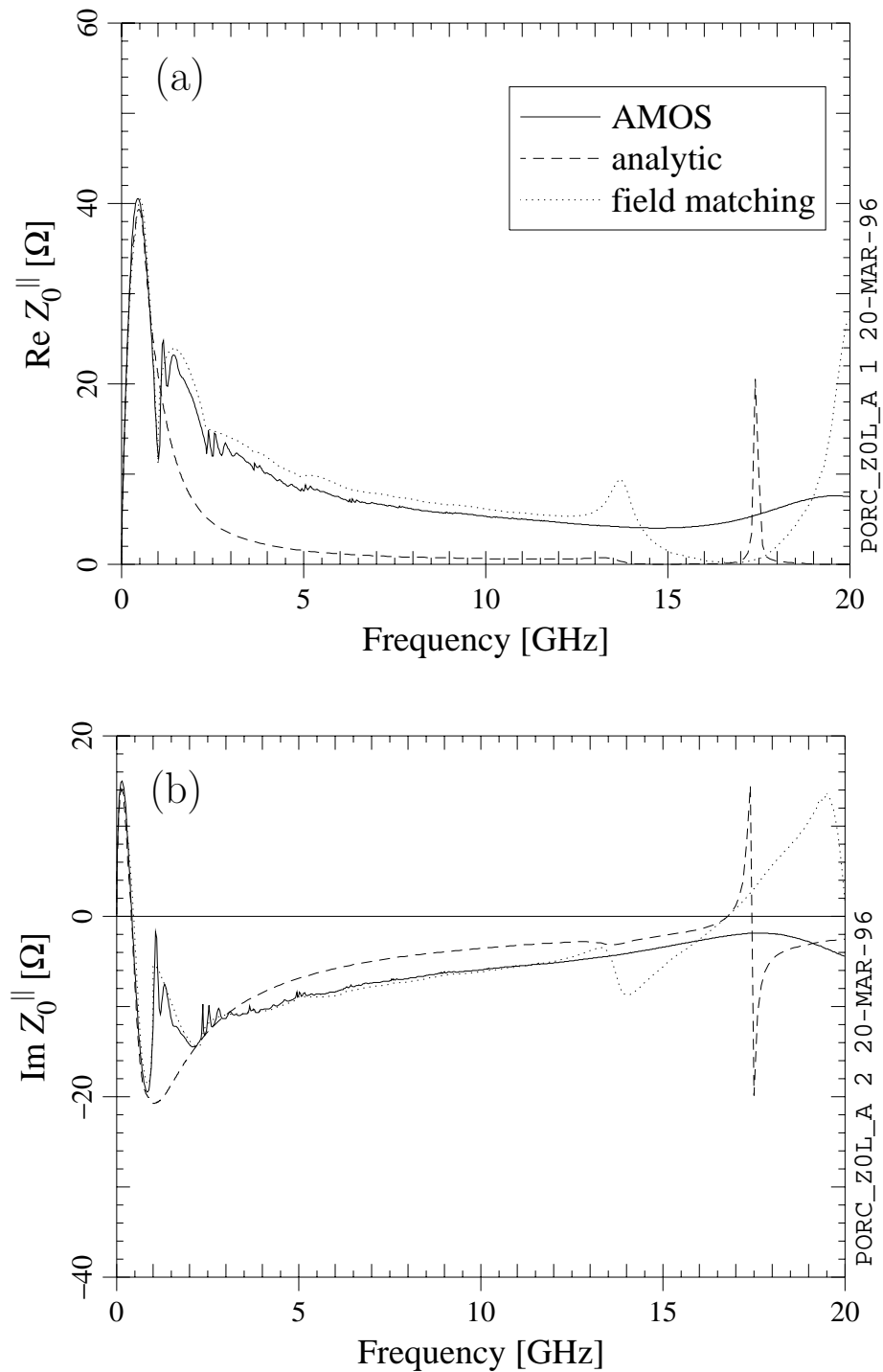


Figure 3.4. Predicted (a) real part and (b) imaginary part of the monopole coupling impedance of the Porcupine load. The complex conjugates of the AMOS values are shown, since the opposite sign convention is used in AMOS.

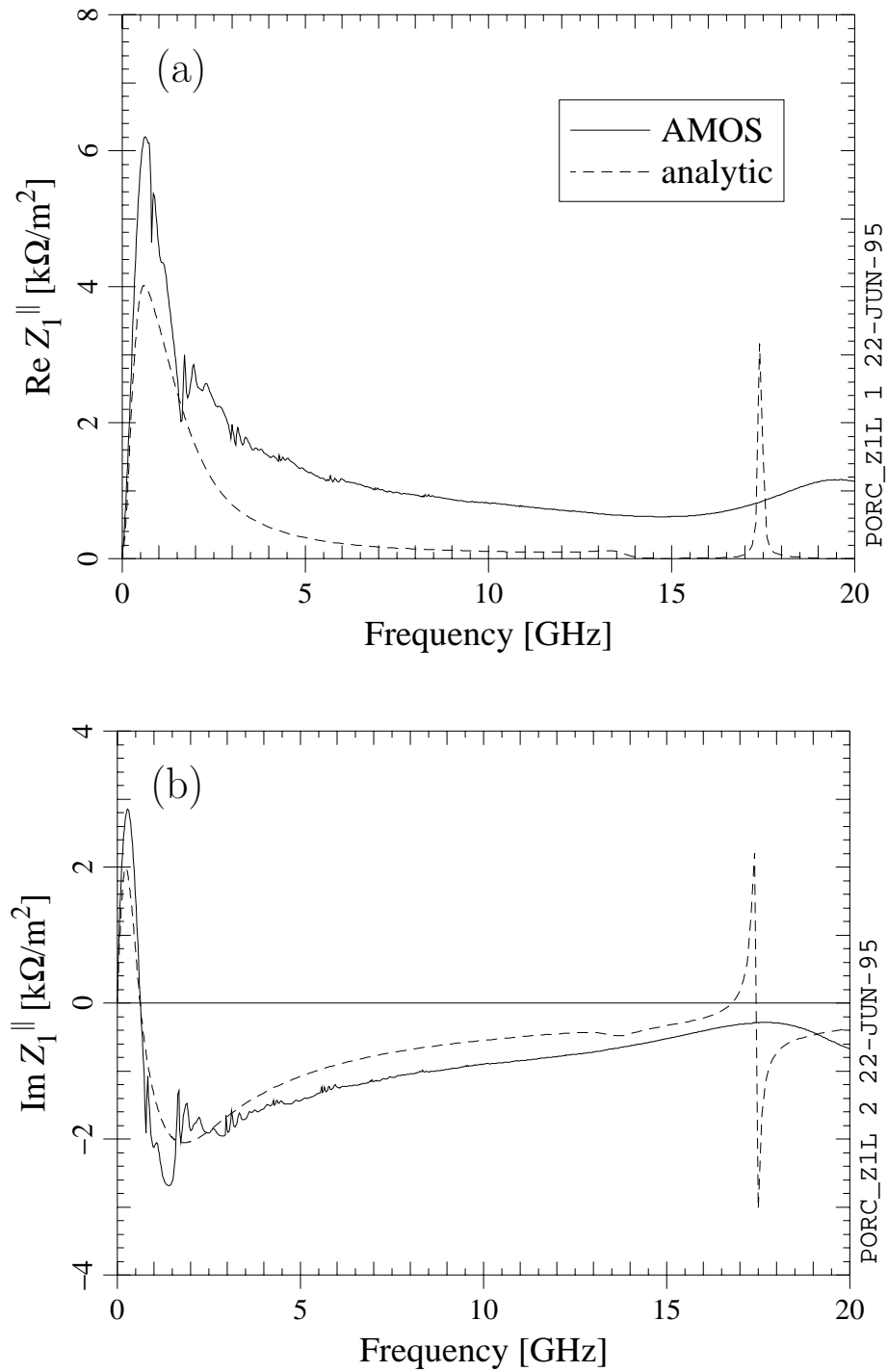


Figure 3.5. Predicted (a) real part and (b) imaginary part of the dipole coupling impedance of the Porcupine load. The complex conjugates of the AMOS values are shown.

cases, because the imaginary parts of μ and ϵ are close to zero, and the relative error in the measurement is quite large. As a result, the AMOS prediction may be the closest to reality for frequencies above 12 GHz, because it is based on fitted values of μ and ϵ whose behaviour is at least plausible at high frequencies. The agreement between the Akasaka and AMOS predictions remains quite good over the entire frequency range if we use the fitted μ and ϵ values for as input to the field matching calculation.

The calculated Z_1^{\parallel} values follow the same pattern as Z_0^{\parallel} , at least qualitatively. The analytic and AMOS predictions are within a factor of 2 below 1 GHz, but, as with Z_0^{\parallel} , they disagree by a factor of 10 or more at high frequencies. There is a less pronounced dip at the cutoff frequency for the first dipole waveguide mode (0.77 GHz).

Monopole and dipole loss factors for a Gaussian bunch of standard deviation σ_z were obtained from Z_0^{\parallel} and Z_1^{\parallel} via Equation (3.8). The results are shown in Figure 3.6. All calculated k_0^{\parallel} values agree quite well for long bunches, but the analytic results increase less rapidly as the bunch length decreases, because of the smaller impedance predicted at high frequencies. The k_1^{\parallel} values follow a similar pattern, although the agreement between the two predictions is not as good for long bunches.

TT2-111-Series L3 Load

We applied the same methods and μ and ϵ values (Figures 3.2 and 3.3) as used for the Porcupine load to predict the coupling impedance of the L3 load. The results are shown in Figures 3.7 and 3.8; the corresponding loss factors are shown in Figure 3.9. The AMOS and analytic predictions agree quite well. The better agreement between the two predictions relative to the Porcupine case is presumably due to the fact that the structure is significantly longer, making the effects associated with the finite length less important. Because of the increase in length and the decrease in radius, a large number of terms must be included in order to get the same accuracy in the Akasaka calculation—more than ten times the number of terms used in the Porcupine case. For expedience, we included fewer terms than would be needed to ensure reasonable accuracy, which probably accounts for the fact that the Akasaka impedance falls rapidly near 10 GHz and remains close to zero thereafter. Even so, all three predictions for the monopole loss factor agree quite well.

The predicted monopole coupling impedance of the L3 load is about 16 times that of the Porcupine load; the predicted dipole impedance of the L3 load is about 80 times that of the Porcupine. In other words, the predictions indicate that the L3 load has about twice the monopole impedance and 10 times the dipole impedance of the eight Porcupine loads that are to be installed in the first step of the CESR RF system upgrade.

In the predictions described above, we have not taken into account the fact that the actual load for the L3 test was split into three units. We will return to this point in Section 5.6.

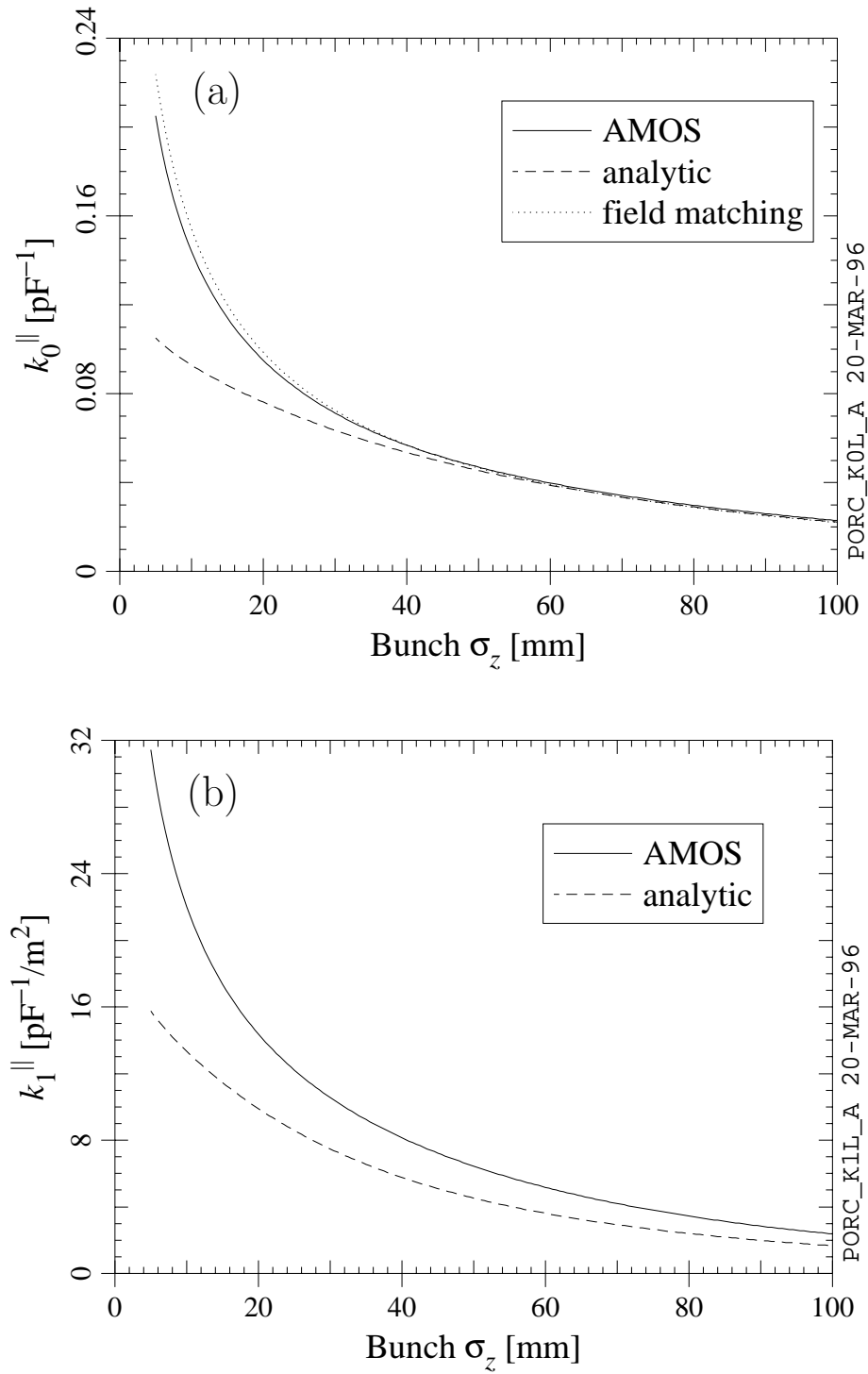


Figure 3.6. Predicted (a) monopole and (b) dipole loss factor for the Porcupine load.

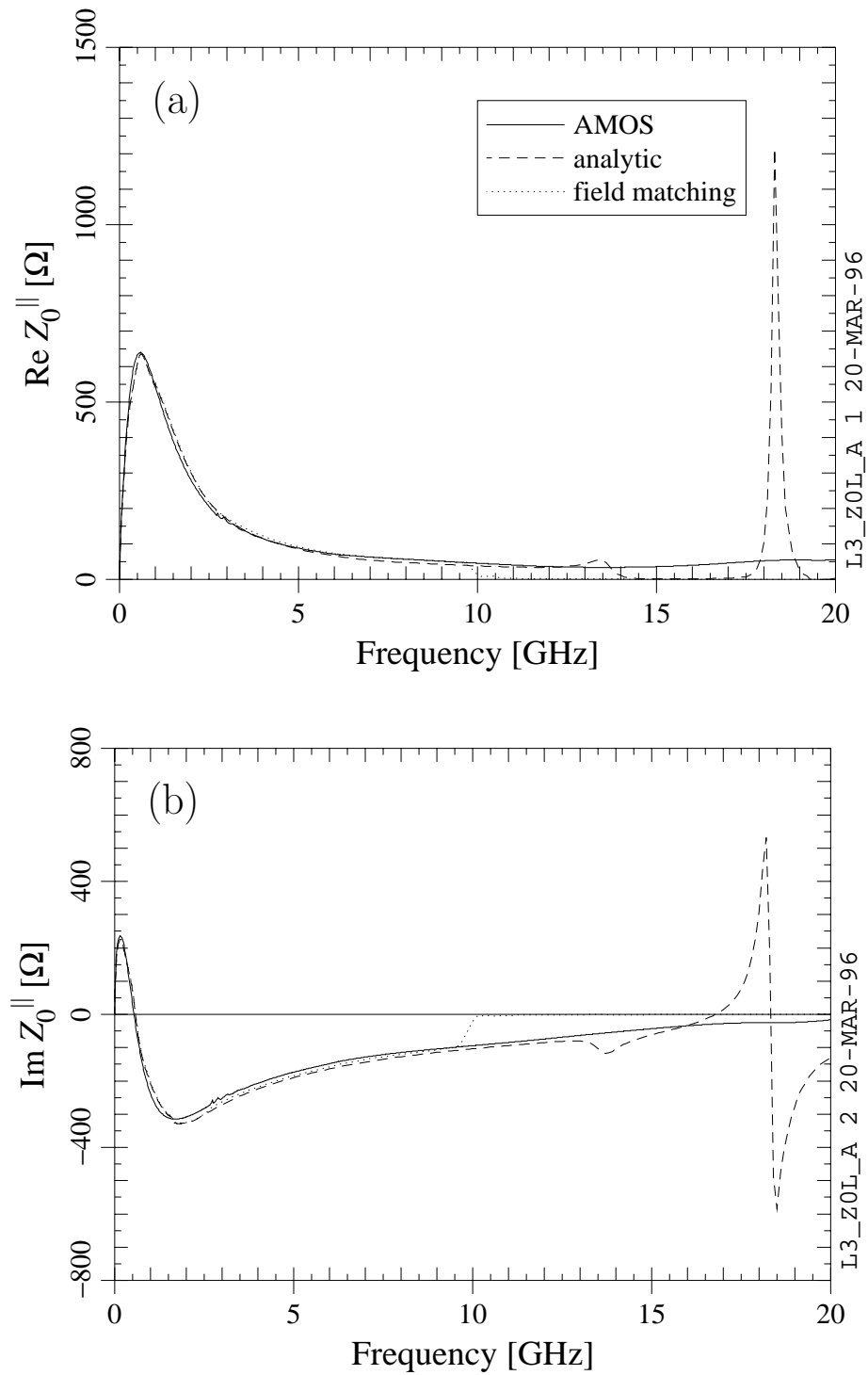


Figure 3.7. Predicted (a) real part and (b) imaginary part of the monopole coupling impedance of the L3 load. The complex conjugates of the AMOS values are shown.

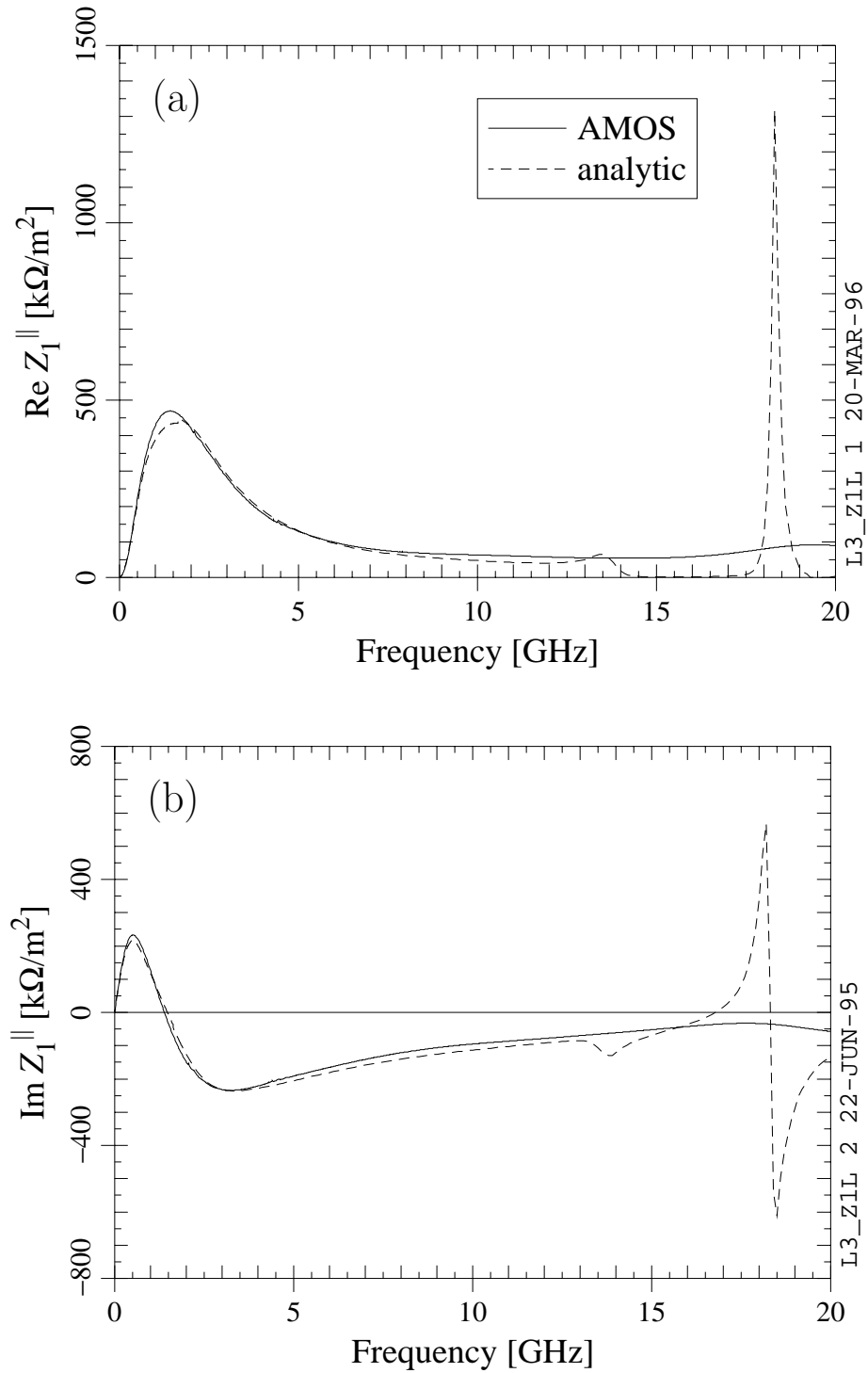


Figure 3.8. Predicted (a) real part and (b) imaginary part of the dipole coupling impedance of the L3 load. The complex conjugates of the AMOS values are shown.

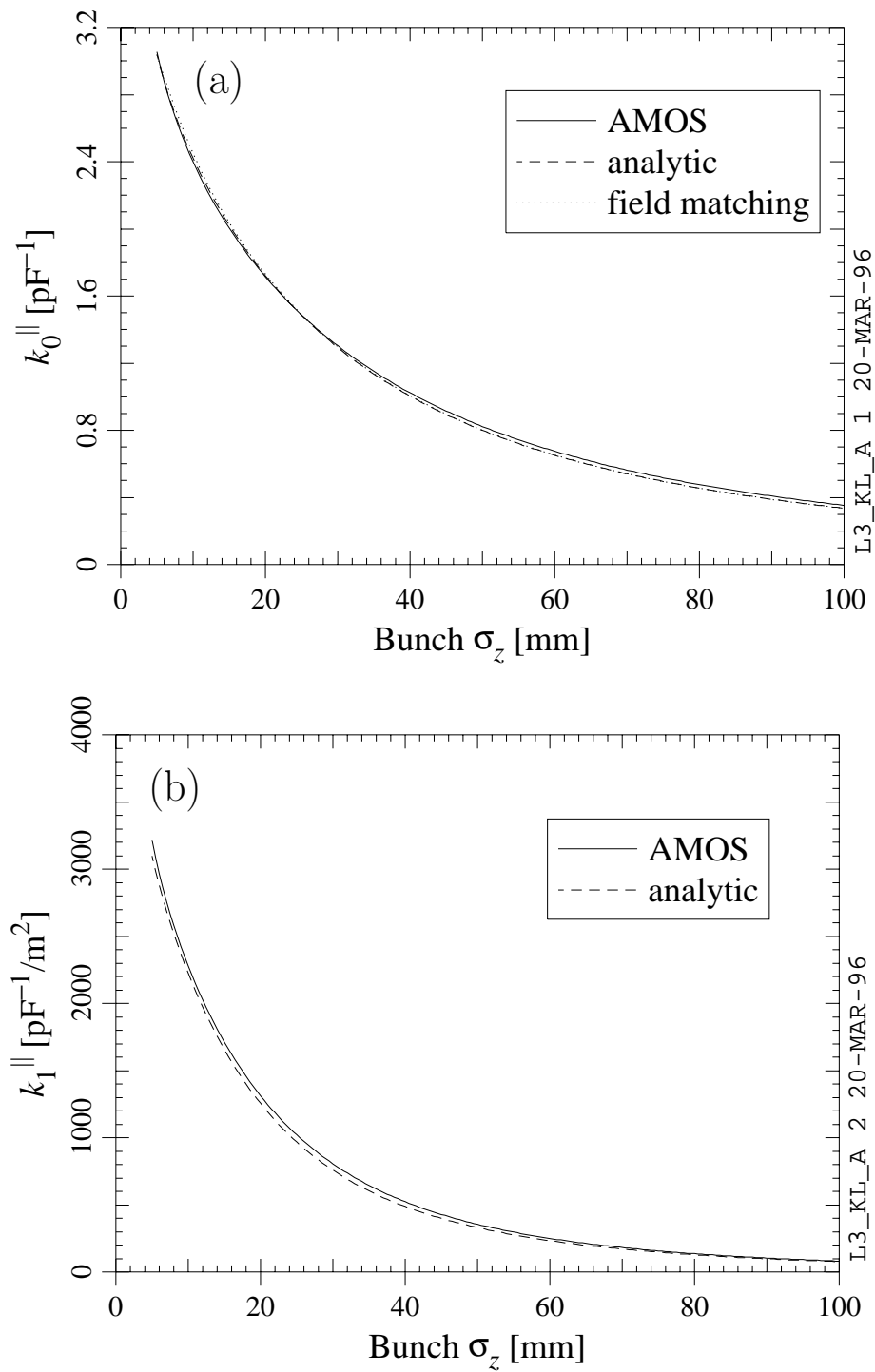


Figure 3.9. Predicted (a) monopole and (b) dipole loss factor for the L3 load.

Small Ferrite-50 Model

Wire measurements were done by L. Walling on a small load model made of Ferrite-50 as a check of the correctness of our predictive methods. Two-term relaxation models were used to input the μ and ϵ of Ferrite-50 into AMOS. The measured μ and ϵ and the fitted values are compared in Appendix A; the fitted parameters are also given in Appendix A. The calculated coupling impedances for the small model are compared to the wire result in Figures 3.10 and 3.11. A Z_0^{\parallel} value calculated via numerical simulation of the wire method using the HFSS program¹ is also shown.

The Z_0^{\parallel} values measured with the wire method are somewhat larger in magnitude than the calculated values. This disagreement may be due in part to batch-to-batch variation in the ferrite properties. The agreement improves significantly if we postulate that $-\text{Im } \epsilon$ is smaller than measured by a factor of 2.5. This is still within the tolerances specified for the conductivity of the material, although we have not measured the batch-to-batch variation in the microwave properties of Ferrite-50. The calculated values of Z_0^{\parallel} agree reasonably well up to about 15 GHz. The cutoff frequency for the first monopole waveguide mode of propagation in the metal beam pipe is 5 GHz; dips in Z_0^{\parallel} are predicted by AMOS and the Akasaka method near this frequency. These dips become less pronounced as L increases.

The measured Z_1^{\perp} values are also somewhat larger in magnitude than the calculated values, except at very low frequencies. Again, the agreement improves if we divide $\text{Im } \epsilon$ by 2.5. The agreement between the calculated Z_1^{\perp} values is not quite as good as for Z_0^{\parallel} .

TT2-111-Series Full-Size Mock-up

Wire measurements were also done in the time domain on a full-size load mock-up. The mock-up's dimensions were about the same as the Porcupine load, except that the mock-up was 1.5 times longer. In the wire measurement, the monopole loss factor for an approximately Gaussian pulse with $\sigma_z \approx 23$ mm was measured. This result is compared to predictions in Figure 3.12. As in the Porcupine case, the analytic k_0^{\parallel} values are smaller than the AMOS and Akasaka predictions for short bunch lengths. The measured value is about 25% smaller than the predictions which account for the finite length of the ferrite layer; the discrepancy may be due to the gaps between the tiles, which are not accounted for in the predictions (see also Section 5.6).

Edge Effects

So far, we have assumed that the ferrite layer is imbedded in the metal pipe, as shown in Figure 3.1. While this is a good assumption in the case of the small Ferrite-50 load, it is not strictly true for the Porcupine load (Figure 1.4) or the L3 load (Figure 5.1), since the ferrite layer protrudes inward toward the beam, as shown schematically in Figure 3.13a. The analytic approximation does not take the finite length into account

¹HFSS is a product of the Hewlett-Packard Corporation.

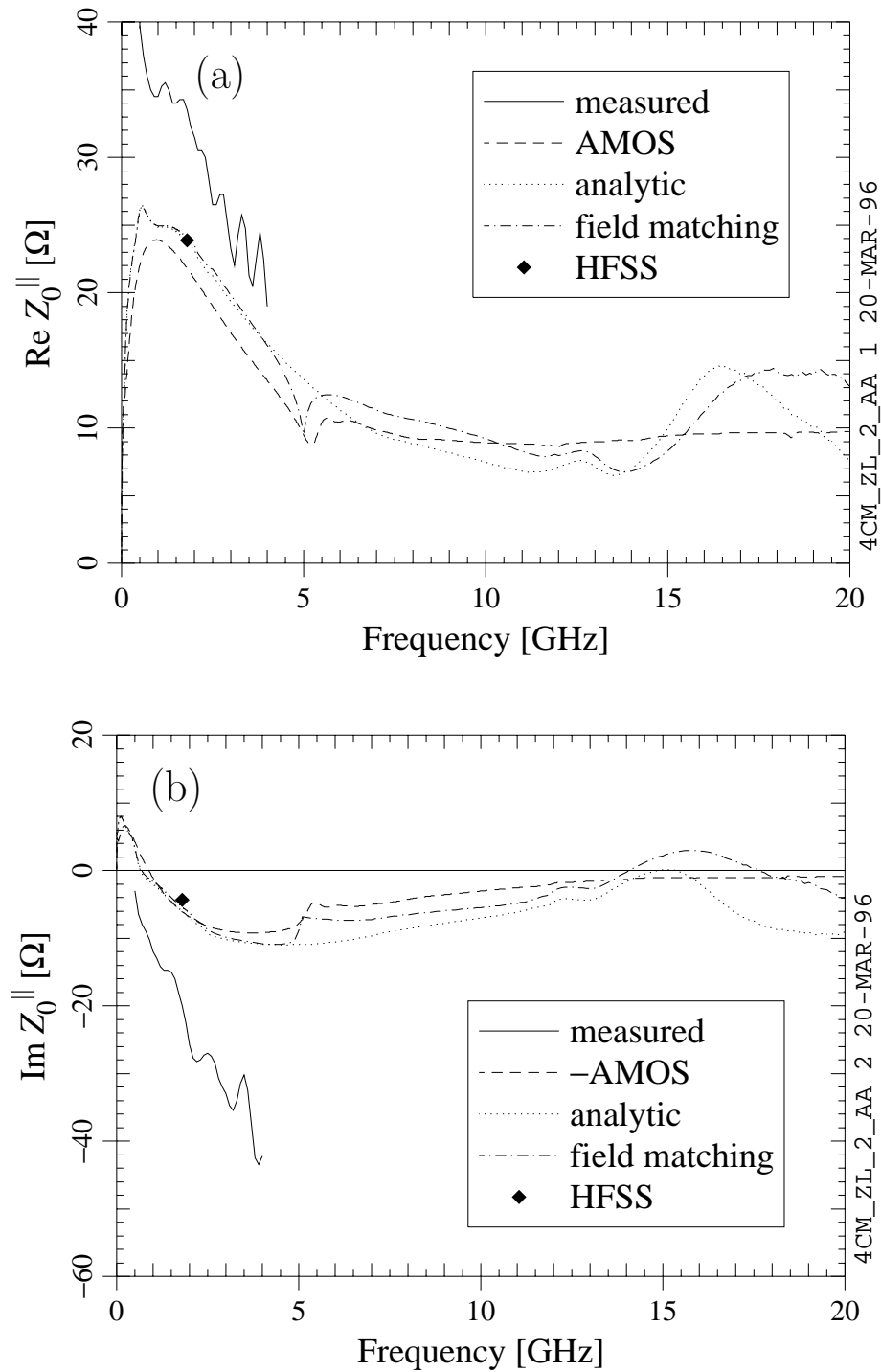


Figure 3.10. Predicted (a) real part and (b) imaginary part of the monopole coupling impedance of the small Ferrite-50 model. The complex conjugates of the AMOS values are shown. The uncertainty in the values measured with the wire method is about $(\pm 1 \pm i6) \Omega$.

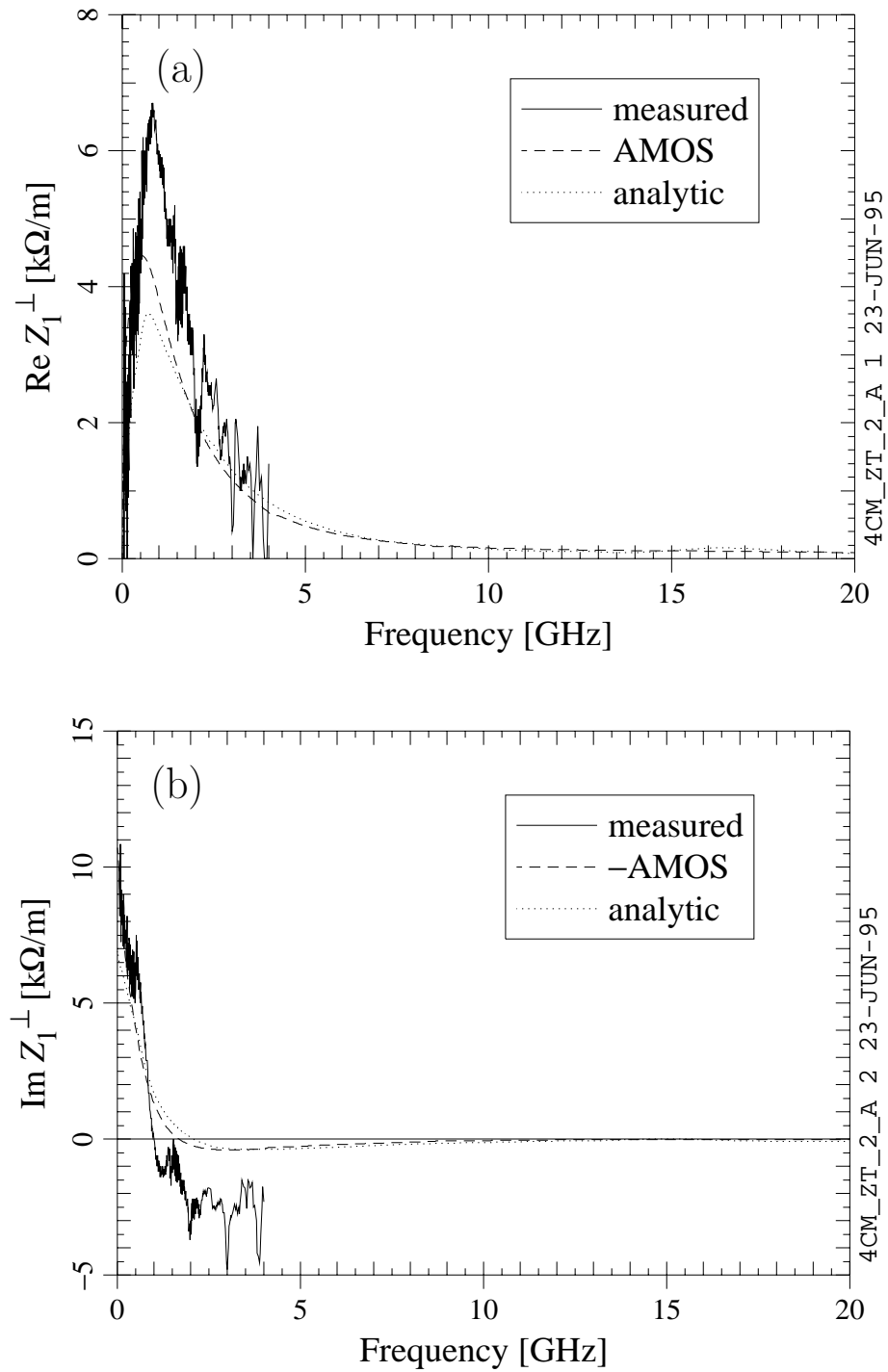


Figure 3.11. Predicted (a) real part and (b) imaginary part of the dipole coupling impedance of the small Ferrite-50 model. The complex conjugates of the AMOS values are shown.

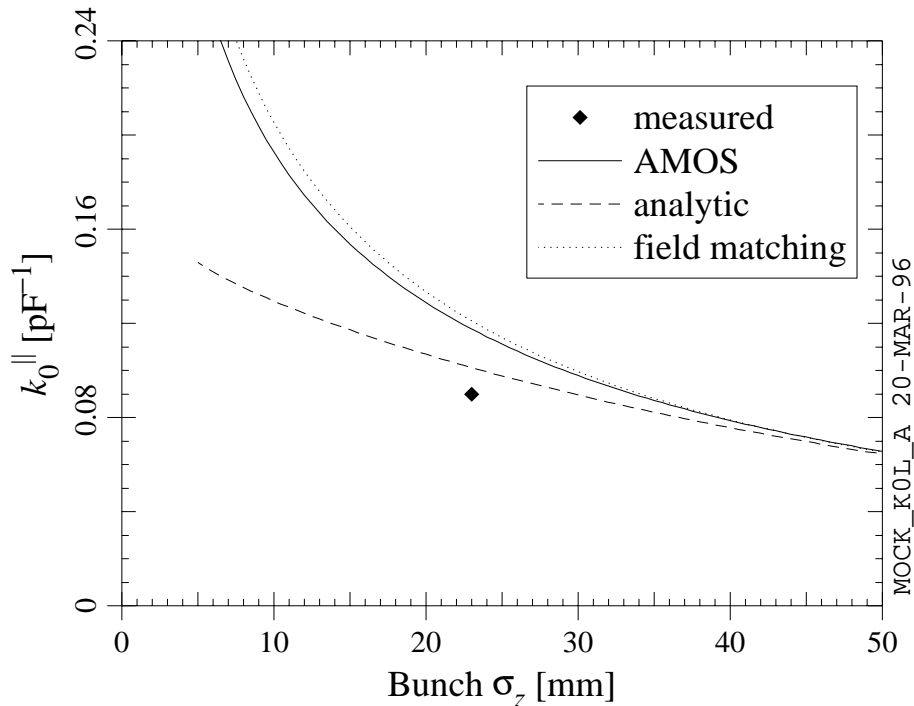


Figure 3.12. Predicted monopole loss factor for a full-size TT2-111-series load mock-up. The measured value is for TT2-111C ferrite, while the calculated values are based on the measured properties of TT2-111V. The reproducibility in the measured value is about $\pm 0.003 \text{ pF}^{-1}$, but the systematic error is probably larger.

at all, so it gives the same answer for Figures 3.1 and 3.13a; the field matching solution is applicable only to the geometry of Figure 3.1. The inwardly-protruding layer can be modelled with AMOS, however, but only after adding tapers to ensure that the end pipes' diameter is less than or equal to the inner diameter of the ferrite, as shown in Figure 3.13b.²

The impedance of a Porcupine load with the geometry of Figure 3.13b was calculated with AMOS. The values of r_o , r_x , and L were the same as before (Table 3.1); a taper angle of 1.2° was used. At low frequencies, the predicted impedance was the same as for the geometry of Figure 3.1. Above the cutoff frequency, the more realistic edge condition produced an increase in $\text{Re } Z_0^{\parallel}$ and a decrease in $|\text{Im } Z_0^{\parallel}|$. For $\sigma_z = 10 \text{ mm}$, the predicted monopole loss factor increased by 6.8% with the more realistic geometry. The additional impedance due to the tapers is a small fraction of the latter (we estimate the tapers' loss factor to be 0.4% of the total). An increase of 6.4 to 6.8% is small enough that we may consider the less realistic treatment of edge effects for the Porcupine case to be adequate for our purposes. The same can be said for the L3 load, a point which we will return to in Section 5.6.

²These are methods for modelling the geometry of Figure 3.13a more directly, but none of them are available with AMOS yet.

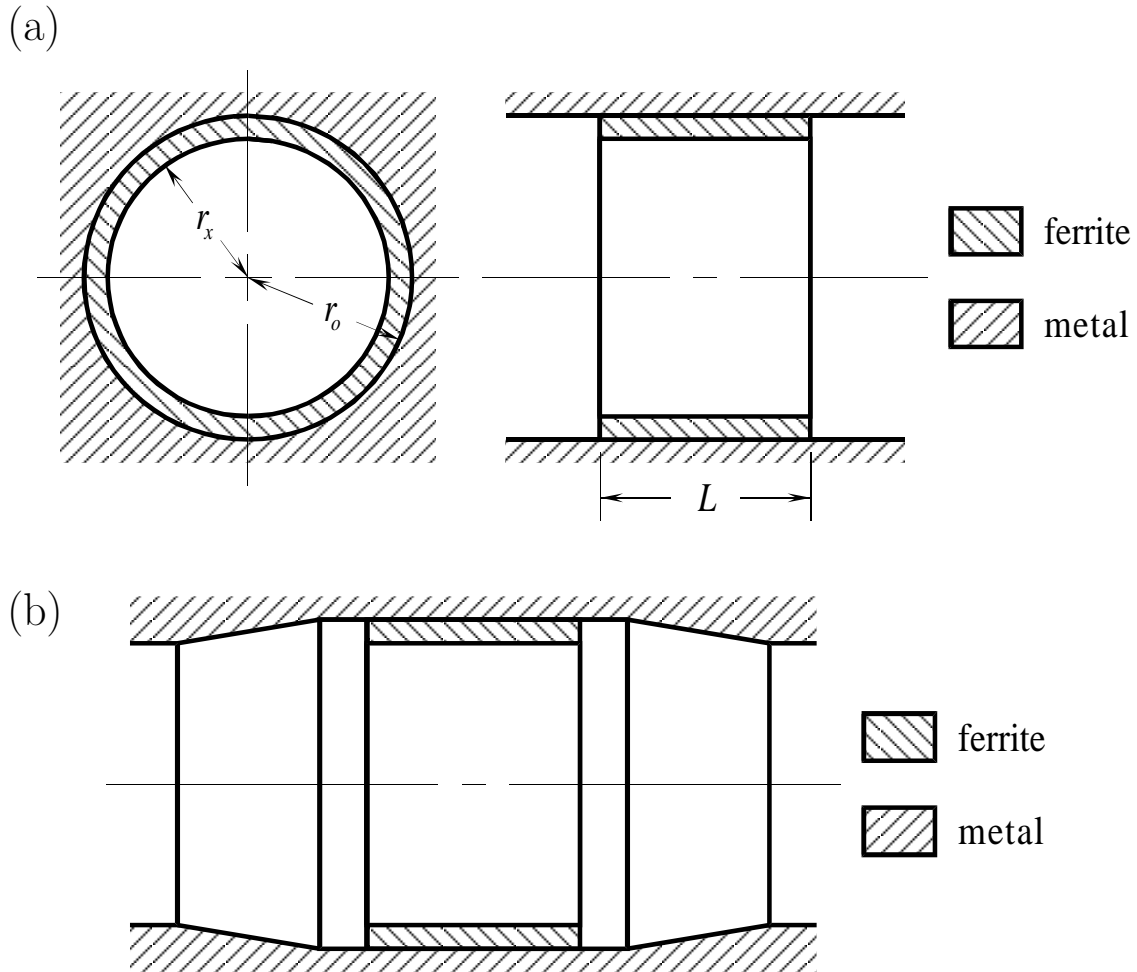


Figure 3.13. An HOM load with the ferrite layer protruding inward, (a) with a straight beam pipe and (b) with a tapered beam pipe. In (b), the inner diameter of the ferrite is the same as that of the end pipes.

3.4 A Highly Simplified Impedance Model

⚡ A striking feature of the predicted coupling impedance for the Porcupine load is the peak in the real part near 0.5 GHz, which can be seen in both the monopole case (Figure 3.4) and the dipole case (Figure 3.5). As $\text{Re } Z_m^{\parallel}$ goes through its maximum, $\text{Im } Z_m^{\parallel}$ goes through zero. For Z_0^{\parallel} , all three calculations predict the same behaviour near 0.5 GHz, but there is some discrepancy between the AMOS and analytic predictions for Z_1^{\parallel} . Even with our analytic formulae for the coupling impedance, it is not obvious that there should be resonant behaviour near 0.5 GHz. As we will now see, this feature can be understood via a simplified coupling impedance model, which we will derive in this section. We will apply the model to the case of a TT2-111V Porcupine load in this section, and to other cases in the next two sections. Our simple model will be no substitute for more rigorous calculations, so we will not use it in subsequent chapters. On the other hand, rigorous calculations are no substitute

Table 3.2. Parameters determining the validity of the simplified impedance model for four different ferrites. Values of μ and ϵ are taken at 0.5 GHz; values of r_x and r_o for the Porcupine load were used.

Material	$\frac{\mu\epsilon}{\mu_0\epsilon_0}$	$ \bar{k}_r r_x $	$ \bar{k}_r(r_o - r_x) $
TT2-111V	309.4	21.0	0.58
CMD10	378.0	23.2	0.65
IB-004	289.8	20.3	0.57
Ferrite-50	4470.7	80.0	2.22

for a simple model.

We will use the analytic formulae, *i.e.* Equations (3.10) and (3.11), as our starting point. Let us consider a limited frequency range (in the Porcupine case, frequencies near 0.5 GHz). Let us assume that $|\bar{k}_r r_x| \gg 1$ and $|\bar{k}_r r_o| \gg 1$, so that the trigonometric approximations given in Equations (3.14) and (3.15) apply. Let us further assume that $|\mu\epsilon| \gg \mu_0\epsilon_0$ and $|\bar{k}_r(r_o - r_x)| \ll 1$. The latter implies that the electromagnetic field does not vary significantly as a function of depth in the material layer. As can be seen in Table 3.2, for the Porcupine geometry, these conditions are satisfied for TT2-111V, as well as CMD10 and IB-004, although the $|\bar{k}_r(r_o - r_x)|$ values are not all that small compared to 1. Ferrite-50, on the other hand, has $|\bar{k}_r(r_o - r_x)| > 1$, so our simplified model will not apply to a Ferrite-50 Porcupine load.

The above assumptions yield an approximate expression for $Z_m^{\parallel}(\omega)$ which, interestingly enough, is independent of $\epsilon(\omega)$. To proceed further, we need an explicit expression for the frequency dependence of μ , or more conveniently, that of $1/\mu$. In the case of TT2-111V, as shown in Figure 3.14, $\text{Re}(1/\mu)$ is approximately constant and $\text{Im}(1/\mu)$ is approximately proportional to ω in the vicinity of 0.5 GHz. As can be seen in Figure 3.14, the same is true for the other ferrites. Hence, let us approximate $\mu(\omega)$ via

$$\frac{1}{\mu(\omega)} \approx \frac{1}{\mu_0} \left(\kappa + i \frac{\omega}{\psi} \right), \quad (3.16)$$

where κ and ψ are real constants. In the case of the dipole impedance, let us also assume that $\kappa^2 \ll \omega^2/\psi^2$.

With the above assumptions, the analytic formulae for the monopole and dipole impedance both reduce to the familiar form of a resonator impedance:

$$Z_m^{\parallel}(\omega) \approx \frac{R_s}{1 + iQ \left(\frac{\omega}{\omega_R} - \frac{\omega_R}{\omega} \right)}. \quad (3.17)$$

In the above formula, R_s , ω_R , and Q are the shunt impedance (non-linear definition), resonant angular frequency, and quality factor, respectively, of the resonator. In the

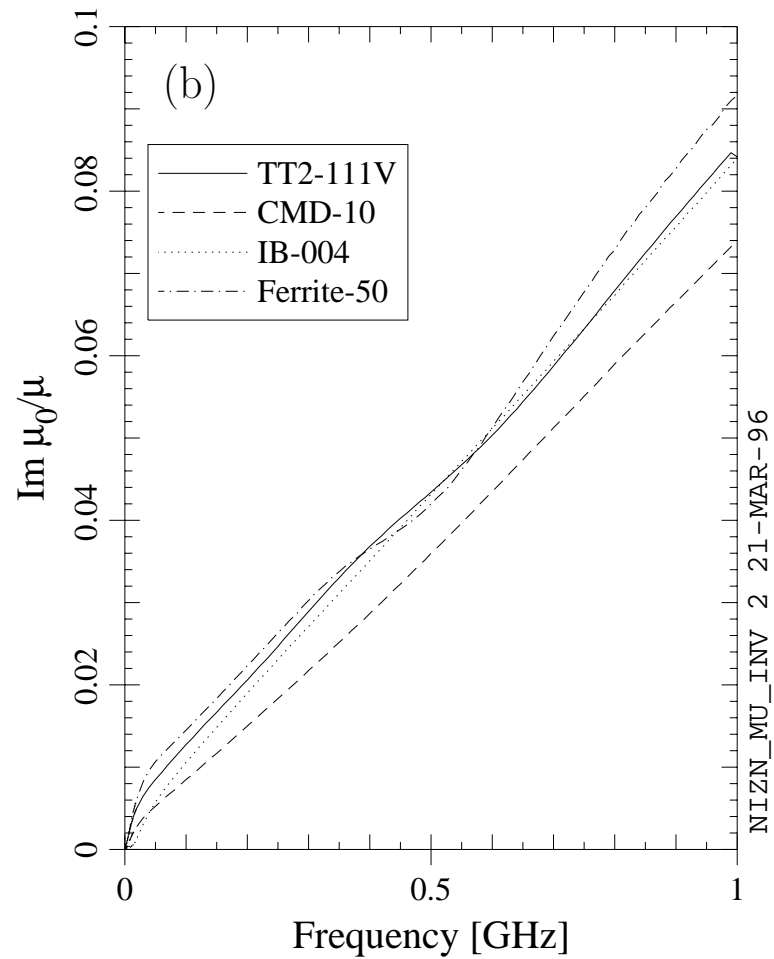
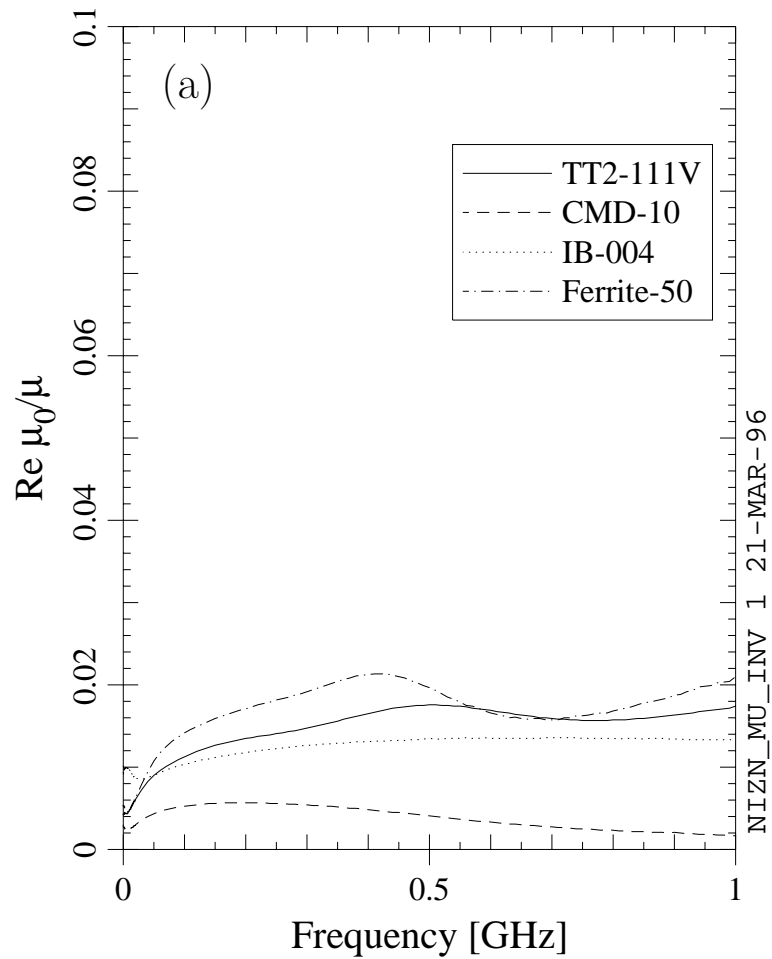


Figure 3.14. Measured values of (a) the real part and (b) the imaginary part of $1/\mu$ for four different ferrites.

monopole case,

$$R_s = \frac{1}{2\pi} \sqrt{\frac{\mu_0}{\epsilon_0}} \frac{L}{r_x} (r_o - r_x) \frac{\psi}{c} \quad (3.18)$$

$$\omega_R = c \sqrt{\frac{2\kappa}{r_x(r_o - r_x)}} \quad (3.19)$$

$$Q = \frac{\psi}{c} \sqrt{\frac{\kappa r_x (r_o - r_x)}{2}} = -\frac{\text{Re } \mu(\omega_R)}{\text{Im } \mu(\omega_R)}. \quad (3.20)$$

In the dipole case,

$$R_s = \frac{1}{\pi} \sqrt{\frac{\mu_0}{\epsilon_0}} \frac{L}{r_x^3} \left[\frac{1}{r_o - r_x} \frac{c}{\psi} + (r_o - r_x) \frac{\psi}{c} \right]^{-1} \quad (3.21)$$

$$\omega_R = c \sqrt{\frac{2}{r_x} \left[\frac{1}{r_x} + \frac{\kappa}{r_o - r_x} - \kappa (r_o - r_x) \frac{\psi^2}{c^2} \right]} \quad (3.22)$$

$$Q = \frac{\omega_R r_x}{c} \frac{1}{2} \left[\frac{1}{r_o - r_x} \frac{c}{\psi} + (r_o - r_x) \frac{\psi}{c} \right]^{-1}. \quad (3.23)$$

Note that, in both cases, R_s depends on $\text{Re}(1/\mu)$ but not on $\text{Im}(1/\mu)$; likewise, in the monopole case, ω_R depends on $\text{Im}(1/\mu)$ but not on $\text{Re}(1/\mu)$, and $1/Q$ is equal to the material's magnetic loss tangent evaluated at ω_R .

For the case of a TT2-111V Porcupine load, we obtain the following monopole impedance parameters: $R_s = 40.4 \Omega$, $\omega_R/(2\pi) = 0.469 \text{ GHz}$, and $Q = 0.425$. The real part of the corresponding resonator impedance is compared to the analytic prediction in Figure 3.15. Our highly simplified resonator model actually agrees quite well with the analytic prediction at ω_R , although it overestimates $\text{Re } Z_0^{\parallel}$ somewhat for $\omega \geq \omega_R$; it underestimates $\text{Re } Z_0^{\parallel}$ somewhat (and overestimates $\text{Im } Z_0^{\parallel}$) below ω_R . The corresponding dipole impedance parameters are $R_s = 3.95 \text{ k}\Omega/\text{m}^2$, $\omega_R/(2\pi) = 0.666 \text{ GHz}$, and $Q = 0.383$. The agreement with the analytic dipole impedance is slightly better than for the monopole case. Of course, our simple model does not reproduce the increase in the impedance above the cutoff frequency due to the finite length of the ferrite layer.

Our resonator model allows us to write down a closed-form expression for the monopole and dipole loss factors. The familiar formula for k_0^{\parallel} in the high- Q limit is not a good approximation for the problem at hand. There is a more general expression, however:

$$k_m^{\parallel}(\sigma_z) = \frac{\omega_R R_s}{4 Q} \frac{b_+ w(ib_+ x) - b_- w(ib_- x)}{\sqrt{\left(\frac{1}{2Q}\right)^2 - 1}}, \quad (3.24)$$

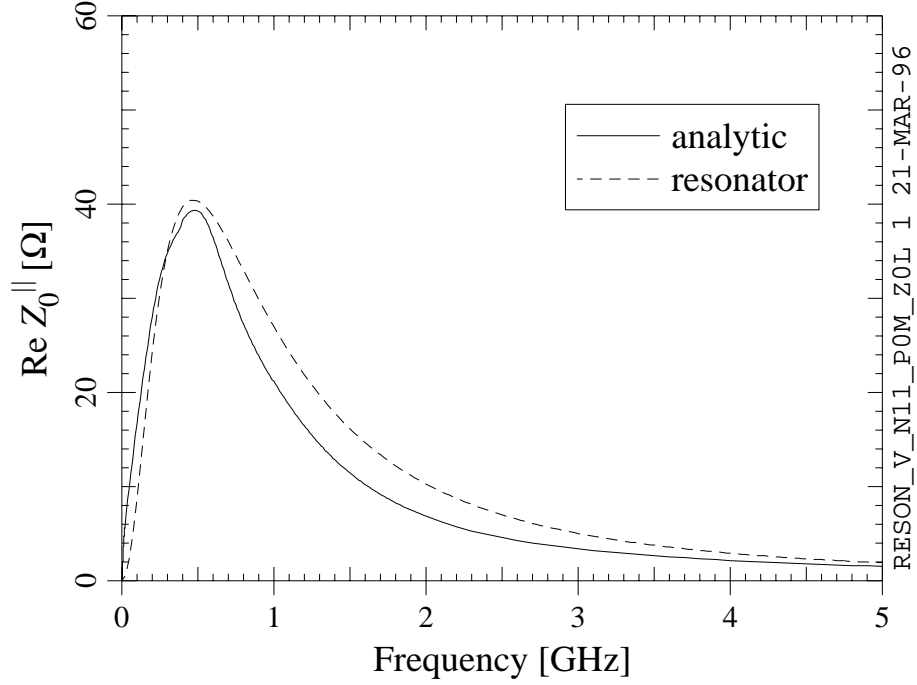


Figure 3.15. Comparison of the real part of the monopole coupling impedance predicted by the analytic formula and by the resonator model for the case of the Porcupine load.

where

$$b_{\pm} \equiv \frac{1}{2Q} \pm \sqrt{\left(\frac{1}{2Q}\right)^2 - 1} \quad (3.25)$$

$$x \equiv \frac{\omega_R \sigma_z}{c} \quad (3.26)$$

$$w(y) \equiv e^{-y^2} \operatorname{erfc}(-iy), \quad (3.27)$$

and $\operatorname{erfc}(y)$ is the (complex) complementary error function [53]. If $Q = \frac{1}{2}$, the above expression is ill-defined, but k_m^{\parallel} can be obtained as a limit or via a separate derivation. The result given in Equation (3.24) was derived in [54], although a different parameter was used for the normalised power loss.

Because of the transcendental functions in the above expressions for k_m^{\parallel} , the dependence on R_s , ω_R , and Q is not transparent. An approximate expression for k_0^{\parallel} , can be obtained, however:

$$k_m^{\parallel}(\sigma_z) \approx \frac{\omega_R R_s}{2 Q} \left(1 - \frac{2x}{\sqrt{\pi}Q} + \frac{x^2}{2Q^2}\right) \exp\left[-x^2 \left(1 - \frac{1}{2Q^2}\right)\right]. \quad (3.28)$$

When Q is of order $\frac{1}{2}$, the above expression is valid for $x \ll 1$. For arbitrary Q , the

Table 3.3. Monopole resonator parameters for Porcupine loads made of different materials. A resonance near 0.5 GHz was assumed when choosing κ and ψ values for each material.

Material	R_s [Ω]	$\omega_R/(2\pi)$ [GHz]	Q
TT2-111V	40.4	0.469	0.425
CMD10	49.0	0.226	0.248
IB-004	41.3	0.411	0.381
Ferrite-50	42.3	0.497	0.471

condition for validity is a bit more complicated.

3.5 Predicted Dependence on Material Properties

Our goal in this section will be to see how the material’s microwave properties affect the coupling impedance of a material-lined pipe. To keep the scope of the discussion finite, we will consider only the four ferrite materials discussed in Chapter 2, we will consider only the Porcupine geometry, and we will examine only the monopole impedance.

Predicted values for the real part of the monopole impedance for loads of different materials are compared in Figure 3.16. For all four materials, the analytic values, which do not account for the finite length of the layer, disagree with the Akasaka results near and above 1 GHz, but the two methods agree quite well at low frequencies. The predicted impedance of IB-004 is very close to that of TT2-111V; CMD10 is predicted to have a peak impedance about 20% higher than TT2-111V; the predicted Ferrite-50 impedance is more than a factor of 2 smaller than TT2-111V at low frequencies, and it remains significantly lower at high frequencies when the finite-length effects are included (Figure 3.16b). The corresponding k_0^{\parallel} for Ferrite-50 is about 2/3 that of TT2-111V for $\sigma_z = 10$ mm. The TT2-111V, IB-004, and CMD10 loss factors are equal within a few percent at this bunch length.

The simplified model from the previous section is adequate to explain the behaviour of CMD10 and IB-004 (and, as we already saw, TT2-111V) below 1 GHz. The resonator parameters obtained with this model for the four materials are compared in Table 3.3. As can be seen, the parameters for IB-004 are very close to those of TT2-111V; a higher R_s and a lower resonant frequency are predicted for CMD10 (due mostly to its smaller κ), which is in agreement with Figure 3.16. The smaller Q predicted for CMD10 also agrees with Figure 3.16, since the width of the resonance is about the same as for TT2-111V and the resonant frequency is smaller.

We saw in the previous section that our simplified model is not valid for a Ferrite-50 Porcupine load. The resonator parameters for Ferrite-50 do indeed disagree with

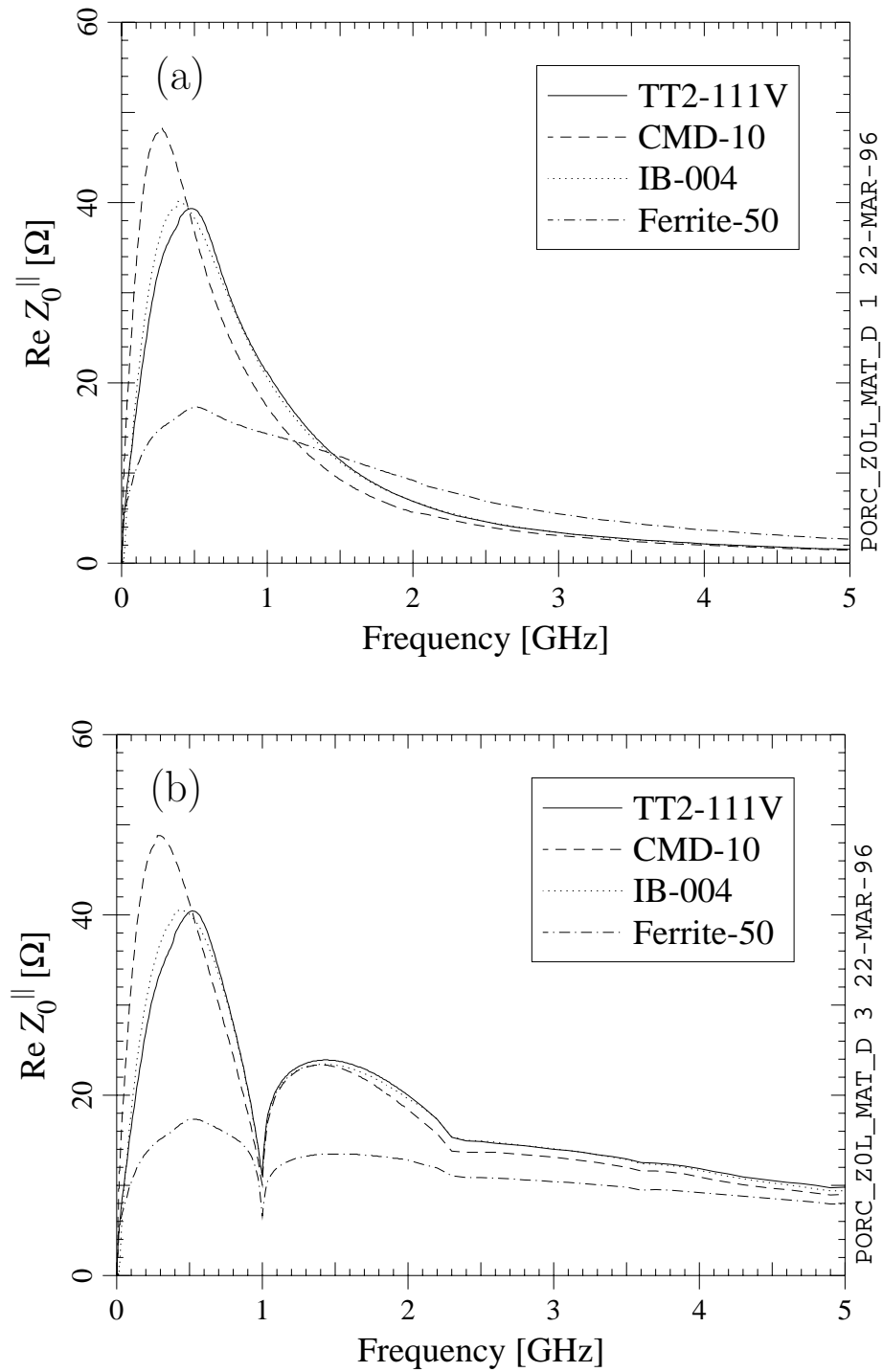


Figure 3.16. Real part of the monopole coupling impedance predicted by (a) the analytic formula and (b) the Akasaka field matching method for Porcupine loads made of various materials.

Figure 3.16, and fail to explain the significantly lower impedance relative to the other materials. With some different assumptions that are better suited to the μ and ϵ of Ferrite-50 near 0.5 GHz, one can obtain an alternate model for the monopole impedance of Ferrite-50, in which

$$Z_0^{\parallel}(\omega) \approx \frac{1}{2\pi} \frac{L}{r_x} \sqrt{\frac{\mu}{\epsilon}}. \quad (3.29)$$

In contrast to our resonator model, ϵ matters but the layer thickness does not (in this case, we assume that the electromagnetic penetration depth is small compared to the layer thickness). The above equation gives about the right answer for the Ferrite-50 Porcupine impedance, at least at 0.5 GHz.

3.6 Predicted Dependence on Load Geometry

We will now examine the coupling impedance's dependence on the geometry of the material-lined tube. To again keep the scope of the discussion finite, we will consider only TT2-111V ferrite, we will consider only simple variations on the Porcupine geometry, and we will discuss only the monopole loss factor for the special case of $\sigma_z = 10$ mm.

As can be seen in Equation (3.10), the analytic formula predicts a simple proportionality between $Z_0^{\parallel}(\omega)$ and the length L of the ferrite layer, and hence also between $k_0^{\parallel}(\sigma_z)$ and L . The same is true of the resonator model. Predicted k_0^{\parallel} values for a Porcupine load as a function of L are given in Figure 3.17. The Akasaka method and AMOS predict a consistently higher loss factor due to finite-length effects. The absolute difference between the Akasaka and analytic predictions is approximately constant for large L , but it decreases to 0 as $L \rightarrow 0$. Fortunately, the resonator model (which we obtained as an approximation to the analytic formula) agrees better with the Akasaka method near $L = 600$ mm.

For all of our models, the dependence of k_0^{\parallel} on the inner radius r_x of the material layer is non-trivial. According to the approximate expression for the resonator k_0^{\parallel} given in Equation (3.28), however, k_0^{\parallel} is proportional to r_x^{-2} to lowest order in $\omega_R \sigma_z / c$. Predicted k_0^{\parallel} values for a Porcupine load as a function of r_x are given in Figure 3.18. As before, the Akasaka method and AMOS predict a consistently higher loss factor. The difference between the Akasaka and analytic predictions decrease as r_x decreases. The resonator model, on the other hand, better approximates the analytic result when r_x is large. The analytic and Akasaka k_0^{\parallel} vary more slowly with r_x than our crude estimate of r_x^{-2} : the analytic k_0^{\parallel} does not follow a power law very closely, but it varies roughly as $r_x^{-1.7}$; the Akasaka k_0^{\parallel} follows a proportionality to r_x^{-1} quite closely over the range of values shown in Figure 3.18.

The dependence of k_0^{\parallel} on the thickness of the material layer is also non-trivial in all of the models. According to the approximate resonator expression, k_0^{\parallel} is independent of thickness to lowest order in $\omega_R \sigma_z / c$; the first-order term is negative and proportional to $(r_o - r_x)^{-1}$. Predicted k_0^{\parallel} values for a Porcupine load as a function

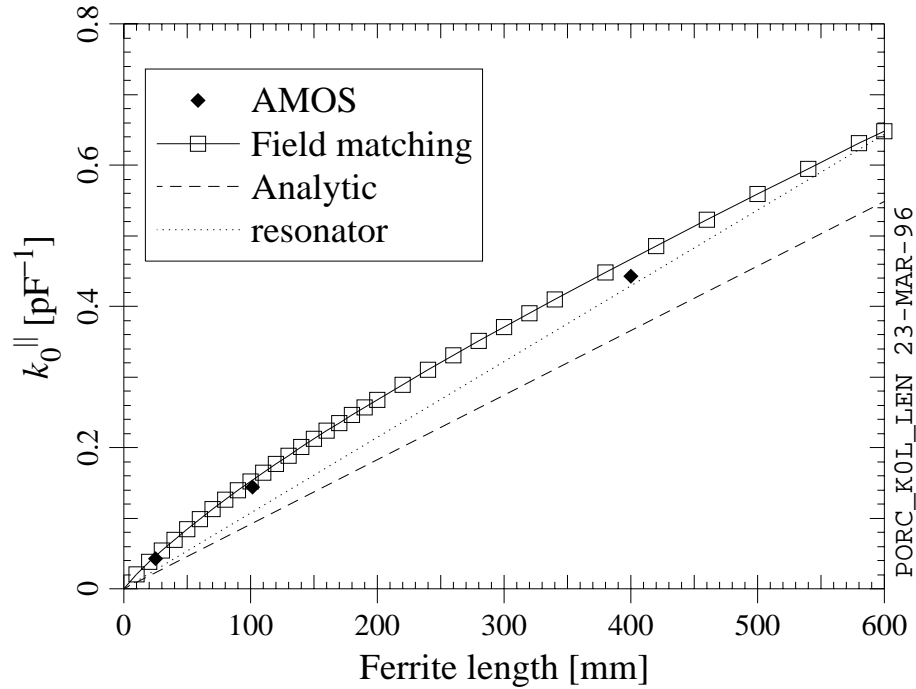


Figure 3.17. Comparison of predicted monopole loss factors as a function of the length of a TT2-111V Porcupine load. In the resonator case, the exact formula for k_0^{\parallel} was used.

of thickness, with r_o held constant, are given in Figure 3.19. As was the case for L , the Akasaka and analytic predictions agree as the thickness goes to zero. The resonator approximation falls between the analytic and Akasaka predictions. The behaviour agrees qualitatively with our expectation, in that k_0^{\parallel} varies more slowly with thickness as the thickness increases.

3.7 Summary

Coupling impedance predictions for the TT2-111-series Porcupine load agree reasonably well at low frequencies; near and above the cutoff frequency, the finite length of the ferrite becomes important, producing an impedance significantly larger than expected from the analytic approximation at high frequencies. The coupling impedances for the L3 load and the Ferrite-50 model predicted by the various calculational methods agree reasonably well, although the latter differ somewhat from the impedance predicted via wire measurements. It is possible to account for the resonator-like behaviour of the Porcupine impedance near 0.5 GHz with a simple model, although finite-length effects are not included.

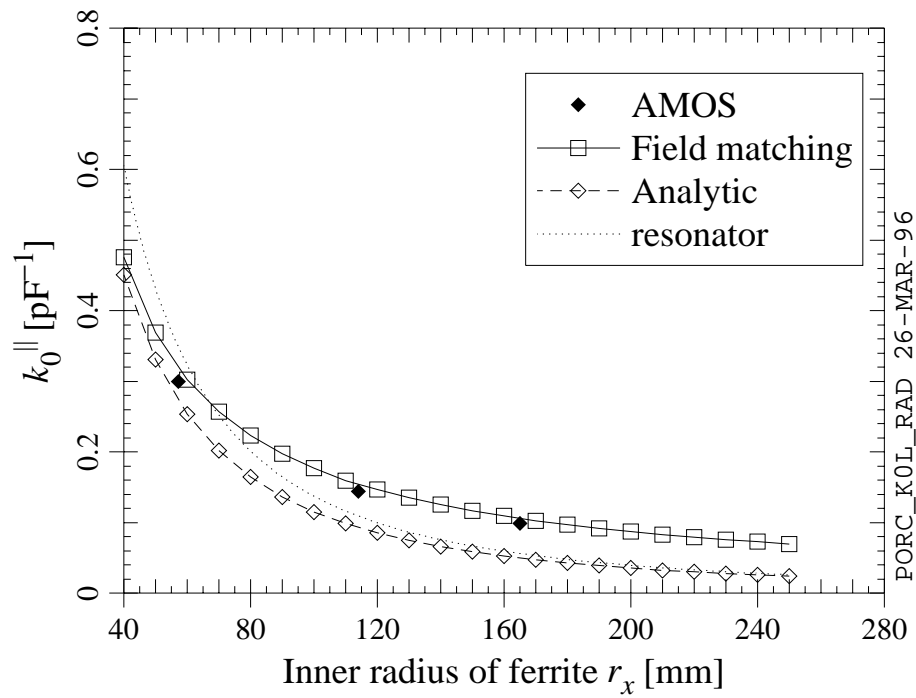


Figure 3.18. Comparison of predicted monopole loss factors as a function of the inner radius of a TT2-111V Porcupine load. The exact formula for the resonator k_0^{\parallel} was used.

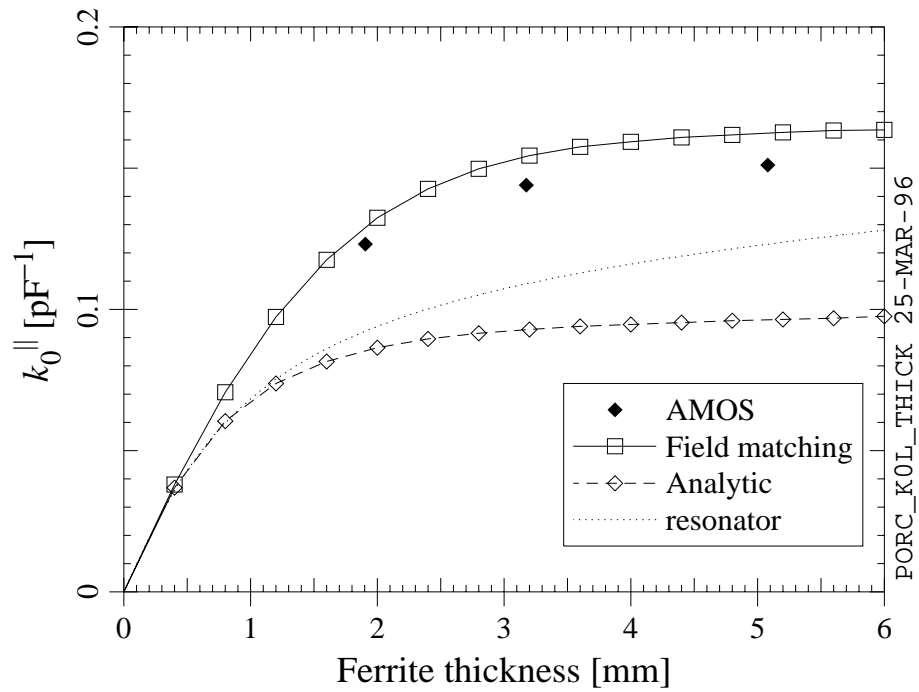


Figure 3.19. Comparison of predicted monopole loss factors as a function of the ferrite layer thickness of a TT2-111V Porcupine load. The exact formula for the resonator k_0^{\parallel} was used.

Chapter 4

Power Transfer and Beam Instability Predictions

As discussed in the previous chapter, wake fields are produced as the beam interacts with its surroundings, and a wake force acts back on the particles in the beam. As the beam current is increased, the wake fields, being proportional to current, will eventually produce enough positive feedback to disrupt the charge distribution in the beam or excite coherent oscillations of the bunches. In this chapter, the effect of the Porcupine HOM load impedance on beam stability will be predicted for a hypothetical future storage ring, which we will call CESR-V. Predictions for the beam-induced power dissipation in the ferrite loads will also be given. For the latter, we will consider two cases: the CESR-V machine parameters and another set of design parameters (which we will call CESR-III.5) for the near-term upgrade of CESR that is in progress.

To construct theoretical models for beam instabilities, one can approximate the beam as a continuous distribution of charge in phase space. The time evolution of the distribution under the influence of the electromagnetic forces (from the ring's guide field and the wake field) is then described by the Vlasov equation. To make the problem tractable, the wake force is treated as a small perturbation relative to the guide field. We will see that the approximate stability criteria obtained with this approach can be expressed in terms of functionals of the coupling impedance and the frequency spectrum of the bunch. The wake field affects both the time-independent solution to the Vlasov equation and the time-dependent solutions. The former topic is the subject of Section 4.4; the latter is the subject of Sections 4.5 through 4.7. In these sections, we will consider only the single-turn and multi-turn wake produced by a single bunch—multi-bunch effects are discussed in Section 4.8. First, we describe the machine parameters that will be used, introduce the effective elastance (a functional whose usefulness will become obvious as we proceed), and consider the beam-induced power dissipation.

Most of the analysis covered herein is based on the “perturbation formalism” given in Chapter 6 of A. Chao's book [43]. Following Chao, we will consider a smooth accelerator (*i.e.* an accelerator in which the guide field is independent of position) in formulating the Vlasov equation, and incorporate the transverse betatron function on an *ad hoc* basis only. Likewise, we will assume that the accelerator is not operating near a coupling resonance, so that the longitudinal, horizontal, and vertical degrees

of freedom of the beam are independent.¹ Our equations will have a form slightly different from Chao's, because of our different sign convention for impedance (see Section 3.1) and our formulation in terms of elastance. We will also use alternate approaches to the analysis of some of the collective effects. The present approach will be somewhat different from the preliminary beam stability estimates for the HOM loads [55], which were based mostly on the bunched-beam instability program ZAP [56], with the HOM loads' coupling impedance parameterised by several low- Q resonators; the present analysis will not require such a parameterisation. The machine parameters have also evolved a bit since the early estimates with ZAP were made.

4.1 Machine Parameters

Selected machine parameters for CESR-III.5 and CESR-V are given in Table 4.1. Since no optical lattice has been designed for CESR-V yet, several of the CESR-V parameters are assumed to be the same as for CESR-III.5. For the convenience of the reader, some additional derived parameters are given in Table 4.2.

CESR-III.5 is a more mature incarnation of CESR-III [2]: the two machines have the same RF system, but the cavities operate at a higher field level in CESR-III.5, thereby producing a smaller bunch length. The decrease in bunch length increases the power dissipation in the ferrite loads. In CESR-III.5, as in CESR-III, the bunches are grouped into trains of 5 bunches spaced 7 buckets (4.2 metres) apart. Because of the pretzel orbits, the beams have a transverse displacement as they travel through the HOM loads. CESR-V is a hypothetical machine with even higher luminosity (more than four times the CESR-III.5 luminosity, one would hope): the charge per bunch is about the same, but the bunches are spaced 7 buckets apart throughout the entire circumference. CESR-V has a somewhat shorter bunch length and more cavities (and hence more ferrite loads). In CESR-V, the beams travel through separate vacuum chambers, but they share a common RF system; the beams' transverse displacement in the HOM loads is larger than in the CESR-III.5 case. Of the three machines, CESR-V has the largest number of bunches, so it can be expected to be the least stable; we will therefore focus on CESR-V in our beam stability analysis.

No wigglers are assumed present in the parameter sets; the addition of wigglers will tend to increase the momentum spread, energy radiated per turn, radiation damping rates, and bunch length (the increase in the latter would presumably be compensated for via a higher RF voltage), which can be expected to enhance the beam stability slightly.

The chromaticity ξ is included in Table 4.1 because a non-zero chromaticity produces a single-bunch transverse instability. Several definitions of chromaticity are in use; we will take

$$\xi \equiv \frac{1}{\omega_0} \frac{d\omega_\beta}{d\delta}, \quad (4.1)$$

¹with one exception: we will include synchro-betatron coupling explicitly in our discussion of the bananer effect in Section 4.4.

Table 4.1. Selected CESR-III.5 and CESR-V machine parameters.

Parameter	CESR-III.5	CESR-V
Ring circumference C	768.43 m	
Energy per particle $q_e E_0$	5.289 GeV	
Current per bunch I_b	11.11 mA	10.93 mA
Bunches per beam M	45	183
Bunch fill pattern	9 trains ^a	uniform
Longitudinal bunch size σ_z (bunch “length”)	11.95 mm	10 mm
Relative momentum spread ^b σ_δ	$6.115 \cdot 10^{-4}$	
Momentum compaction	0.0118	
RF Frequency	499.8 MHz	
Horizontal betatron frequency	4105.64 kHz	
Vertical betatron frequency	3744.22 kHz	
Horizontal chromaticity	1	
Vertical chromaticity	1	
Energy radiated per turn ^b U_0	1.029 MeV	
Longitudinal radiation damping rate ^b	76.72 s^{-1}	
Horizontal radiation damping rate ^b	37.09 s^{-1}	
Vertical radiation damping rate ^b	37.94 s^{-1}	
Number of HOM loads	8	20
Maximum beam displacement near the cavities x_\perp	20 mm	41 mm
Maximum transverse β -function near the cavities β_Z	40 m	

^abunches within a train are 7 buckets apart^bwithout wigglers

Table 4.2. Some derived parameters for CESR-III.5 and CESR-V.

Parameter	CESR-III.5	CESR-V
Revolution frequency $f_0 = \omega_0/(2\pi)$	390.14 kHz	
Current per beam	0.5 A	2 A
Charge per bunch q_b	28.48 nC $1.778 \cdot 10^{11} e$	28.01 nC $1.748 \cdot 10^{11} e$
Slippage factor η	0.0118	
Harmonic number	1281	
Peak RF voltage	12 MV	17.12 MV
Synchrotron frequency $\omega_{s0}/(2\pi)$	28.82 kHz	34.43 kHz
Synchrotron tune	0.07388	0.08826
Horizontal betatron tune	10.5236	
Vertical betatron tune	9.5972	
Number of RF cavities	4	10

where ω_0 is the revolution angular frequency, ω_β is the betatron angular frequency, and δ is the relative difference in the energy of the particle. Note that this definition is different from Chao's.

4.2 The Effective Elastance

Definitions

In anticipation of the discussion to follow, it will be useful to introduce a functional of the impedance and the charge distribution of the bunch. Its dimensions will be inverse capacitance in the monopole case and inverse capacitance per unit length in the dipole case, so we will call it the effective elastance.² We will consider the case of a Gaussian distribution only. We define the effective monopole elastance of order j as follows:

$$\Xi_{0,j}(\sigma_z; \omega_0, \Delta\omega) \equiv \frac{1}{2\pi i} \frac{c\omega_0}{\sigma_z} \sum_{p=-\infty}^{\infty} \frac{Z_0^{\parallel}(\omega_p)}{\omega_p} \left(\frac{\omega_p \sigma_z}{\sqrt{2}c} \right)^j \exp\left(-\frac{\omega_p^2 \sigma_z^2}{c^2}\right), \quad (4.2)$$

where

$$\omega_p \equiv p\omega_0 + \Delta\omega. \quad (4.3)$$

²For readers who are unfamiliar with the less common derived quantities in electromagnetism, elastance is indeed defined as the reciprocal of capacitance.

The arguments are the bunch length σ_z , the angular frequency of revolution ω_0 , and an angular frequency shift $\Delta\omega$. The latter will either be 0 or an integer multiple of the synchrotron frequency, depending on the context. Our analysis of the longitudinal motion of the beam will involve the monopole elastance.

If the monopole wake function has a short range (*i.e.* if $W_0^{\parallel}(t)$ has decayed to 0 for $t \geq$ one revolution), then $Z_0^{\parallel}(\omega)$ varies slowly between $\omega = \omega_p$ and $\omega = \omega_{p+1}$, and, in the limit, the sum in Equation (4.2) reduces to an integral obtained via the substitutions

$$\sum_{p=-\infty}^{\infty} \rightarrow \int_{-\infty}^{\infty} \frac{d\omega}{\omega_0} \quad ; \quad \omega_p \rightarrow \omega. \quad (4.4)$$

The result is

$$\Xi_{0,j}(\sigma_z; \omega_0, \Delta\omega) = \Xi_{0,j}(\sigma_z) = \frac{1}{2\pi i} \frac{c}{\sigma_z} \int_{-\infty}^{\infty} d\omega \frac{Z_0^{\parallel}(\omega)}{\omega} \left(\frac{\omega \sigma_z}{\sqrt{2}c} \right)^j \exp\left(-\frac{\omega^2 \sigma_z^2}{c^2}\right). \quad (4.5)$$

In other words, Equations (4.2) and (4.5) are equivalent when the impedance is broad-banded enough so that there are no multi-turn effects. As indicated, when the integral formulation of Equation (4.5) is applicable, $\Xi_{0,j}$ is independent of ω_0 and $\Delta\omega$; it depends solely on σ_z (we placed a semi-colon in front of ω_0 and $\Delta\omega$ in the arguments to $\Xi_{0,j}$ to underscore this distinction).

In the general case, $\Xi_{0,j}$ is complex. If Equation (4.5) applies, however, the symmetry in $Z_0^{\parallel}(\omega)$ requires $\Xi_{0,j}$ to be either purely real or purely imaginary: when j is even, $\Xi_{0,j}$ is real, and is a functional of the imaginary part of $Z_0^{\parallel}(\omega)$ only; when j is odd, $\Xi_{0,j}$ is imaginary, and is a functional of the real part of $Z_0^{\parallel}(\omega)$ only.

We define the effective dipole elastance of order j to be

$$\Theta_j(\sigma_z, \omega_\xi; \omega_0, \Delta\omega) \equiv \frac{1}{2\pi i} c \omega_0 \sum_{p=-\infty}^{\infty} \frac{Z_1^{\parallel}(\omega_p)}{\omega_p} \left[\frac{(\omega_p - \omega_\xi) \sigma_z}{\sqrt{2}c} \right]^j \exp\left[-\frac{(\omega_p - \omega_\xi)^2 \sigma_z^2}{c^2}\right], \quad (4.6)$$

with ω_p again given by Equation (4.3). In the dipole case, we have a fourth argument, the chromatic angular frequency ω_ξ :

$$\omega_\xi \equiv \frac{\xi \omega_0}{\eta} = \frac{1}{\eta} \frac{d\omega_\beta}{d\delta}, \quad (4.7)$$

where η is the slippage factor. The angular frequency shift $\Delta\omega$ will either be 0 or $\omega_\beta + l\omega_{s0}$. Our analysis of the transverse motion of the beam will involve the dipole elastance.

As in the monopole case, if the dipole wake function has a short range, the sum reduces to an integral:

$$\begin{aligned} \Theta_j(\sigma_z, \omega_\xi; \omega_0, \Delta\omega) &= \Theta_j(\sigma_z, \omega_\xi) \\ &= \frac{1}{2\pi i} c \int_{-\infty}^{\infty} d\omega \frac{Z_1^{\parallel}(\omega)}{\omega} \left[\frac{(\omega - \omega_\xi) \sigma_z}{\sqrt{2}c} \right]^j \exp\left[-\frac{(\omega - \omega_\xi)^2 \sigma_z^2}{c^2}\right]. \end{aligned} \quad (4.8)$$

When the integral formulation applies in the transverse case, Θ_j depends on σ_z and ω_ξ , but not on ω_0 or $\Delta\omega$ (as indicated again by the semi-colon).

As before, Θ_j is complex in general. However, if $\xi = 0$ and Equation (4.8) applies, Θ_j is purely real for even j 's and purely imaginary for odd j 's. The chromaticity dependence presents a significant conceptual complication. For the sake of conceptual insight, it is useful to note that the dipole elastance of order j can be expressed approximately in terms of achromatic dipole elastances of like orders:

$$\begin{aligned} \Theta_j(\sigma_z, \omega_\xi; \omega_0, \Delta\omega) &\approx \Xi_{1,j}(\sigma_z; \omega_0, \Delta\omega) \\ &+ \chi \left[\Xi_{1,j+1}(\sigma_z; \omega_0, \Delta\omega) - \frac{j}{4} \Xi_{1,j-1}(\sigma_z; \omega_0, \Delta\omega) \right], \end{aligned} \quad (4.9)$$

where χ is the so-called head-tail phase:

$$\chi \equiv 2\sqrt{2} \frac{\omega_\xi \sigma_z}{c} = 2\sqrt{2} \frac{\xi \omega_0 \sigma_z}{\eta c}. \quad (4.10)$$

The achromatic dipole elastance is a close analog of the monopole elastance, and is defined as

$$\Xi_{1,j}(\sigma_z; \omega_0, \Delta\omega) \equiv \frac{1}{2\pi i} c \omega_0 \sum_{p=-\infty}^{\infty} \frac{Z_1^\parallel(\omega_p)}{\omega_p} \left(\frac{\omega_p \sigma_z}{\sqrt{2}c} \right)^j \exp\left(-\frac{\omega_p^2 \sigma_z^2}{c^2}\right). \quad (4.11)$$

Equation (4.9) is valid to linear order in ω_ξ . If this approximation and the integral formulation are both applicable, Θ_j has a real part that is independent of ω_ξ and an imaginary part that is proportional to ω_ξ when j is even. We will see later that the imaginary part will produce a growth rate proportional to ω_ξ . Although the linear-order approximation of Equation (4.9) would probably be accurate enough for our purposes, we will use the more exact formula for our instability predictions, since there is no significant calculational advantage in the approximation.

The sum formulation of the monopole and dipole elastance includes multi-turn effects, and provides a convenient formalism for including multiple turns in the loss factor. By defining

$$k_0^\parallel = -\frac{1}{i} \sqrt{2} \Xi_{0,1}(\sigma_z; \omega_0, 0) \quad (4.12)$$

$$k_1^\parallel = -\frac{1}{i} \sqrt{2} \frac{1}{\sigma_z} \Theta_1(\sigma_z, \omega_\xi; \omega_0, 0), \quad (4.13)$$

we can account for the effect of constructive or destructive interference in the multi-turn wake fields on the power dissipation. In the case of a short-range wake, the integral formulation for elastance can be used, in which case the above formulae reduce to Equation (3.8). By symmetry, k_0^\parallel and k_1^\parallel remain real in the multi-turn case, at least for $\xi = 0$. The effect of chromaticity on the dipole loss factor is a subtlety that need not concern us here.

The Predicted Effective Elastance of the Porcupine Load

We have two formulae for calculating the monopole elastance, Equation (4.2), an infinite-sum formulation which includes multi-turn effects, and Equation (4.5), an integral formulation which does not. The monopole elastances of order 0 through 8 obtained via the two formulae are compared in Figure 4.1 for the case of the coupling impedance predicted by AMOS for the Porcupine load. In both cases, we have assumed $\sigma_z = 10$ mm, as appropriate for CESR-V. For the multi-turn summations, we have set $\Delta\omega = j\omega_{s0}/2$ for even j 's and $\Delta\omega = (j-1)\omega_{s0}/2$ for odd j 's and have used the CESR-V values for ω_0 and ω_{s0} . The elastance values obtained via the two different methods agree quite well. The same observation can be made for the monopole elastances obtained from the analytically-predicted Porcupine impedance. We conclude that the Porcupine's monopole wake function has a range that is short compared to the CESR-V revolution period. The integral formulation will hence be adequate for most of our subsequent analysis. In particular, the single-pass loss factor will be adequate for power loss calculations. Note that, as expected, $\Xi_{0,j}$ is very close to being real for even j 's and imaginary for odd j 's.

The monopole elastances obtained from the analytic coupling impedance prediction for the Porcupine load are compared to AMOS values (using the integral formulation for both) in Appendix B. The magnitude of the AMOS $\Xi_{j,0}$ is consistently greater than or equal to the magnitude of the corresponding analytic value. Since, as will be demonstrated in subsequent sections, the elastance is a measure of the disruptive effect on the beam caused by the impedance, the AMOS values can be expected to give us more pessimistic beam stability predictions. For the sake of conservatism, we will use the AMOS values for subsequent predictions, except when indicated otherwise. Since the agreement between the summation results and the integral results is good enough for our purposes, we will use the integral formulation of Equation (4.5), except when indicated otherwise.

The dipole elastances of order 0 through 8 obtained via the summation of Equation (4.6) and the integral of Equation (4.8) are compared in Figure 4.2 for the AMOS Porcupine impedance. We used CESR-V parameters ($\sigma_z = 10$ mm, $\omega_\xi/(2\pi) = 33.1$ MHz, ...), and set $\Delta\omega = \omega_\beta + j\omega_{s0}/2$ or $\omega_\beta + (j-1)\omega_{s0}/2$ in the summation. As in the monopole case, the elastances obtained via the two different approaches agree reasonably well for the AMOS case, as well as the analytic case (although the latter are not shown). Thus, the Porcupine's dipole wake function also has a short range for our purposes. Note that, because ξ is not zero, Θ_j has a non-zero imaginary part for both even j 's and odd j 's.

The analytic dipole elastances are compared to the AMOS values (with both obtained via the integral formulation) in Appendix B. The AMOS values are again greater than or equal to their analytic counterparts. We will use the AMOS dipole elastance values based on the integral formulation in future sections, except when indicated otherwise.

Because they depend on $Z_m^{\parallel}(\omega)/\omega$, $\Xi_{0,0}$ and Θ_0 are sensitive to the low-frequency behaviour of $Z_m^{\parallel}(\omega)$. As a result, we can expect a significant error in the calculated values of $\Xi_{0,0}$ and Θ_0 based on AMOS, although this is not obvious in Figures 4.1

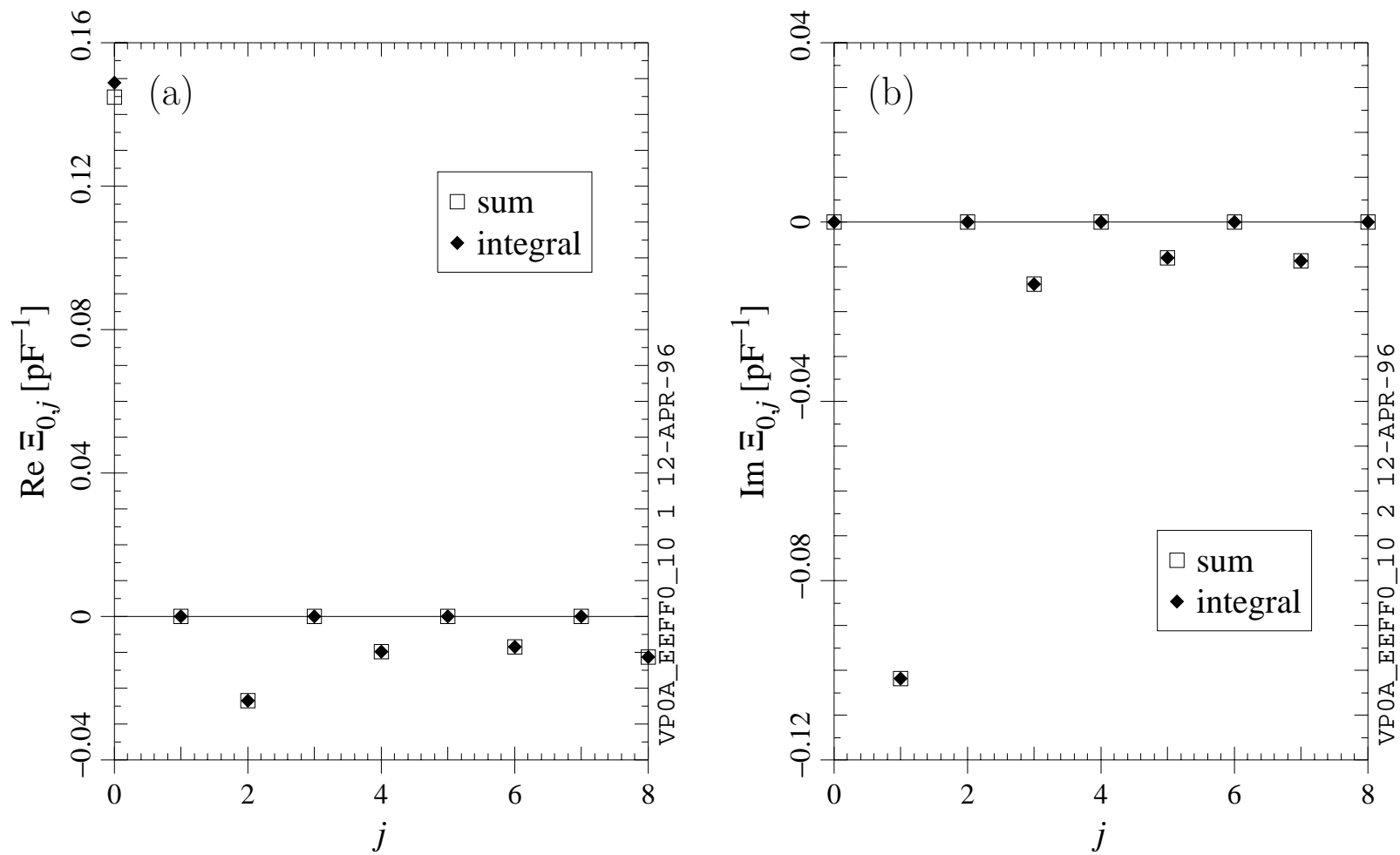


Figure 4.1. Comparison of summed and integrated values of (a) the real part and (b) the imaginary part of the effective monopole elastance for one Porcupine load, based on the coupling impedance from AMOS, with $\sigma_z = 10$ mm.

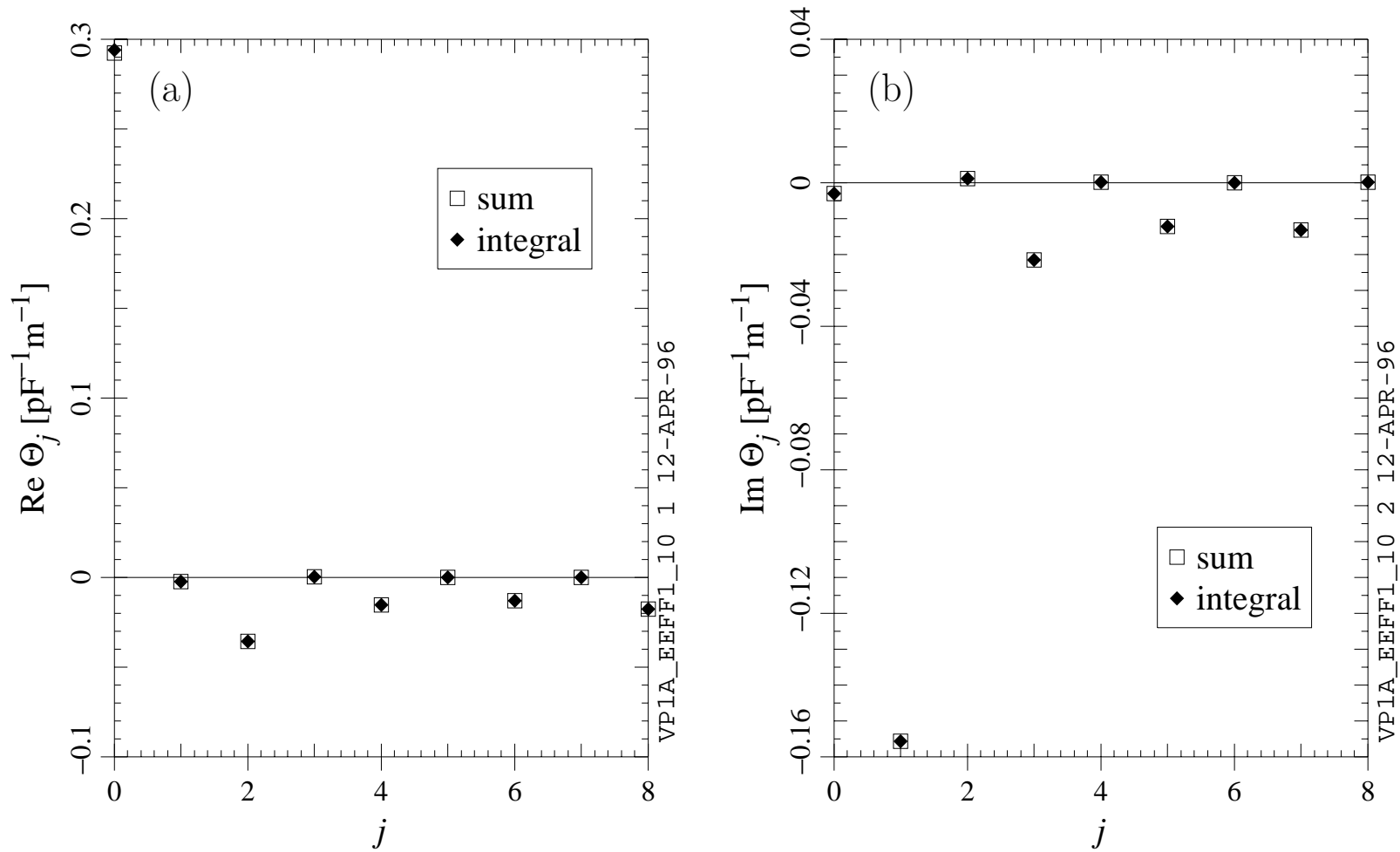


Figure 4.2. Comparison of summed and integrated values of (a) the real part and (b) the imaginary part of the effective dipole elastance for one Porcupine load, based on the coupling impedance from AMOS, with $\sigma_z = 10$ mm and $\xi = 1$.

and 4.2. We will return to this point in Sections 4.7 and 4.8.

4.3 Beam-Induced Power Dissipation

Direct Power Transfer

The direct power transfer from the beam to the ferrite loads can be estimated in a straightforward manner from the loss factor. In the case of two beams, each with multiple bunches travelling through the structure once per revolution, Equation (3.7) becomes

$$P_d = \frac{2Mk^{\parallel}I_b^2}{f_0}, \quad (4.14)$$

where P_d is the power lost by the beam (averaged over time), M is the number of bunches per beam, I_b is the current per bunch, f_0 is the revolution frequency, and k^{\parallel} is the total longitudinal loss factor. If the beam is travelling on axis, $k^{\parallel} = k_0^{\parallel}$; if the beam is travelling off axis, there is a multipole contribution to the total dissipation, and

$$k^{\parallel} = k_0^{\parallel} + k_1^{\parallel}x_{\perp}^2, \quad (4.15)$$

where x_{\perp} is the transverse displacement of the beam from the axis of the vacuum chamber. We have included only the two lowest-order terms in Equation (4.15), *i.e.* monopole and dipole, since the higher moments of the beam can usually be neglected. As we saw in the previous section, the wake fields have a short enough range so that we can use the single-pass loss factor instead of having to consider multiple turns.

Predictions for the direct power transfer from the beam to Porcupine loads made of TT2-111V ferrite are given in Table 4.3. The calculations are based on the monopole and dipole loss factors predicted by AMOS.

The average power dissipation per unit area can be obtained from the total power in the obvious way. However, when the beam is off axis, the azimuthal distribution of the power density is in general non-uniform. In general, several field components may contribute to the dissipation. For TT2-111V ferrite, however, the dissipation is associated mostly with the azimuthal component of the magnetic field, so we will make the (conservative) assumption that all of the dissipation is due to a single field component as we consider the power density distribution.

In general, there may be partial or complete interference between the monopole and dipole fields (for example, the interference is complete for the resistive wall impedance). In the CESR-III.5 and CESR-V cases, however, we have two equally-filled beams with equal and opposite displacements in the HOM loads, in which case the contributions from the interference terms to the power density cancel out.³ Even with-

³There is obviously no cancellation of interference terms if the machine is operated with a single beam. If there is full interference between the monopole and dipole wake fields, a single beam with a displaced orbit may produce significantly less uniform power dissipation. However, the maximum power density in the single-beam case is less than or equal to the maximum power density in the corresponding 2-beam case with the same current per beam.

Table 4.3. Predictions for direct power transfer from the beam to the loads for CESR-III.5 and CESR-V. The AMOS results were used.

CESR-III.5		
Quantity	Beam on axis	$x_{\perp} = 20$ mm
k^{\parallel} per load [pF ⁻¹]	0.130	0.138
Power per load [kW]	3.71	3.94
Average power per unit area [W/cm ²]	5.10	5.41
Maximum power per unit area [W/cm ²]	≥ 5.10	≥ 5.72
CESR-V		
Quantity	Beam on axis	$x_{\perp} = 41$ mm
k^{\parallel} per load [pF ⁻¹]	0.144	0.181
Power per load [kW]	16.1	20.3
Average power per unit area [W/cm ²]	22.2	27.9
Maximum power per unit area [W/cm ²]	≥ 22.2	≥ 33.5

out an interference term from the dipole fields, the power density is non-uniform.⁴ The maximum power density is

$$p_{max} = \langle p_0 \rangle + 2 \langle p_1 \rangle , \quad (4.16)$$

where $\langle p_0 \rangle$ and $\langle p_1 \rangle$ are the average power densities induced by beams with a pure monopole distribution and a pure dipole distribution, respectively. As indicated in Equation (4.16), the monopole and dipole contributions add algebraically, but the maximum dipole power density is twice the average. The maximum power densities obtained via Equation (4.16) are also given in Table 4.3.

We have not taken into account the longitudinal distribution in the power density in this analysis (although, according to the analytic approximation for the load impedance, the dissipation is uniform in z). As a result, the values given in Table 4.3 are lower bounds for the maximum power density. According to the AMOS impedance prediction, 14% of the monopole beam power intercepted by a Porcupine load is above the cutoff frequency for the CESR beam pipe when $\sigma_z = 10$ mm.

Indirect Power Transfer

In addition to the direct power transfer from the beam, the ferrite loads absorb power transferred from the beam into higher-order modes of the cavity and other nearby

⁴Depending on the relative times at which the bunches pass through the HOM loads, there might be some destructive interference between the dipole wake fields of the two beams. Such interference would tend to further reduce the non-uniformity in the power density.

structures. We will estimate the indirect power transfer using the composition rule (see Section 3.3), which implies that the total loss factor of a structure is approximately equal to the sum of the loss factors of each of its elements.

Predictions for the indirect power transfer to the Porcupine loads are given in Table 4.4. The values are based on loss factor calculations done with ABCI [1, 57] and MAFIA [58] for the “BB1-2” cavity module. The cavity module includes the cavity cell, tapered beam tube transitions, and a large-bore sliding joint. For $\sigma_z = 10$ mm, about 3/4 of the indirect power transfer is due to the tapered transitions. The contribution from the flutes in the beam tube (see Figure 1.3) was included via the composition rule; a three-dimensional loss factor calculation of the flutes’ loss factor was done by S. Belomestnykh using MAFIA. Details on the loss factor calculations for the BB1-2 module are given in a separate report [59]. In Table 4.4, we assume that the power is split equally between the two HOM loads in the module.

Estimates of the maximum power per unit area deposited in the ferrite are also given in Table 4.4. The azimuthal dependence is taken into account via Equation (4.16). An estimate of the longitudinal distribution in the power density also was included in the values of Table 4.4, although only the monopole wake was accounted for. The estimate is based on frequency-domain calculations of the resonant modes of the module, with the ferrite loads present [20, 60], using the computer program CLANS [22]. All of the monopole modes below the cutoff frequency were included (with the exception of some low- Q “ferrite modes”). The distribution in the net power dissipation was obtained using the predicted field distribution in the ferrite and the loss factor for each mode. The ratios of the maximum power density to the average power density were 1.945 and 1.893 for $\sigma_z = 10$ and 12 mm, respectively. The maxima in the power density were predicted to occur along the edges of the loads. The radial distribution in the power per unit volume was predicted to be uniform, at least up to a few percent. It should be noted that the modes below cutoff accounted only for about half of the total loss factor. Some fraction of the beam power intercepted by modes above cutoff may propagate into the beam tube instead of being dissipated in the ferrite. It should also be noted that the structure used in the CLANS calculations was somewhat different from the BB1-2 module that was input to ABCI.

Total Power Transfer

Predictions for the total power transfer to the HOM loads are given in Table 4.5. Ultimately, it is envisaged that two or more cavities will share one pair of tapers, which will reduce the loss factor per cavity. However, it is not clear that the beam power intercepted by the tapers will be shared equally between all of the loads; in the worst case, the loads adjacent to tapers might intercept all of the extra power. The power values given in Table 4.5 would apply to the loads adjacent to the tapers (and the others would dissipate less power) in this scenario, as well as in the case of a single cavity module.

Table 4.4. Predictions for indirect power transfer from the beam to the loads for CESR-III.5 and CESR-V. The loss factors given include only parasitic effects.

CESR-III.5		
Quantity	Beam on axis	$x_{\perp} = 20$ mm
k^{\parallel} per module [pF ⁻¹]	0.325	0.361
Power per load [kW]	4.62	5.14
Average power per unit area [W/cm ²]	6.64	7.38
Maximum power per unit area [W/cm ²]	12.56	14.06
CESR-V		
Quantity	Beam on axis	$x_{\perp} = 41$ mm
k^{\parallel} per module [pF ⁻¹]	0.458	0.679
Power per load [kW]	25.7	38.0
Average power per unit area [W/cm ²]	36.8	54.6
Maximum power per unit area [W/cm ²]	71.6	107.2

Table 4.5. Predictions for the total power transfer from the beam to the loads for CESR-III.5 and CESR-V. The AMOS results were used for the direct power transfer calculation. The loss factors given include only parasitic effects.

CESR-III.5		
Quantity	Beam on axis	$x_{\perp} = 20$ mm
k^{\parallel} per module [pF ⁻¹]	0.586	0.638
Power per load [kW]	8.34	9.09
Average power per unit area [W/cm ²]	11.7	12.8
Maximum power per unit area [W/cm ²]	≥ 17.7	≥ 19.8
CESR-V		
Quantity	Beam on axis	$x_{\perp} = 41$ mm
k^{\parallel} per module [pF ⁻¹]	0.746	1.041
Power per load [kW]	41.8	58.3
Average power per unit area [W/cm ²]	59.0	82.5
Maximum power per unit area [W/cm ²]	≥ 93.8	≥ 140.7

4.4 Static Effects

Longitudinal: Potential Well Distortion

The longitudinal wake field produces a current-dependent distortion in the time-independent phase space distribution of the beam. The non-linearity in the RF voltage, exacerbated by the phase shift required to compensate for synchrotron radiation, also contributes to the distortion. In electron-positron machines, in the absence of wake effects and non-linearity in the RF voltage, the distributions in δ and z are both Gaussian, with standard deviations σ_δ and σ_{z0} , respectively; the particles oscillate at angular frequency ω_{s0} .

The distorted distribution that results from a wake force and/or a non-linear RF voltage is a time-independent solution to the Vlasov equation. It can be shown via a more general analysis that the δ -distribution remains Gaussian. The z -distribution, however, does not remain Gaussian in general; it must satisfy an integral equation, sometimes referred to as the Haïssinski Equation. This equation does not have a closed-form solution for an arbitrary wake function. If the wake force is of the same order as the force due to the RF voltage, or if the particles in the bunch stray a significant distance from the zero crossing of the RF voltage, the distorted z -distribution can be expected to be quite different from the undistorted one, and the full integral equation must be solved in order to understand the beam's behaviour. On the other hand, if the wake voltage is small compared to the RF voltage and the bunch remains close to the zero crossing, the distortion can be treated as a small perturbation, and approximate solutions to the integral equation may be sought. We will presume the latter, and see whether we end up with a self-consistent result.

One way to obtain an approximate solution to the Haïssinski Equation is to do a second-order Taylor Series expansion of the bunch's wake function $W_0^{\parallel}(z)$. This approach is discussed by A. Chao in his section on potential well distortion [43]. B. Zotter [61] obtained the same end results via a different approach. The omission of the higher-order terms in the expansion yields a Gaussian distribution, albeit with a shifted mean \bar{z} and a standard deviation σ_z different from σ_{z0} . Two equations are obtained via this analysis, one from the first-order term and the other from the second-order term, from which σ_z and \bar{z} can be deduced. The Taylor approach can be expected to give good results if $W_0^{\parallel}(z)$ can be well-approximated by a linear function of z over distances of order σ_z .

There is an alternative to the Taylor expansion of $W_0^{\parallel}(z)$: differentiating the Haïssinski Equation directly. By taking the first and second derivatives, one can obtain two exact equations analogous to the two approximate equations obtained with the Taylor approach. This approach is discussed in a separate report [62].

In both of these approaches, the two equations are transcendental and coupled. However, if we neglect the non-linearity in the RF voltage, the Taylor-expansion equations become more tractable. Making the same idealisation in the differentiation approach, with the further assumption that the z -distribution is still approximately Gaussian (again, with mean \bar{z} and standard deviation σ_z), we can obtain an alternate pair of equations analogous to the first two.

Dispersive Tendency

With the approximations given above, the equations obtained from the second-order term in the Taylor expansion or the second derivative of the Haïssinski Equation can be written in a common form:

$$\left(\frac{\sigma_z}{\sigma_{z0}}\right)^2 = 1 + \frac{I_b}{\sigma_\delta^2 \eta E_0} X_s, \quad (4.17)$$

where $q_e E_0$ is the energy per particle. In Equation (4.17), X_s is a functional of the impedance and the bunch's frequency distribution which can be thought of as an effective reactance. In terms of the effective elastance introduced in Section 4.2,

$$X_s = 2\sqrt{2} \frac{\sigma_z}{c} \Xi_{0,2} \left(\frac{\sigma_z}{\sqrt{2}}; \omega_0, 0 \right) \quad (4.18)$$

in the Taylor method and

$$X_s = 2 \frac{\sigma_z}{c} \Xi_{0,2} (\sigma_z; \omega_0, 0) \quad (4.19)$$

in the differentiation method. Because the frequency shift in the elastance is 0, it follows from the symmetry in $Z_0^{\parallel}(\omega)$ that X_s is real, and dependent only on the imaginary part of $Z_0^{\parallel}(\omega)$. As indicated above, the Taylor approach yields a good approximation only when the wake function varies slowly across the bunch's z -distribution. In terms of frequency domain quantities, the impedance must be confined to frequencies that are small compared to c/σ_z . If so, the exponential term in Equation (4.2) can be replaced by 1, and $\Xi_{0,2}(\sigma_z; \omega_0, 0)$ will be proportional to σ_z , so that Equations (4.18) and (4.19) should give the same X_s . In the present case, the impedance is not negligible at frequencies of order c/σ_z , so the two approaches do not give the same results. The differentiation method might give a somewhat better prediction, since it requires fewer assumptions.

Note that X_s is a function of σ_z in both cases, so that, strictly speaking, Equation (4.17) is transcendental when we consider σ_{z0} to be known and σ_z to be unknown. An easy way to side-step this complication is to treat σ_z as an independent parameter and solve for σ_{z0} , or, equivalently, σ_z/σ_{z0} .

Calculated values of X_s as a function of σ_z for the Porcupine load impedance predicted by AMOS are shown in Figure 4.3a. Note that the predicted values of X_s are negative, which means, according to Equation (4.17), that the wake function tends to reduce the bunch length. The corresponding values of σ_z/σ_{z0} as a function of σ_{z0} (obtained parametrically for a range of σ_z values) for the CESR-V case are shown in Figure 4.3b. Note that the Taylor method predicts a more dramatic change in bunch length. The relevant régime is $\sigma_{z0} \approx 10$ mm, in which case the Taylor method predicts $\sigma_z \approx 0.987\sigma_{z0}$, *i.e.* a slight decrease in the bunch length due to the wake function. The result is consistent with our premise that the distortion can be treated as a small perturbation. We will ignore the distinction between σ_z and σ_{z0} in the rest of this chapter.

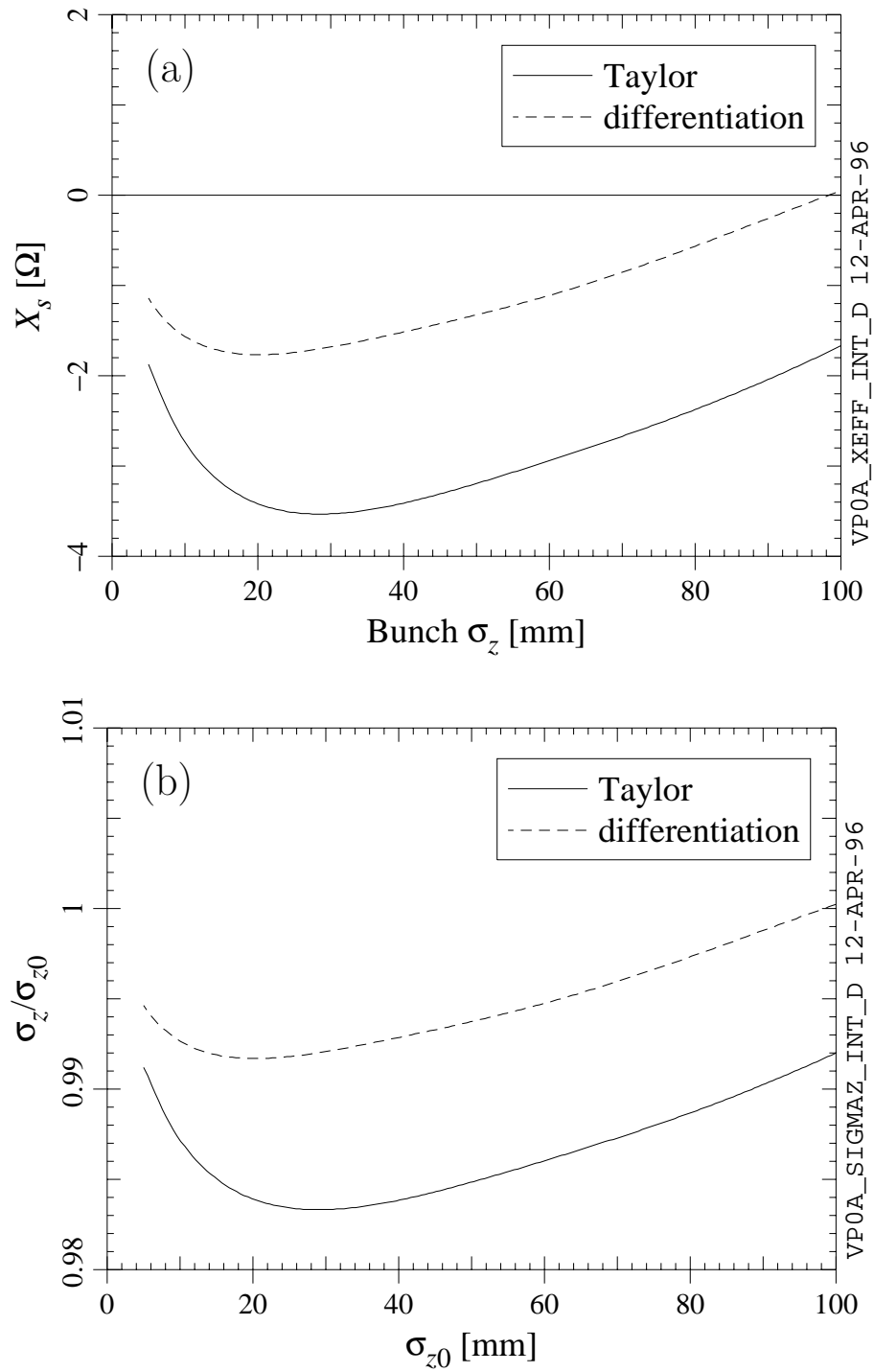


Figure 4.3. Comparison of (a) X_s values and (b) σ_z/σ_{z0} values based on the Taylor method and the differentiation method. The integral formulation for elastance was used in both cases.

Central Tendency

The approximate form of the equation obtained from the first-order term in the Taylor expansion is

$$\bar{z} = \frac{U_0 \sigma_z^2}{\eta C E_0 \sigma_\delta^2} + \frac{I_b}{\sigma_\delta^2 \eta E_0} \frac{\sigma_z^2}{c} k_0^\parallel \left(\frac{\sigma_z}{\sqrt{2}} \right), \quad (4.20)$$

where U_0 is the energy loss per particle per turn due to synchrotron radiation and C is the machine circumference. The analogous equation from the first derivative of the Haüssinski Equation is

$$\bar{z} = \frac{U_0 \sigma_z^2}{\eta C E_0 \sigma_\delta^2} + \frac{I_b}{\sigma_\delta^2 \eta E_0} \frac{\sigma_z^2}{c} k_0^\parallel(\sigma_z). \quad (4.21)$$

In both cases, k_0^\parallel is the loss factor introduced previously. The first term in both equations represents the z shift due to synchrotron radiation; the second term gives the z shift due to the longitudinal wake.

In this case, it is clear that the differentiation method is more general: Equation (4.21) can be obtained from the requirement that the total momentum of the bunch remain constant, which is obviously necessary for a stationary distribution. In the Taylor method, this requirement is only satisfied approximately; as discussed above, the Taylor approach provides a good approximation only when the impedance is confined to frequencies that are small compared to c/σ_z . If so, $k_0^\parallel(\sigma_z) \approx k_0^\parallel(\sigma_z/\sqrt{2}) \approx k_0^\parallel(0)$, and Equations (4.20) and (4.21) should give the same answer. In the present case, the Taylor formula for \bar{z} is not a good approximation.

With the CESR-V parameters and the AMOS value of k_0^\parallel for the Porcupine load (for $\sigma_z = 10$ mm), Equation (4.21) gives us $\bar{z} = 6.19$ mm, with 5.74 mm due to the synchrotron radiation term and 0.45 mm due to the wake term. The contribution from the wake field is thus small compared to the radiation term, and both shifts are small compared to the RF wavelength of 600 mm. Thus, the result is consistent with our premise that the distortion can be treated as a small perturbation, and we were justified in ignoring the non-linearity in the RF voltage. Since the shift produced by the wake field is small compared to σ_z , “thermodynamic” bunch lengthening [63] should not be expected.

Transverse: The “Bananer Effect”

As was pointed out by A. Chao [43], there is a transverse analog to potential well distortion if the beam’s closed orbit is such that it does not pass through the axis of symmetry of the surrounding vacuum chamber. This is the case for CESR-V, since the beams are displaced transversely as they travel through the Porcupine loads. We will now estimate the effect on the beam of this displaced orbit in the loads.

The transverse wake of the displaced bunch produces an additional displacement of the bunch’s centre and a “tilt” in the distribution of particles [64]. The latter is due to the larger transverse kick experienced by particles in the tail of the bunch relative to particles in the head. A tilted distribution is the result when the transverse

damping rate is large compared to the synchrotron frequency. In the present case, however, the opposite is true. We expect, therefore, that individual particles will never reach an equilibrium closed orbit; instead, they will experience a transverse kick that is modulated by their longitudinal oscillation at the synchrotron frequency, which will cause them to oscillate about a shifted closed orbit in the transverse plane. In other words, the longitudinal and transverse motion of the particles are coupled through the dependence of the transverse wake force on the longitudinal position of the particle. Because the transverse oscillations are incoherent, as a whole, the transverse distribution of particles remains a static one. Since the transverse beam size is typically small compared to the longitudinal beam size, coupling of longitudinal motion into transverse motion could adversely affect the luminosity. The closed orbit shift, on the other hand, is probably not as serious, since it can presumably be corrected by adjusting the guide field as the current increases.

To quantify the effects described above, we can do a two-term Taylor series approximation of the transverse wake function. We will ignore chromaticity effects for simplicity. The result is that the normal modes for single-particle motion are no longer purely longitudinal or purely transverse: the betatron motion acquires a small longitudinal component, while the synchrotron motion acquires a small transverse component. Moreover, there is a shift in the mean values of x_\perp and z . In terms of the unperturbed displacement $x_{\perp 0}$, the displacement in the presence of the transverse wake is

$$x_\perp = \left(1 - \frac{\beta_Z^2 Y_0}{1 + \beta_Z^2 Y_0}\right) x_{\perp 0}. \quad (4.22)$$

In the absence of other effects, the ratio of the transverse and longitudinal amplitudes for the synchrotron motion determines the transverse beam size corresponding to a given longitudinal distribution. For our beam with its Gaussian distribution in the longitudinal plane, we can expect a Gaussian distribution in the transverse plane with standard deviation σ_x , where

$$\frac{\sigma_x}{\sigma_z} = \left| \left[\frac{1}{\beta_Z^2} - \left(\frac{\omega_s}{c}\right)^2 \right]^{-1} Y_1 x_\perp \right|. \quad (4.23)$$

In the above formulae, Y_0 and Y_1 are related to the transverse elastance:

$$Y_0 \equiv \frac{-I_b}{cE_0} \Theta_0 \left(\frac{\sigma_z}{\sqrt{2}}, 0; \omega_0, 0 \right) \quad (4.24)$$

$$Y_1 \equiv \frac{2}{i} \frac{I_b}{c\sigma_z E_0} \Theta_1 \left(\frac{\sigma_z}{\sqrt{2}}, 0; \omega_0, 0 \right) \quad (4.25)$$

The above results are applicable when

$$\left[\left(\frac{\omega_\beta}{c}\right)^2 - \left(\frac{\omega_s}{c}\right)^2 \right]^2 \gg 4|\eta| (Y_1 x_\perp)^2 \quad (4.26)$$

Table 4.6. Predictions for the wake-induced transverse orbit shift and transverse beam size for Porcupine loads in CESR-V.

Quantity	AMOS	Analytic
$x_{\perp} - x_{\perp 0}$ [μm]	2.24	1.08
σ_x [μm]	2.39	1.32

and

$$\left(\frac{\omega_s}{c}\right)^2 \left[\left(\frac{\omega_{\beta}}{c}\right)^2 - \left(\frac{\omega_s}{c}\right)^2 \right] \gg |\eta| (Y_1 x_{\perp})^2, \quad (4.27)$$

both of which are good approximations in the present case. The derivation of the formulae is given in a separate report [62]. Note that $\sigma_z/\sqrt{2}$ appears in the elastance arguments, as was the case for the Taylor approach used in the longitudinal case. Note also that, in a realistic machine, x_{\perp} and σ_x will both vary with position along the ring according to the betatron function (although the effect is still a static one in the sense that x_{\perp} and σ_x depend on position but not on time); the above formulae give the worst-case values, since we are assuming the maximum betatron function to be at the loads' location and we are calculating x_{\perp} and σ_x at the same spot.

Applying the above formulae to the case of Porcupine loads in CESR-V, we can estimate the shift in transverse position of the beam due to the Porcupine wake and the transverse beam size produced by coupling through the Porcupine wake. The results are given in Table 4.6. As mentioned previously, AMOS values for Θ_0 are not reliable because of the sensitivity to the impedance at low frequencies. The AMOS value for the closed orbit shift is therefore suspect, so we have included predictions from the analytic Porcupine impedance in Table 4.6, in addition to the AMOS values. In both cases, however, the shift in x_{\perp} is small enough compared to our unperturbed value of 41 mm to be negligible for our purposes. Likewise, since σ_x is typically of the order of 0.3 mm when the betatron function is at its minimum, we do not expect the incoherent transverse oscillations produced by the Porcupine loads to be a significant problem.

4.5 Modes of Oscillation to Linear Order

Longitudinal

In the absence of wake effects, time-dependent solutions of the longitudinal Vlasov equation correspond to normal-mode sinusoidal oscillations of the beam in the longitudinal direction. The angular frequencies of the unperturbed normal modes are $l\omega_{s0}$ for integer l , *i.e.* the normal mode frequencies are integer multiples of the unperturbed synchrotron frequency. The index l describes the azimuthal dependence (or, in action-angle terminology, the angular dependence) of the time-varying disturbance in

longitudinal phase space; the normal modes are sometimes called “azimuthal modes.” The unperturbed normal-mode frequencies do not depend on the radial (action) distribution of the disturbance.

The longitudinal wake produces a current-dependent shift in the frequency of each azimuthal mode; the perturbed motion may have an exponentially growing or decaying amplitude. A time-dependent amplitude can be represented in terms of a complex frequency, whose imaginary part gives the damping rate (with a negative damping rate denoting growth). The wake function splits the radial (action) degeneracy of the unperturbed modes: each azimuthal mode becomes a family of “radial modes,” with a different radial structure in phase space for each family member. By neglecting the coupling between radial modes, an approximate expression can be obtained for the perturbed complex angular frequency $\Omega_{n,l}$ of the n th radial mode (for $n = 0, 1, 2, \dots$) in the l th family:

$$\Omega_{n,l} = l\omega_{s0} + \frac{I_b}{\sigma_\delta E_0} \frac{l \Xi_{0,2|l|+4n}(\sigma_{z0}; \omega_0, l\omega_{s0})}{n!(|l|+n)!} - \frac{I_b}{\sigma_\delta E_0} l \Xi_{0,2}(\sigma_{z0}; \omega_0, 0) . \quad (4.28)$$

The real part of $\Omega_{n,l}$ is the perturbed angular frequency, while the imaginary part is the damping rate (the growth rate is $-\text{Im } \Omega_{n,l}$). In Equation (4.28), the second term is due to the wake field produced by the time-dependent disturbance in the charge distribution. The third term is due to the wake field produced by the stationary, time-independent part of the charge distribution, which is responsible for the static longitudinal effects discussed previously. The latter is usually omitted from the frequency shift analysis; a derivation which excludes the last term is given by A. Chao [43]. A derivation which includes the last term is given in a separate report [62]. We have included only the leading-order contribution from the stationary wake in Equation (4.28); the exact expression is a bit more complicated.

Let us ignore the third term for a moment. As a rule of thumb, both the real and imaginary parts of the second term tend to decrease in magnitude as n increases, because of the presence of n in the denominator and because of the general decrease in the magnitude of $\text{Re } \Xi_{0,j}$ and $\text{Im } \Xi_{0,j}$ as j increases (as can be seen in Figure 4.1 and B.1, however, this decrease with j is not always monotonic). So, in the absence of the stationary wake term, we expect $\Omega_{n,l}$ to be between $\Omega_{0,l}$ and $l\omega_{s0}$. This defines a range of frequencies and growth rates within which the family of radial modes for a given l should lie. The frequency ranges obtained via this prescription for the case of Porcupine loads in CESR-V are shown as a function of current in Figure 4.4a. When we include the stationary wake term, the difference is significant, as can be seen in Figure 4.4b. With the third term included, there is no net shift in the frequency of the $l = 1, n = 0$ mode, as expected in the case of a short-range wake. The $l = 0$ mode is a trivial solution whose frequency remains zero even in the presence of the wake field. In the present case (*i.e.* longitudinal), the shifts for the $-l$ and $+l$ families are equal in magnitude and opposite in sign.

As we have seen, $\Xi_{0,j}$ is real for a short-range wake when j is even, in which case the growth rates obtained via Equation (4.28) are zero. If the wake is not exactly zero after one turn, however, the growth rates will not be exactly zero either. In this case,

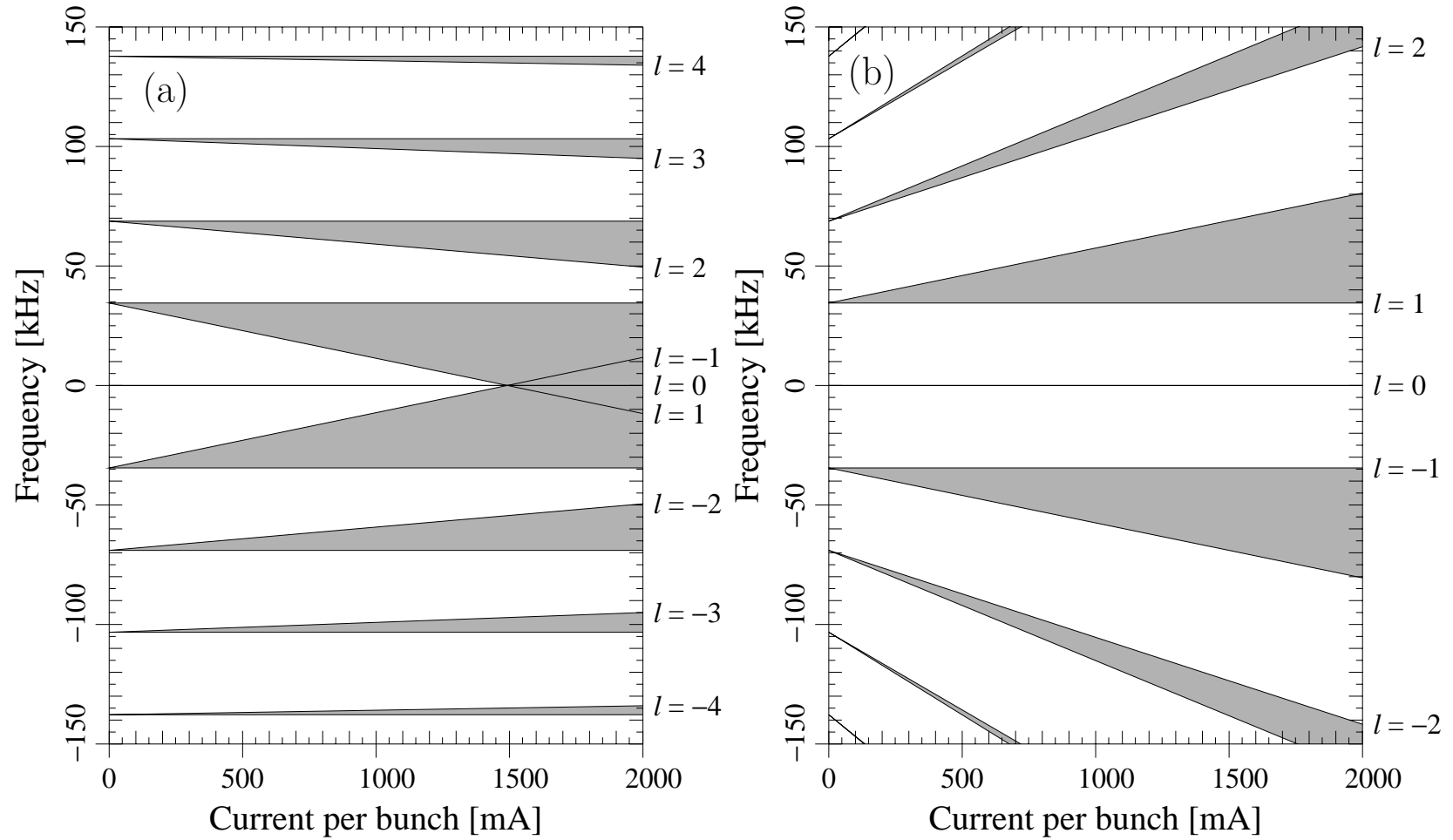


Figure 4.4. Predicted longitudinal mode frequencies for CESR-V with Porcupine loads, (a) without and (b) with the stationary wake term. Each shaded area corresponds to one family of radial modes; the $n = 0$ mode of each family is labelled with the family's l value on the right side. The AMOS coupling impedance and the integral elastance formulation were used.

the number of bunches present (or, more precisely, the spacing between successive bunches) becomes an important consideration. We will hence defer our discussion of longitudinal growth rates until Section 4.8. Note that, because $\Xi_{0,2}(\sigma_z; \omega_0, 0)$ is real, the growth rates are not affected by the stationary wake term.

Transverse

The analysis of the transverse motion of the beam is quite similar to the longitudinal analysis. In the absence of wake effects, time-dependent solutions of the Vlasov equation correspond to dipole oscillations of the beam in the transverse directions. There are normal modes whose angular frequencies are $\omega_\beta + l\omega_{s0}$, where l again describes the azimuthal dependence of the time-varying disturbance in longitudinal phase space. The major difference is that it is a dipole disturbance in the transverse plane whose longitudinal structure is being described. Again, the unperturbed azimuthal modes frequencies do not depend on the radial (action) distribution of the disturbance in longitudinal phase space.

The transverse wake splits each azimuthal mode into a family of radial modes, and produces a complex frequency shift in each radial mode. In the absence of coupling between radial modes, the angular frequency of the n th radial mode in the l th family is approximately

$$\Omega_{n,l} = \omega_\beta + l\omega_{s0} - \frac{\beta_Z I_b}{2E_0} \frac{\Theta_{2|l|+4n}(\sigma_{z0}, \omega_\xi; \omega_0, \omega_\beta + l\omega_{s0})}{n!(|l| + n)!} - \frac{I_b}{\sigma_\delta E_0} l \Xi_{0,2}(\sigma_{z0}; \omega_0, 0) , \quad (4.29)$$

where β_Z is the value of the betatron function at the impedance's location in the case of a localised coupling impedance. The third term is due to the dipole wake produced by the time-dependent disturbance in the dipole moment of the distribution. The fourth term, as before, is the leading-order contribution from the monopole wake produced by the stationary distribution, which is usually omitted from the analysis. Equation (4.29) is derived without the last term by A. Chao [43] and with the last term in a separate report [62].

If we ignore the last term and, as before, assume the radial modes in the l th family fall between $\omega_\beta + l\omega_{s0}$ and $\Omega_{0,l}$, we obtain the result shown in Figure 4.5a for the case of Porcupine loads in CESR-V. When the last term is included, there is a significant shift in all mode families except for the $l = 0$ family, as can be seen in Figure 4.5b. In contrast to the longitudinal case, the $l = 0$ family is no longer a trivial solution. The $-l$ and $+l$ families are still degenerate in the case of a short-range wake, although this is no longer true in the case of a long-range wake (Equation (4.29) has been generalised to apply for both $l > 0$ and $l < 0$). The predictions shown in Figure 4.5 are for motion in the horizontal plane—since we assume the same β_Z and ξ in both planes, the predictions for the vertical plane are the same, except for an overall frequency shift due to the difference between the horizontal and vertical betatron frequencies. Note that we are assuming a worst-case β_Z for both planes, *i.e.* β_Z equal to the largest value in the machine (excluding the interaction region).

Unlike the longitudinal case, the growth rate can be non-zero even in the case of

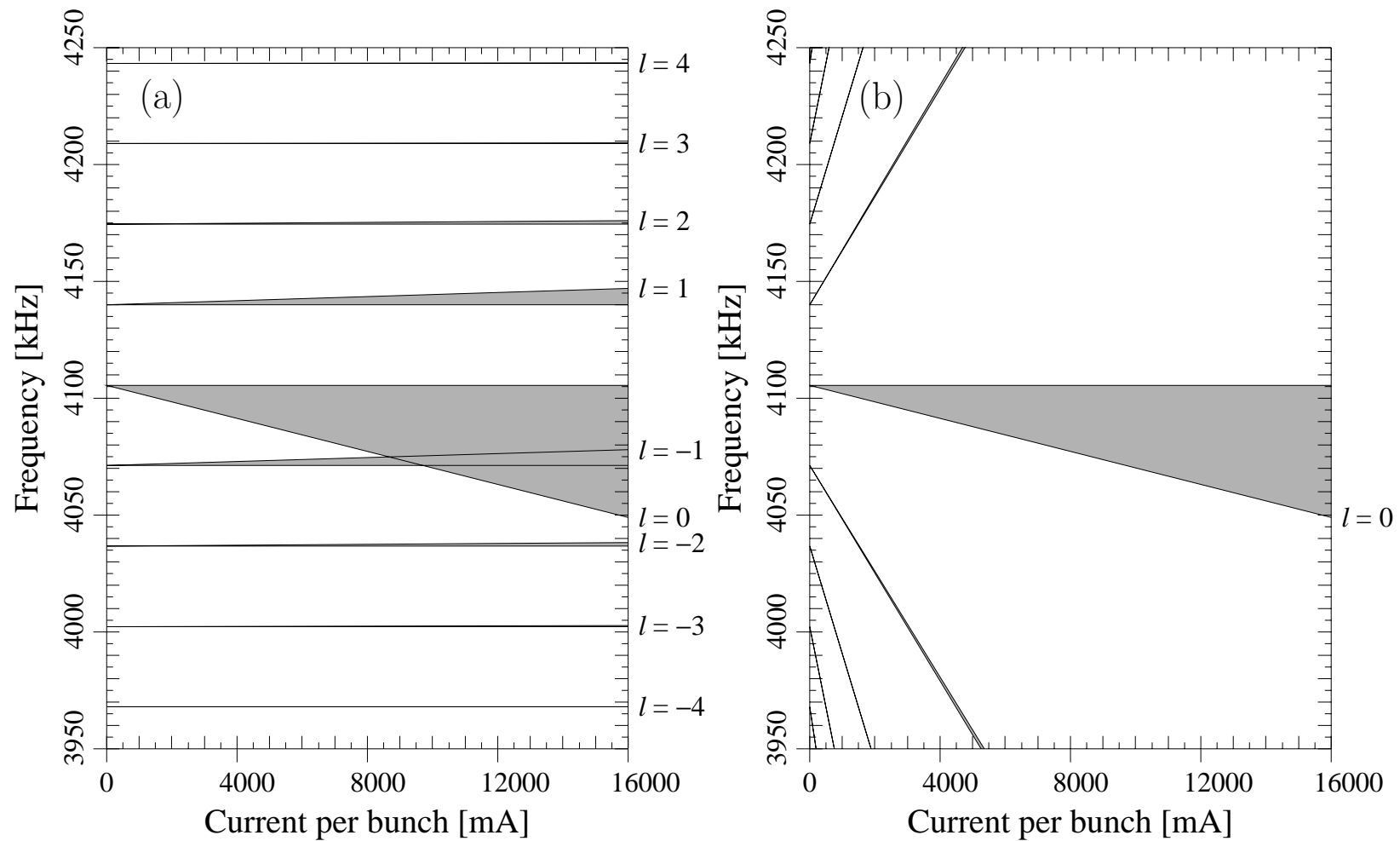


Figure 4.5. Predicted transverse mode frequencies for CESR-V with Porcupine loads, (a) without and (b) with the stationary wake term. Each shaded area corresponds to one family of radial modes; the $n = 0$ mode of each family is labelled with the family's l value on the right side. The AMOS coupling impedance and the integral elastance formulation were used.

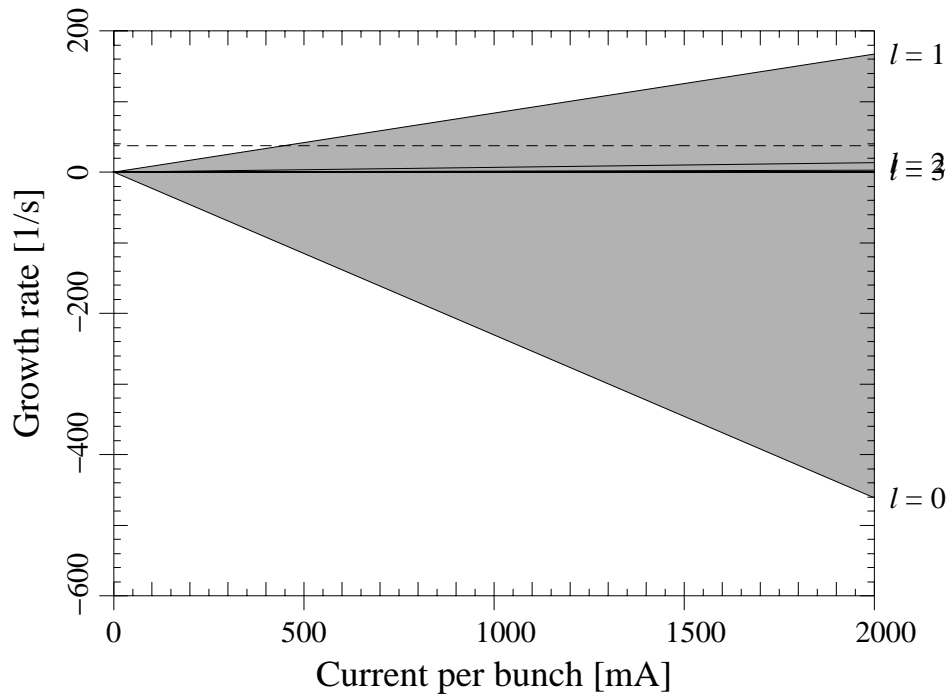


Figure 4.6. Predicted transverse mode growth rates for CESR-V with Porcupine loads. The AMOS coupling impedance and the integral elastance formulation were used.

a short-range wake, provided ω_ξ is non-zero. The growth or damping due to ω_ξ is sometimes called the transverse head-tail effect. The growth rates for the Porcupine load in CESR-V are shown in Figure 4.6 (note the different horizontal scale relative to Figure 4.5). The positive chromaticity produces damping for the $l = 0$ mode, which is the most affected one, and growth for the rest of the modes. These trends would be reversed in the case of negative ξ . The dashed line in Figure 4.6 shows the level at which the growth rate is equal to the horizontal radiation damping rate: we can expect a horizontal head-tail instability for the $l = 1$ mode when the current per bunch reaches about 400 mA. The same behaviour can be expected in the vertical plane (albeit at a slightly higher current, because of the slightly larger radiation damping rate). As in the longitudinal case, the stationary wake term does not affect the predicted growth rates.

As mentioned in Section 4.2, Θ_0 is sensitive to the low-frequency behaviour of $Z_1^{\parallel}(\omega)$, and our Θ_0 value from AMOS is therefore of dubious validity. We will obtain a better estimate for the frequency shift and growth rate for the $l = 0$ mode in Section 4.8.

4.6 Mode Coupling

Longitudinal

In the previous section, we ignored the coupling between modes in different azimuthal families, and obtained complex frequency shifts that increased linearly with the bunch current. If the frequencies of two modes with different l 's get close enough to each other, we can expect the coupling between the modes to become important, in which case the shifts will become non-linear. To simplify the discussion, we will ignore the contribution from the stationary wake. The uncoupled frequency shifts are then as shown in Figure 4.4a in the previous section. We see that the $n = 0$ modes in the $l = 1$ and $l = -1$ families are the first to converge, so we can hope to get an approximate picture of the effect of mode coupling by considering the coupling between these two modes only (the $l = 0$ mode does not couple to any other families). As discussed by A. Chao [43], if we consider only the $n = 0$ mode in each family, but include coupling between different l 's, the mode frequencies are the solutions to the following determinant equation:

$$\left| \left(\frac{\Omega}{\omega_{s0}} - l \right) \mathbf{I} - \mathbf{K} \right| = 0, \quad (4.30)$$

where \mathbf{I} is the identity matrix and \mathbf{K} is a matrix whose elements are given by

$$K_{l,l'} = \frac{I_b}{\omega_{s0}\sigma_\delta E_0} \frac{l(-1)^l i^{|l|+|l'|} \Xi_{0,|l|+|l'|}(\sigma_{z0}; \omega_0, l\omega_{s0})}{\sqrt{|l|!|l'|!}}. \quad (4.31)$$

In general, \mathbf{I} and \mathbf{K} have an infinite number of elements. If we consider only the coupling between two azimuthal modes, l and l' , however, there are only two non-zero off-diagonal elements, and Equation (4.31) reduces to a 2 by 2 determinant, which is easily solved for the two possible values of the mode frequency Ω :

$$\frac{\Omega}{\omega_{s0}} = \frac{(l + K_{l,l}) + (l' + K_{l',l'})}{2} \pm \sqrt{\left[\frac{(l + K_{l,l}) - (l' + K_{l',l'})}{2} \right]^2 + K_{l,l'} K_{l',l}}. \quad (4.32)$$

If we set $l = 1$ and $l' = -1$, and make use of the fact that $K_{l,-l'} = K_{l,l'} = -K_{-l,l'}$, our solutions can be written as

$$\frac{\Omega}{\omega_{s0}} = \pm \sqrt{1 + \frac{2I_b}{\omega_{s0}\sigma_\delta E_0} \Xi_{0,2}(\sigma_{z0}; \omega_0, \omega_{s0})}, \quad (4.33)$$

which reduces to the correct result to linear order as $I_b \rightarrow 0$.

The frequencies and growth rates obtained via Equation (4.33) for the $n = 0$, $l = \pm 1$ modes in the case of the Porcupine load in CESR-V are shown as a function of current in Figure 4.7. At low current, the predictions are consistent with the linear frequency shifts of Figure 4.4a; as the modes get closer together, the frequency shift increases non-linearly. The coupling causes the frequencies to converge at a current half as large as the current at which they crossed in the uncoupled case.

As soon as the frequencies are equal, the growth rate of one mode increases rapidly with current (while the damping rate of the other mode increases commensurably). Figure 4.8 shows a close-up of the growth rate as the modes converge. As can be seen, the growth rate of the unstable mode rapidly exceeds the radiation damping rate (indicated by the dashed line) once the frequencies have converged. Thus, we expect a longitudinal mode coupling instability for the $l = 1$ mode when the current per bunch reaches about 750 mA.

So far, we have ignored the contribution from the stationary wake. When the latter is included, none of the first few modes cross in the uncoupled case, as can be seen in Figure 4.4b. We can speculate that the mode coupling instability will tend to be inhibited by the stationary wake term. A quantitative analysis would be more difficult: although a determinant equation that includes the stationary contribution can be derived, the coupling elements tend to vanish to leading order, so that a meaningful calculation would probably require a more rigorous treatment of radial modes, *i.e.* the inclusion of more than one radial mode and of coupling between radial modes.

Transverse

The analogy between longitudinal and transverse mode coupling is quite close. If we ignore the stationary wake term, the uncoupled transverse mode frequency shifts are as shown in Figure 4.5a in Section 4.5. The $n = 0$ modes in the $l = 0$ and $l = -1$ families are the first to converge, so we want to estimate the effect by considering the coupling between this pair of modes. If we consider only the $n = 0$ mode in each family, the coupled mode frequencies are given via [43]

$$\left| \left(\frac{\Omega - \omega_\beta}{\omega_{s0}} - l \right) \mathbf{I} - \mathbf{K} \right| = 0. \quad (4.34)$$

In the present case, the matrix \mathbf{K} has elements

$$K_{l,l'} = -\frac{I_b \beta_Z}{2\omega_{s0} E_0} \frac{(-1)^l i^{|l|+|l'|} \Theta_{|l|+|l'|}(\sigma_{z0}, \omega_\xi; \omega_0, \omega_\beta + l\omega_{s0})}{\sqrt{|l|!|l'|!}}. \quad (4.35)$$

If we consider only the coupling between two azimuthal modes, l and l' , we can solve for the two possible frequencies:

$$\frac{\Omega - \omega_\beta}{\omega_{s0}} = \frac{(l + K_{l,l}) + (l' + K_{l',l'})}{2} \pm \sqrt{\left[\frac{(l + K_{l,l}) - (l' + K_{l',l'})}{2} \right]^2 + K_{l,l'} K_{l',l}}. \quad (4.36)$$

We want to set $l = 0$ and $l' = -1$. Equation (4.36) does not reduce to the simplicity of Equation (4.33), but it is still easily evaluated. Like its longitudinal counterpart, Equation (4.36) reduces to the correct result to linear order for small I_b .

The frequencies and growth rates obtained via Equation (4.36) for the $l = 0$ and $l = -1$ modes in the case of the Porcupine load in CESR-V are shown in Figure 4.9.

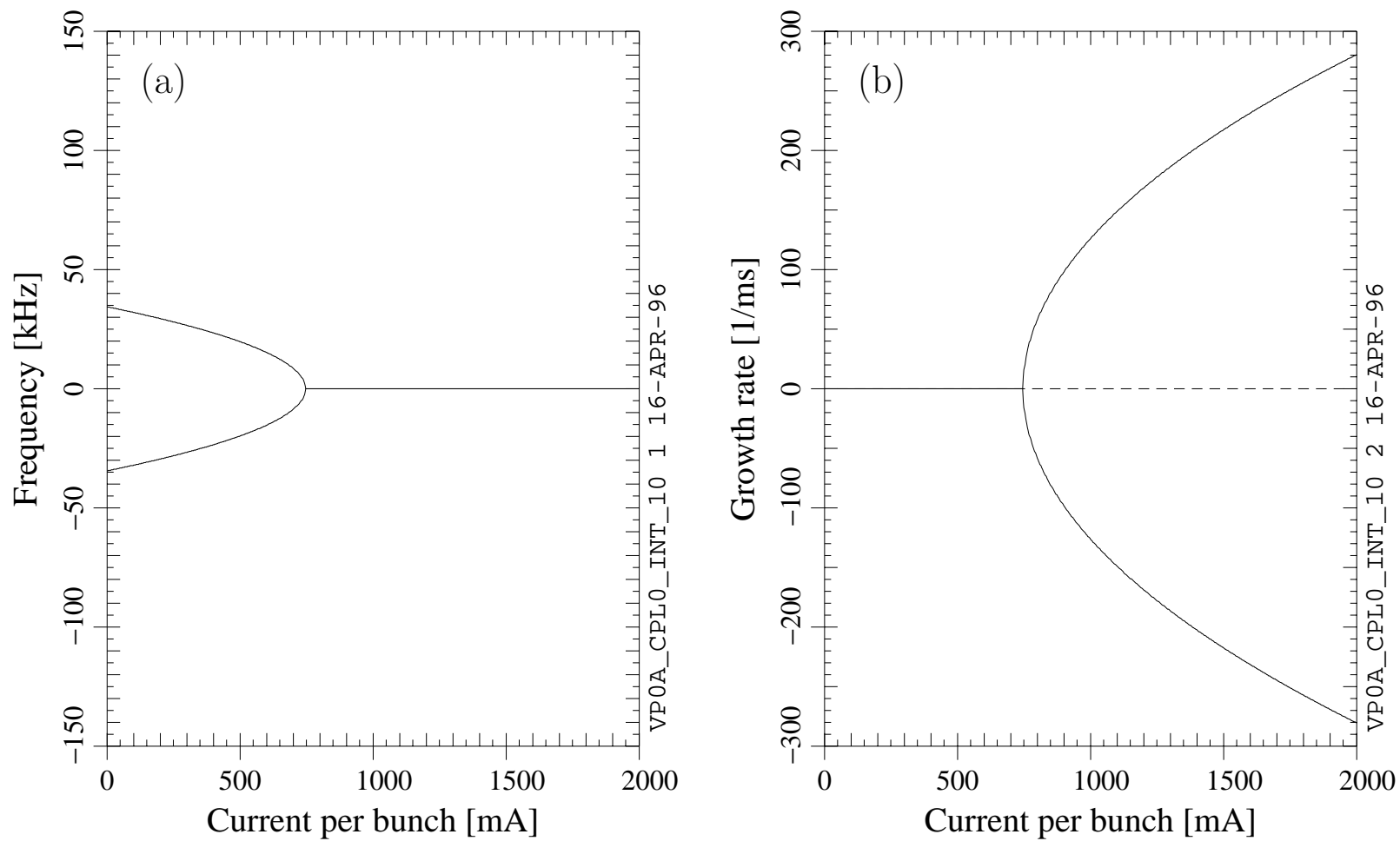


Figure 4.7. Predicted (a) frequencies and (b) growth rates for the longitudinal $l = \pm 1$ modes, with coupling, for CESR-V with Porcupine loads. The AMOS coupling impedance and the integral elastance formulation were used.

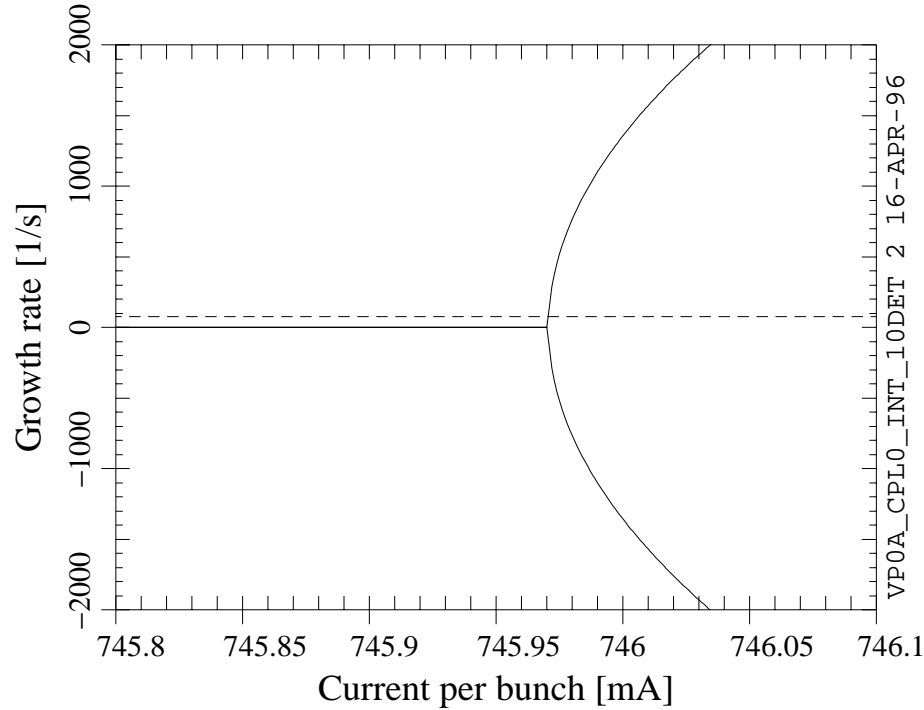


Figure 4.8. Detail of the predicted growth rates for the longitudinal $l = \pm 1$ modes, with coupling.

At low current, the predictions are consistent with Figures 4.5a and 4.6. As the current increases, the behaviour is qualitatively similar to the longitudinal case: the frequencies converge faster than in the uncoupled case, and the growth rate of the unstable mode increases rapidly once the frequencies have converged. Again, the modes converge at a current about half as large as in the linear case. The chromaticity, as discussed previously, produces a linearly increasing growth rate in one mode (and a linearly increasing damping rate in the other mode) below currents at which the coupling dominates. As can be seen in the close-up in Figure 4.10, the unstable mode exceeds the radiation damping rate at about the same current as it did in the uncoupled case (Figure 4.6). Thus, for our choice of ξ , the head-tail effect produces an instability long before the transverse mode coupling becomes important. The chromaticity also produces a slight frequency split between the modes above the mode coupling threshold, as the observant reader may notice in Figure 4.9a.

Again, when we include the stationary wake, none of the first few modes cross in the uncoupled case, as is evident from Figure 4.5b. As in the longitudinal case, a quantitative analysis that includes the stationary wake would be more difficult.

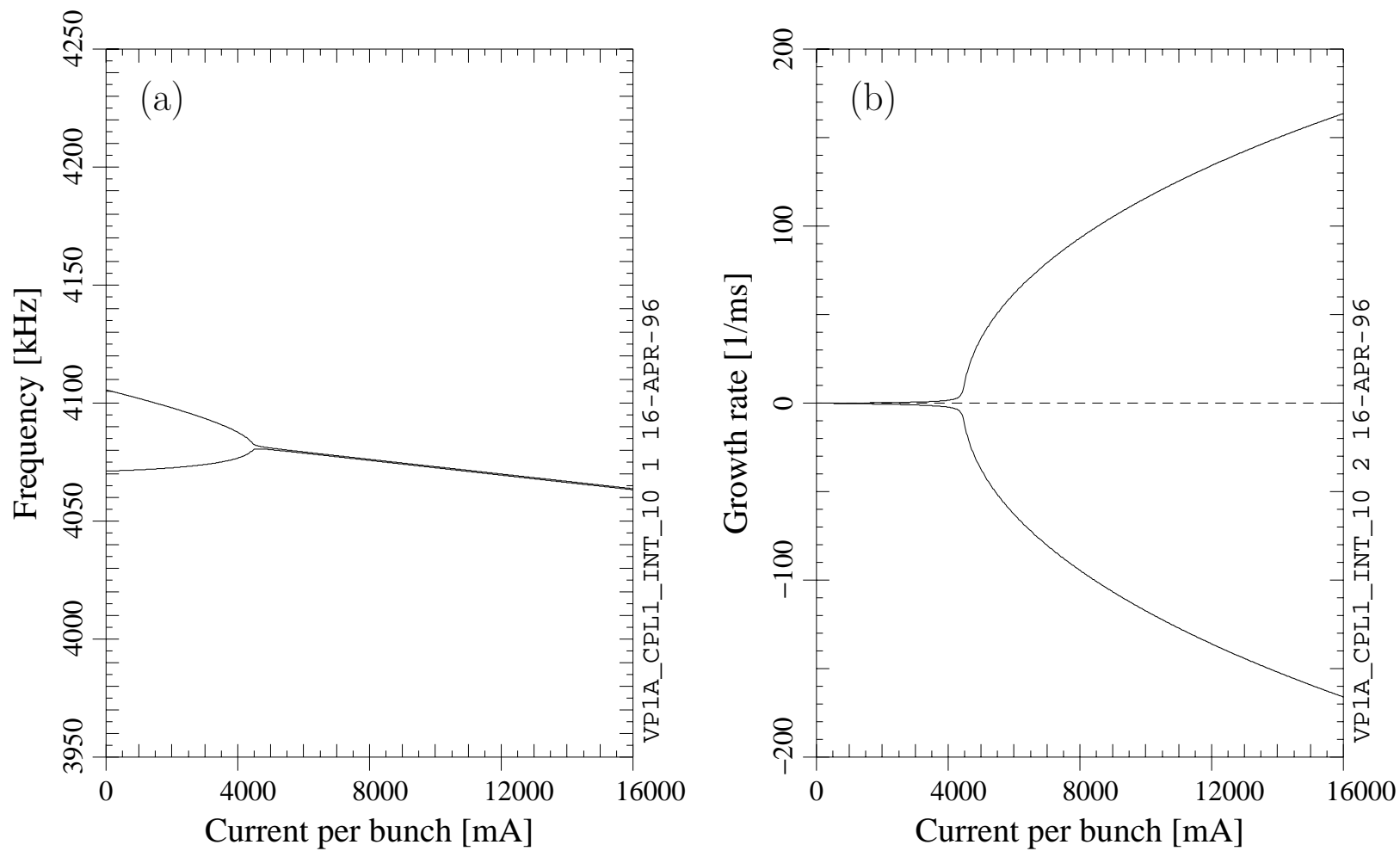


Figure 4.9. Predicted (a) frequencies and (b) growth rates for the transverse $l = 0$ and $l = -1$ modes, with coupling, for CESR-V with Porcupine loads. The AMOS coupling impedance and the integral elastance formulation were used.

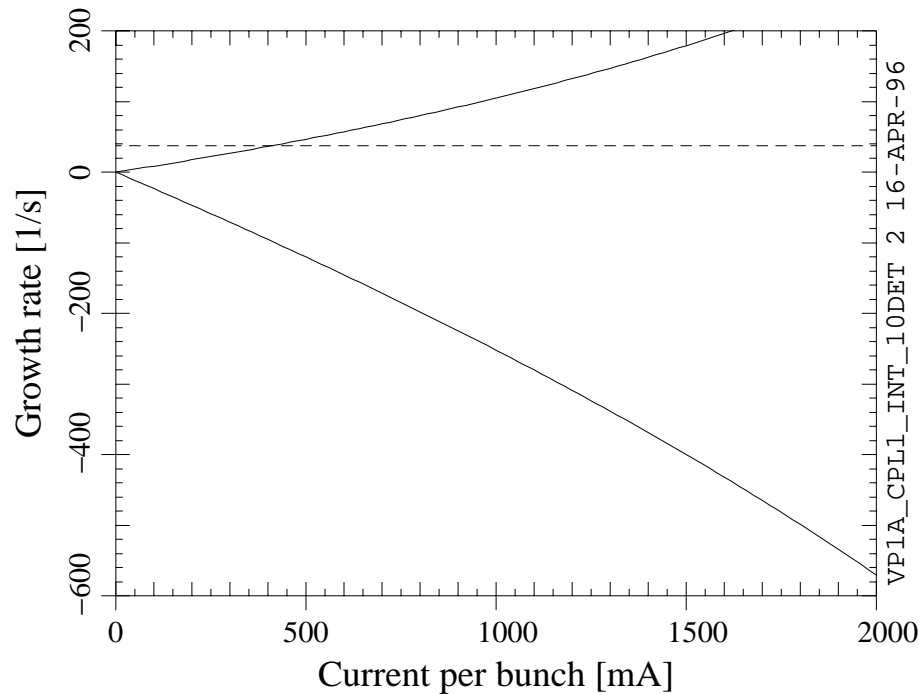


Figure 4.10. Detail of the predicted growth rates for the transverse $l = 0$ and $l = -1$ modes, with coupling.

4.7 Microwave Instability

Mode coupling, as discussed in the previous section, is one model for instabilities due to non-linear effects at high beam currents. There is, however, an alternate approach, the “microwave instability” model. The original inspiration for this model came from the instability in unbunched beams that carries the same name. The analogy between bunched-beam instabilities and the microwave instability in unbunched beams was first made by D. Boussard [65]. The mode coupling instability and the microwave instability should probably not be considered to be two different instability mechanisms; it is more likely that they are two different models for the same instability mechanism, each model having its own idealisations and approximations. Because the approaches are different, the two models can be expected to complement each other to some degree. As we will see, the microwave instability model will give us a sufficient condition for stability, without a guarantee that the beam is unstable when that condition is not satisfied.

The analysis of the microwave instability begins, as usual, with the Vlasov equation. The longitudinal and transverse cases have been worked out by J. Wang & C. Pellegrini [66] and R. Ruth & J. Wang [67], respectively. Instead of expanding the Vlasov equation in azimuthal and radial modes and treating the impedance as a perturbation which produces a complex frequency shift for each mode, one postulates that an unstable solution to the Vlasov equation exists, and that this unstable solu-

tion has a growth rate that is of order ω_s or larger. One then derives a self-consistency condition: if the self-consistency condition is satisfied, the unstable solution exists; otherwise, the beam is stable. As in the analysis of mode coupling, the contribution from the stationary wake is ignored.

The exact self-consistency condition is transcendental. A simpler inequality can be derived from it, however, with the disadvantage that the result is a sufficient condition for stability, as opposed to a necessary and sufficient one.

At this point, it is customary to specialise to the case of a $Q = 1$ resonator impedance and consider frequencies above the resonant frequency (usually referred to as the cutoff frequency, for reasons that we need not get into), in order to further simplify the inequality. This is the approach followed by Wang and his colleagues [66, 67]. However, by making use of the Hadamard Theorem [68], it is possible to obtain an analogous result that is applicable to an arbitrary impedance. In either case, the result is a sufficient condition for stability which takes the form

$$I_b \leq I_{th} , \quad (4.37)$$

where I_{th} is the threshold current for the microwave instability.

The threshold current is a functional of the coupling impedance and the bunch's frequency spectrum. In this complementary model, the functional takes a form that is somewhat different from the effective elastance. Let us introduce effective microwave impedances:

$$\Lambda_0(\sigma_z, \omega_\Delta; \omega_0) \equiv \frac{1}{2\pi} \omega_0 \sum_{p=-\infty}^{\infty} \left| \frac{Z_0^\parallel(p\omega_0 - \omega_\Delta)}{p\omega_0 - \omega_\Delta} \right| \exp\left(-\frac{p^2 \omega_0^2 \sigma_z^2}{2c^2}\right) \quad (4.38)$$

$$\Lambda_1(\sigma_z, \omega_\Delta; \omega_0) \equiv \frac{1}{2\pi} \sigma_z \omega_0 \sum_{p=-\infty}^{\infty} \left| \frac{Z_1^\parallel(p\omega_0 - \omega_\Delta)}{p\omega_0 - \omega_\Delta} \right| \exp\left(-\frac{p^2 \omega_0^2 \sigma_z^2}{2c^2}\right) . \quad (4.39)$$

We have ignored chromatic effects in formulating Equation (4.39). The dimensions are impedance for Λ_0 and impedance per unit length for Λ_1 . Note that Λ_0 and Λ_1 are functionals of the bunch's frequency spectrum, while the elastance depends on its square. Because of the division by $p\omega_0 - \omega_\Delta$, the effective microwave impedance tends to be dominated by the low-frequency behaviour of $Z_0^\parallel(\omega)$ and $Z_1^\parallel(\omega)$, which is usually inductive (which motivates us to use the symbol Λ). As with the elastance, an integral formulation of Equations (4.38) and (4.39) is possible when the wake function has a short range, in which case Λ_0 and Λ_1 are independent of ω_0 (indicated by the semi-colon in the arguments list).

The threshold current can be expressed in terms of the effective microwave impedances:

$$I_{th} = \frac{\eta \sigma_\delta^2 E_0}{\Lambda_0(\sigma_z, j\omega_0; \omega_0)} \quad (4.40)$$

$$I_{th} = \frac{\eta \sigma_\delta E_0}{\beta_Z \Lambda_1(\sigma_z, j\omega_0 - \omega_\beta; \omega_0)} . \quad (4.41)$$

Equations (4.40) and (4.41), along with (4.38) and (4.39), give us approximate longitudinal and transverse current thresholds for the microwave instability. They are derived in a separate report [62]. In Equations (4.40) and (4.41), j can be any integer; the value of j that minimises I_{th} is the one that is relevant for our needs. We will be content to find the values of ω_Δ that maximise Λ_0 and Λ_1 .

The problem is most straightforward in the integral formulation: we need to maximise the integral of the product of two functions of ω . The functions in question are shown in Figure 4.11 for the case of a Porcupine load in in CESR-V. As can be seen, $|Z_0^\parallel(\omega)/\omega|$ and $|Z_1^\parallel(\omega)/\omega|$ have sharp peaks at $\omega = 0$, while the bunch spectrum has a broad peak there. The analytically predicted coupling impedance is shown in Figure 4.11; in the AMOS calculation, the frequency step is 24.4 MHz, which, as can be judged from the close-ups of Figure 4.12, is not small enough for a good representation of the sharp peak (in the analytic calculation, a step size of 0.1 MHz was used for the lowest frequency range, to wit from 0.3 MHz to 20 MHz). We will hence make an exception in the case of the microwave instability, and use the analytically-calculated impedance instead of the AMOS impedance. Note that the same argument applies to $\Xi_{0,0}$ and Θ_0 .

In light of Figure 4.11, we expect a broad maximum in Λ_0 and Λ_1 for ω_Δ near 0. And, as can be seen in Figure 4.13, this is indeed what we find for Λ_0 . Although it is easier to predict the dependence on ω_Δ under the integral formulation, the sum formulation gives the same dependence, as evident in Figure 4.13. The same statements apply to Λ_1 . We conclude that $\omega_\Delta = 0$ is the right choice in the Porcupine case. The corresponding threshold currents are given in Table 4.7. The sum and integral formulations give reasonably consistent answers. The thresholds are significantly lower than what we expect from the mode coupling model. However, since $I_b \leq I_{th}$ is merely a sufficient condition for stability, the two models do not necessarily contradict each other.

A different formula for the longitudinal microwave instability threshold has been given by M. Zisman [69]. His threshold current can be expressed in terms of the effective monopole elastance we introduced in Section 4.2:

$$I_{th} = \frac{\eta\sigma_\delta^2 E_0}{\sqrt{2}\frac{\sigma_z}{c} |\Xi_{0,0}(\sigma_z; \omega_0; 0)|}. \quad (4.42)$$

As was the case for Λ_0 , $\Xi_{0,0}$ is sensitive to the low-frequency behaviour of $Z_0^\parallel(\omega)$, so we must use the analytically-predicted coupling impedance instead of the AMOS impedance. Threshold currents obtained from the Zisman formula are also given in Table 4.7. They are significantly higher than the thresholds obtained via Λ_0 . Again, since Λ_0 only gives a sufficient condition, a contradiction cannot be inferred.

4.8 Multi-Bunch Effects

So far, we have considered only the effect of a bunch's wake on itself. In this section, we will examine multi-bunch effects, and we will see that, in the absence of head-

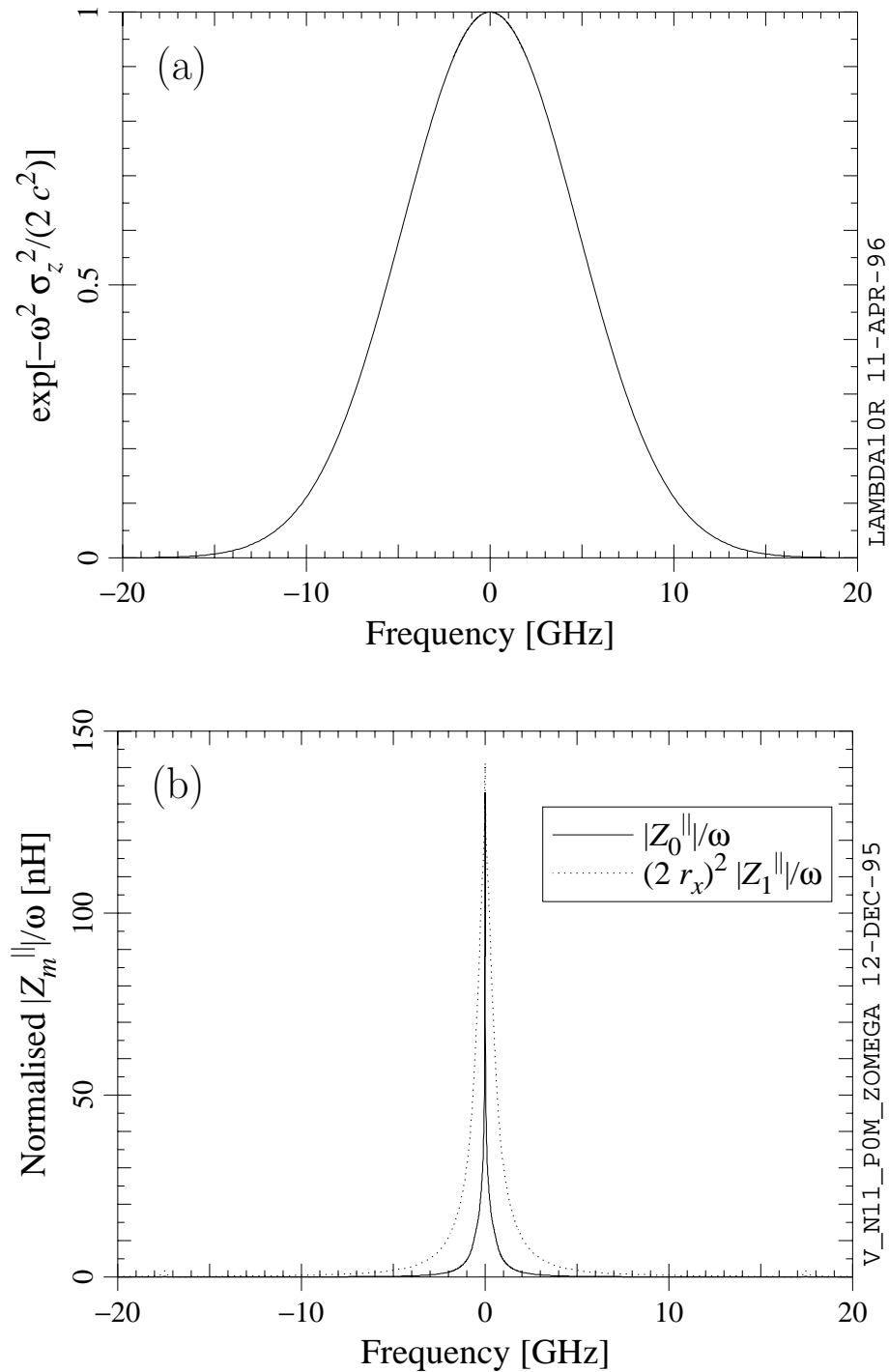


Figure 4.11. (a) Frequency spectrum for a bunch with $\sigma_z = 10$ mm. (b) Dependence of $|Z_0^{\parallel}(\omega)/\omega|$ and $|Z_1^{\parallel}(\omega)/\omega|$ on frequency in the case of the analytic Porcupine impedance; the dipole impedance is normalised by multiplying by $(2r_x)^2$ (see Table 3.1).

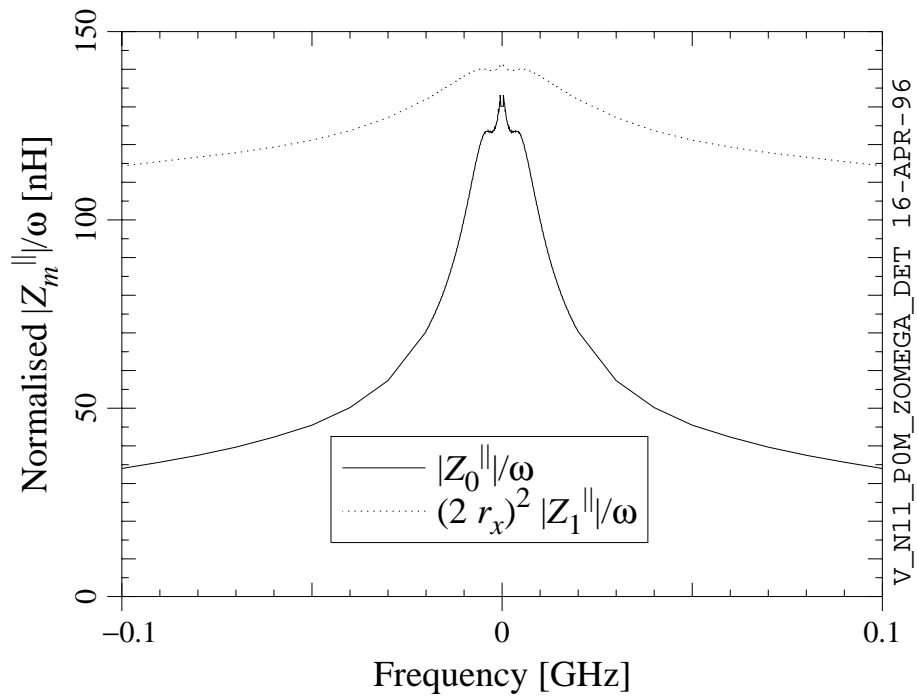


Figure 4.12. Detail of the dependence of $|Z_0^{\parallel}(\omega)/\omega|$ and $|Z_1^{\parallel}(\omega)/\omega|$ on frequency.

Table 4.7. Predicted microwave instability threshold currents due to Porcupine loads in CESR-V. The values given are based on the analytically-calculated Porcupine impedance with $\omega_{\Delta} = 0$.

Direction	Source	I_{th} [mA]	
		sum	integral
longitudinal	Λ_0	27.09	27.06
transverse	Λ_1	1228.7	1228.3
longitudinal	Zisman formula	234.9	232.8

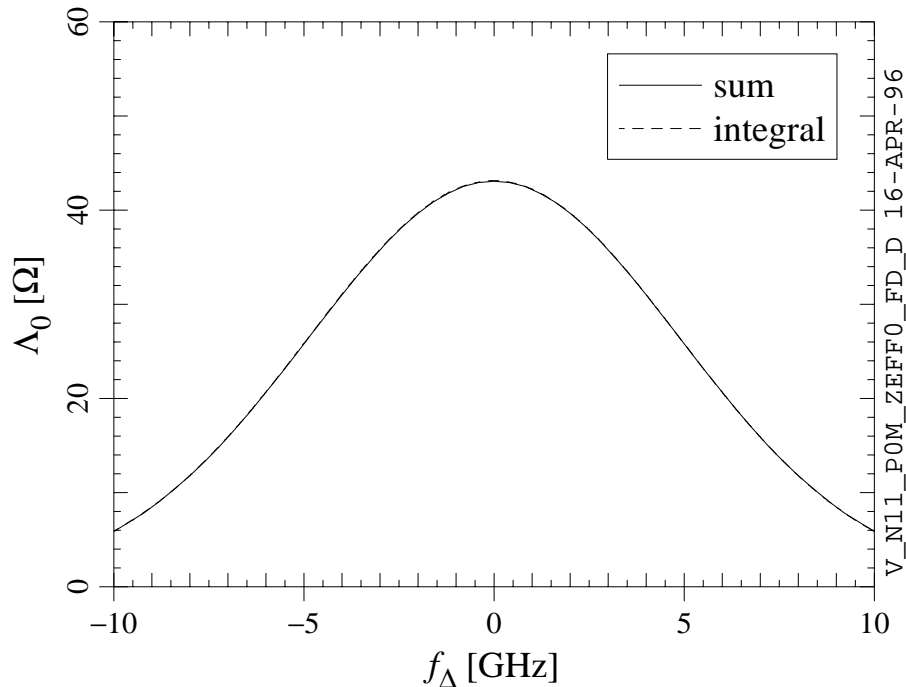


Figure 4.13. Dependence of the effective monopole microwave impedance of the Porcupine load on the frequency shift ($f_\Delta \equiv \omega_\Delta/(2\pi)$). Effective impedances obtained via both a summation and an integral of the analytic coupling impedance are shown.

tail effects, the multi-bunch effects determine the growth rates of modes of beam oscillation.

We saw in Section 4.5 that the longitudinal growth rates are zero in the single-bunch case if the wake function decays to zero within one turn. In practice, we can expect the wake fields to decay very rapidly in a low- Q device, but we should not expect them to be exactly zero after one turn, or by the time the next bunch arrives. In such a situation, the time between the arrival of successive bunches determines the growth rates, and we must account for the effect of one bunch's wake field on the next bunch.

The above arguments also apply to the transverse growth rates if $\xi = 0$. With a non-zero chromaticity, however, the single-pass growth rates are non-zero due to the transverse head-tail effect.⁵ We will see that the latter dominates the picture in the case of $l > 0$. As mentioned previously, however, for $l = 0$, the strong dependence of $Z_1^\parallel(\omega)/\omega$ on ω near $\omega = 0$ requires more careful attention; as we will see, this will affect the growth rate of the $l = 0$ mode significantly. From a time domain

⁵The same can be said in the longitudinal case if the “longitudinal chromaticity,” *i.e.* the dependence of η on energy, is included. However, longitudinal chromaticity generally has a much smaller effect on the beam's motion, so we will not include it in our analysis. It is presumably the dominant growth mechanism in the short-range wake limit, however.

point of view, this result is due to the contribution to the wake function from very low frequencies (note that, for a resonance of given Q , the decay time of the field increases as the frequency decreases).

The inclusion of multiple bunches into the complex frequency shift analysis is discussed by A. Chao [43]. We will consider the case of M bunches, with uniform spacing between bunches and the same charge per bunch for each. With M bunches, each single-bunch mode of beam oscillation splits into a family of M multi-bunch modes. Each mode in the family can be characterised by an integer s ; the phase shift between successive bunches is $2\pi s/M$. To avoid ambiguity, we will require $0 \leq s \leq M - 1$. One mode of oscillation is now identified by three indices: n , l , and s . In the longitudinal case, we get the complex angular frequency shift $\Omega_{n,l,s}$ for a multi-bunch mode by replacing $\Xi_{0,j}(\sigma_{z0}; \omega_0, l\omega_{s0})$ with $\Xi_{0,j}(\sigma_{z0}; M\omega_0, l\omega_{s0} + s\omega_0)$ in the formulae of Section 4.5. In the transverse case, likewise, we replace $\Theta_j(\sigma_{z0}, \omega_\xi; \omega_0, l\omega_{s0})$ with $\Theta_j(\sigma_{z0}, \omega_\xi; M\omega_0, l\omega_{s0} + s\omega_0)$. In this section, we will consider only the $n = 0$ radial mode. If the wake has a short range, the effective elastances are independent of s in the limit, and are the same for the multi-bunch, single-bunch, and single-pass cases. If the wake has a long range, on the other hand, the frequency shift and growth rates will generally differ for the single-pass case, and depend on s .

Figure 4.14 shows the imaginary part of $\Xi_{0,j}(\sigma_{z0}; M\omega_0, l\omega_{s0} + s\omega_0)$ for a Porcupine load as a function of s for the first few even j 's, which determines the growth rates for the first few longitudinal modes. We have used the AMOS Porcupine impedance and the CESR-V values for σ_{z0} , ω_0 , and ω_{s0} and have set $l = j/2$. Although s is an integer, we can consider it to be a continuously varying parameter as we interpret Figure 4.14. The symmetry with respect to ω of the real and imaginary parts of $Z_0^{\parallel}(\omega)$ accounts for some of the features: since the multi-bunch elastance is a sum over harmonics of $M\omega_0$ with a shift of $l\omega_{s0} + s\omega_0$, we should have $\text{Im } \Xi_{0,j} = 0$ for j even when $l\omega_{s0} + s\omega_0 = 0$. Because $l\omega_{s0}/\omega_0 < 1$, we expect $\text{Im } \Xi_{0,j} = 0$ between $s = 0$ and $s = 1$. We also expect the same values for $s \rightarrow M$ as for $s = 0$. These expectations are consistent with Figure 4.14. In addition, the symmetry requires $\text{Im } \Xi_{0,j} = 0$ for j even when $l\omega_{s0} + s\omega_0 = M/2$, with opposite signs on either side of this crossing point, which accounts for the zeros near $s = 92$. The transverse case is similar, although the additional betatron frequency shift in the revolution harmonics shifts the zeros by ω_β/ω_0 , *i.e.* by about 10 in our case. Moreover, the head-tail effect shifts the average value of Θ_j .

There is a family of multi-bunch growth rates for each l . The maximum and minimum growth rates per unit current for each longitudinal family are given in Table 4.8 for the case of AMOS Porcupine loads in CESR-V. As expected from Figure 4.14, the minima and maxima are opposite in sign and approximately equal in magnitude. The fastest growth occurs for the $l = 1$ mode; the corresponding growth rate for $I_b = 10.93$ mA is 0.73 s^{-1} , which is about a factor of 100 smaller than the longitudinal radiation damping rate. The corresponding multi-bunch frequency shifts are not very different from the single-pass frequency shifts calculated previously (Figure 4.4): they differ by 0.1% or less.

In the transverse case, the $l = 0$ mode can be significantly influenced by multi-

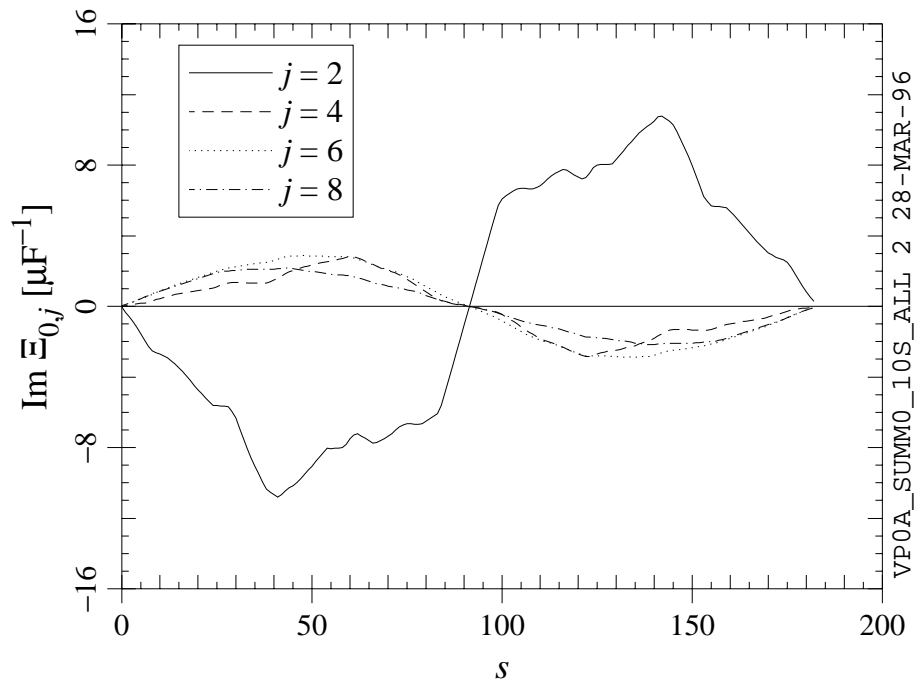


Figure 4.14. The imaginary part of the effective multi-bunch monopole elastance as a function of the multi-bunch mode index s for a few even values of j . The values are based on the AMOS prediction for the monopole Porcupine impedance with $M = 183$.

bunch effects because of the low-frequency behaviour of $Z_1^\perp(\omega)$. (Note, however, that the predicted Porcupine $Z_1^\perp(\omega)$ remains finite as $\omega \rightarrow 0$. This is in contrast to the resistive wall $Z_1^\perp(\omega)$ for a wall of infinite thickness, but is consistent with the case of a resistive wall of finite thickness [43].) As mentioned in the previous section, AMOS does not provide a good prediction of the impedance at low frequencies because of the large step size; to get a meaningful result, we must use the analytically-calculated impedance. The single-pass and multi-bunch predictions based on the analytic Porcupine impedance for the $l = 0$ mode are compared in Table 4.9. As can be seen, the multi-bunch frequency shifts split at the 2% level. The splitting in growth rates is more significant: while the single-pass growth rate is negative (*i.e.* the mode is damped), the maximum multi-bunch growth rate is positive. For $I_b = 10.93$ mA, the maximum growth rate is 0.56 s^{-1} , which is about a factor of 65 smaller than the transverse radiation damping rate. Note that the positive chromaticity still provides a reduction in the growth rates, although the largest growth rate is positive when the multi-bunch effects are included. There is also a multi-bunch correction to the single-pass frequency shifts and growth rates for $l > 0$ (Figures 4.5 and 4.6); the multi-bunch frequency shifts differ by up to 0.2%, while the multi-bunch growth rates differ by up to 4% (using AMOS results for both cases).

The multi-bunch correction to the frequency shifts and growth rates is due to incomplete cancellation between the impedance at positive and negative ω 's. Multi-

Table 4.8. Predicted multi-bunch longitudinal growth rates per unit current per bunch for Porcupine loads in CESR-V. The AMOS impedance was used.

l	(Growth rate)/ I_b [s ⁻¹ A ⁻¹]	
	minimum	maximum
1	-66.64	66.84
2	-17.53	17.54
3	-8.90	8.91
4	-2.24	2.24

Table 4.9. Predicted multi-bunch transverse $l = 0$ frequency shifts and growth rates per unit current per bunch for Porcupine loads in CESR-V. The analytic impedance was used.

Item	Single-pass	Multi-bunch	
		minimum	maximum
(Frequency shift)/ I_b [kHz/A]	-1.902	-1.871	-1.935
(Growth rate)/ I_b [s ⁻¹ A ⁻¹]	-140	-331	51

Table 4.10. Predicted values of the current per bunch at the threshold for various instabilities produced by Porcupine loads in CESR-V.

Instability	I_b at threshold [mA]
Single-bunch transverse oscillation	440
Longitudinal mode coupling	750
Transverse mode coupling	~ 4000
Longitudinal microwave	≥ 27
Transverse microwave	≥ 1230
Multi-bunch longitudinal oscillation	1150
Multi-bunch transverse oscillation	730

bunch effects thus depend sensitively on the detailed dependence of $Z_m^{\parallel}(\omega)$ on ω . As a result, it is difficult to calculate the required sums correctly without an exact expression for the impedance as a function of frequency (something which we do not have even in the analytic case, since we have measured μ and ϵ only for a finite set of frequencies). Hence, the error in the results given in this section can be expected to be significant; it is likely that we have overestimated the importance of multi-bunch effects due to the Porcupine loads.

4.9 Summary

Alternate formulae were derived for potential well distortion effects, the bananer effect, complex frequency shifts, and the microwave instability. Most of the collective effects formulae were expressed in terms of the “effective elastance,” a functional of the coupling impedance and the bunch’s frequency spectrum.

For the CESR-V case, the direct and indirect power transfer from the beam to the HOM loads is predicted to produce an average power dissipation per unit area of 82.5 W/cm^2 in the Porcupine loads, with the maximum power density being at least 1.7 times larger. For the CESR-III.5 case, the predicted power density is 12.8 W/cm^2 on average, with a maximum at least 1.5 times higher. Since the highest average power density reached so far with a prototype Porcupine load was about 21 W/cm^2 (see Section 5.1), the power dissipation requirements for CESR-V will probably require some design changes.

Potential well distortion is predicted to shorten the bunch length by 1.3% or less. Static effects in the transverse plane are predicted to have no significant effect on the transverse size of the bunch. The predicted thresholds for various dynamic phenomena are summarised in Table 4.10. All of the instability thresholds are above the design current per bunch by more than a factor of 2.

Chapter 5

A Beam Test of a Ferrite-Lined Chamber

To test our ability to make correct predictions about the beam-ferrite interaction, beam measurements were done in CESR in December 1994 on a ferrite load of magnified coupling impedance. This beam test and the fabrication of the test structure for it are described in this chapter.

5.1 Load Fabrication

The design and construction of a test ferrite structure (and of Porcupine loads) able to handle power densities of 10 to 20 W/cm² was a development effort. When it became clear that the first generation HOM load [19] was not a complete success in terms of power-handling capability, a number of small-scale bonding tests were done, with the aim of improving the thermal contact between the ferrite tiles on the inside of the beam tube and the cooling water outside, without compromising the compatibility with ultra-high vacuum. In the recipe that was eventually chosen, a layer of nickel is sputtered onto the back side of the ferrite tiles (after the tiles are radiused, cleaned, and fired in air) and the tiles are soldered to a copper substrate. A cooling tube is brazed to the copper substrate before soldering. The soldering is done by clamping the tile and substrate together with a foil of silver-tin solder (10% Ag by mass) sandwiched between them, and heating the assembly to about 320°C under an inert atmosphere (N₂ gas). This recipe was chosen after a number of “bond-and-peel” tests with metal foils and some small-scale high power density RF tests. It was found to produce relatively good (but certainly not perfect) wetting of the two surfaces by the solder; the joint was found to be able to handle a power density of about 16 W/cm². This bonding scheme was used for the fabrication of both the ferrite test structure and the Porcupine loads [70], although the two designs ended up being somewhat different. The bond development effort was led by D. Moffat.

The test structure, which we named the “L3 load” after the site it occupied in the storage ring, had a beam tube diameter 2.5 times smaller and a ferrite-bearing length 6 times larger than the Porcupine load. As was discussed in Chapter 3, the predicted coupling impedance of this test structure is ~ 16 times the predicted monopole impedance and ~ 80 times the predicted dipole impedance of one Porcupine load. The

L3 load was split into three units, with sections of straight beam tube (with pumping ports) between them.

Each ferrite unit in the structure consisted of a copper tube with 40 tiles of TT2-111-series ferrite soldered to the inside and a water cooling tube wrapped around the outside, as shown in Figures 5.1 and 5.2. The steps in fabricating one unit were to (i) braze stainless steel collars to the ends of the copper shell, (ii) braze the copper refrigeration tube to the outside of the shell, (iii) weld vacuum flanges to the collars, and (iv) solder the tiles to the inside of the copper shell (see Figure 5.3). The brazing was done in a vacuum furnace; the welds were of the tungsten-inert gas type.

A total of four units were fabricated. Three of these were assembled into a vacuum-tight module with four ion-getter vacuum pumps, baked out, and installed in CESR. The assembled module is shown in Figure 5.4.

A prototype unit with only 10 tiles was made first for evaluation in a high power density RF test with a 500 MHz klystron. In this test, the ferrite-lined tube became the outer conductor of a coaxial line, with an RF short placed to produce relatively uniform dissipation in the ferrite. An average surface power density of 15 W/cm^2 was reached without visible damage to any of the tiles. The maximum measured tile surface temperature was 96°C with a cooling water flow rate of 130 mL/s (the tiles were not in a vacuum). A power density of about 21 W/cm^2 was reached in another high-power test of a Porcupine load, with the surface temperature of the ferrite exceeding 150°C at a serial flow rate of 27 mL/s .

5.2 Overview of the Beam Test

The beam measurements on the ferrite section were done over several days, interleaved with machine start-up activities following a down period. Measurements were done with 1, 2 and 9 bunches. Positrons were used almost exclusively, because we did not have complete masking for direct synchrotron radiation from the electron beam. Two different optical lattices with slightly different beam energies were used in the course of the test, one at the centre of mass energy of the $\Upsilon(2s)$ particle and the other at the $\Upsilon(1s)$ energy. Selected CESR machine parameters are given in Table 5.1. Several parameters were varied in the course of the test and are not listed.

Most of the predictions presented in this chapter are based on the impedance calculations discussed in Chapter 3, in which we assumed an axisymmetric geometry with a 3.175 mm layer of ferrite, and did not split the ferrite into three sections. As we saw in Section 3.3, the analytic formulae agree quite well with the AMOS predictions in the case of the L3 load; the analytically-calculated impedance was therefore used in the instability predictions except when indicated otherwise. Some refinements in the impedance calculations will be discussed in Section 5.6.

Potential well distortion predictions indicate that the ferrite impedance should produce bunch shortening at the 5 or 10% level (depending on the model—see Section 4.4) for the maximum single-bunch current (40 mA). This could be extenuated or aggravated by other impedances in the storage ring, although past experiments have found no bunch lengthening or shortening in CESR for single bunches. In the latter,

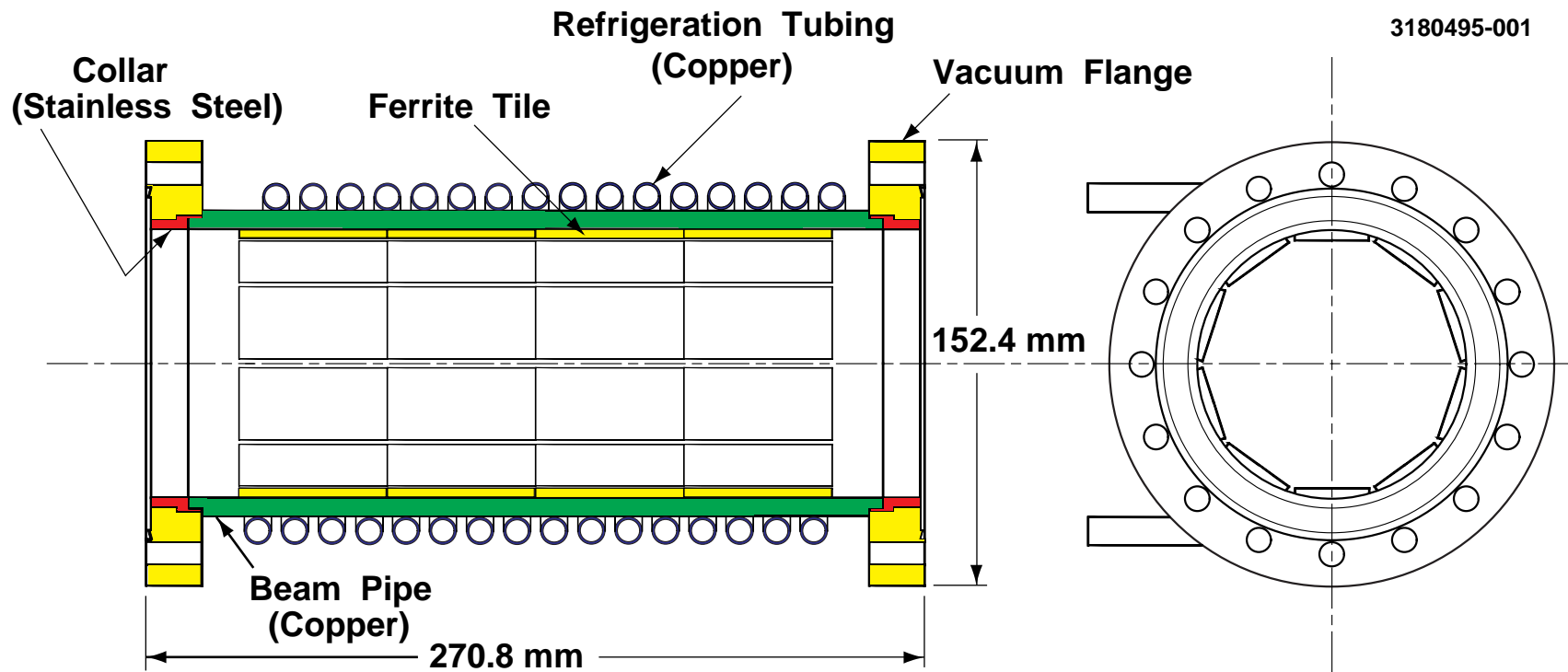


Figure 5.1. One unit of the ferrite structure. The inner diameter of the Cu tube is 92.1 mm; the ferrite tiles are 50.8 mm by 25.4 mm by 3.175 mm before radiusing.

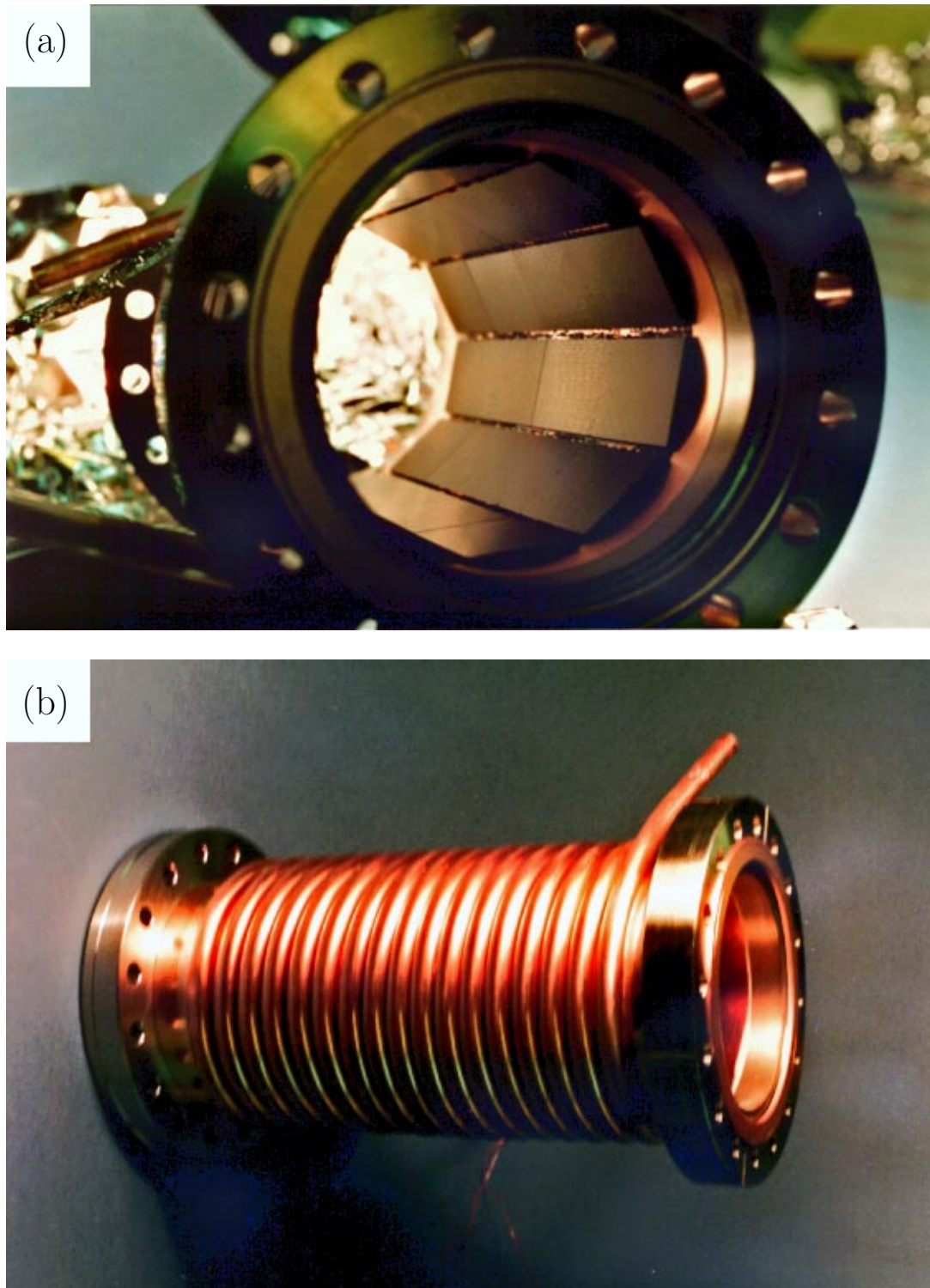


Figure 5.2. (a) Through view and (b) side view of one completed unit of the ferrite structure.

Table 5.1. Selected CESR machine parameters. The values listed do not account for the effect of the wigglers, as they were kept open during the measurements.

Fundamental Parameters		
Parameter	2s optics	1s optics
Ring circumference C	768.43 m	
Energy per particle $q_e E_0$	5.0 GeV	4.7 GeV
Relative momentum spread σ_δ	$5.782 \cdot 10^{-4}$	$5.433 \cdot 10^{-4}$
Momentum compaction	0.0112	0.0115
RF Frequency	499.8 MHz	
Energy radiated per turn U_0	0.822 MeV	0.642 MeV
Longitudinal radiation damping rate	64.80 s^{-1}	53.86 s^{-1}
Horizontal radiation damping rate	31.36 s^{-1}	26.00 s^{-1}
Vertical radiation damping rate	32.05 s^{-1}	26.62 s^{-1}
Horizontal β -function in L3	0.821 m	0.822 m
Vertical β -function in L3	6.933 m	6.930 m
Derived Parameters		
Revolution frequency $f_0 = \omega_0/(2\pi)$	390.14 kHz	
Slippage factor η	0.0112	0.0115
Harmonic number	1281	



Figure 5.3. Tiles being soldered to one unit of the ferrite structure. The upper-most of four “Mini-Tribendis Wheels” (used to clamp the tiles in place while they are being soldered) is visible.

a current of up to 26 mA was reached with $\sigma_z = 20$ mm [71] and a current of 20 mA was obtained with $\sigma_z = 15$ mm [72]. Unfortunately, we did not have the means to measure the bunch length in this test. However, a theoretical bunch length can be obtained from the synchrotron frequency f_s or the RF voltage. We used f_s to get the bunch length, although it is not necessarily the best indicator (according to models, the bunch length is correlated with the incoherent synchrotron frequency, which is generally different from the coherent synchrotron frequency that we measure). As will be seen below, we infer significant bunch lengthening with 9 bunches on the basis of f_s , but only a slight change in the bunch length on the basis of the RF voltage.

The longitudinal microwave instability threshold (see Section 4.7) predicted for the ferrite is about 25 mA per bunch, depending on σ_z . However, since the threshold gives only a sufficient condition for stability, we cannot conclude that the beam should be unstable (*i.e.* that the bunch length and momentum spread should increase “turbulently,” as predicted by the models) at the maximum current per bunch of 40 mA. No evidence of an instability was seen, but we might not have been able to see it without a direct measurement of the bunch length or the momentum spread (although one could argue that there would be indirect evidence that we would have noticed). According to the Zisman formula, we remained below the longitudinal microwave instability threshold by a factor of about 2. The predicted transverse microwave instability thresholds are higher than the latter by order of magnitude.

5.3 Calorimetric Measurements

The power dissipation in each unit was obtained calorimetrically via the flow rate, inlet temperature, and outlet temperature of the cooling water. Water temperatures were obtained via sheathed thermocouples protruding into the inlet and outlet tubes; the flow rate was measured using a paddle-wheel gauge. The volume flow rate of water was ~ 50 mL/s per unit for most of the test. The total power dissipation of the ferrite is the sum of the power dissipation in each of the three units. The measured power dissipation was found to be about the same in each unit.

Monopole Loss Factor Measurements

The monopole loss factor k_0^{\parallel} of the ferrite units can be obtained directly from the total power dissipation P_d and total beam current I . The measured k_0^{\parallel} as a function of I is shown in Figure 5.5a for a single bunch. The noise in the data at low I is due to the poor resolution of the small ΔT values. At higher I , a slight decrease in the measured k_0^{\parallel} as function of I is visible. Possible explanations for this effect include (i) systematic error in the calorimetry, (ii) non-linearity in the ferrite response to the beam's electromagnetic fields, or (iii) the temperature dependence in the microwave properties of the ferrite.

Figure 5.5b shows the single-bunch data plotted as a function of the longitudinal bunch size σ_z , calculated from the measured synchrotron frequency (see Section 5.5), along with the predicted k_0^{\parallel} . It can be seen that, inasmuch as f_s is a reliable indicator of the bunch length, the decrease in k_0^{\parallel} with I cannot be explained as being due to changes in σ_z as a function of I . There is no sign of the bunch shortening expected due to the ferrite.

As can be seen in Figure 5.6, the 9-bunch results are consistent with the single-bunch results, except for a slight decrease in the loss factor for the shortest bunch length. The latter effect is not understood, as the predicted loss factor is the same for the single-pass, single-bunch, and 9-bunch cases; one possibility is that it is result of bunch lengthening produced by the medium-range wake of other elements in the ring. The change in σ_z with current obtained from f_s is larger in the 9-bunch case, but it still does not account for the decrease in k_0^{\parallel} with current. As we will see in Section 5.5, the change in σ_z expected from the dependence of the RF voltage on beam current is much smaller. In both the single-bunch and 9-bunch cases, the measured k_0^{\parallel} is smaller than predicted by about a factor of 2; the likely explanation for this discrepancy will be given in Section 5.6.

Sampling the Wake Function

We used the Temnykh method [73] to sample the wake field: with two bunches of equal charge ($I_b =$ current per bunch = 20 mA for each), we measured the power dissipation in the ferrite as a function of the spacing Δz between the bunches. In

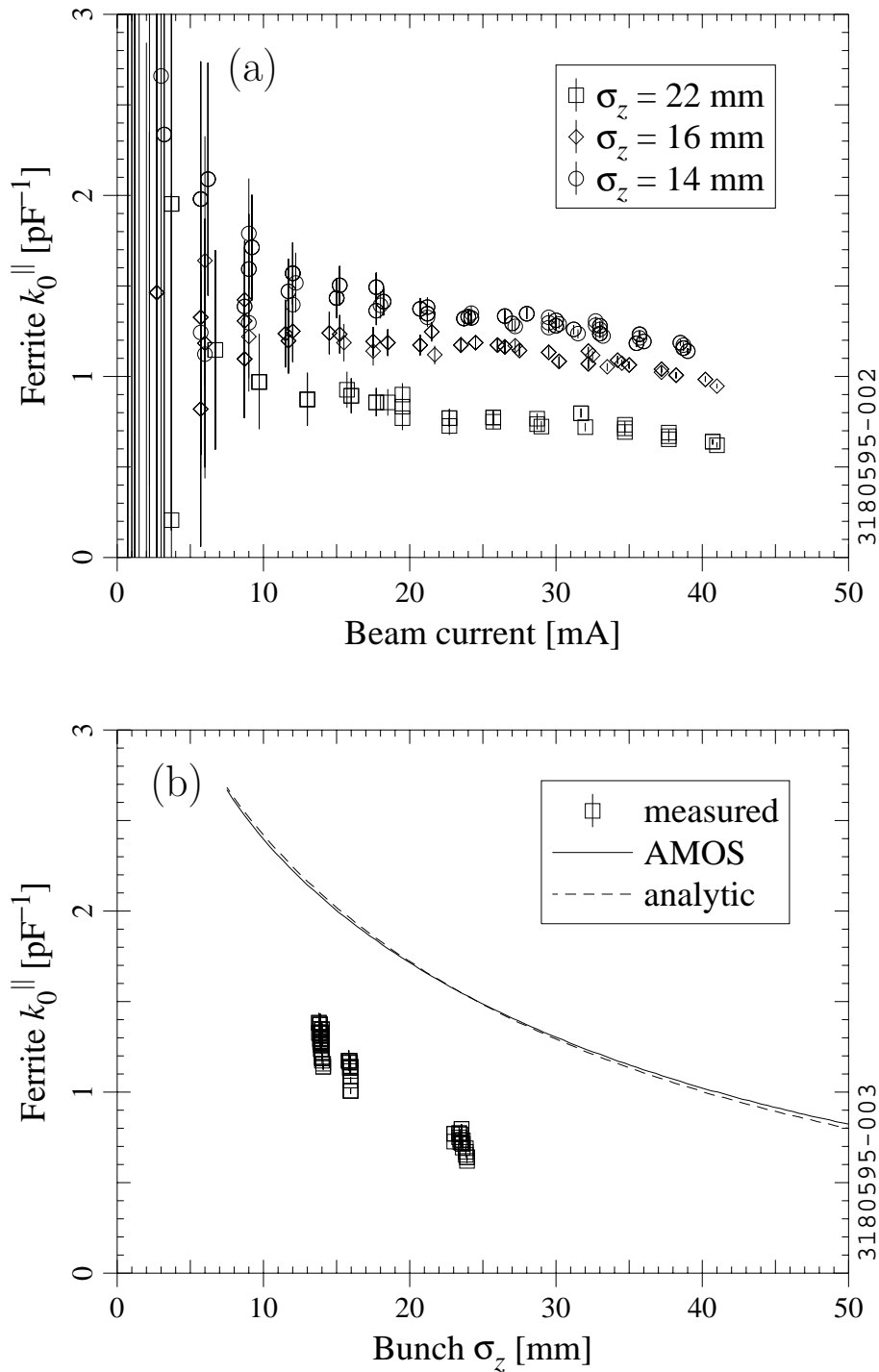


Figure 5.5. Calorimetrically measured single-bunch loss factor (summed over all 3 units) of the ferrite section as a function of (a) beam current, and (b) bunch length (with predictions). The RF voltage was adjusted to vary the bunch length. Noisy low-current points ($I < 20$ mA) are omitted in (b).

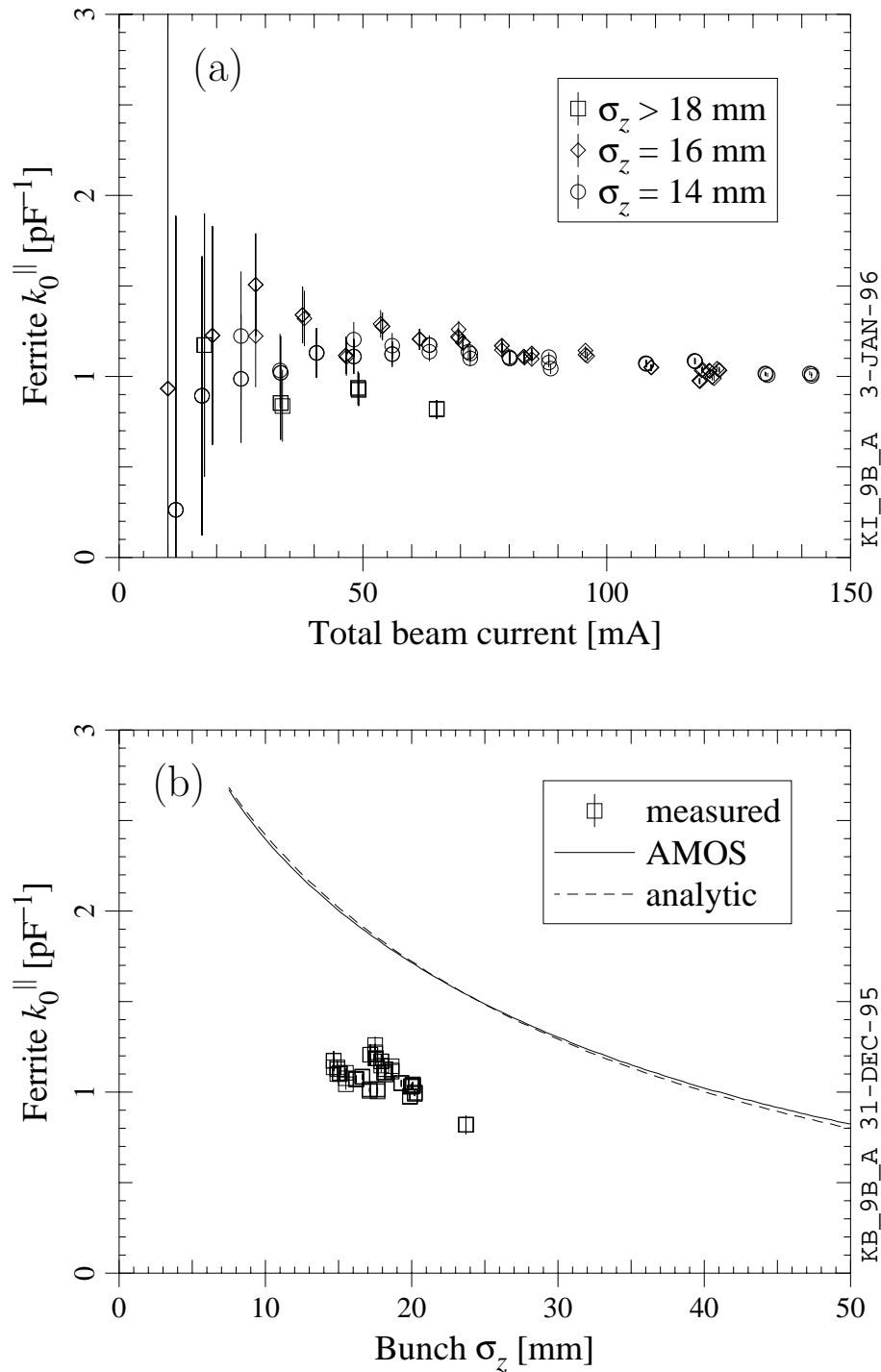


Figure 5.6. Calorimetrically measured 9-bunch loss factor (summed over all 3 units) of the ferrite section as a function of (a) beam current, and (b) bunch length (with predictions). The RF voltage was adjusted to vary the bunch length. Noisy low-current points ($I < 60$ mA) are omitted in (b).

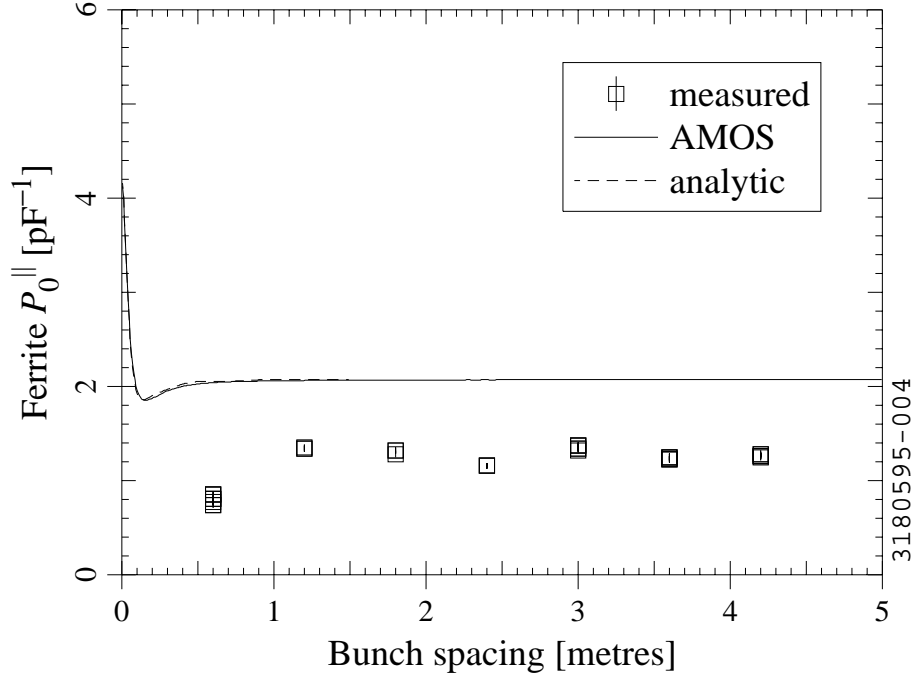


Figure 5.7. Calorimetrically measured and predicted 2-bunch power loss factor of the ferrite as a function of spacing, with $\sigma_z = 14$ mm (from f_s). Because the RF frequency is 500 MHz, the smallest measurable Δz is 0.6 m.

terms of a power loss factor

$$P_0^{\parallel} \equiv \frac{P_d f_0}{M I_b^2}, \quad (5.1)$$

where M = number of bunches and f_0 = revolution frequency, we should have $P_0^{\parallel} = k_0^{\parallel}$ if the wake fields have vanished by the time the second bunch arrives and $P_0^{\parallel} \rightarrow 2k_0^{\parallel}$ as $\Delta z \rightarrow 0$. The results are shown in Figure 5.7, along with a prediction obtained by integrating the calculated coupling impedance with the appropriate form factor. The measurement suggests that the ferrite section's wake fields endure longer than predicted; for $\Delta z >$ one RF bucket (*i.e.* 0.6 m), however, the measurements and predictions seem to agree that the wake field has decayed to zero. There may be another explanation for the anomalously loss power dissipation when the bunches are one bucket apart, as will be discussed in Section 5.8.

Dipole Loss Factor Measurements

We used magnetic and electrostatic elements near the ferrite chamber's location in the storage ring to produce a transverse displacement of the beam in the ferrite chamber. The measured calorimetric single-bunch loss factor as a function of displacement is shown in Figure 5.8, along with predictions based on the calculated monopole and dipole loss factors. Though the measurement suggests that there is some dependence

on displacement, the signal-to-noise ratio is not very favourable.

5.4 RF Power Measurements

It is possible to infer the total loss factor of a storage ring by applying the appropriate book-keeping methods to the cavity RF power and synchrotron radiation power [74]. One obtains the parasitic power lost by the beam by measuring the forward power supplied to each cavity and subtracting off the power reflected back from the cavity input coupler, the power dissipated in the cavity walls, and the power lost by the beam due to synchrotron radiation. We applied this technique with and without the ferrite in order to get an independent measure of the power loss due to the L3 ferrite load. The results are compared in Figure 5.9. The predicted k_0^{\parallel} of CESR shown in Figure 5.9 was obtained from scaling laws for various machine elements [75]. The scaling laws were updated to account for recent modifications to the storage ring, as discussed in Appendix C. The total k_0^{\parallel} measurement gave less accuracy than the calorimetric measurement—the power loss in the ferrite is close to the noise level in the RF measurement—but the RF and calorimetric results do not overtly contradict each other. As in the calorimetric measurement, the 9-bunch results show a slight decrease in the loss factor for the shortest bunch length. Because the results are sensitive to power offsets, it is difficult to say whether the total loss factor of the ring depends on the beam current (as was seen for the calorimetric measurements).

5.5 Frequency Shift and Damping Rate Measurements

As was discussed in Chapter 4, the total ring impedance produces shifts in the frequencies and damping rates of the oscillatory modes of the beam; in the absence of coupling, the shift in the frequency f and damping rate α should be proportional to I . We used established techniques [76] to measure the lowest-order frequencies and corresponding α 's as a function of I , with and without ferrite. We did the damping rate measurements with the CESR distributed ion pumps turned off, in order to eliminate anomalous growth effects [77].

Longitudinal

Single-bunch and 9-bunch measurements of the synchrotron frequency f_s (*i.e.* the longitudinal $l = 1$ azimuthal mode, with $s = 0$ in the multi-bunch case) as a function of current were done for three different RF voltages. In the single-bunch measurements, the f_s frequency domain resonance curve often had a double peak, which complicated matters a bit. The results are shown in Figure 5.10. These are some obvious offsets (possibly due to imperfect matching of machine parameters between the measurements with and without the ferrite), but the differences in slope due to the ferrite are probably below the reproducibility threshold of the measurement.

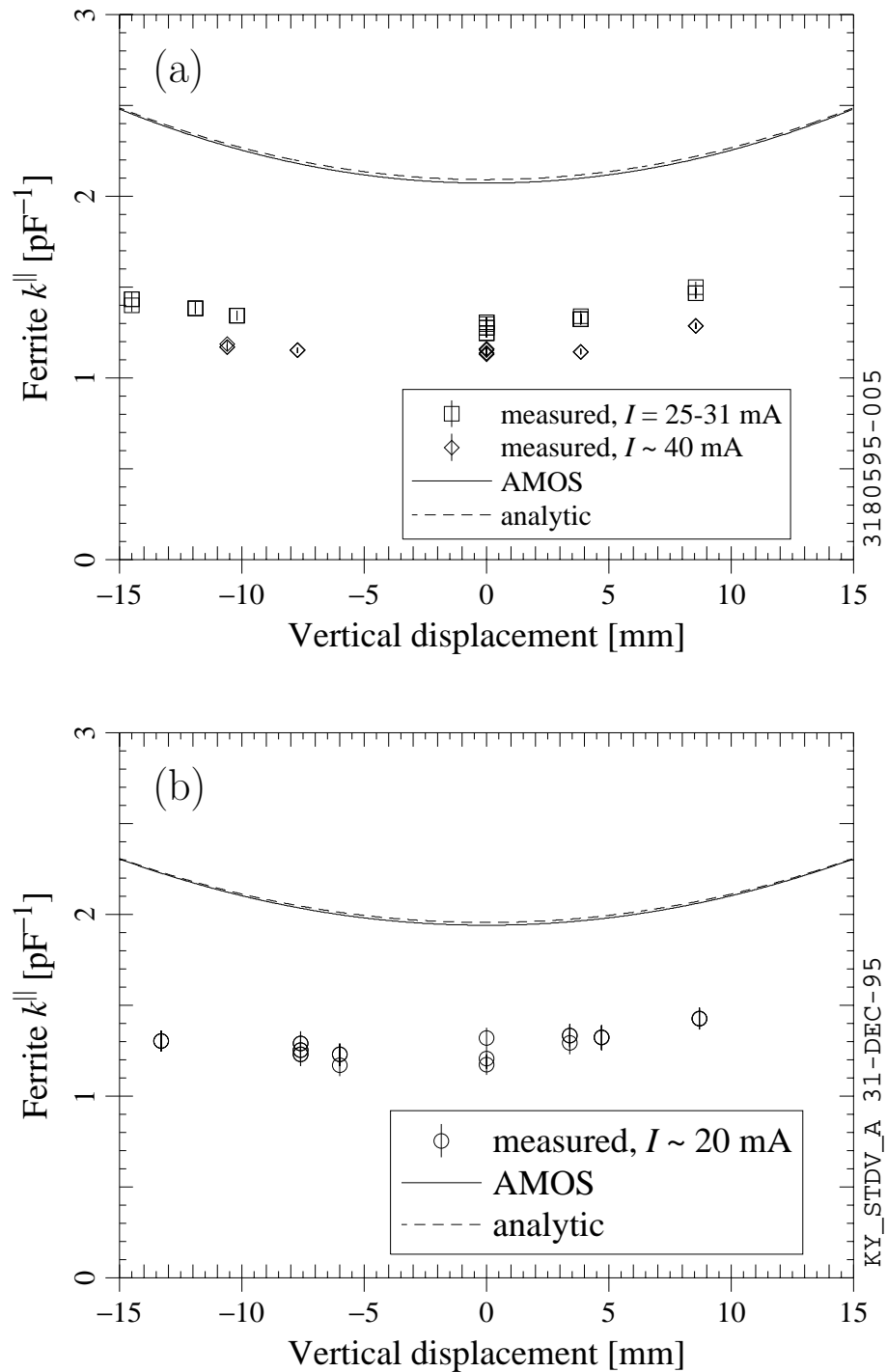


Figure 5.8. Calorimetrically measured and predicted loss factor of the ferrite section as a function of the vertical displacement of the beam, with (a) $\sigma_z = 14$ mm and (b) $\sigma_z = 16$ mm (from f_s).

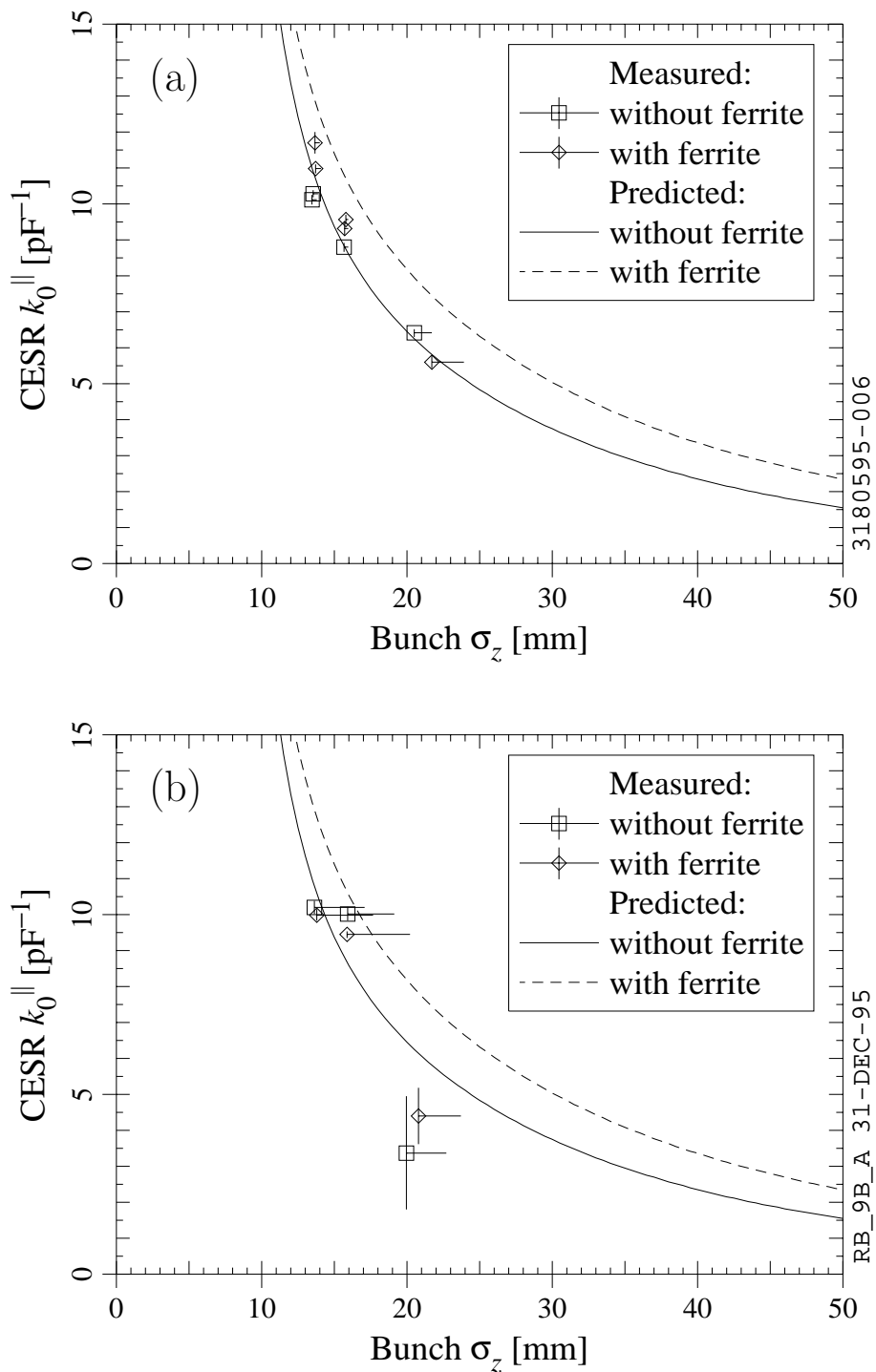


Figure 5.9. Measured and predicted (a) single-bunch and (b) 9-bunch loss factor of CCSR, with and without ferrite present.

Recall that, when we included the stationary wake in our analysis, we predicted that there would be no shift in the f_s mode to linear order due to the Porcupine load's impedance. The same holds true for the L3 load, a prediction which is consistent with Figure 5.10. The predicted mode coupling threshold due to the ferrite (in the absence of the stationary wake) is about a factor of 10 higher than the maximum current per bunch achieved in the test. (In hindsight, it would have been better to measure a different azimuthal mode, and we probably would have if I had understood the effect of the stationary wake at the time of the test.)

Interestingly, the frequency shifts are quite a bit larger with 9 bunches than with a single bunch, even though more than twice the current per bunch was reached in the single-bunch case. As has been hinted at already, a decrease (or, in one out of six cases, an increase) in the RF voltage as a function of current was observed in the test.¹ The voltage changes were indeed larger with 9 bunches, but the corresponding frequency shift one would expect is small. This is also illustrated via the solid and dashed lines in Figure 5.10, which are predictions based on the measured dependence of the RF voltage on beam current. The combined effect of the non-linearity in the RF voltage and the shift in the bunch's longitudinal position as a function of current due to the total loss factor of the ring are also included in the prediction. The increase in the predicted loss factor of the ring due to the ferrite accounts for the slight difference in slope between the predictions with and without the ferrite, although this effect is below the noise level in the measurements.

In the single-bunch case, there is no systematic difference between the measurements and the predictions (the measured slopes are sometimes the same, sometimes smaller, and sometimes larger than predicted). In the 9-bunch case, on the other hand, the measured frequency shifts are much larger than predicted. The measured dependence of f_s on frequency with 9 bunches can be accounted for via a model which includes the coupling impedance of the fundamental mode of the cavities and the shift in the fundamental mode frequency as a function of current [78]. This detuning of the fundamental mode frequency with current (done to compensate for the beam-induced voltage in the cavity) accounts for the non-linear dependence of f_s on I . The shift due to the fundamental impedance is a coherent one, so our assumption that the bunch length is inversely proportional to f_s is perhaps not the best one for the 9-bunch case—a direct measurement of σ_z would certainly be much better.

Single-bunch measurements of the damping rate of the f_s mode were attempted, but the results were not deemed meaningful, because of the non-exponential decay in the signal (seen both with and without the ferrite).

Transverse

The single-bunch horizontal and vertical betatron frequencies and associated damping rates were measured for two different RF voltages. The results for one case are shown

¹This change in the RF voltage with current was diagnosed to be mismatch between cavity pairs in which one cavity's voltage decreased (or increased) when the other's was held constant via a control loop—the inter-cavity phase has since been adjusted in an attempt to eliminate this problem.

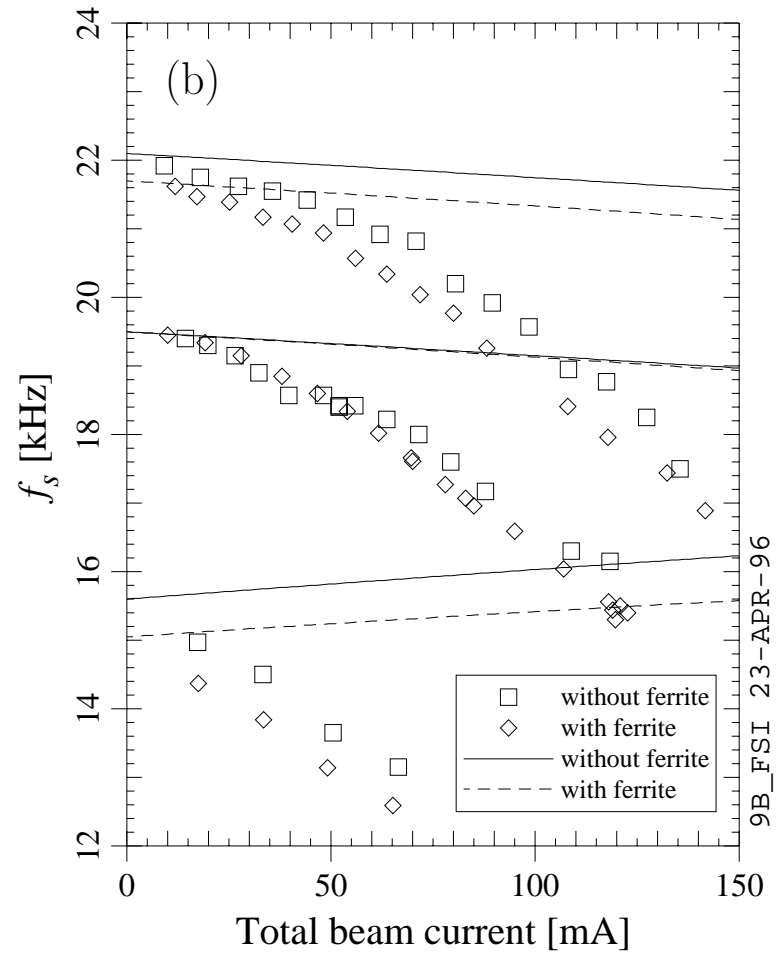
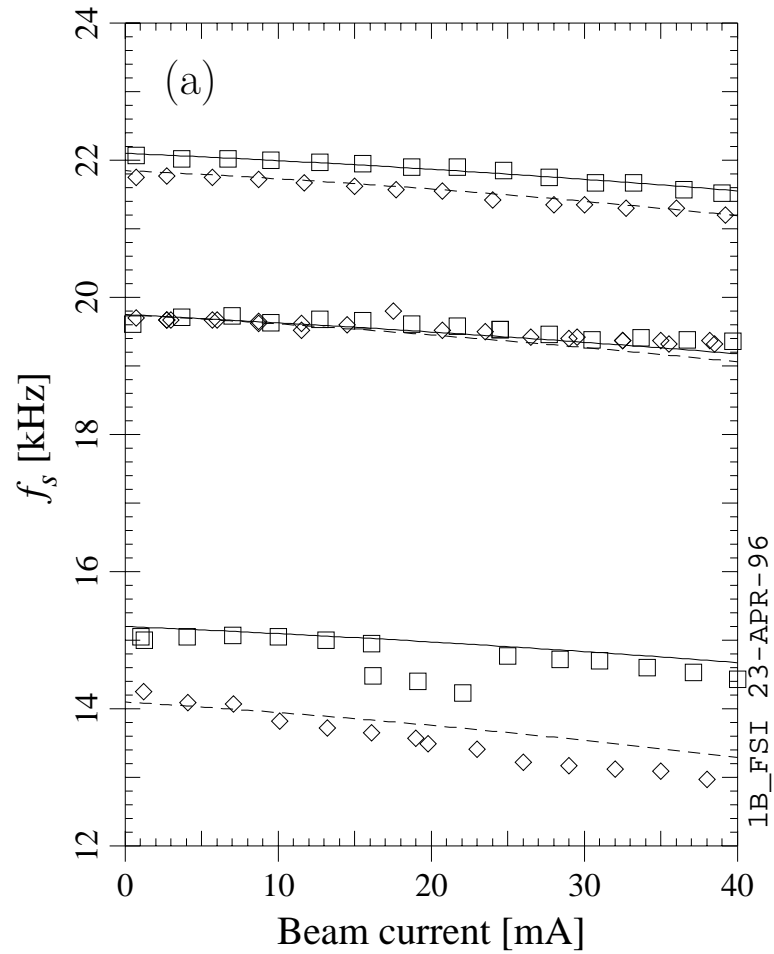


Figure 5.10. Comparison of (a) single-bunch and (b) 9-bunch synchrotron frequency measurements with and without ferrite. The three families of points correspond to three different RF voltages. Predictions are also shown (solid and dashed lines).

Table 5.2. Comparison of measured and predicted single-bunch transverse frequency shift and damping rate slopes. The values given are the differences in slope due to the ferrite. The integral and sum formulations for the complex frequency shift agree for the number of digits given.

Plane	ξ	σ_z [mm]	$\Delta f'$ [kHz/A]		$\Delta\alpha'$ [(ms A) ⁻¹]	
			measured	predicted	measured	predicted
Horizontal	2.2	16	~ 0	-0.456	-3.7	0.1030
Vertical	2.0	16	~ 13	-3.9	-5.8	0.791
Horizontal	4.7	14	~ 5	-0.462	2.9	0.195
Vertical	1.8	14	~ 0	-3.90	-5.7	0.630

in Figure 5.11. For the most part, the frequency shifts and damping rates grow quite linearly with frequency, as expected in the absence of coupling (the predicted horizontal and vertical mode coupling thresholds are of the order of 20 A per bunch and 2.5 A per bunch, respectively, not accounting for the stationary wake); in two cases, there were anomalies in the damping rate's behaviour between 5 and 15 mA per bunch. In three out of four cases, there were offsets in the betatron frequency between the measurements with and without ferrite—our attempts to return to the same machine conditions were not completely successful. The measurements are summarised in Table 5.2. Predictions based on the formulae given in Section 4.5 are also given in Table 5.2 (recall that, for the $l = 0$ mode, the stationary wake does not affect the frequency shift). The differences in the measured slope are near the threshold for statistical significance in the case of the frequency shift, and probably do not reflect the effect of the ferrite impedance.

In the case of the damping rate, the differences are well above the noise level and much larger than predicted. To see whether these differences could indeed be attributed to the ferrite, some reproducibility measurements were done. A difference in damping rate slope of 3.5 to 4 (ms A)⁻¹ was seen between measurements made and repeated after about one day under the same conditions. The differences seen between the measurements with and without ferrite are slightly larger, but, relative to the reproducibility measurements, more time elapsed and more changes were made to the storage ring between measurements. Thus, it cannot be said that the measured differences in slope are due to the ferrite.

5.6 Refinements to the Loss Factor Predictions

As discussed in Section 5.3, there is a factor of ~ 2 discrepancy between the calorimetrically measured loss factor of the ferrite structure and the loss factor predicted for the L3 load in Chapter 3. The loss factor of the full-size HOM load mock-up was also smaller than predicted (see Section 3.3). There are several idealisations in our model

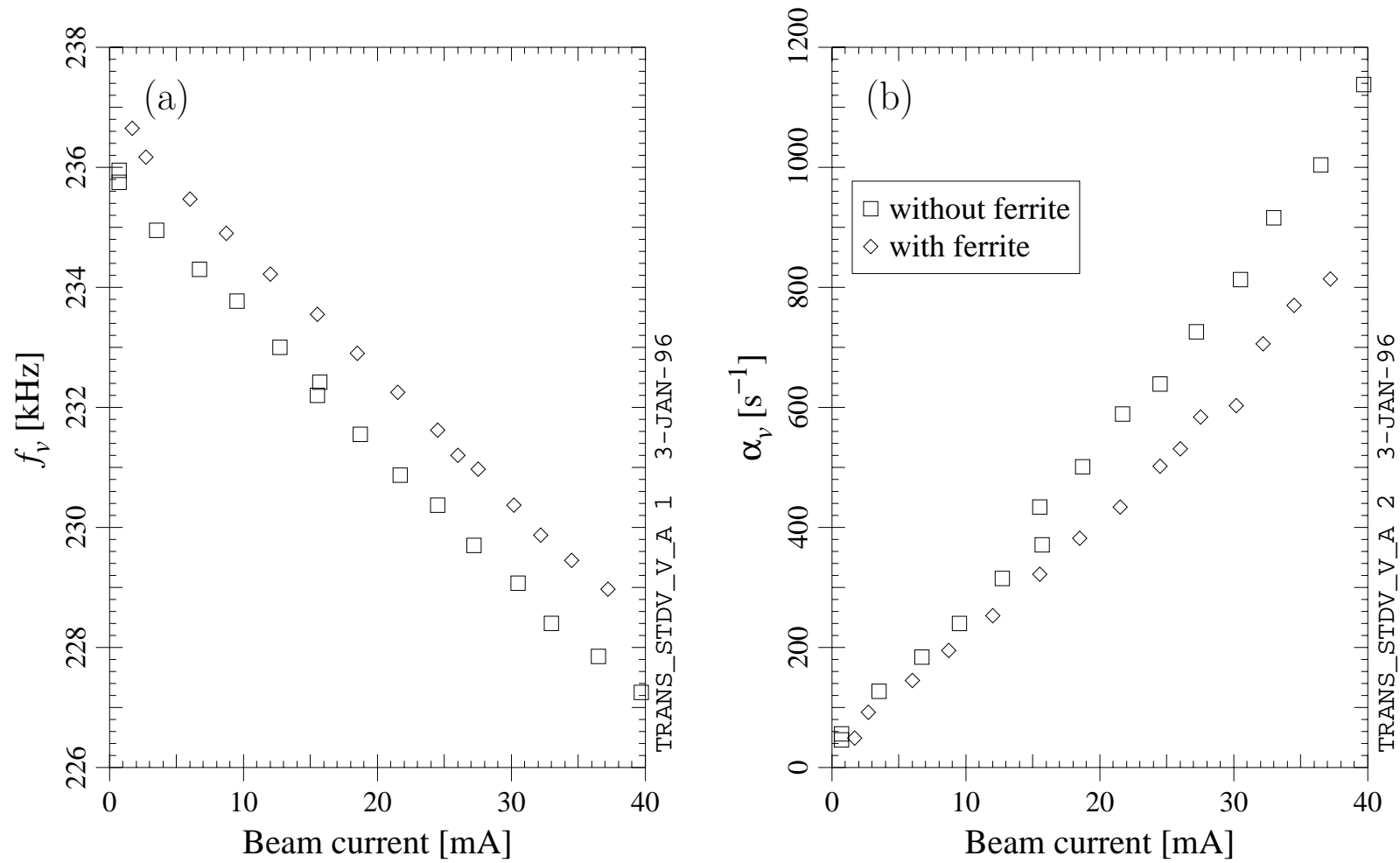


Figure 5.11. Comparison of single-bunch measurements of (a) the vertical betatron frequency and (b) the corresponding damping rate, with and without ferrite.

which one might turn to in order to account for this factor of 2. We will examine them in this section. It is also possible that the systematic error in the measurement is the cause; another beam test would be required to rule out this possibility.

One idealisation that was made was to assume that all the power lost by the beam is dissipated in the ferrite; in practice, it is possible that some of the energy will propagate into the beam tube and eventually be dissipated elsewhere in the ring. We estimated the importance of this effect by comparing the fraction of the power transfer above the beam tube's cutoff frequency to the total power transfer from the beam. The latter is obtained via a direct application of Equation (3.8), while the former is obtained by excluding frequencies below cutoff from the integral in Equation (3.8). In the extreme case in which all of the power above cutoff propagates into the beam tube, the predicted power dissipation in the ferrite decreases by 11% at most, depending on the bunch length. Thus, this idealisation does not account for the discrepancy.

A second idealisation we made was to approximate the three ferrite units as a single section of ferrite with three times the length of one unit. To estimate the importance of the longitudinal distribution of the ferrite, we did a more realistic AMOS calculation with the ferrite layer split into three parts. We also tried to improve the realism in the end effects. AMOS predicts a 5% *increase* in the loss factor in the more realistic case (for the shortest bunch length, which shows the most dramatic change). This idealisation does not account for the discrepancy either.

A third idealisation we made was to assume that the microwave properties of the ferrite tiles used in the L3 load are identical to those measured for TT2-111V. In reality, there is significant batch-to-batch variation in the properties, particularly in ϵ . The firing processes also have an influence on the microwave properties. To estimate the variation in the loss factor to be expected due to these effects, we predicted the loss factor for four other batches of TT2-111-series ferrite, whose μ and ϵ were measured after they were fired in air at 900°C and in nitrogen gas at 250°C [25]. This firing cycle approximates the preparation and soldering cycle that the tiles undergo. For the relevant range of σ_z values, the predicted loss factors based on the treated ferrites' properties were between 1% and 14% smaller than the loss factor based on untreated TT2-111V. Thus, the variation in ferrite properties cannot be said to account fully for our factor of ~ 2 .

A fourth idealisation is that the ferrite layer has a uniform thickness of 3.175 mm. This is in fact the thickness of the tiles before they are radiused for soldering to the inside of the copper tube—after radiusing, the thickness remains 3.175 mm in the middle of the tile, but decreases to a minimum value of about 1.33 mm at the edges. There are also gaps between the tiles (see Figures 5.1 and 5.2). One might expect to get better agreement with the measurements by using an “isochoric” model, *i.e.* choosing an equivalent ferrite layer thickness for which the total volume of ferrite is the same as in the actual load (to wit, 2.33 mm), rather than using the maximum thickness of ferrite. The analytically-predicted dependence of the loss factor on the thickness of the ferrite layer is compared to the measured single-bunch loss factors in Figure 5.12. The measurements agree with the predicted loss factor for a thickness

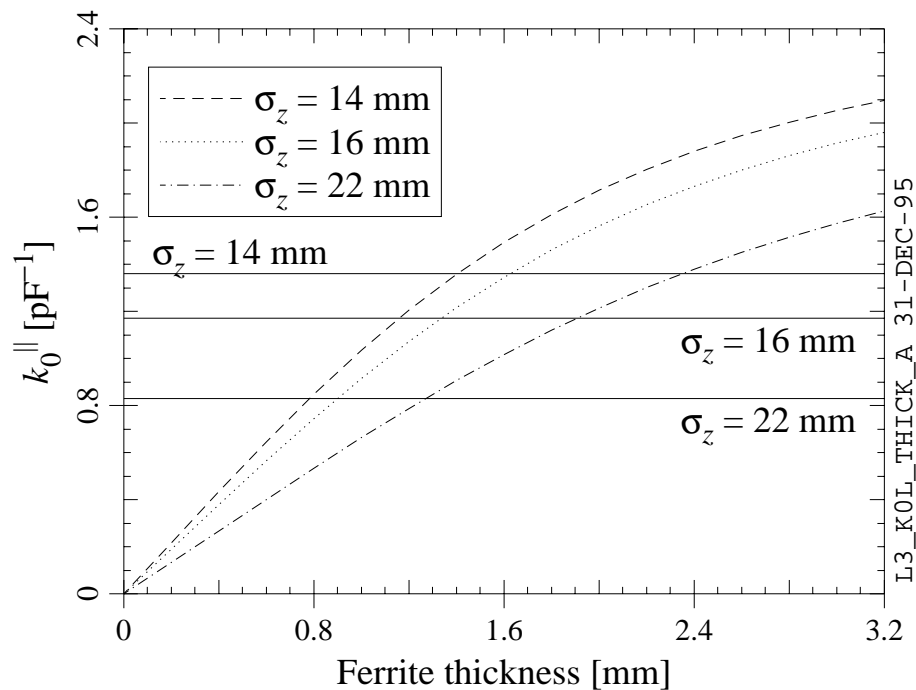


Figure 5.12. Comparison of analytically-predicted (dashed and dotted lines) and measured (solid lines) loss factors for three different bunch lengths. The measured values shown are based on a single bunch of about 20 mA.

between 1.25 and 1.4 mm, which is close to the thickness at the edge of the tiles. The implication may be that the gaps between the tiles are more effective at reducing the loss factor than can be accounted for via a simple-minded isochoric approximation. Of course, the effects discussed above may contribute to the overall reduction.

5.7 Load Performance

The maximum (total) power dissipation in the ferrite was 5.8 kW according to calorimetry, corresponding to an average power density = 3.8 W/cm²; this was obtained with $I = 142$ mA in 9 bunches. At this current, the pressure gauges read ≤ 30 pbar, although pressures as high as 50 pbar were recorded (at lower I) during an earlier “beam processing” shift. Several vacuum “spikes” occurred in the course of the test, with the pressure rising to 100–200 pbar or higher. Prior to installation, the pressure in the ferrite assembly reached 1 pbar at 17°C after a vacuum bake-out to 150°C.

An inspection of the ferrite chamber after removal from CESR revealed that one corner of one tile had broken off; it was found lying on the bottom of one of the ferrite sections. The piece appeared to have been unsoldered except along one edge. There was no obvious damage to any other tiles.

If the current per bunch is sufficiently high, the electromagnetic fields which travel with the bunch can be expected to produce a non-linear response in the ferrite. Based on the beam currents and bunch lengths obtained in the beam test, the maximum (instantaneous) magnetic field at the surface of the ferrite was 4.1 mT. The corresponding surface electric field was 1.2 MV/m. As suggested in Section 5.3, the slight decrease in the measured loss factor with current might be associated with these high surface fields. Unfortunately, we do not have much information on the ferrite's response to high fields. However, we measured an order-of-magnitude change in the L-band lossiness of a TT2-111-series tile in the presence of a magnetostatic field. The strength of this field was measured to be of the order of 250 mT [79], which might be consistent with the hypothesis that the beam's magnetic field produced a slight decrease in the loss factor. Because of the smaller load diameter and higher current per bunch (and accounting for the longer bunch length), the maximum surface fields obtained in the beam test are about a factor of 7 higher than the surface fields expected due to the direct interaction with the beam for Porcupine loads in CESR-V.

5.8 Other Related Beam Tests

Cavity Test in CESR

Prototypes for the superconducting cavity, cryostat, and Porcupine HOM loads for the CESR upgrade were subjected to a beam test in CESR in August 1994 [14, 80, 70, 81]. Among other things, the loss factor of the cavity, tapers, and HOM loads was measured calorimetrically. Reasonable agreement was found between the measured values and predictions based on the composition rule (see Section 3.3), although there were indications that the loss factor was smaller than predicted for the shortest bunch length (about 10.3 mm). No correlation was seen between the beam current and the loss factor.

Wake sampling measurements with 2 bunches were also done for the loss factor of the cavity assembly (as determined calorimetrically via the Porcupine HOM loads); the results, when considered in conjunction with the results of the analogous measurements in the L3 ferrite test, suggest that there might be another explanation for the anomalous results of Figure 5.7. In the discussion in Section 5.3, we assumed that the wake function of the first bunch cancelled out the wake function of the second bunch in order to reduce the net power dissipation in the case of a spacing of one RF bucket (0.6 m) between the two bunches. If so, the loss factor should be independent of the current per bunch, provided both bunches have equal charge. In the L3 test, we did not vary the charge per bunch in the 2-bunch measurements (we did measurements at 20 mA per bunch only), so we have no knowledge of the dependence on current; in the cavity test, however, analogous measurements were done at three different currents (5, 10, and 15mA per bunch). The results are more easily interpreted when expressed in terms of power dissipation versus total current squared instead of loss factor. The cavity test results are compared to the normalised L3 test results in Figure 5.13. As can be seen, all of the data for spacings of more than one bucket fall on a straight

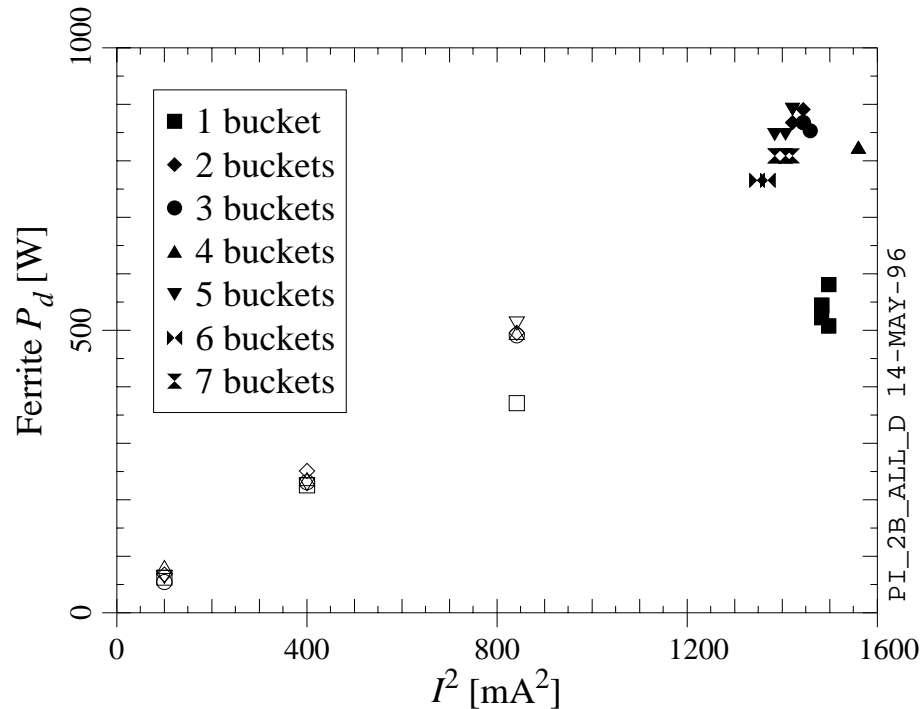


Figure 5.13. Comparison of the measured power dissipation in the Porcupine HOM loads (hollow symbols) during the cavity beam test with that measured in the L3 test (solid symbols). Values of P_d for the L3 test were multiplied by 0.356 to account for the larger loss factor of the L3 load (this value was chosen because the multi-bucket data then followed a straight line). In the cavity test, measurements were done for spacings of 1, 2, 3, 4, and 5 buckets, with $\sigma_z \approx 15$ mm.

line. The data for 1-bucket spacing, on the other hand, do not increase linearly with I^2 —at the two lowest currents, the 1-bucket and multi-bucket points overlap, but the 1-bucket points are significantly lower for the two highest currents. The single-bucket data have a plausibly smooth dependence on I^2 , however. We may speculate that this is the result of another coupling impedance in CESR which produces bunch lengthening when two bunches are very closely spaced (the likely explanation being that the short-range wake of the leading bunch causes lengthening of the trailing bunch). This hypothesis would explain why the 1-bucket loss is anomalously low, even though the predictions based on the L3 load impedance (Figure 5.7) and the cavity module impedance [80] indicate that there should be no difference between one bucket and multiple buckets. Since this hypothesis is based on a total of two anomalous data points from two different experiments, however, it is not altogether convincing.²

²We might add that, since the smallest spacing between bunches that is envisaged for future CESR operation is 7 buckets, the question is somewhat academic for the problem at hand.

Ferrite Load Test in TRISTAN

A prototype HOM load for the KEK-B superconducting RF system was tested by T. Tajima in the TRISTAN Main Ring in May 1995 [82]. The HOM load was axisymmetric; it was fabricated via hot isostatic pressing of ferrite powder onto a copper shell. At the shortest bunch lengths, the calorimetric loss factor of the ferrite and tapers was somewhat higher than expected from predictions. The bunch lengths in this test ($\sigma_z = 4$ to 8 mm) were smaller than those used in CESR tests, so that propagation into the beam pipe might be more significant.

5.9 Summary

CESR beam measurements with a ferrite-lined section of magnified impedance indicate that the loss factor is a factor of ~ 2 smaller than predicted, possibly due to the thickness variation along the tiles and the gaps between tiles. The measured wake field may endure longer than predicted, but there is no visible effect for $\Delta z = 4.2$ m, the smallest spacing envisaged for future incarnations of CESR; hence there is no indication that multi-bunch instabilities due to the ferrite will be a problem. The signal-to-background ratio made it difficult to pick out effects from the ferrite via measurements on the beam only; this is consistent with predictions, if the stationary wake term is included.

Chapter 6

Conclusion

6.1 The Beam-Ferrite Interaction: Review

The purpose of this thesis was to (i) quantify the interaction, via the coupling impedance, between a beam and a layer of microwave-absorbing material on the inside of a beam tube, (ii) predict the power dissipation in the absorbing layer due to the interaction, (iii) predict the beam instability thresholds in a storage ring due to the interaction, and (iv) test the predictions in a storage ring. In order to predict the coupling impedance as required in step (i), it was first necessary to measure the microwave properties of the material.

Microwave Properties

The coaxial transmission line technique was used to measure the complex permeability and permittivity as a function of frequency for TT2-111-series nickel-zinc ferrite and other microwave-absorbing materials over a large frequency range (300 kHz to 20 GHz). To improve the accuracy of the results, different sample lengths were used for different portions of the frequency spectrum. We found our ϵ values to be sensitive to gaps between the sample and the walls of the coaxial line: it was necessary to fill the gaps with liquid metal in order to obtain reproducible results for materials with large ϵ . We found it helpful to measure both the forward and reverse S-parameters in gauging the systematic error; in particular, the phases of the two reflection coefficients were found to be good indicators of sample misalignment.

Because of the strong frequency dependence in the μ and ϵ values for the absorbing ferrites, we found that the standard algorithm for calculating μ and ϵ from the measured S-parameters was not appropriate. We used a different algorithm to determine the number of whole wavelengths in the sample. Because of the large frequency range involved, we were able to confirm the consistency of our μ values for TT2-111-series ferrite using a Kramers-Kronig relation. For ϵ , the Kramers-Kronig test suggests that the material has significant absorption at frequencies above 20 GHz. For the frequency range of overlap, our results agree reasonably well with the majority of the measurements we have seen in the literature.

Coupling Impedance

An analytic approximation for the coupling impedance of a microwave-absorbing layer on the inside of a circular beam tube was derived. The measured microwave properties were used to predict the coupling impedance of a beam tube section with a layer of TT2-111-series ferrite using this analytic approximation, a field matching method derived by Akasaka, and a fully numerical solution (the AMOS program written by DeFord *et al.*). All of the predictions agreed reasonably well below the cutoff frequency, but the more exact methods (which account for the finite length of the structure) predicted a significantly larger impedance at high frequencies for the Porcupine geometry intended for use in the new RF system for CESR. The predicted impedance was checked against impedance measurements done by Walling on a smaller structure using the wire method. The analytic approximation, the Akasaka field matching method, and the AMOS numerical solution are applicable to arbitrary $\mu(\omega)$ and $\epsilon(\omega)$, although the frequency dependence must be fitted to the relaxation model for AMOS. A simple model was derived to account for the low-frequency behaviour of the coupling impedance for TT2-111-series ferrite; the low-frequency impedance was found to be dominated by μ and insensitive to ϵ in that particular case.

Power Transfer and Beam Instabilities

An alternate formula was derived for the bunch length in the presence of potential well distortion. The transverse analog of potential well distortion (the “bananer effect”) was analysed for the case in which the synchrotron angular frequency is large compared to the transverse radiation damping rate. Formulae were derived for the shifts in the complex frequencies of oscillation of the beam, with the lowest-order contribution from the stationary wake term included. Formulae applicable to a general coupling impedance (as opposed to a $Q = 1$ resonator impedance) were derived for the longitudinal and transverse microwave instability thresholds. The “effective elastance” was introduced as a means of unifying the treatment of multi-turn power dissipation, potential well distortion, the bananer effect, complex frequency shifts, and mode coupling. An extension of the effective elastance to include multi-bunch effects was given. All of the above results were formulated in a manner applicable to an arbitrary coupling impedance.

The direct power transfer to the ferrite was predicted from the calculated ferrite impedance. Including the indirect power transfer from the cavity and tapers, the predicted average power density is 12.8 W/cm^2 for the Porcupine loads in CESR-III.5; for CESR-V, the average power density is predicted to be 82.5 W/cm^2 . The maximum power density is predicted to be at least 1.5 to 1.7 times higher than the average.

Estimates were made for the static effects and instability thresholds to be expected from Porcupine loads in CESR-V. The ferrite was predicted to produce a slight shortening of the bunch ($\leq 2\%$) and a negligible static distortion in the transverse plane; of the various possible beam instabilities, the longitudinal microwave instability

was predicted to have the lowest threshold current, namely 27 mA per bunch. This value represents a lower bound, so the actual instability may arise at a significantly higher current. Since the design current for CESR-V is 11 mA per bunch, we do not expect the Porcupine loads to produce an instability.

Beam Measurements

A ferrite-lined section of decreased radius and increased length was fabricated and subjected to a beam test in CESR. The monopole and dipole loss factors of the ferrite assembly were measured calorimetrically; the short-range wake of the ferrite structure was also sampled via a calorimetric measurement. The measured monopole loss factor was within a factor of 2 of the predicted value. The dipole loss factor was consistent with predictions, although the signal-to-noise ratio for the dipole dissipation was not very favourable. The short-range wake results agreed with the predictions in the régime of interest (bunches more than one RF bucket apart). The monopole loss factor of the ferrite was checked independently via the RF power consumption of the beam: the RF power and calorimetric measurements were consistent, although the former was significantly less accurate than the latter. The effect of the ferrite on the beam, as manifested by the complex frequency shift, was near the reproducibility threshold of the measurements, a result which is consistent with our present understanding. An average power dissipation of 3.8 W/cm^2 was reached; 1 ferrite tile out of a total of 120 failed in the course of the test.

6.2 Discussion

The present Porcupine load design will likely be able to handle the power dissipation predicted for CESR-III.5; for CESR-V, the predicted power dissipation is excessive. If a CESR-V-like storage ring is to be built, a redesign of the HOM loads will probably be required. A reduction in the loss factor of the tapered transition from the 240 mm diameter beam tube would be a good start.

No beam instabilities due to the ferrite are predicted, even for the CESR-V case. Likewise, the distortion in the beam's longitudinal and transverse charge distribution is predicted to be insignificant. The results of the CESR beam test of the ferrite-lined section of magnified impedance are consistent with our predictions. Thus, there is no beam mechanics argument against the use of ferrite in future incarnations of CESR. Historically, however, the experimental arm of beam mechanics has always been a few paces ahead of its theoretical counterpart, so there may yet be some surprises in store for us. Although the results presented herein are more or less self-consistent, there are certainly aspects of the problem that are not yet fully understood; some of the unanswered questions are discussed in the next section.

The scaling with machine parameters for the various collective effects is fairly transparent in the approximate formulae that we have used; for example, when calculating static distortion or instability thresholds, the effective elastance (or the effective impedance, Λ_m , in the case of the microwave instability) is always multiplied by the

current per bunch and divided by the beam energy. Thus, by halving the impedance of the HOM loads, one could operate with the same stability margins at twice the current per bunch.

The fact that the beam is predicted to be stable even for the rather extreme machine parameters of CESR-V suggests that the scheme of placing the HOM loads on the beam line holds promise for use in RF systems for future cyclic accelerators. The placement of the HOM loads on the beam line is particularly attractive for a superconducting RF system, because the reduction in the accelerating mode's shunt impedance due to the increased beam tube diameter is offset by operation at a higher accelerating gradient. Thus, a similar HOM damping scheme is planned for the superconducting RF system for KEK-B [83]. HOM loads on the beam line (with absorption via a high electrical resistivity, in this case) are even being incorporated to supplement the waveguide coupler damping scheme in the normal-conducting RF system for the ATF Damping Ring at KEK [84]. Although we have considered only the storage ring case herein, HOM loads on the beam line may be of interest for future linear accelerators as well, since strongly-damped HOMs are an attractive solution to the problem of beam instabilities in linear accelerators. There might be yet another application for a layer of material on the inside of a beam tube: passive bunch shortening, as proposed by A. Burov [85].

6.3 Possibilities for Future Work

Microwave Properties

It would be worthwhile to measure the dependence of $\mu(\omega)$ and $\epsilon(\omega)$ on temperature, on the amplitude of the RF field, and on the amplitude of the external magnetostatic field. Such measurements might help to explain the slight dependence of the loss factor on current.

Coupling Impedance

It would be worthwhile to do more impedance measurements with the wire method in the frequency domain. A closer reconciliation between the wire results and the impedance predictions would be helpful. Wire measurements on a smaller diameter load would be preferable, because of the problems that can be expected due to waveguide modes with large-diameter tubes. Additional wire measurements might give more insight into the discrepancy between the predicted loss factor and the loss factor measured with the beam.

Power Transfer

A numerical prediction should be obtained for the longitudinal distribution in the power density induced directly by the beam in the Porcupine load. There are other interesting questions about the indirect power transfer to the ferrite: What fraction of

the power from the tapers and cavity propagates into the CESR beam tube instead of being dissipated in the ferrite? How do the modes above cutoff affect the distribution in the indirectly-induced ferrite power density? Can the worst-case power per load be reduced by placing multiple cavities in a large-diameter section of beam tube with tapers only at the ends, or does all the taper power end up in the load closest to it? A better understanding of these issues would be helpful in redesigning the RF system for operation at currents beyond the CESR-III goals.

Beam Instabilities

It would be worthwhile to apply a more general theory in the beam instability predictions. Things that could be incorporated include a more rigorous treatment of radial modes, a more realistic model for the machine (in which, for example, the localised nature of impedance-producing structures and the the betatron function's dependence on position are included in a less *ad hoc* manner), a treatment of counter-rotating beams, and the inclusion of the stationary wake term in the analysis of mode coupling. It would be worthwhile also to include the impedance of other elements in the storage ring in a more complete analysis of the ring's stability. In addition, a time domain simulation of the beam's motion would complement the perturbation approach that was used herein.

Beam Measurements

Much more could be learned by repeating the L3 ferrite beam test. Things that could be done include

1. frequency shift measurements for the $l = 2$ longitudinal mode or an $l = \pm 1$ transverse mode. This would allow us to check the frequency shift prediction for the ferrite's stationary wake.
2. single-bunch calorimetric power measurements at lower cooling water flow rates. This would indicate whether the ferrite loss factor retains its slope at low currents.
3. calorimetric measurements as a function of current with 2 bunches spaced one bucket apart. This would indicate whether the power dissipation is indeed non-quadratic in I , as expected from the hypothesis about lengthening in the second bunch.

Additional possibilities which would require further preparation include

1. bunch length measurements. If the bunch length in CESR could be measured to better than 5%, the bunch shortening predictions could be checked.
2. a "bunch phase" measurement of the total loss factor of the ring with and without the ferrite present. This technique might give better sensitivity than the measurement of RF power consumption.

3. the use of a magnetostatic field to reduce the dissipation in the ferrite. This might allow more sensitive measurements of the effect of the ferrite on the beam.
4. a long-term evaluation of the loads' performance in the presence of a high density of beam-induced power.

A few of the aforementioned measurements could be made with the Porcupine loads in the second beam test of the superconducting RF system, for which preparations are presently being made.

Appendix A

Permittivity and Permeability Models for AMOS

As discussed in Chapter 3, simplified models were used to specify the μ and ϵ of the ferrite materials in the AMOS calculations. In the calculations with TT2-111V, ϵ was assumed to have a constant real part and an imaginary part given by a constant electrical conductivity σ_e via $\text{Im } \epsilon = -\sigma_e/\omega$. The values used were $\text{Re } \epsilon = 14$ and $\sigma_e = 0.0023 \text{ } (\Omega \text{ m})^{-1}$. A three-term relaxation model was used for μ (see Equation (3.9)). The fitted parameters are given in Table A.1.

In the calculations with Ferrite-50, two-term relaxation models were used for both μ and ϵ . The parameters are also given in Table A.1. The measured μ and ϵ and the fitted values for the Ferrite-50 case are compared in Figures A.1 and A.2.

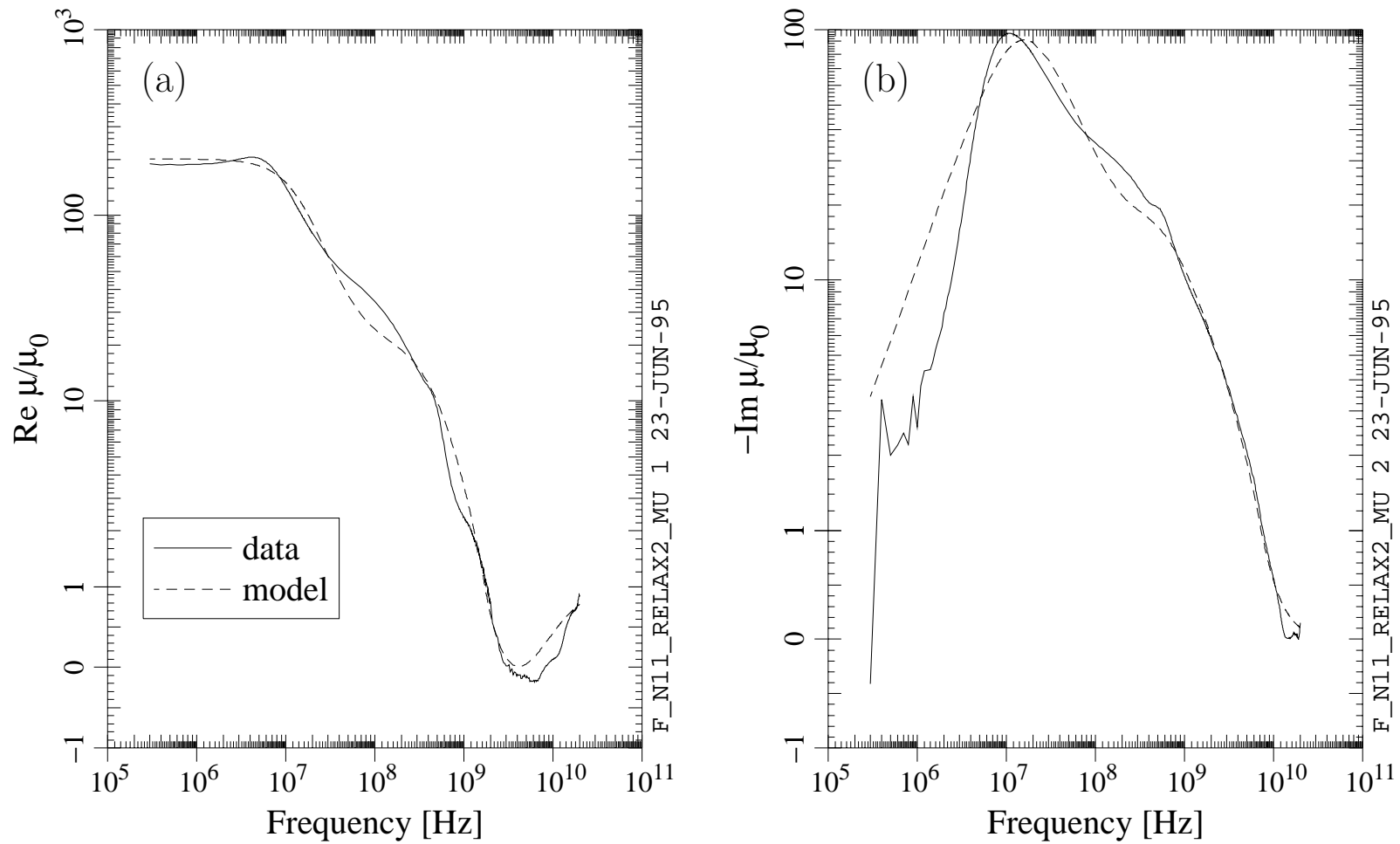


Figure A.1. Measured and fitted values of (a) the real part and (b) the imaginary part (times -1) of μ for Ferrite-50 used in the coupling impedance predictions.

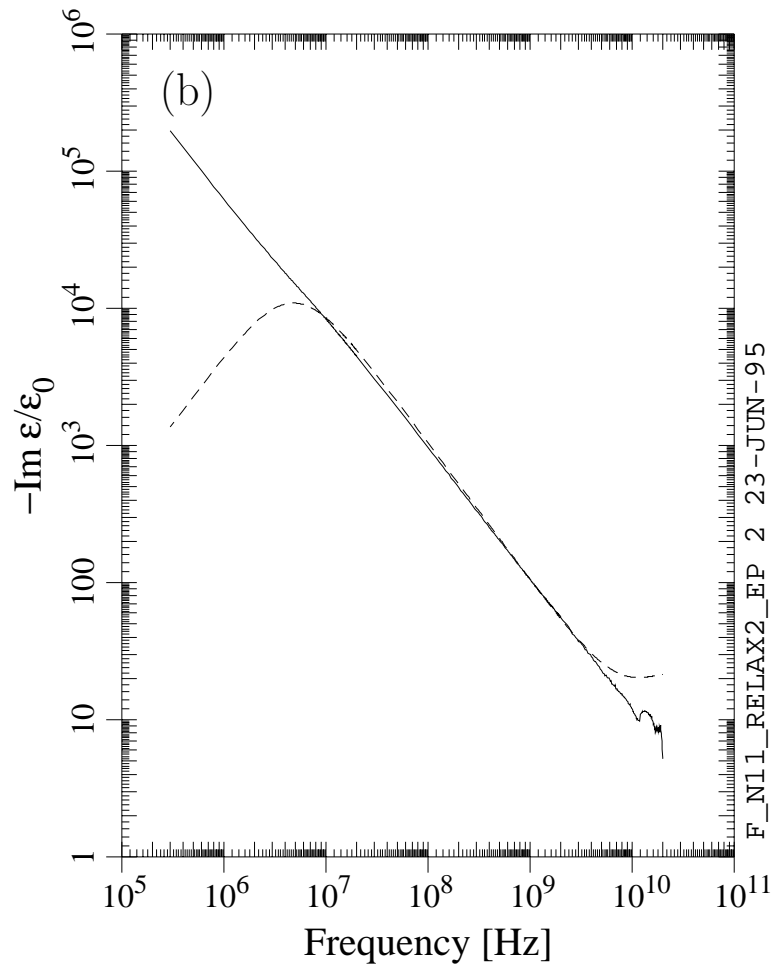
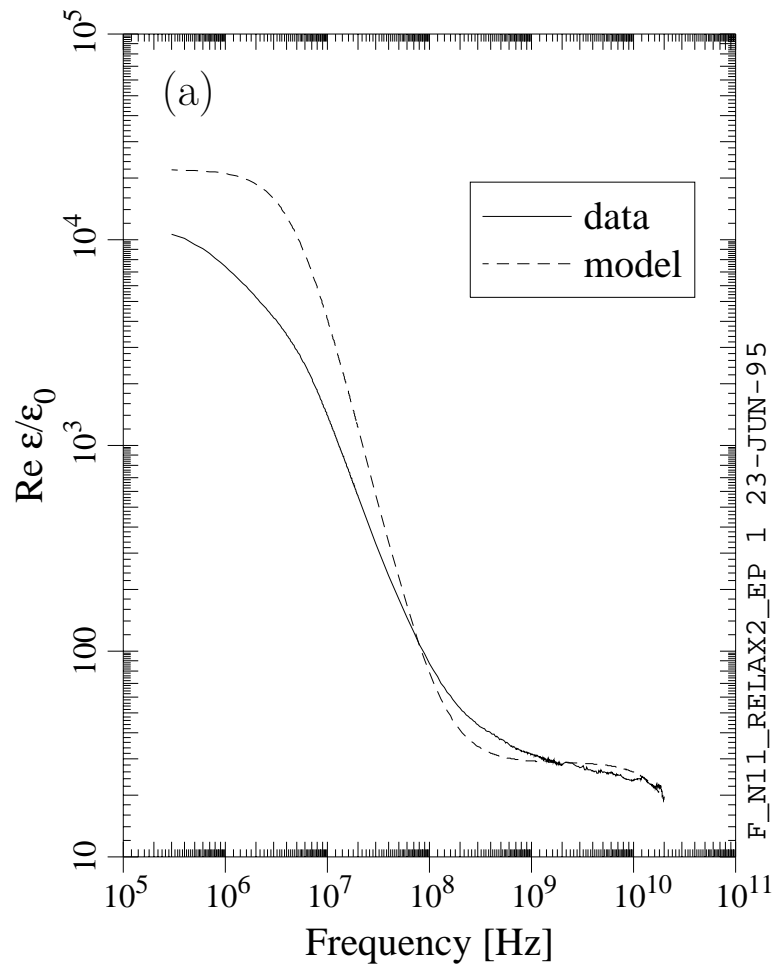


Figure A.2. Measured and fitted values of (a) the real part and (b) the imaginary part (times -1) of ϵ for Ferrite-50 used in the coupling impedance predictions.

Table A.1. Relaxation model parameters used in AMOS.

Item	j	$\alpha_j/(2\pi)$ [GHz]	$(\beta_j - \gamma_j)/(2\pi)$ [GHz]	$(\beta_j + \gamma_j)/(2\pi)$ [GHz]
3-term fit for μ of TT2-111V	1	3	0.009	12
	2	8	0.08	12
	3	14	0.3	12
2-term fit for μ of Ferrite-50	1	5.75	0.016	14
	2	20.8	0.485	7.08
2-term fit for ϵ of Ferrite-50	1	4800	40	80
	2	210	0.0048	48

Appendix B

The Effective Porcupine Elastance: AMOS vs. Analytic

The monopole elastances (see Section 4.2) obtained from the analytic coupling impedance prediction for the Porcupine HOM load with $\sigma_z = 10$ mm are compared to AMOS values in Figure B.1; the integral formulation was used in both cases. The corresponding analytic and AMOS values for the dipole case are compared in Figure B.2.

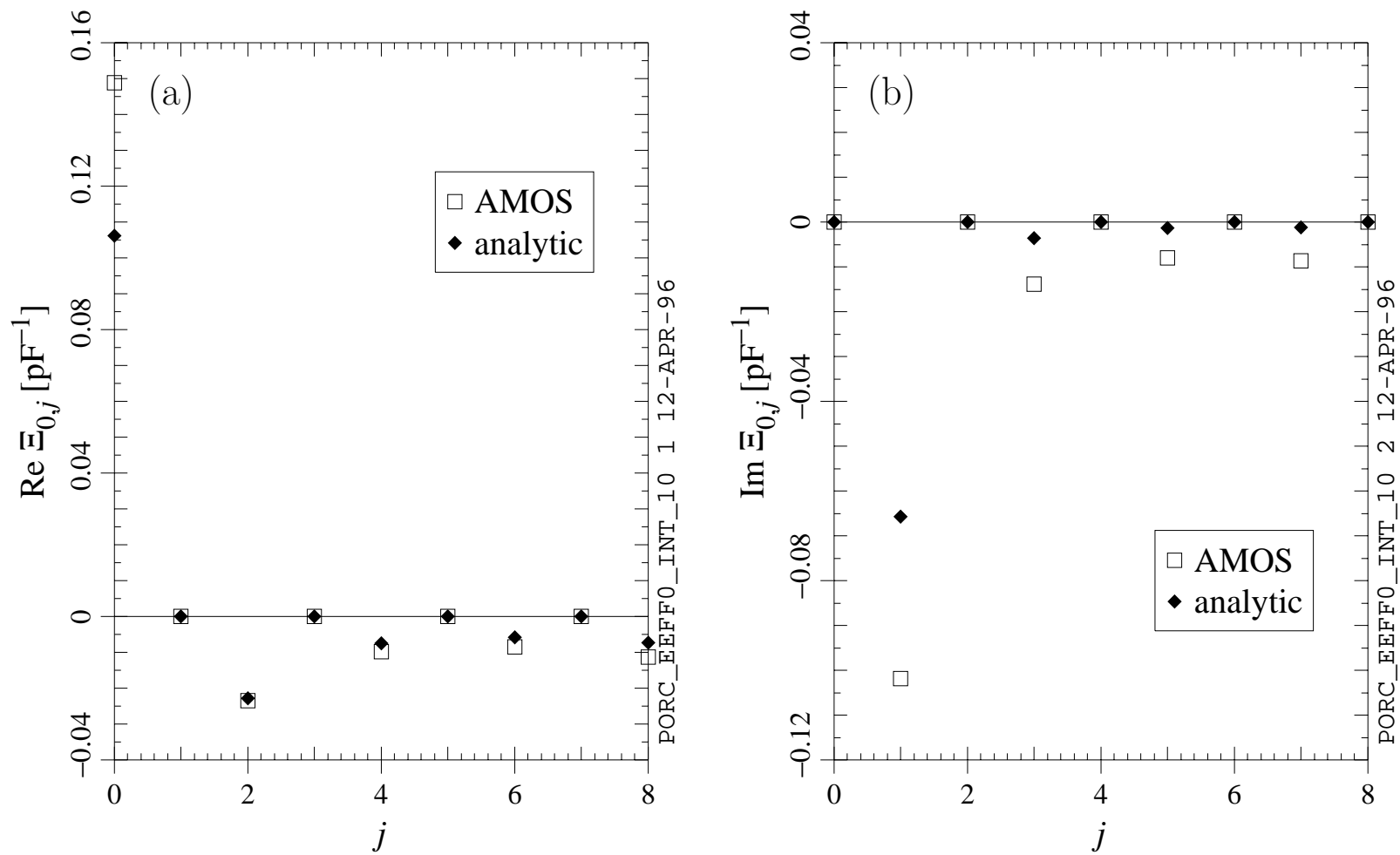


Figure B.1. Comparison of AMOS and analytic values for (a) the real part and (b) the imaginary part of the effective monopole elastance for one Porcupine load, based on the integral formulation, with $\sigma_z = 10$ mm.

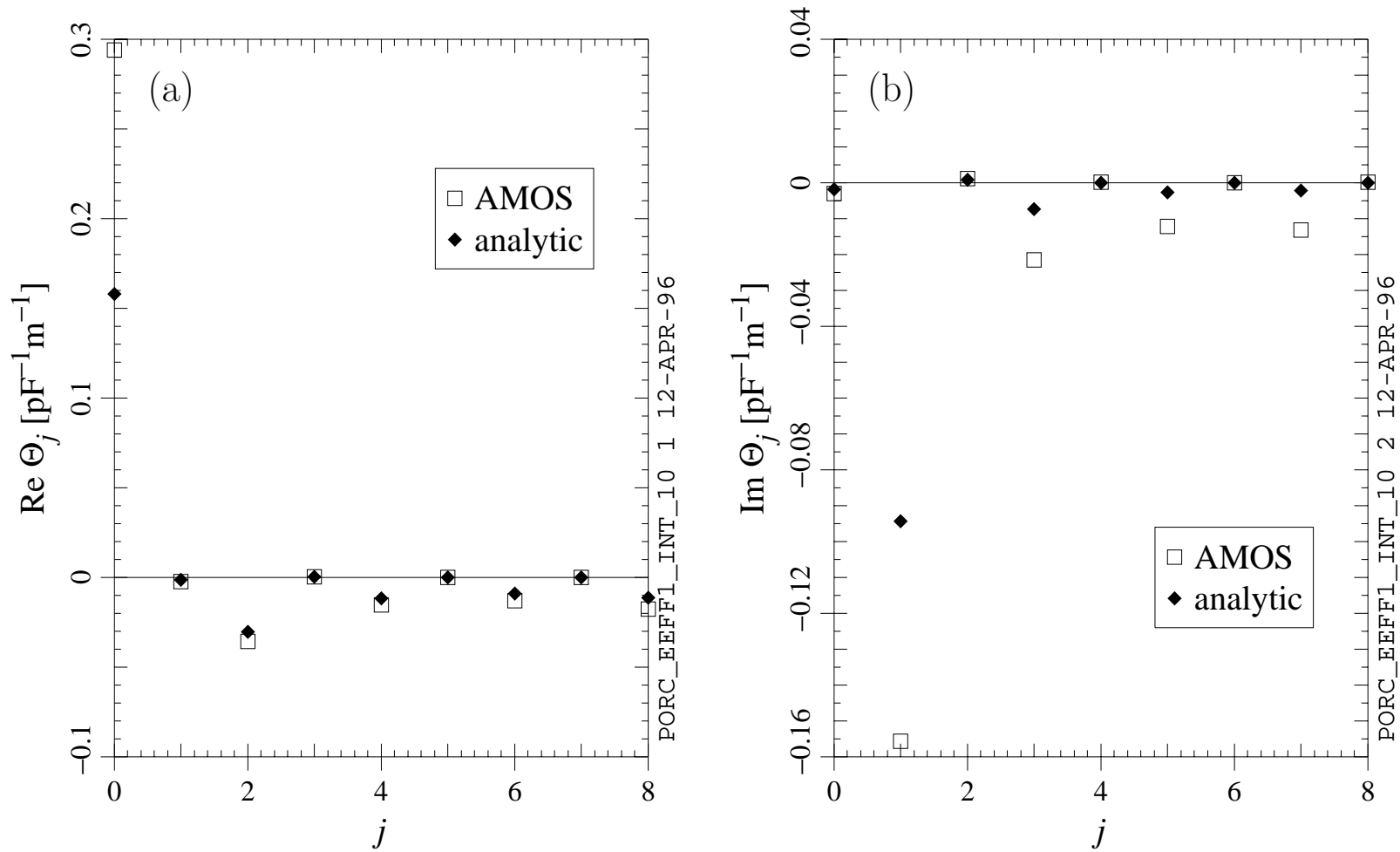


Figure B.2. Comparison of AMOS and analytic values for (a) the real part and (b) the imaginary part of the effective dipole elastance for one Porcupine load, based on the integral formulation, with $\sigma_z = 10$ mm and $\xi = 1$.

Appendix C

Model for the CESR Loss Factor

The predicted loss factor as a function of bunch length for CESR discussed in Chapter 5 was obtained via scaling laws derived by M. Billing for various machine elements [75]. In the past, good agreement has been seen between this model and the loss factor measured via the RF power [86]. Because of recent changes in CESR, the scaling laws given in [75] are a little bit out of date. The scaling laws that we used in the analysis of the L3 test are given in Table C.1. The values given in Table C.1 reflect the elements present in CESR during the L3 test, not the present state of the storage ring. The values are given in terms of G_0^{\parallel} , which is related to k_0^{\parallel} as follows:

$$k_0^{\parallel} = \frac{G_0^{\parallel}}{4\pi\epsilon_0}. \quad (\text{C.1})$$

The quantity G_0^{\parallel} is the equivalent of k_0^{\parallel} in the Gaussian system of units.

The primary difference in the CESR loss factor is due to the change in the number of RF cavity cells (reduced from a total of 28 to a total of 20 when the two 14-cell NRF cavities were replaced by four penta-cell NRF cavities). The other difference is in the horizontal separators. At the time of the L3 test, three of the separators had been replaced by new models with a lower impedance [87]. The loss factor of the new separators is believed to be 1/2 to 1/4 that of the old separators for $\sigma_z \approx 23$ mm [88]; the dependence of the new separators' loss factor on σ_z is not yet known. As an approximation, we assumed the same dependence on σ_z as for the old separators, with a factor of 1/2 between old and new models (as indicated in Table C.1).

Table C.1. Scaling laws for CESR elements. Only the parasitic term is included in the G_0^{\parallel} of the RF cavity cells.

Item	G_0^{\parallel} per unit	Number in CESR
RF cavity cell	$64 \text{ m}^{-1} \exp\left(-\frac{\sigma_z}{19.4 \text{ mm}}\right)$	20
Fast kicker ceramic	$2.62 \text{ m}^{-1} \left(\frac{10 \text{ mm}}{\sigma_z}\right)$	4
Bumper ceramic	$0.74 \text{ m}^{-1} \left(\frac{10 \text{ mm}}{\sigma_z}\right)$	13
Gate valve	$0.68 \text{ m}^{-1} \left(\frac{10 \text{ mm}}{\sigma_z}\right)$	22
Horizontal separator (old)	$116.9 \text{ m}^{-1} \left(\frac{10 \text{ mm}}{\sigma_z}\right)^{1.176}$	1
Horizontal separator (new)	$58.45 \text{ m}^{-1} \left(\frac{10 \text{ mm}}{\sigma_z}\right)^{1.176}$	3
Vertical separator	$60.5 \text{ m}^{-1} \left(\frac{10 \text{ mm}}{\sigma_z}\right)^{1.176}$	2
Sliding joint	$1.41 \text{ m}^{-1} \left(\frac{10 \text{ mm}}{\sigma_z}\right)^2$	100
Horizontal scrapers	$4.18 \text{ m}^{-1} \left(\frac{10 \text{ mm}}{\sigma_z}\right)^5$	100
Vertical scrapers	$41.8 \text{ m}^{-1} \left(\frac{10 \text{ mm}}{\sigma_z}\right)^5$	8
Distributed pumps (per metre)	$0.046 \text{ m}^{-1} \left(\frac{10 \text{ mm}}{\sigma_z}\right)^5$	600 m
Lumped pumps	$0.55 \text{ m}^{-1} \left(\frac{10 \text{ mm}}{\sigma_z}\right)^5$	100

Bibliography

- [1] Y. H. Chin, in *Proceedings of the 1993 Particle Accelerator Conference*, IEEE Publishing, Piscataway, New Jersey, 1993, p. 3414–3416.
- [2] D. Rubin, in *Proceedings of the 1995 Particle Accelerator Conference*, IEEE Publishing, Piscataway, New Jersey, 1996, p. 481–485.
- [3] J. T. Seeman, *ibid.*, p. 486–490.
- [4] Shin-Ichi Kurokawa, *ibid.*, p. 491–494.
- [5] M. P. Level *et al.*, in *Proceedings of the 1993 Particle Accelerator Conference*, IEEE Publishing, Piscataway, New Jersey, 1993, p. 1465–1467.
- [6] S. Greenwald *et al.*, in *Conference Record of the 1991 IEEE Particle Accelerator Conference*, IEEE Publishing, New York, p. 226–228.
- [7] J. Kirchgessner *et al.*, “Superconducting RF Activities at Cornell University,” presented at the Seventh Workshop on RF Superconductivity, Saclay, Gif sur Yvette, France, 17–20 October 1995.
- [8] D. Moffat *et al.*, in *Proceedings of the 1993 Particle Accelerator Conference*, IEEE Publishing, Piscataway, New Jersey, 1993, p. 763–765.
- [9] E. Nordberg *et al.*, *ibid.*, p. 995–997.
- [10] J. Kirchgessner *et al.*, in *Proceedings of the 6th Workshop on RF Superconductivity*, CEBAF, Newport News, Virginia, 1994, p. 67–76.
- [11] W. Hartung, “In Search of a Coupler for a *B* Factory Cavity,” Report SRF-900924/6, Cornell LNS, Ithaca, New York (October 1990).
- [12] D. Metzger *et al.*, in *Proceedings of the 1993 Particle Accelerator Conference*, IEEE Publishing, Piscataway, New Jersey, 1993, p. 1399–1401.
- [13] M. Pisharody *et al.*, in *Proceedings of the 1995 Particle Accelerator Conference*, IEEE Publishing, Piscataway, New Jersey, 1996, p. 1720–1722.
- [14] H. Padamsee *et al.*, *ibid.*, p. 1515–1517.
- [15] E. Haebel, P. Marchard, & J. Tückmantel, “On the Calculation of Beam

- Tube Propagation of Cavity Modes from SUPERFISH or URMEL,” Report CERN/EF/RF 84-1, CERN, Geneva, Switzerland (March 1984).
- [16] S. Fornaca *et al.*, in *Proceedings of the 1987 IEEE Particle Accelerator Conference*, IEEE Publishing, New York, 1987, p. 1818–1820.
- [17] W. Hartung & E. Haebel, in *Proceedings of the 1993 Particle Accelerator Conference*, IEEE Publishing, Piscataway, New Jersey, 1993, p. 898–900.
- [18] V. Veshcherevich *et al.*, in *Proceedings of B Factories: The State of the Art in Accelerators, Detectors, and Physics*, Report SLAC-400/CONF-9204126, SLAC, Stanford, California, 1992, p. 177–180.
- [19] D. Moffat *et al.*, in *Proceedings of the 1993 Particle Accelerator Conference*, IEEE Publishing, Piscataway, New Jersey, 1993, p. 977–979.
- [20] B. Vakoc, “HOM Spectra and Dissipated Power Density Profiles for the SRF cavity with a Ferrite HOM Load: Calculations with CLANS and Analysis,” Report SRF-950811-11, Cornell LNS, Ithaca, New York (August 1995).
- [21] M. de Jong, F. Adams, & R. Hutcheon, *Journal of Microwave Power and Electromagnetic Energy* **27**, p. 136–142 (1992).
- [22] D. G. Myakishev & V. P. Yakovlev, in *Proceedings of the 1995 Particle Accelerator Conference*, IEEE Publishing, Piscataway, New Jersey, 1996, p. 2348–2350.
- [23] W. Hartung *et al.*, “Measurements of the Microwave Properties of Some Absorbing Materials,” presented at the Microwave-Absorbing Materials for Accelerators Workshop, CEBAF, 22–24 February 1993 (also SRF-930322/04).
- [24] W. Hartung, D. Moffat, & T. Hays, “Measurements of the Electromagnetic Properties of Some Microwave-Absorbing Materials,” Report SRF-930113/01, Cornell LNS, Ithaca, New York (January 1993).
- [25] Robert Chiang, “Additional Measurements of the Microwave Properties of Some Absorbing Materials,” Report SRF-940907/09, Cornell LNS, Ithaca, New York (August 1994).
- [26] Ph. Barnes (Cornell University), private communication.
- [27] F. Caspers, “Experience with UHV-Compatible Microwave Absorbing Materials at CERN,” presented at the Microwave-Absorbing Materials for Accelerators Workshop, CEBAF, 22–24 February 1993.
- [28] W. H. von Aulock, Ed., *Handbook of Microwave Ferrite Materials*, Academic Press, New York, 1965, p. 385–388.
- [29] W. B. Weir, *Proc. IEEE* **62**, p. 33–36 (January 1974).

- [30] “Materials Measurement: Measuring the Dielectric Constant of Solids with the HP 8510 Network Analyzer,” Product Note 8510-3, Hewlett-Packard, Palo Alto, California (August 1985).
- [31] W. Barry, *IEEE Trans. Microwave Theory Tech.* **MTT-34**, p. 80–84 (January 1986).
- [32] R. M. Hutcheon *et al.*, in *Conference Record of the 1991 IEEE Particle Accelerator Conference*, IEEE Publishing, New York, 1991, p. 795–797.
- [33] D. Moffat, “Measuring the Complex Permeability, ϵ_r , and Permittivity, μ_r , using the HP 8720A Network Analyzer and the HP 9816 Computer,” Report SRF/D-910306/30, Cornell LNS, Ithaca, New York (March 1991).
- [34] W. Hartung, D. Moffat, & T. Hays, “Computer-Controlled Network Analyser Measurements of Electromagnetic Properties: A User’s Guide,” Report SRF/D-950526/1, Cornell LNS, Ithaca, New York (May 1995).
- [35] T. Tajima *et al.*, in *Proceedings of the 6th Workshop on RF Superconductivity*, CEBAF, Newport News, Virginia, 1994, p. 962–980.
- [36] R. Boni *et al.*, “Studies of Parasitic Mode Absorbers for the Frascati Φ -Factory RF Cavities,” presented at the Microwave-Absorbing Materials for Accelerators Workshop, CEBAF, 22–24 February 1993.
- [37] G. P. Rodrigue, “Magnetic Loss in Ferrites,” *ibid.*
- [38] John David Jackson, *Classical Electrodynamics*, Second Edition, John Wiley & Sons, New York, 1975.
- [39] Alexander W. Chao, in *Physics of High Energy Particle Accelerators*, AIP Conference Proceedings no. 105, American Institute of Physics, New York, 1983, p. 353–523.
- [40] Bruno Zotter, in *Physics of Particle Accelerators*, AIP Conference Proceedings no. 153, American Institute of Physics, New York, 1987, p. 663–696.
- [41] L. Palumbo & V. G. Vaccaro, in *CERN Accelerator School: Advanced Accelerator Physics—Proceedings*, Report CERN 87-03, CERN, Geneva, Switzerland, 1987, p. 341–369.
- [42] S. A. Heifets & S. A. Kheifets, *Rev. Mod. Phys.* **63**, p. 631–673 (July 1991).
- [43] Alexander Wu Chao, *Physics of Collective Beam Instabilities in High Energy Accelerators*, John Wiley & Sons, New York, 1993.
- [44] Michael G. Billing, Joseph L. Kirchgessner, & Ronald M. Sundelin, *IEEE Trans. Nucl. Sci.* **NS-26**, p. 3583–3585 (1979).

- [45] L. S. Walling *et al.*, *Nucl. Instrum. Methods Phys. Res.* **A281**, p. 433–447 (1989).
- [46] T. Weiland, *Nucl. Instrum. Methods Phys. Res.* **212**, p. 13–21 (1983).
- [47] J. F. DeFord, G. D. Craig, & R. McLeod, in *Proceedings of the 1989 IEEE Particle Accelerator Conference*, IEEE Publishing, New York, 1989, p. 1181–1183.
- [48] B. Zotter, *Part. Accel.* **1**, p. 311–326 (1970).
- [49] A. Piwinski, *IEEE Trans. Nucl. Sci.* **NS-24**, p. 1364–1366 (1977).
- [50] N. Akasaka (KEK Laboratory), private communication.
- [51] H. Henke, *IEEE Trans. Nucl. Sci.* **NS-32**, p. 2335–2337 (October 1985).
- [52] W. Chou & Y. Jin, in *Proceedings of the 1989 IEEE Particle Accelerator Conference*, IEEE Publishing, New York, 1989, p. 909–911.
- [53] Milton Abramowitz & Irene A. Stegun, Eds., *Handbook of Mathematical Functions*, Dover, New York, 1965.
- [54] M. Furman, H. Lee, & B. Zotter, “Energy Loss of Bunched Beams in RF Cavities,” Report SSC-86, SSC CDG, LBL, Berkeley, California (August 1986).
- [55] W. Hartung *et al.*, *Proceedings of the 1993 Particle Accelerator Conference*, IEEE Publishing, Piscataway, New Jersey, 1993, p. 3450–3452.
- [56] M. Zisman, *Part. Accel.* **23**, p. 289–307 (1988).
- [57] Y. H. Chin, “User’s Guide for ABCI Version 8.8,” LBL-35258, LBL, Berkeley, California, also CERN SL/94-02 (AP), CERN, Geneva, Switzerland (February 1994).
- [58] F. Ebeling *et al.*, “MAFIA User Guide,” Report LA-UR-90-1307, LANL, Los Alamos, New Mexico (November 1989).
- [59] S. Belomestnykh & W. Hartung, “Calculations of the Loss Factor of the BB1 Superconducting Cavity Assemblies,” Report SRF-960202/01, Cornell LNS, Ithaca, New York.
- [60] S. Belomestnykh & B. Vakoc (Cornell University), private communication.
- [61] B. Zotter, “Potential-well bunch lengthening,” Report CERN SPS/81-14 (DI), CERN, Geneva, Switzerland (May 1981).
- [62] W. Hartung, Internal Report, Cornell LNS, Ithaca, New York (to be written).
- [63] R. E. Meller, in *Proceedings of the 1987 IEEE Particle Accelerator Conference*, IEEE Publishing, New York, 1987, p. 1155–1157.

- [64] A. W. Chao & S. Kheifets, *IEEE Trans. Nucl. Sci.* **NS-30**, p. 2571–2572 (August 1983).
- [65] D. Boussard, “Observation of Microwave Longitudinal Instabilities in the CPS,” Report LABII/RF/Int./75-2, CERN, Geneva, Switzerland (April 1975).
- [66] J. M. Wang & C. Pellegrini, in *Proceedings of the 11th International Conference on High-Energy Accelerators*, Experientia Supplementum Vol. 40, Birkhäuser Verlag, Basel, 1980, p. 554–561.
- [67] R. D. Ruth & J. M. Wang, *IEEE Trans. Nucl. Sci.* **NS-28**, p. 2405–2407 (1981).
- [68] I. S. Gradshteyn & I. M. Ryzhik, *Table of Integrals, Series, and Products*, English translation of the Fourth Russian Edition, Academic Press, San Diego, 1980, p. 1110.
- [69] Michael S. Zisman, in *Beam Dynamics Issues of High-Luminosity Asymmetric Collider Rings*, AIP Conference Proceedings no. 214, American Institute of Physics, New York, 1990, p. 81–129.
- [70] S. Belomestnykh *et al.*, in *Proceedings of the 1995 Particle Accelerator Conference*, IEEE Publishing, Piscataway, New Jersey, 1996, p. 3394–3396.
- [71] E. B. Blum *et al.*, *Nucl. Instrum. Methods Phys. Res.* **207**, p. 321–324 (1983).
- [72] Z. Greenwald *et al.*, in *Conference Record of the 1991 IEEE Particle Accelerator Conference*, IEEE Publishing, New York, p. 1246–1248 (also CLNS-91/1084).
- [73] Alexander Temnykh, “Wake function study using two spaced bunches,” Report CBN 95-11, Cornell LNS, Ithaca, New York (July 1995).
- [74] D. Rice *et al.*, *IEEE Trans. Nucl. Sci.* **NS-28**, p. 2446–2448 (1981).
- [75] M. Billing, “Higher Mode Power Loss Limitations for Beam Currents in CESR,” Report CBN 84-15, Cornell LNS, Ithaca, New York (1984).
- [76] M. Billing, in *Particles and Fields*, Series 52, AIP Conference Proceedings no. 281, American Institute of Physics, New York, p. 55 (also CLNS 93/1203).
- [77] M. G. Billing *et al.*, in *Proceedings of the 1989 IEEE Particle Accelerator Conference*, IEEE Publishing, New York, 1989, p. 1163–1165.
- [78] S. Belomestnykh (Cornell University), private communication.
- [79] M. Tigner (Cornell University), private communication.
- [80] S. Belomestnykh *et al.*, in *Proceedings of the 1995 Particle Accelerator Conference*, IEEE Publishing, Piscataway, New Jersey, 1996, p. 3391–3393.
- [81] S. Belomestnykh *et al.*, “The Interaction between a Beam and a Superconduct-

- ing Cavity Module: Measurements in CESR and CESR-Phase III Goals,” presented at the International Workshop on Collective Effects and Impedance for B-Factories, Tsukuba, Japan, 12–17 June 1995.
- [82] T. Tajima *et al.*, “Beam Test of Ferrite Absorber in TRISTAN MR for KEKB-SCC,” *ibid.*
- [83] T. Furuya *et al.*, “Superconducting Accelerating Cavity for KEK B-Factory,” presented at the Seventh Workshop on RF Superconductivity, Saclay, Gif sur Yvette, France, 17–20 October 1995.
- [84] F. Hinode & S. Sakanaka, in *Proceedings of the 1995 Particle Accelerator Conference*, IEEE Publishing, Piscataway, New Jersey, 1996, p. 1756–1758.
- [85] A. V. Burov & A. V. Novokhatski, “The Device for Bunch Selffocussing,” Preprint 90-28, BINP, Novosibirsk, Russia (1990).
- [86] D. Morse (Cornell University), private communication.
- [87] James J. Welch & Zhong Xiong Xu, in *Conference Record of the 1991 IEEE Particle Accelerator Conference*, IEEE Publishing, New York, 1991, p. 1851–1853.
- [88] J. Welch (Cornell University), private communication.